Utilization of synchrotron radiation X-ray microscopy, micro-probe, and spectroscopy to characterize the carbon, sulfur, and iron speciation of particles from buoyant, deep-sea hydrothermal plumes in the

A dissertation
SUBMITTED TO THE FACULTY OF
UNIVERSITY OF MINNESOTA
BY

Brandi Kamermans

IN PARTIAL FULFILLMENT OF THE REQUIREMENTS
FOR THE DEGREE OF
DOCTOR OF PHILOSOPHY

Advisor: Brandy Toner, Ph.D.

April 2017

Acknowledgements

For financial support, I thank the National Science Foundation Graduate Research Fellowship program (BRK), the University of Minnesota Graduate School Doctoral Dissertation Fellowship (BRK), the Department of Earth Sciences Sam Goldrich Footsteps Award, and the University of Minnesota Graduate School Travel Research Fellowship. This work was supported by a grant from Gordon and Betty Moore Foundation (Brandy M. Toner, Greg J. Dick, J.A. Breier, Housuhou J.). The SUPR-V2 was funded by the Gordon and Betty Moore Foundation through Grant GBMF 2764 to JAB, whose time was also supported by NSF (OCE- 1028990). I would like to thank the ROV *Jason* operations team, the R/V *Atlantis* crew (AT18–16), and the OASES 2012 science party for assistance and support with all aspects of the cruise, which was supported jointly by grants to CRG from the National Science Foundation (NSF; OCE-1061863) and National Aeronautics and Space Administration′s (NASA) Astrobiology Science and Technology for Exploring Planets (ASTEP) program (NNX09AB75G) and to M.C. from the NSF(OCE-1061881).

Thank you to my thesis committee (William Seyfried, Jake Baily, Brandy Toner, and Cody Sheik). I appreciate all the feedback you have provided to make this dissertation complete. Thank you to Jake and Bill for all your support, starting with my preliminary written and oral examinations.

I am grateful for my advisor, Dr. Brandy Toner. When I decided on the University of Minnesota, it was the best decision I have made for myself. It's because of Dr. Toner's support that I was successful. Thank you for being a role model, inspirational science mom, and a colleague and friend.

I am thankful for Sarah L. Nicholas (University of Minnesota, UMN), Jeffry V. Sorensen (UMN), Rebecca H. Sims (UMN), Collen Hoffman (UMN), Matthew A. Marcus (Advanced Light Source, ALS), Josep Roque-Rosell (ALS), Sirine Fakra, and Teng Zeng (UMN, now Syracuse University) for assistance with data collection at ALS beamline 10.3.2. Rebecca H. Sims, Colleen Hoffman, Brian T. Glazer (Hawaii), Amanda Haddad, and David Kilcoyne (ALS) for assistance with data collected at the ALS beamline 5.3.2.2. Aubrey Dunshee (UMN), Jeffry V. Sorenson, Amy J. Gartman, and Nobu Tamura (ALS) for assistance with data collected at the ALS beamline 12.3.2. Sarah L. Nicholas and Mike Ottman for assistance with data collection at the APS beamline 13-ID-E. Olha Furman (UMN, now University of Canberra), Jill Coleman Wasik, and Rebecca Sims for assistance with data collection at the APS beamline 9-BM. Olha Furman, Rebecca Sims, David Vine (now ALS), and Benjamin Stripe for assistance with data collection at 2-ID-B. The Advanced Light Source is supported by the Director, Office of Science, Office of Basic Energy Sciences, of the U.S. Department of Energy under Contract No. DE-AC02-05CH11231. The Advanced Photon Source is an Office of Science User Facility operated for the U.S. Department of Energy Office of Science by Argonne National Laboratory.

Thank you to everyone in the Department of Earth Sciences at the University of Minnesota. Thank you to Sharon Kressler, Kathy Ohler, and Jennifer Petrie for making Pillsbury Hall a second home. Thank you to everyone in the Department of Soil, Water, and Climate for making Soil, Water, and Climate a haven for me while I worked and wrote in S503. I am especially grateful to Kari Jarcho and Marjorie Bonse. A special thank you to Beth Fisher, Sarah L. Nicholas, Colleen Hoffman, Rebecca Sims, Aubrey Dunshee, and Mike Ottman for being great colleagues and friends.

I'm thankful for my family. The sulfur oxidation indices in CHAPTER 3 would not have been possible without you, dad, living with me in 'the room' and going to the library with

me those last few months I spent in Saint Paul. I'm thankful to both my mom and my dad for being the greatest grandparents to Atticus while I wrote this dissertation. The time you spent with Atticus will be precious to him and to me forever. These chapters were written because of you, "Ayóó ánííníshí". Finally, I am grateful to my husband for accepting my invitation to go on this adventure. We could not have spent the first 4 years of our marriage in a better place than the Twin Cities. I look forward to our next adventure together.

Dedication

This thesis is dedicated to my son, Robert Atticus Kamermans.

Abstract

The purpose of this research study was to investigate the geochemical inputs to rising hydrothermal vent plumes of the Mid-Cayman Rise. Physical, biological, and chemical processes active within the fluids lead to particle alteration and modulate hydrothermal fluxes to the deep ocean. To assess how chemical, physical, and biological processes modulate hydrothermal fluxes to the deep ocean at the Mid-Cayman Rise, the speciation of Fe, S, and C was measured for particles and aggregates using: (1) microprobe S 1s and Fe 1s X-ray absorption near edge structure (XANES) spectroscopy, (2) microprobe X-ray fluorescence (XRF) chemical mapping, and (3) scanning transmission X-ray microscopy (STXM) based C 1s and Fe 2p XANES. The high resolution spectromicroscopy and X-ray microprobe analyses allowed for the characterization and speciation of nanoparticulate minerals at spatial scales relevant to in situ microbial and chemical processes.

The Mid-Cayman Rise is an ultraslow spreading center located in the Caribbean Sea. The Mid-Cayman Rise hosts two hydrothermal vents that produce geochemically diverse fluids: (1) Beebe, the deepest (5000 ± 50 meters) known high-temperature (398 oC) vent site with high iron and sulfur, and (2) Von Damm (2300 ± 50 meters) with fluids at 110 to 200 oC, with high methane, hydrogen, and sulfur, and low iron (Kinsey and German, 2013). My samples were collected with a newly developed instrument, called the SUPR (SUspended Particle Rosette) (Breier et al., 2014). The SUPR was developed for high-precision collection of deep-sea samples, and it also made it possible to collect samples for complementary research efforts. Particle samples were collected in-situ on 0.2 micrometer (μm; 10-6 meter) polycarbonate filters, and kept anoxic to preserve the oxidation state of the materials.

Carbon XANES of Von Damm fluids reveal the presence of biomolecules such as proteins, lipids, polysaccharides, and chitin in plume particles. Iron 2p imaging and

XANES indicate that nano-particulate Fe minerals are associated with particulate organic C (POC). The S 1s XANES and chemical mapping data suggests metal sulfides are formed in the Von Damm and Beebe Vents fluids either in the subsurface or as the fluids emerge into the deep ocean. The presence of sulfonate, sulfone, and ester sulfate, as well as elemental S, indicate that microbial processes and chemical oxidation occur in the subsurface or in the near vent samples. In the Von Damm particles, a shift from strongly reduced to oxidized, including the appearance of intermediate S-bearing functionalities, suggests turbulent mixing of Von Damm fluids with seawater provide oxic and pH neutral conditions where chemical and biological interactions can occur. The Fe 1s XANES observations capture trends that suggest particles within the Von Damm and Beebe Vents could be sourced from chemical processes within the plume and physical entrainment processes from multiple sources.

Table of Contents

CHAPTER 4.
Iron 1s X-ray absorption near edge structure (XANES) spectroscopy of particles within the buoyant plume at Von Damm and Beebe Vents

List of Tables

CHAPTER 4

Supplemental tables

List of Figures

CHAPTER 1

CHAPTER 2

Supplemental figures

CHAPTER 3

Supplemental figures

Chapter 1

INTRODUCTION

Hydrothermal vents are located along the global mid-ocean ridge, a 60,000km-long volcanic mountain range that crosses all the major ocean basins on Earth (Figure 1.1; German and Seyfried, 2014). Hydrothermal vents emit hot, iron (Fe)- and sulfur (S)-rich fluids into the deep-ocean. The deep-ocean is cold (2 °C) and oxygen-rich (~200µmol/kg), whereas the fluids from vents can be very hot (350 °C) and anoxic. Along hydrothermal venting, seawater is circulated through fractures in the earth's crust. The fractures act as conduits for seawater as seawater is circulated into the earth, it is heated, then the seawater is chemically altered because it reacts with the host rock as it travels downward, reaching temperatures that exceed 400oC (German and Seyfried, 2014). The seawater is re-emitted to the deep-sea as heated, reduced, and chemically altered fluids. The composition of the seawater is changed through interactions with rocks under hydrothermal conditions, enriching the fluids in some elements and depleting others (German and Seyfried, 2014). Elements, such as silicon (Si), manganese (Mn), and Fe, and compounds, such as hydrogen sulfide (H2S) are enriched in the altered seawater while others, such as magnesium (Mg) and sulfate (SO42-) become depleted. As hydrothermally altered fluids are vented back to the deep ocean, copper (Cu), zinc (Zn) and Fe sulfide minerals precipitate to form massive sulfide deposits, chimney structures, and plume particles due primarily to changes in the temperature dependence of mineral solubility.

Within the buoyant plume, strong geochemical gradients, rapid entrainment of near bottom seawater, and turbulent conditions prevail. Vent fluids initially rise because it is more buoyant than seawater when it is injected into the water column and these fluids are called the 'buoyant plume' (Figure 1.2b; Lupton et al., 1998). As the fluids mix with ambient seawater, they begin to spread laterally and become the "non-buoyant" plume (Figure 1.2b). The non-buoyant plume is diluted and transported with deep ocean currents

(German and Seyfried, 2014; Lupton et al., 1998).

Seawater quickly mixes with the vent fluid near the orifice and reduces the buoyancy of the fluids (Lupton et al., 1998). After ~10 minutes the high-temperature fluids become diluted with seawater and the presence of subseafloor communities within the vent fluids become negligible (Reed et al., 2015). Transport time along the rising buoyant plume is short compared to the doubling time of low-temperature, deep-sea microbial populations. On average, transport along rising hydrothermal plumes occurs within 10s of minutes before the fluids reach the non-buoyant plume (Reed et al, 2015).

Water-rock interactions affect the global biogeochemical cycling of many elements during the circulation of seawater in the crust. Microbial populations capable of utilizing mineral substrates in the buoyant plume, as the fluids rise and laterally spread into the non-buoyant plume, have been characterized previously (Li et al., 2015; Dick et al., 2009). A mathematical model derived from fluid dynamics of the ABE vent field of the Lau Basin demonstrated active metabolic communities within rising hydrothermal plume are entrained from ambient seawater communities (Reed et al., 2015). Previous work has also demonstrated that Mn-oxidizing microbial communities within the Guaymas Basin hydrothermal plumes and communities such as members of the S-oxidizing ε-proteobacteria SUP05 in the Eastern Lau Spreading Center respond to and alter the geochemical gradients within the buoyant plume (Dick et al., 2009; Anantharaman et al., 2016). The net effect that biotic and inorganic processes have on minerals within plumes goes beyond the plume. As the plume rises and spreads, it can be detected thousands of kilometers from their vent source (Baker and Massoth, 1987; Walker and Baker ,1988).

1. BACKGROUND

1.1 Phase Separation

The primary mechanisms that effect changes in fluid composition of hydrothermal fluids are (1) phase separation; (2) water-rock interactions; (3) biological processes; and (4)

magmatic degassing (German and Seyfried, 2014). In this section I will explain phase separation. It is a process that is dependent on the pressure and temperature of a specific hydrothermal circulation system. When seawater initially enters the oceanic crust it is heated. Seawater has different physical properties than pure water and the critical point for seawater is 407 oC and 298 bar (Bischoff and Rosenbauer, 1985). The two-phase curve developed by Bischoff and others separates the pressure-temperature (P-T) space in which only a liquid exists, from the P-T space in which both liquid and vapor exist. If at any point during circulation through the ocean crust seawater crosses the two-phase curve below the critical point of 407 oC and pressure of 298 bars (Figure 1.3), the water will "boil." Phase separation of seawater at temperatures less than the critical point produces a vapor, and separation at temperatures greater than critical point produce brine (Figure 1.3).

1.2 Mineral precipitation in the subseafloor and as hydrothermal fluids emerge

The interaction between the hydrothermal fluids (enriched in Fe and S) with the seawater forms iron-rich mineral aggregates (Yücel et al., 2011; German and Seyfried, 2014).Within the subsurface, and within the hydrothermal vent, fluids produce sulfide minerals (pyrite (FeS2), chalcopyrite (CuFeS2), and troilite (FeS)) because Fe, S, and copper (Cu) react within the vent conduit (Ono et al., 2007; Yücel et al., 2011; Syverson et al., 2013; Mcdermott et al., 2015). Seawater contains ~280 mmol/kg of sulfate, and during seafloor hydrothermal circulation dissolved sulfate in seawater is precipitated during seawater recharge of the hydrothermal system because anhydrite (CaSO4) precipitates at temperatures ~130 oC (German and Seyfried, 2014). Most of the sulfide in mid-ocean ridge vents is derived from two processes: (1) leaching of rocks, and (2) chemical reduction of seawater derived sulfate.

In the subseafloor, H2S and Fe(II) react to produce iron sulfides and polysulfides. These reactions occur quickly and outcompete microbial metabolic processes in the first few meters of the rising plume (Rickard and Luther, 2007; Yücel et al., 2011; Findlay et al.,

2014). Dissolved H2S released to the ocean undergoes rapid precipitation as sulfide minerals or oxidation in the water column (German and Seyfried, 2014).

When Fe-enriched fluids first enter the ocean, the fluids are first rapidly cooled, which leads to the precipitation of sulfides (German and Seyfried, 2014). Also, once Fe(II) reaches the oxygenated seawater abiotic Fe(II) oxidation produces Fe(III) in first few meters (Findlay et al., 2014). Then, Fe(III) and Fe(II) react with organic carbon and some of it gets dispersed beyond the plume (Bennet et al., 2008; Bennett et al., 2011; Breier et al., 2012; Toner et al, 2009, and references therein; Yücel et al., 2010; Toner et al., 2016).

2. SITE DESCRIPTIONS

The MCR is an ultraslow spreading ridge located in the Western Caribbean Sea in the Cayman Trough (Rosencrantz and Mann, 1991). In 2009-2010 two hydrogen-rich vent sites were discovered along the MCR (Figure 1.4; German et al., 2010; Connelly et al., 2012). The vents include “Von Damm,” named after the late Karen L. Von Damm who dedicated her life to studying the effect of hydrothermal vent geochemistry on the Earth’s oceans (Figure 1.4c). As well as “Beebe,” named after William Beebe who from 1930 to 1934, used the Bathysphere to dive off the coast of Nonsuch Island (Figure 1.4d).

At Beebe Vents, the seawater is oxygen-rich (200 µmol/kg), the fluids contain H2S concentration like other basalt-hosted systems (~12 mmol/L). The Beebe Vents have S/Fe ratios that are typical of gas-rich (excess H2S) hydrothermal plumes (16.8; Feely et al., 1994). At Van Damm, the seawater is oxygen-rich (200 µmol/kg), and the dissolved H2S abundances are 3.24 mmol\L, which is like those observed at Rainbow (1.2 to 1.4 mmol/L), but depleted in particulate Fe (Fe = 0.12µmol/kg) (McDermott, 2014). The expectation for the Von Damm fluids is different than Beebe Vents. Von Damm should contain less sulfide-rich particles, but based on H2S concentrations, and the oxygenated seawater, S- and Fe- bearing minerals should be present within the particles.

2.1 Piccard hydrothermal vent field, home of the Beebe Vents Site

The Piccard vent field is the world's deepest mid-ocean ridge hydrothermal system (4960 m) and is located 21 km away from Von Damm on basaltic host rock in the neovolcanic zone of the MCR spreading center (Figure 1.4 and 1.2a; Kinsey and German, 2013). The Beebe Vents Field lies 3 km to the east of the main spreading axis of the MCR within the Piccard vent field. High-temperature venting occurs at Beebe Vents site from a linear array of slender 2-3 meter tall focused chimneys atop a 40m diameter mound (Figure 1.4). High-temperature (398 oC) venting occurs with pH measured at 2.95 to 3.3 in low-Mg fluids (McDermott, 2014).

Chimney samples show chalcopyrite (CuFeS2) and bornite (Cu5FeS4) on the interior, and calcite (CaCO3) crystals with an anhydrite (CaSO4) /pyrite (FeS2) mix. The sulfides are Cu-rich (see Table 1.1; 47wt% Cu and 0.03-0.24 wt%Zn) (Webber et al, 2015). Beebe Vents megafauna include Rimicaris hybisae, anemones, and gastropods (Nye et al., 2012; Kinsey and German, 2013; Plouviez et al., 2015). The Particulate Organic Carbon (POC) of the Beebe Vents fluids is influenced by the metabolic processes of sulfide and Fe-oxidizing communities, and the internal S cycle between S-oxidizers, ε-, and γ-proteobacteria living symbiotically with the Rimicaris hybisae (Bennett et al., 2015).

The hottest vent fluids measured at the seafloor are at Turtle Pits field on the Southern Mid-Atlantic Ridge (Haase et al., 2007; Koschinsky et al., 2008). Phase separation at Turtle Pit is occurring at 407 oC at 2990m depth. Due to the greater depths at Piccard, the two-phase boundary at the seafloor occurs at a higher temperature (483 oC ; Figure 1.3; Bischoff and Rosenbauer, 1987). Therefore, at the Beebe Vents, there is the possibility for circulating fluids to attain extremely high temperatures (>500 oC) in the subsurface. McDermott (2014) characterized the endmember fluids from Beebe to determine the effects of high pressure and temperature on water-rock reaction conditions at the Beebe Vents site.

The temperatures measured were lower (390-398 oC) than 483oC (496 bar) and indicate the Beebe Vents site fluids are not actively phase separating at seafloor conditions (McDermott, 2014). However, phase separation could occur several kilometers below the ocean floor, as is seen in other mid-ocean ridge systems. In fact, McDermott (2014) describes several lines of evidence that indicate the endmember black smoker fluids emanating from the Piccard vent hydrothermal field attained higher temperatures at depth relative to the measured seafloor temperatures that were measured. These include (1) depletion of Cl in the fluids; (2) quartz geothermometry indicate fluids equilibrated with quartz at temperatures substantially higher than the measured seafloor temperatures measured, but cooled prior to venting; and, (3) the Fe/Mn geothermometer recently developed (Pester et al., 2011), predicts a temperature of 452 °C . Several lines of evidence also indicate the Beebe Vents fluids are from a single source fluid (McDermott, 2014).

2.2 Von Damm hydrothermal vent

The Von Damm hydrothermal system was found on a 200 m diameter mound located on the eastern slope of an oceanic core complex (Hayman et al., 2011). The mound is 13 km off-axis from the ultra-slow spreading MCR spreading center. Ultramafic, gabbroic, and basaltic rocks are associated with the oceanic core complex (Ballard et al., 1979; Hayman et al., 2011). Samples were collected from high-temperature fluids emitting from the summit of the mound (maximum temperature was 226 oC) and from a large orifice downslope from the summit (maximum temperature was 107 oC) (Figure 1.5; McDermott, 2014).

Previous investigations of total organic carbon (TOC) at Von Damm found concentrations in the plume ranged between 42.1 and 51.1 µM (Bennett et al., 2013). The study predicted a microbial food web comprised of three distinct regions (near-field plume, non-buoyant plume, and above plume) where chemoautotrophs support microbial

heterotrophs (Bennett et al., 2013). Based on S isoptope δ34S values, phototsynthetic and chemosynthetic organic carbon inputs were identified in Von Damm megafauna, Rimcaris hybisae (δ34S = 13.3 ± 0.8%0) and vent fluid (δ34S = 10.3 ± 10.6%0) (Bennett et al., 2015).

The Von Damm fluids are methane (CH4 aq) and sulfide (H2S aq) rich, but are relatively low in dissolved metals (Connelly et al., 2012; Mcdermott, 2015). The highest temperature fluids from the large orifice are near-neutral pH (5.56) with high dissolved hydrogen (H2 aq), CH4, low dissolved metals, and near-zero concentrations of dissolved magnesium (Mg) (Mcdermott, 2014).

High concentrations of dissolved H2, CH4, and low molecular weight hydrocarbons suggest that Von Damm vent fluids are influenced by serpentinization reactions in subseafloor reaction zones. Carbon isotope values (δ13C = -15.4%0) (McDermott, 2014) provide evidence for an abiotic origin for CH4 (Proskurowski et al., 2008). This value is within the range of values (δ13C = -9 to -16%0) reported from other ultramafic influenced systems such as Rainbow, Logatchev, and Lost City hydrothermal fields and is substantially higher than microbial production of CH4 from CO2 (δ13C =-30 to -70%0) (Proskurowksi et al., 2008).

All fluids at Von Damm are thought to be derived from a single source fluid (McDermott, 2014). The maximum fluid temperatures at Von Damm are cooler than the two-phase boundary of seawater (407oC) at seafloor pressure and there is minor chloride (Cl- aq) enrichment, suggesting there cannot be subsurface phase separation (Bischoff and Dickson, 1975; Mcdermott, 2014).

Several geochemical characteristics of the vent fluid suggest that chemoautotrophic carbon fixation pathways should occur in the Von Damm fluids. These include elevated CH4 aq, H2 aq, and H2S aq concentrations. Each of which could provide energy for methanotrophs (Bennett et al., 2013), hydrogen oxidizers (Connelly et al., 2012), and S

oxidizers (German et al., 2010).

Bennett and colleagues (2015) evaluated the isotopic composition of megafauna, microbial mats, and Particulate Organic Matter (POM) at both Von Damm and Beebe Vents sites. They found that there is a greater diversity of C sources in the Von Damm fluilds compared to Beebe. The δ13C values provide evidence for two dominant sources of organic C in the Beebe fluids. These include both H2S or Fe oxidizers in the white filamentous micirobial mats and bacteria symbionts living in the Rimicaris hybisae. Sulfur oxidizing Epsilonproteobacteria sulfurimonas and Gammaproteobacteria SUP05 have also been already been identified in the Von Damm plume fluids (German et al., 2010; Breier et al., 2014).

3. X-RAY ABSORPTION SPECTROSCOPY (XAS)

The X-ray Absorption Spectroscopy (XAS) analysis of both Von Damm and Beebe Vents is described CHAPTERS 3 and 4. In this section, I will provide some background information about the history for electron configuration of elements, as well as how X-rays are used for XAS. I will also provide some information about how XAS is used to determine the speciation of Fe and S in dissolved and particulate materials found in natural systems.

Atoms contain protons, neutrons, and electrons. The nucleus of an atom contains positively charged protons and uncharged neutrons. The nucleus is surrounded by negatively charged electrons. Electrons populate orbitals that surround the nucleus of the atoms. Bohr's model for an atom was developed around 1913 (Figure 1.6). In his model, the electrons most tightly bound to the nucleus are K-shell electrons (1s) and the next group are L-shell (2s and 2p), and so on. The shells (electrons) are classified as K, L, M, N, etc. according to the n values of 1, 2, 3, 4, etc. and each shell is capable of housing 2n2 electrons. After Schrödinger and Pauling, it is now known that many electrons are housed in atomic orbitals designated in states s, p, d, and f. In X-ray spectroscopy, the

absorption edges are labeled in order of increasing energy, by K, LI, LII, LIII, etc., corresponding to the excited of an electron from the 1s, 2s, 2p, etc., orbitals (states) (Teo, 1986).

X-rays are special class of particles in the range of electromagnetic spectrum (gamma to radio wavelengths). Photons have energy $1 \leq E \leq 200$keV. X-rays react with matter through the photo-electron effect. The photo-electron effect occurs when an X-ray is absorbed by an atom and the energy is transferred to a core-level electron (K, L, or M shell) which is promoted from the atom. The atom is left with an empty electronic level, a core hole. When this occurs, an excited core-hole will relax back to a ground state of the atom. If a core hole (or valency) is created in the innermost (K) shell, then according to Bohr theory, an electron of the L or M shell can fall into the K shell, and a quantum of radiation is emitted called fluorescence. Once this occurs, lines Kα, Kβ will appear in the emission spectrum (Figure 1.7; Agarwal, 1979).

Fluorescence occurs at discrete energies that are characteristic of the absorbing atom. When X-rays are absorbed by a molecule, the innermost electrons from the 1s(K), 2s (L), and 2p (L) orbitals of the X-ray absorbing atom (absorber) are promoted into unoccupied molecular orbitals and continuum state of the molecule. These types of transitions occur with the highest probability when the incident energy (I0) (Figure 1.8a) is equal to the binding energy of core electrons of the absorber. The spectroscopy that deals with near- and pre-edge part of the X-ray absorption spectrum is referred to as X-ray Absorption Near Edge Structure (XANES) spectroscopy (Figure 1.8b). The XANES region can provide information on the oxidation state and coordination environment of the absorber. The XANES can be applied to solid and dissolved compounds in pure, synthetic materials, as well as complex and heterogeneous natural materials. XANES is particularly useful for the study of natural particles because it is a non-destructive tool for measuring chemical speciation of one element at a time within chemically complex matrices (Manceau et al., 2000).

3. THESIS SUMMARY

Biogeochemical processes occurring within buoyant hydrothermal plumes alter the net effect of venting on the chemistry of the ocean, and when and how these biogeochemical processes begin to alter the geochemistry of hydrothermal vent particle is still unknown. This thesis evaluates the C (CHAPTER 2), S (CHAPTER 3), and Fe (CHAPTER 4) particle geochemistry of hydrothermal fluids from hydrothermal vents recently discovered in the Cayman Trough, the Mid-Cayman Rise to try to understand chemical and microbial processes that occur in rising plumes.

In CHAPTER 2, we discuss the likelihood of microbial activity influencing the fluids at Von Damm based on images of microorganisms, cellular material, and biomolecules using C 1s STXM and XANES. Images of dense accumulations of Fe(III) mineral aggregates embedded in organic matrices co-located with organic carbon compounds at Von Damm demonstrate that hydrothermal plumes are a source of Fe(III) the deep ocean. The lack of cells and low abundance of organic C in the Beebe Vents indicate abiotic chemical processes influence the types of Fe and S species present in the Beebe Vents hydrothermal plume.

CHAPTER 3 details the wide variety S oxidation-reduction (redox) states from S(-2) to S(+6) and the phases of S moietites spanning metal sulfides to organosulfides present in the Von Damm and Beebe Vents. The data suggest metal sulfides are formed in the Von Damm and Beebe Vents fluids either in the subsurface or as the fluids emerge into the deep ocean. The presence of organosulfur indicates that S species react with organic material. The presence of intermediate S, and elemental S, indicates that both microbial processes and chemical oxidation occur.

In CHAPTER 4, we present results from Fe 1s XANES and microprobe XRF chemical mapping. By describing the variety of Fe minerals in the buoyant plumes at the submicron scale, we capture trends that suggest particles within the Von Damm and

Beebe Vents could be sourced from both chemical processes within the plume and physical entrainment processes from multiple sources.

In CHAPTER 5, we synthesize the datasets with careful consideration for all the physical, biological, and chemical processes active within the Mid-Cayman hydrothermal fluids. The APPENDIX introduces two types of XRD were used to investigate the range of particles sizes that occur in the samples: (1) powder XRD with monochromatic X-rays for randomly oriented nanoparticulate minerals, and (2) Laue XRD with polychromatic X-rays for single-crystal sulfides.Replace with the body of your thesis.

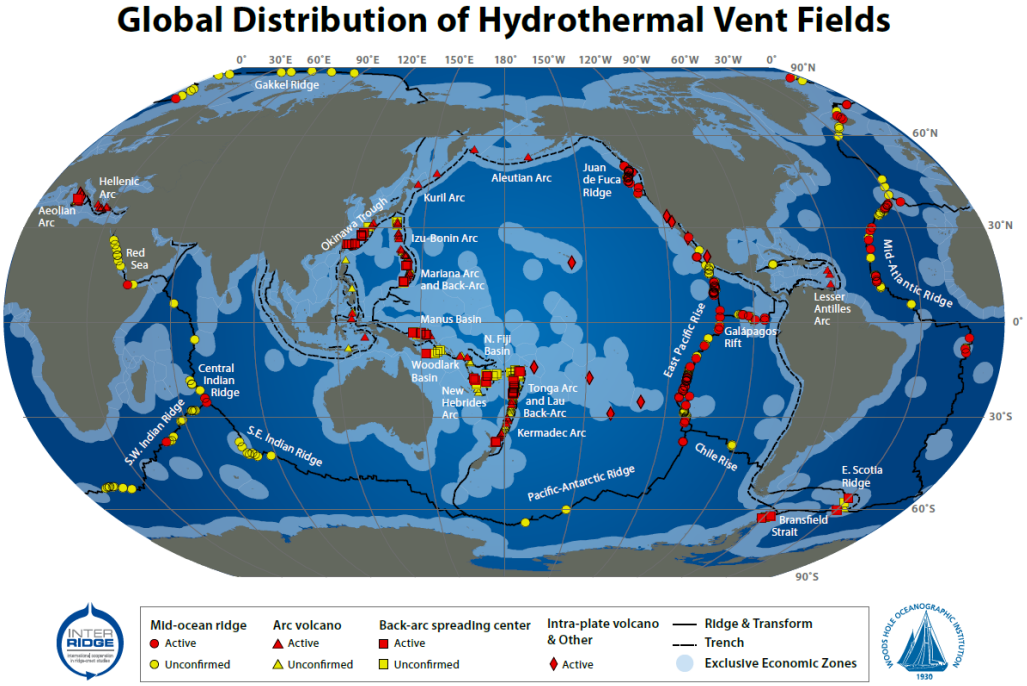

Figure 1.1: Map showing the major sections of the 60,000km-long global mid-ocean ridge crest (black lines) from (German and Seyfried, 2014). Red symbols represent currently known locations of active hydrothermal venting and yellow symbols represent unconfirmed vent locations. This map is continuously updated and is hosted by the international InterRidge program at: http://www.interridge.org/irvents/.

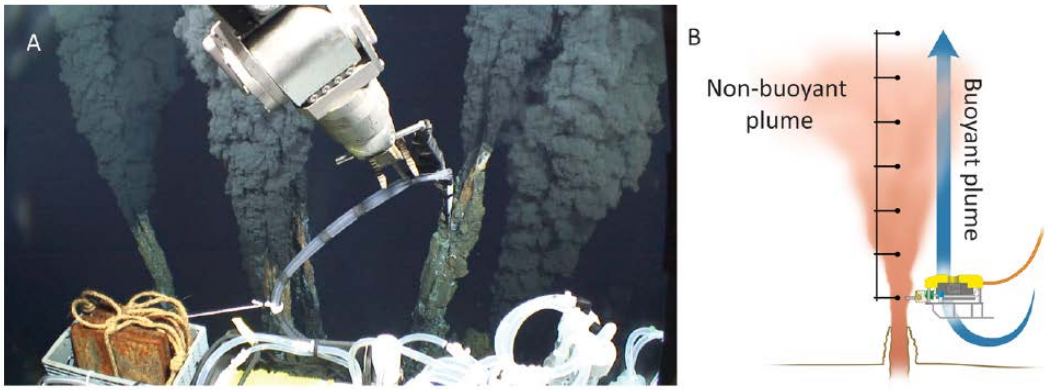

Figure 1.2: (a) JASON imagery of the rising plume at Beebe Vents with SUPR sampler arm shown collecting SUPR22-0.5m sample; (b) schematic showing the buoyant plume, non-buoyant plume and Remotely Operate Vehicle sampling within the rising buoyant plume. (figure from Toner et al., 2016)

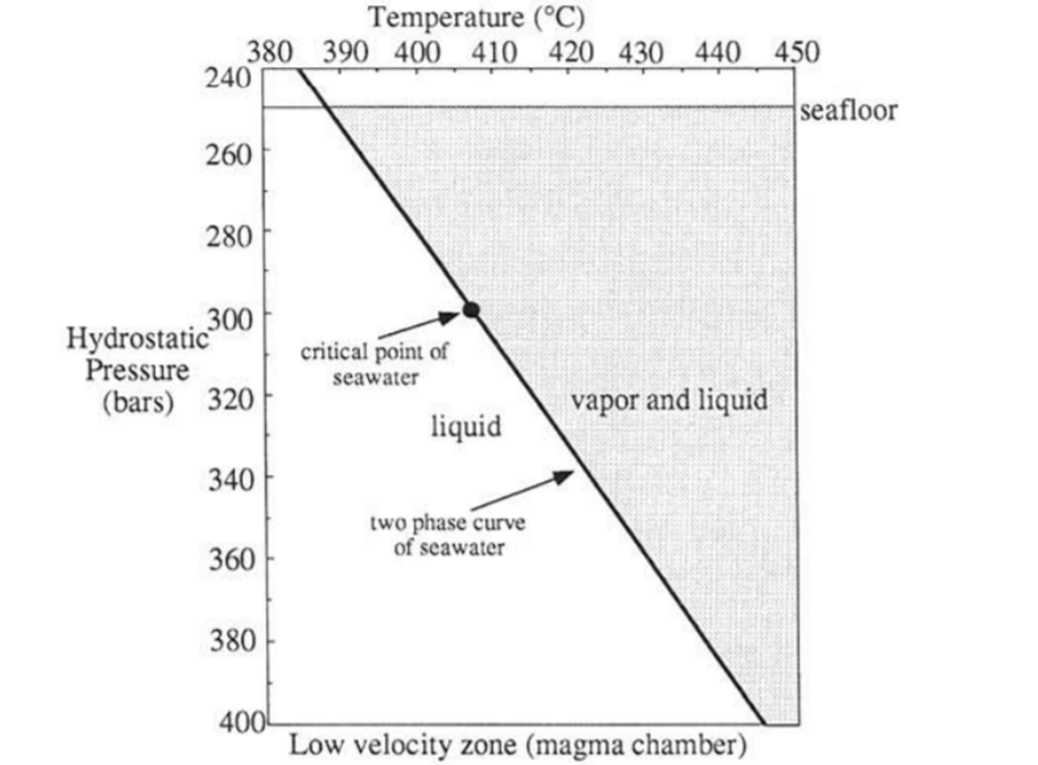

Figure 1.3: Temperature-pressure figure from Oosting and Von Damm (1996) showing the two-phase curve of seawater and the critical point of seawater for East Pacific Rise.

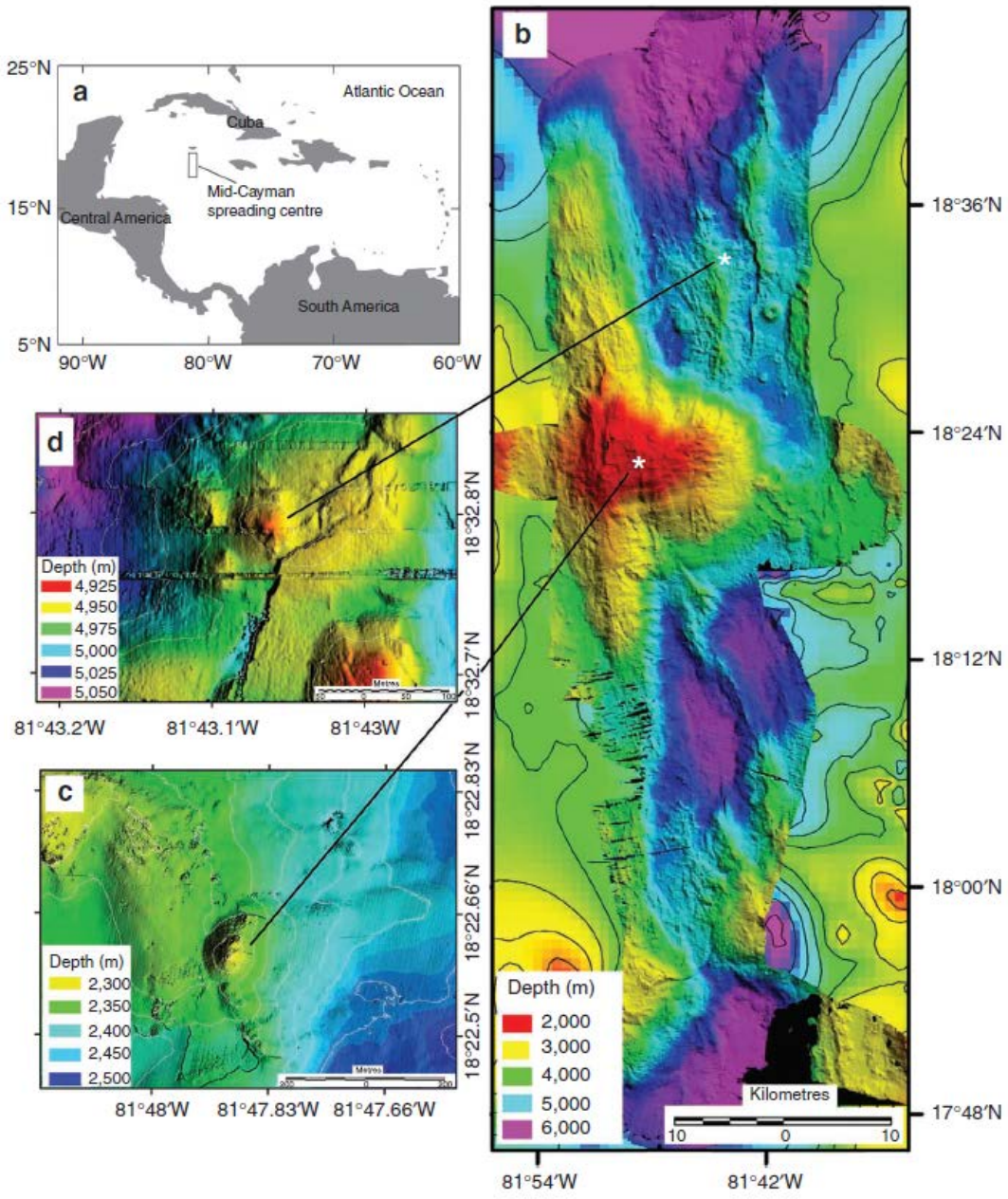

Figure 1.4: Figure shows the (a) location of the Mid-Cayman Rise; (b) relative locations of Von Damm and Beebe Vents sites; (c)Von Damm and (d) Beebe hydrothermal vents (figure from Connelly et al., 2012).

Figure 1.5: Image of the Von Damm hydrothermal vent with Hercules. This image of Von Damm came from video collected by the Okeanos Explorer.

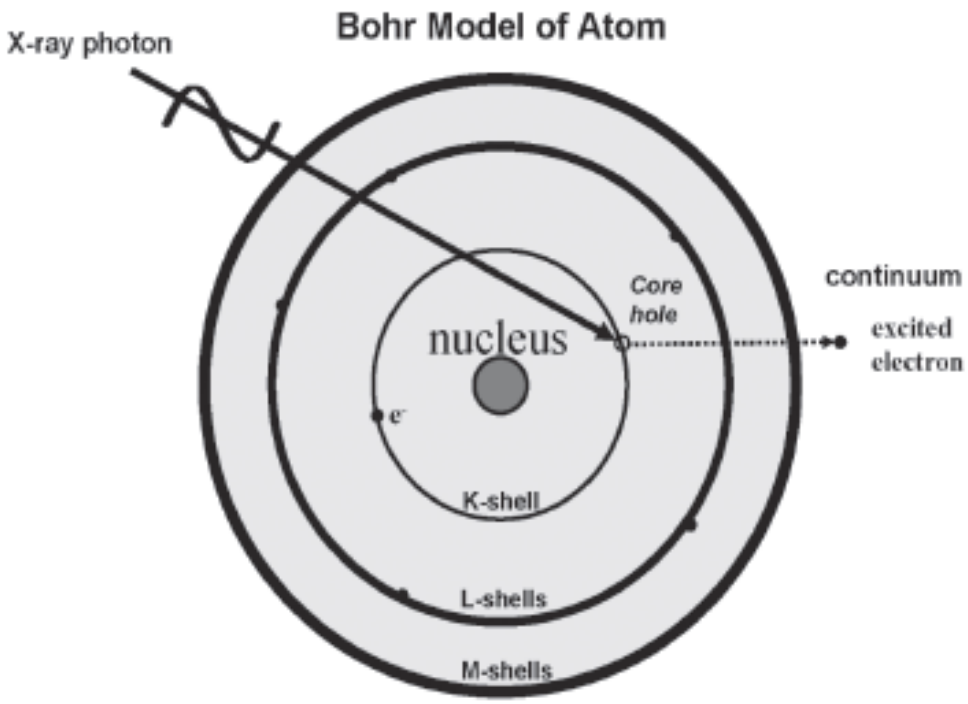

Figure 1.6: Bohr's model for an atom which was given around 1913.

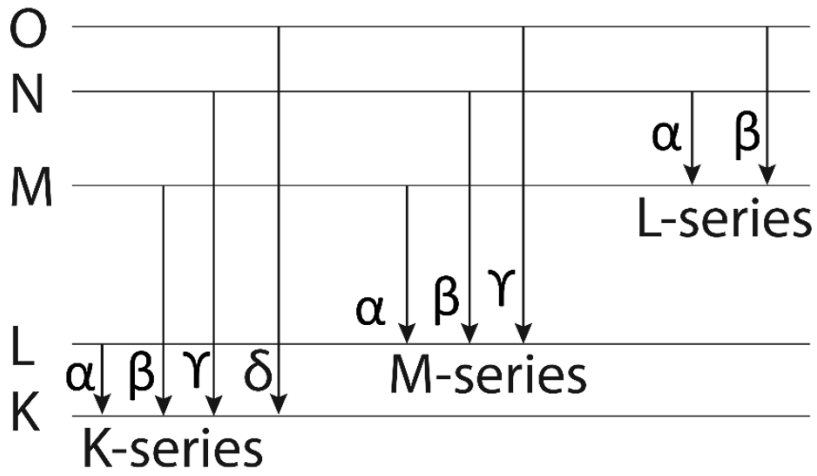

Figure 1.7: Schematic of shells in an atom. The electronic transitions correspond to the X-ray emission lines in the quantum theory of Bohr.

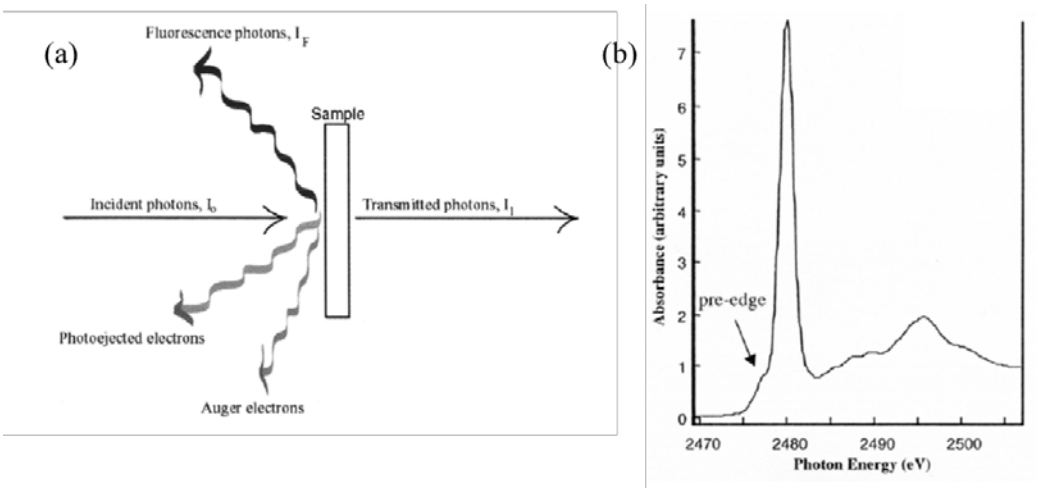

Figure 1.8: To determine the valence state and coordination geometry of a particular element within a sample, we (a) use incident photons (I_0) from synchrotron sources to create fluorescence radiation. Ion chambers or detectors are placed at different locations around the sample to detect fluorescence. The ratio of I_f to I_0 gives the X-ray absorption spectrum in fluorescence detection mode; (b) X-ray absorption spectrum (plotted as absorption as a function of incident energy) represents the XANES spectrum of S in ferric sulfate. The pre-edge region of the XANES spectrum that represents transitions from 1s→ 3p orbitals are shown (from Myneni 2000).

Table 1.1: Mid-Cayman Rise hydrothermal plume particle chemistry*, **. These analyses were made on a Varian 730-ES axial Inductively Coupled Plasma-Optical Emission Spectrometry instrument with quantification by external calibration. Depth in meters, elevation (Elev.) in meters, volume (V) in L, Temerpature in ^{o}C, H_2S, H_2 in mmol/L, Cu in mmol/L, and Al in μmol/kg.

						Dissolved volatile species		**Particulate metals**	
Vent		**Depth**	**Elev.**	**V**	**T**	**H_2S**	**H_2**	**Fe**	**Cu**
Von Damm	Endmember fluid[a]	2296	1	-	226	3.24	19.9±1.7	5.7-450	-
	SUPR58	1479	818	26	2	-	-	0.06	-
	SUPR57	2254	37	22	2	-	-	0.03	-
		2290	7	24	2	-	-	0.32	0.003
	SUPR11	2288	8	6	18	-	-	0.18	0.067
	SUPR05	2290	1	5	64	-	-	0.17	0.26
	SUPR03	2296	1	5	77	-	-	0.12	0.15
Beebe	Endmember fluid[a]	4956	0.5	-	398	12±1.2	18.6	6.7***	-
	SUPR44	3501	1456	-	-	-	-	-	-
	SUPR30	4906	50	21	4	-	-	0.74	0.12
	SUPR28	4926	30	15	4	-	-	0.73	0.12
	SUPR26	4941	15	18	6	-	-	3.84	0.59
	SUPR24	4950	5	19	8	-	-	5.38	0.85
	SUPR22	4956	1	10	98	166	591.3	716	67.1

a. From McDermott, 2014
*All filters 0.2 um poresize, 142 mm diameter
**Environmental detection limits (dFe:0.15; pFe:0.0012; pCu:0.0002; pAl:0.024)
***mmol/L

CHAPTER 2

Carbon 1s X-ray absorption near edge structure (XANES) spectroscopy and scanning X-ray transmission microscopy (STXM) of particles and aggregates from Von Damm and Beebe Vents

1. SYNOPSIS

Here we investigate the carbon (C) from the Von Damm hydrothermal mound and Beebe Vents site, Mid-Cayman Rise, Caribbean Sea. Hydrothermal plume particles from the buoyant plume were collected by in situ filtration at four elevations above the Von Damm vent (1m, 8m, 37m, 812m above the vent orifice) as well as six elevations above the Beebe Vents site (0.5m, 5m, 15m, 30m, 50m, and Above Plume Background (APB)). Scanning transmission X-ray microscopy (STXM) based C 1s and Fe 2p XANES were collected to measure the speciation of C and Fe for particles and aggregates. Overall, our study reveals a chemically complex suite of particulate C in the Von Damm fluids, and a lower concentration and richness of particulate C in the Beebe Vents fluids.

Carbon XANES of Von Damm fluids reveal the presence of biomolecules such as proteins, lipids, polysaccharides, and chitin in plume particles. Particles close to the vent are composed of chitin-rich materials from vent shrimp, while protein-rich microbial cells become more abundant in the rising plume. Iron 2p imaging and XANES indicate that nano-particulate Fe minerals are associated with particulate organic C (POC) at the 8m and 37m elevations. Previous genomic research has established the presence of heterotrophic and chemoautotrophic microbial communities within the subsurface and the surrounding seawater at Von Damm. The C STXM results from Von Damm provide additional evidence that biological processes contribute to POC in the plume.

The Beebe C images, maps, and XANES spectra reveal that the C concentration is much lower than Von Damm. The C-bearing particles at 0.5 m are very dilute in C, and it is not

until the fluids reach 50 m and the APB that the Beebe particles begin to resemble C consists of proteins, lipids, and polysaccharides. Transmission images and C maps from Beebe reveal microbial cells in the SUPR44-APB sample. Unlike Von Damm, where POC is rich in cellular material and biomass, the Beebe Vents data suggests that the Beebe plume particle geochemistry is influenced primarily by inorganic processes.

2. INTRODUCTION

In this chapter, we describe C 1s and Fe 2p results from Scanning Transmission X-ray Microscope (STXM) spectroscopy. In STXM, the sample is raster scanned through a fixed X-ray beam. To acquire useful information in a reasonable time, high photon flux in a small spot is required. Therefore, STXM requires a focused photon energy source, called a synchrotron radiation facility. To suppress unwanted signal-to-background noise, a zone plate, for focusing, with a central stop is used. To remove higher order light an Order Selection Aperture (OSA) is also used (Kilcoyne et al., 2003). Careful transverse and longitudinal alignment of the OSA with the zone plate is essential for tuning and operating the scanning X-ray microscope(Warwick et al., 2002; Kilcoyne et al., 2003). The STXM measurements are useful for the study of environmental (Cody et al., 1998; Toner et al., 2009) and biological (Chan et al., 2004; Cosmidis and Templeton, 2016) processes that involve microscopically variable chemistry on the scale of nanometers to micrometers (Toner et al., 2016). The STXM measurements are significant because the measurement itself exposes the sample to relatively low radiation damage, and compositional information that is provided by XANES spectroscopy provides information about elements with absorption edges in the soft X-ray energy range (C, nitrogen (N), and O) (Warwick et al., 2002; Kilcoyne et al., 2003).

Microbial communities in the following generas Methanothermococcus, Archaeoglobus and Sovum are found in the subsurface at Von Damm (Reveillaud et al., 2016). Their cellular material and metabolic biproducts are likely contributing to organic carbon from biomass to the subsurface and subsequent near vent samples. It has been determined that

the CH3SH within the endmembers fluids at Von Damm is derived from abiotic thermal decomposition of preexisting biomass and biological derived compounds (Reeves et al., 2014). The subsurface is also a source of abiotic organic carbon, including species such as CH4 and ethane (C2H6) (McDermott et al., 2015b).

As hydrothermal vent fluids rise from the subsurface they are immediately physically mixed with deep ocean seawater (Lupton et al., 1985; Reed et al., 2015). Entrainment can pull in oxygenated seawater, particles, and microbial communities originating from both the upper water column and background seawater. Microbial communities from the demersal deep ocean background seawater can be entrained as far up as 10m above the seafloor (Reed et al., 2014; 2015). Entrainment also pulls in debris (including shrimp) and microbial communities from the host vent site (Estrapa et al., 2016). There is also entrainment of aged particles that reside in the background seawater and the host vent site (Estrapa et al., 2016; Reed et al., 2015; Bennett et al., 2015; Reed et al., 2014; Sheik et al., 2014; Lupton et al., 1985). Entrainment of flocculent material from background seawater also pulls in particulate organic carbon in the Von Damm hydrothermal vent fluids that comes from the surface ocean. The photosynthetic processes likely contribute recalcitrant C that is highly degraded to the plume geochemistry (i.e., marine snow; Bennett et al., 2015).

Overall, our study of the Von Damm fluids provides unprecedented spatial and chemical resolution for the young buoyant plume of a newly discovered vent site. We find that the particulate organic C (POC) source is dominated by vent mega-fauna (shrimp) initially, but trends to microbial biomass during transport. Despite the relatively low metals concentrations, the vent POC often contains Fe-bearing nano-particles. For Beebe, the POC is low in the near the vent orifice, but that cells and organic material begin to appear at 50m into the rising plume. We predict seawater and microbial communities are entrained into the rising plume as it rises into the deep ocean.

3. METHODS

3.1 Sample collection

Samples were collected during a research cruise to the Mid-Cayman Rise in January 2012 on the RV Atlantis. Hydrothermal plume particles were captured by in situ filtration equipment deployed on the ROV JASON or a CTD rosette using 147 mm diameter, 0.2 µm pore size polycarbonate membrane filters (SUPRV2) (Breier et al., 2014). All filter holders and filter membranes were cleaned in 10 % trace grade hydrochloric acid prior to use. The sample names, in-plume elevations, and total volume filtered are summarized in Table 2.1 and Table 2.2.

3.2 Anaerobic sample preparation

Shipboard, the unopened filter holders were rinsed with a dilute ammonium solution and opened in a glove bag with a nitrogen atmosphere. While in the glove bag, the 147 mm filters were sectioned using acrylic punches/knives for bulk geochemical analysis, mineralogy, microbiology, and C, S, and Fe speciation measurements. The bulk geochemical sub-samples were stored in teflon digestion vials until analysis. Sub-samples for S and Fe speciation were placed in sterile plastic petri dishes with a plastic bag wrap, and sealed in a mylar pouch (PAKDRY 7500, 7.5 mm) with an oxygen absorbent (Mitsubishi Gas Chemical Co., Inc., AnaeroPack). The filters were then stored frozen until sample preparation for synchrotron analysis. Sub-samples for C speciation were initially handled under ambient conditions shipboard. Filter sub-samples were placed in ~ 0.5 mL of purified water, shaken gently by hand, and ~ 1 µL of the resulting suspension was deposited on a silicon nitride membrane (Silson, LTD) attached to an Al sample holder (Toner et al., 2016). After air-drying, the sample holder was placed in a plastic box with a plastic bag wrap, sealed in a mylar pouch under N2, and stored frozen until synchrotron analysis.

Sample preparation for synchrotron analyses was conducted in a glove bag under positive

pressure of inert gas (N2 or Ar). For analysis at beamline 5.3.2.2 (Advanced Light Source, Lawrence Berkeley National Laboratory, Berkeley, CA, USA) (Warwick et al., 2002; Kilcoyne et al., 2003). At the synchrotron, for each sample, the mylar pouch containing the sample holder was opened and immediately loaded into a He atmosphere for analysis. The in situ filtration, sample handling, and analysis was designed to limit sample exposure to ambient oxygen but the conditions were not strictly anaerobic.

3.3 Scanning Transmission X-ray Microscope (STXM) microscopy

X-ray images, elemental maps, and spectra were acquired in transmission mode using a scintillator-photomultiplier detector assembly at ALS beamline 5.3.2.2. Transmission images at energies below and at the relevant absorption edges were converted into optical density images and used to derive elemental maps (optical density is equal to ln (I0/I). Where I0 is the incident X-ray intensity and I is the transmitted intensity through the sample. Image sequences, also called stacks, were recorded at energies spanning the C 1s (280-320eV) and Fe 2p(700-730eV) absorption edges. All STXM data processing was carried out using the IDL freeware package aXis2000 (Hitchcock, 2009). To minimize radiation damage to the sample, spectra were collected from unique areas (multiple C stacks were never collected at the same location). All measurements were carried out at ambient temperature and ≤1 atm He. The Rydberg transitions of gaseous CO2 at 292.74 and 294.96 eV were used for calibration at the C 1s edge.

4. RESULTS

4.1 Carbon 1s and Fe 2p spectromicroscopy for Von Damm

Carbon 1s STXM images and XANES spectra were collected for Von Damm plume particles from the following samples: SUPR05-1m (hereafter referred to as VD-1; large vent at the base of the mount, 64 oC) , SUPR11-8m (above the large vent, 18oC), SUPR57-37m (above the large vent, 2oC), and SUPR03-1m (hereafter referred to as VD-

2; small vent at top of the mound, 77 oC) (Figure 1.5 and Table 2.1). Transmission images (Figures 2.1 and 2.2 “Transmission image” panels), C maps (Figure 2.1 and 2.2 “C map” panels), and C XANES spectra (Figure 2.3a-c) reveal that the C-bearing particles in the Von Damm plume consist of the following: microbial cells, fragments of hydrothermal vent shrimp, and exopolymeric-like materials. The transmission images show a variety of C-bearing particle morphologies, all of which have strong resemblance to biological materials, but well-preserved microbial cells were observed only in the SUPR57-37m sample (Figure 2.2i-p). Shrimp biomass, as indicated by chitin-like C XANES spectra (Figure 2.3a-b) was observed in the rising plume (SUPR11-8m; Figure 2d-f) and near the top of the mound (VD-2; Figure 2.1k-l). Exopolymeric-like material was found in near vent (cD-1 and VD-2) samples (Figure 2.1a-f), as well as the 8m (SUPR57-37m) sample (Figure 2.2i-p).

The C 1s XANES spectra for the samples verify the presence of organic C and are consistent with biomolecules such as proteins, lipids, alginate (polysaccharides), and chitin (Figure 2.3a-b; Table 2.1). Protein has peaks at 285.2eV, typical of an unsaturated or aromatic C (electron transition 1s □ π* C = C), and at 288.2eV, indicative of a peptide bond (electron transition 1s □ π* C = O) (Figure 2.3, see spectra labeled “Protein”; Table 2.3) (Chan et al., 2011). Protein-like spectral signatures were observed in all the samples, and exemplary spectra were observed the near-vent samples (VD-1 and VD-2, see Figure 2.3a) and in the SUPR57-37m highest elevation sample (Figure 2.3c). The protein-like spectral signatures correlate spatially with intact microbial cells in the SUPR57-37m sample (Figure 2.2i-p). Lipids and polysaccharides have a peak at 288.5 eV that is representative of carboxylates (electron transition 1s □ π * C=O transitions) (Figure 2.3, see spectra labeled “lipid” and “polysaccharide”; Table 2.3) (Cody et al., 1998; Boyce et al., 2002). Exopolymeric-like features in SUPR05-1m (Figure 2.1a-f) and SUPR11-8m (Figure 2.2a-h) have spectra consistent with lipids and polysaccharides. Finally, chitin has a peak at 289.4eV, typical of an alcohol moiety (electron transition 1s-3p/ σ* transitions) (Figure 2.3, see spectra labeled “Chitin”; Table 2.1) (Cody et al., 2009; Solomon et al., 2009). Carbon-rich particles from samples in close proximity to sections

of the mound with very high shrimp density, VD-2 (small vent at the top of the mound) and SUPR11-8m (above the large vent and adjacent to the sheer mound wall), have morphologies that resemble shrimp biomass and have spectra similar to chitin and protein.

Iron 2p STXM and XANES were collected for the SUPR11-8m sample and the SUPR57-37m sample (Table 2.1). Iron 2p XANES spectra have peaks similar to Fe(III) oxyhydroxides (Figure 2.3d). Although Fe 2p XANES spectra cannot reveal the exact Fe(III) oxyhydroxide form, the Fe from these samples have peaks at ~708.4 and ~709.8eV that are indicative of Fe(III) oxyhydroxides such as ferrihydrite (Figure 2.3d) (Chan et al. 2004; Toner et al., 2009). The Fe(III) minerals observed are nano-particulate and associated with organic C at two elevations. The C 1s and Fe 2p STXM images for the SUPR11-8m sample (Figure 2.2c,f) reveal Fe-rich minerals associated with shrimp biomass. The C 1s STXM images for the 37m sample (Figure 2.2m,p) reveal dense microbial communities associated with Fe-rich matrices.

4.2 Carbon 1s spectromicroscopy for Beebe

Carbon 1s STXM images and XANES spectra were collected for Beebe plume particles from the following samples: VD-1 (98 oC) , SUPR24-5m (8o C), SUPR26-15m (6 oC), SUPR28-30m (4 oC), SUPR30-50m (4 oC), and SUPR44-APB (Table 2.2; Figures 2.4-2.6; Supplemental figure (Fig.S2.1-2.3); Table 2.4). Transmission images (Figures 2.4 and Fig.S2.1-2.2 “Transmission image” panels and Figures 2.5-2.6), C maps (Figures 2.4 and Fig.S2.1-2.2 “Transmission image” panels and Figures 2.5-2.6), and C XANES spectra (Fig.S2.3) reveal that the C concentration is low in the particles and C-bearing particles in the Beebe plume consist of organic C (Figure 2.3). Transmission images show a variety of C-bearing morphologies (Figures 2.6-2.8, Fig.S 2.15-2.16) and the SUPR44-APB samples have C-bearing particles that have strong resemblance to biological materials (Figure 2.4a,b).

Protein has peaks at 285.2eV, typical of an unsaturated or aromatic C (electron transition 1s → π* C = C), and at 288.2eV, indicative of a peptide bond (electron transition 1s → π* C = O) (Fig.S2.3, see spectra labeled "Protein"; Table 2.4) (Chan et al., 2011). Protein-like spectral signatures were observed in SUPR44-APB (see figure 2.4a, b, e, f) and correlate spatially with intact microbial cells and exopolymeric-like features. Lipids and polysaccharides have a peak at 288.5 eV that is representative of carboxylates (electron transition 1s □π* C=O transitions) (Fig.S2.3, see spectra labeled "lipid" and "polysaccharide"; Table 2.4) (Cody et al., 1998; Boyce et al., 2002). Exopolymeric-like features in SUPR30-50m (Fig.S2.2) and SUPR44-APB (Figure 2.4c,d) have spectra consistent with lipids and polysaccharides.

5. DISCUSSION

The Von Damm C STXM and X-ray nanomicroprobe images show intact microbial cells in SUPR05-1m and SUPR57-37m samples (Figures 2.1a-f-2.2i-p). Our C 1s XANES spectra show shrimp biomass is in the VD-2 (Figure 2.1k-l), and shrimp biomass and cells in SUPR11-8m (Figure 2.2d-h) samples. Therefore, in the Von Damm buoyant plume, the microbial cell signature disappears in SUPR11-8m and reappears in SUPR57-37m. Then, the shrimp disappear in SUPR57-37m. The shrimp detritus is a strong local source of POC with distinct signatures in the C XANES. Due to dilution and particle setting of the near vent biomass by SUPR57-37m, is most likely the shrimp community is washed out from the samples. Entrainment of ambient seawater communities could be a source of POC and cellular material in the 37m sample.

The Beebe C STXM and X-ray nanomicroprobe images for particles in the APB sample reveal the presence of protein, lipids, and polysaccharides (Fig.S2.3). The C STXM spectra for SUPR30-50m resemble extracellular products (both lipids and polysaccharides) (Fig.S2.3). The presence of shrimp biomass in VD-2, suggests the POC is predominately from shrimp. The temperature of this vent is 226 oC, above the limit for

life. The cells and organic C in SUPR30-50m (Figure 2.5) and SUPR44-APB (Figure 2.4) could be produced either in the subsurface by microbial communities (Reveillaud et al., 2016) or from microbial activity in the surrounding seawater. Bennett and colleagues (2015), using δ13C, have already determined that the POC in the Beebe fluids come from the entrainment of flocculent material from background seawater where chemoautotrophic processes contribute to complex organic C molecules. Overall, the C STXM and X-ray nanomicroprobe images reveal low concentrations of C in the Beebe fluids.

6. CONCLUSIONS

For Von Damm hydrothermal plume fluids, particles were analyzed with C STXM images and XANES reveal the presence of microorganisms, cellular material, and biomolecules. These materials reveal a pattern that provide evidence that the Von Damm plume fluids evolve over short temporal (minutes) and spatial (37m) scales. The Fe 2p STXM images and XANES show dense accumulation of Fe(III) mineral aggregates that are embedded in organic matrices. Fe(III) co-located with organic carbon compounds is consistent with recent reports on Fe co-located with biomolecules in non-buoyant plumes at mid-ocean ridge hydrothermal plumes (Bennett et al., 2008; Toner et al., 2009; Toner et al., 2012b; Breier et al., 2012). These findings demonstrate that hydrothermal plumes are a source of iron-bearing sulfide to the ocean in addition to Fe oxidizes to form Fe(III) solids or oxides (Yücel et al., 2011).

In Beebe Vents, C STXM images reveal the presence of microorganisms, cellular material, and biomolecules in SUPR30-50m and SUPR44-APB samples. The lack of cells and low abundance of organic C in the first 50m of the plume combined with the high concentration of reduced Fe (see CHAPTER 4) and S-bearing minerals (see CHAPTER 3) indicate abiotic chemical processes influence the types of Fe and S species present in the first 50m at Beebe Vents.

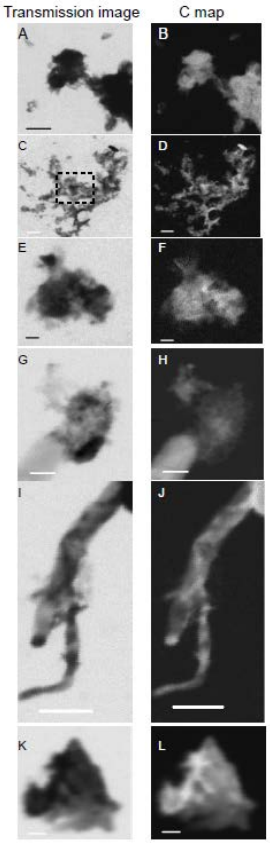

Figure 2.1: **(A)** STXM image recorded at C 1s edge (288.2 eV) from area 1 of SUPR05; scale bar is 2µm. **(B)** Carbon distribution map for **(A)**; optical density = 3.56; **(C)** STXM image recorded at C 1s edge (288.2 eV) from area 2 of SUPR05; scale bar is 2 µm; dashed box represents area C 1s XANES were collected; **(D)** carbon distribution map for **(C)** optical density = 1.98. The regions that were selected for the collection of C 1s XANES encompass the entire area and only the dashed are for **(C)**; **(E)** STXM image recorded at C 1s edge (288.2 eV) from area 3 of SUPR05; scale bar is 500nm; **(F)** carbon distribution map for **(E)**; optical density = 1.42; **(G)** STXM image recorded at C 1s edge (288.2 eV) from area1 of SUPR03; scale bar is 1µm; **(H)** C distribution map for **(G)**; optical density = 3.22; **(I)** STXM image recorded at C 1s edge (288.2 eV) from area 2 of SUPR03: scale bar is 2 µm; **(J)** Carbon distribution map for **(I)**; optical density = 2.74; **(K)** STXM image recorded at C 1s edge (280 eV) from area 3 of SUPR03; scale bar is 1µm; **(L)** Carbon distribution map for **(K)**; optical density = 2.88. Except for **(C)**, the regions that were selected for the collection of C 1s XANES encompass the entire area shown in each carbon image. For **(C),** C 1s XANES were collected in the area enclosed by the dashed box.

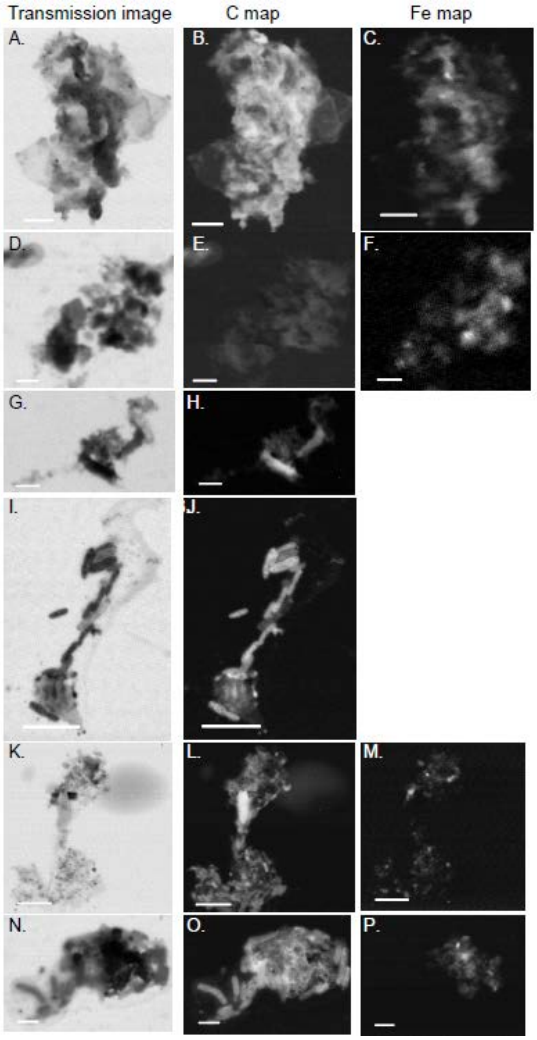

Figure 2.2: Carbon spectromicroscopy from SUPR11 (A-H) and SUPR57 (I-P) showing vent aggregate size and distribution. **(A)** STXM image recorded at C 1s edge (288.2eV) from area 1 of SUPR11; scale bar is 2 µm; **(B)** Carbon distribution map for **(A)**; optical density = 2.01; **(C)** Iron distribution map for **(A)**; optical density = 1. 07; **(D)** STXM image recorded at C 1s edge (288.2eV) from area 2 of SUPR11; scale bar is 1µm; **(E)** Carbon distribution map for **(D)**; optical density = 1.03; **(F)** Iron distribution map for **(D)**; optical density = 0.528; **(G)** STXM image recorded at C 1s edge (288.2eV) from area 3 of SUPR11; scale bar is 1µm; **(H)** Carbon distribution map for **(G)**; optical density = 2.26; **(I)** STXM image recorded at C 1s edge (288.2eV) from area 1 of SUPR57; scale bar is 5 µm; **(J)** Carbon distribution map for **(I)**; optical desnsity = 1.29. **(K)** STXM image recorded at C 1s edge (288.2eV) from area 2 of SUPR57; scale bar is 5µm; **(L)** carbon distribution map for **(K)**; optical density = 2.16; **(M)** iron distribution map for **(K)** optical density = 0.67; **(N)** STXM image recorded at C 1s edge (290eV) for area 3 of SUPR57; scale bar is 2 µm; **(O)** Carbon distribution map for **(N)**; optical density = 1.76; **(P)** Iron distribution map for **(N)**; optical density = 1.15; The regions that were selected for the collection of C 1s XANES encompass the entire area shown in each carbon image.

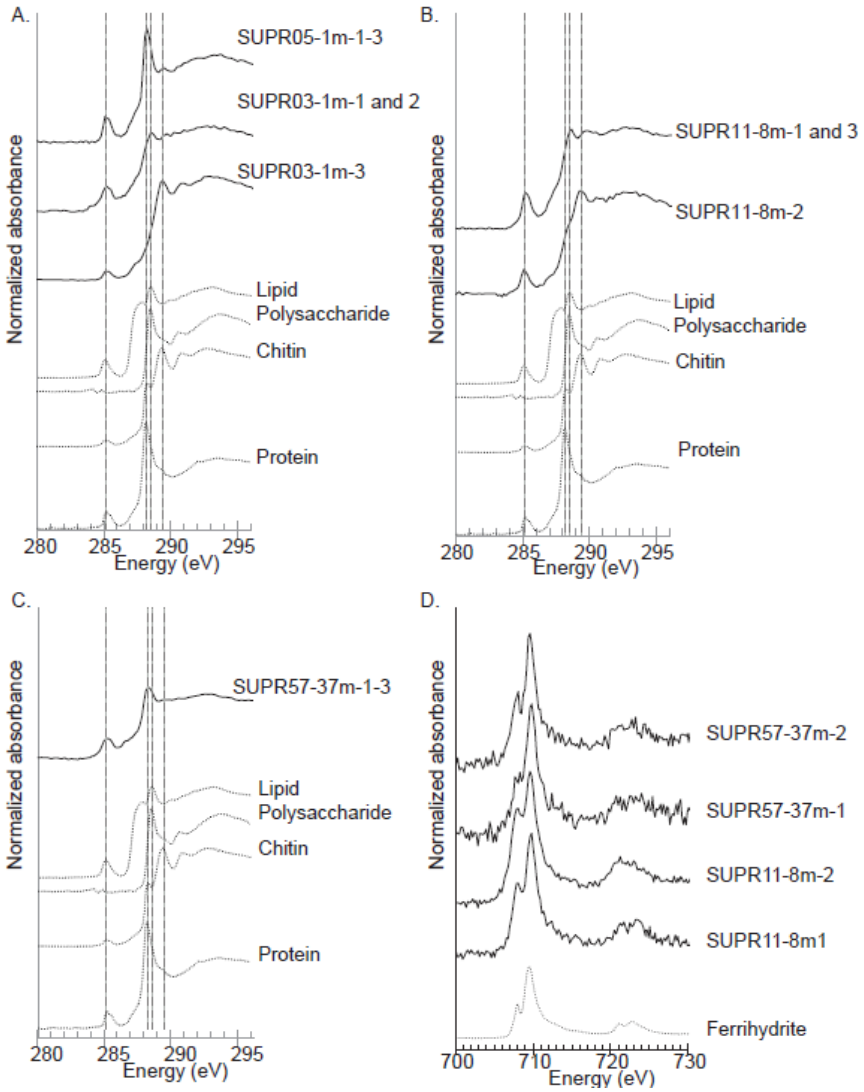

Figure 2.3: Carbon 1s and Fe 2p XANES collected from SUPR03, SUPR05, SUPR11, and SUPR57 that show biomolecular signatures. Spectra shown in **(A)** are three representative spectra for SUPR05-1m areas 1-3, SUPR03-1m area 1 and 2, and SUPR03-1m area 3; **(B)** spectra collected for SUPR11-8m area 2 and 3 and SUPR11-8m area 1; **(C)** representative spectra collected for SUPR57-37m areas 1-3; **(D)** representative Fe 2p XANES spectra collected from SUPR57-37m (areas 1-2) and SUPR11-8m (areas 1-2) shown with spectra for lepidocrocite. Iron 2p XANES for Fe(III) oxyhydroxides such as ferrihydrite and lepidocrocite
have peaks at ~708.4 and ~709.8eV.

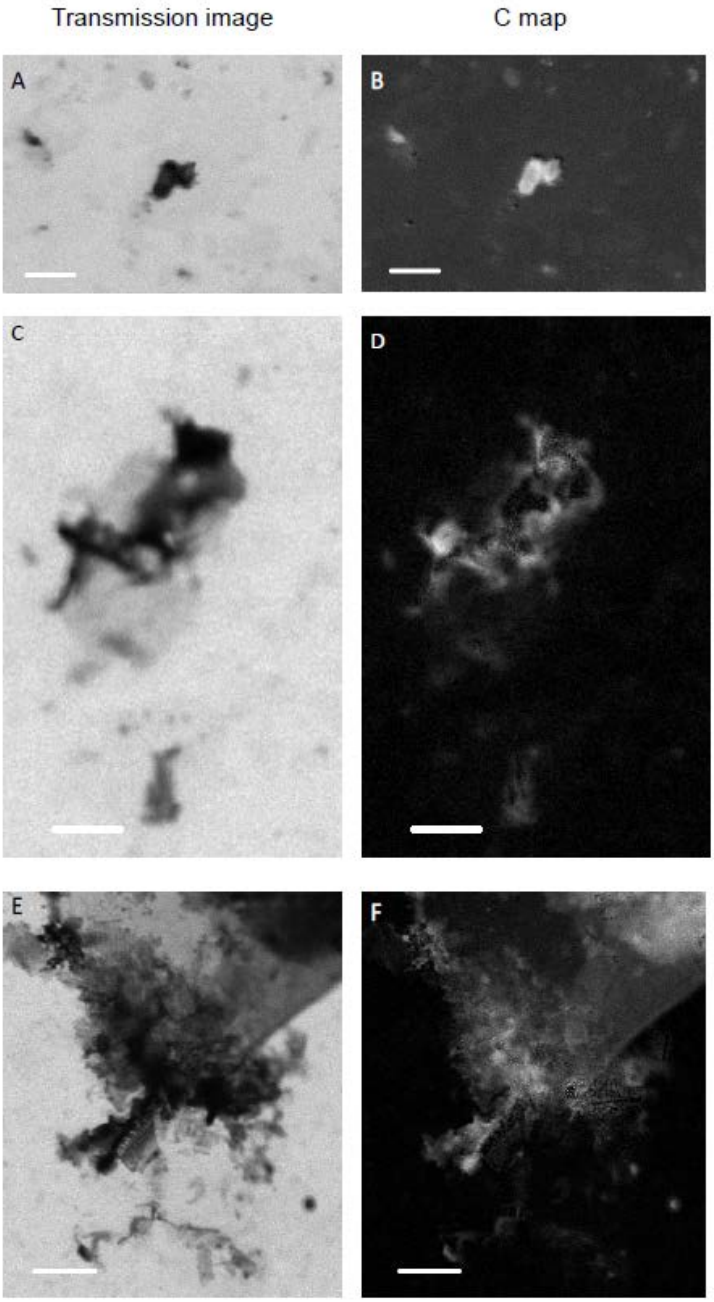

Figure 2.4: C STXM images for SUPR44-APB. **(A)** STXM image recorded at C 1s edge (288.6 eV) from region 1 of SUPR44; scale bar is 2µm; **(B)** C distribution map for **(A)**; optical density = 1.24; **(C)** STXM image recorded at C 1s edge (288.6 eV) from area 2 of SUPR44; scale bar is 2µm; **(D)** carbon distribution map for **(C)** optical density = 1.94; **(E)** STXM image recorded at C 1s edge (288.6 eV) from area 3 of SUPR44; scale bar is 5µm; **(F)** carbon distribution map for **(E)**; optical density = 3.52.

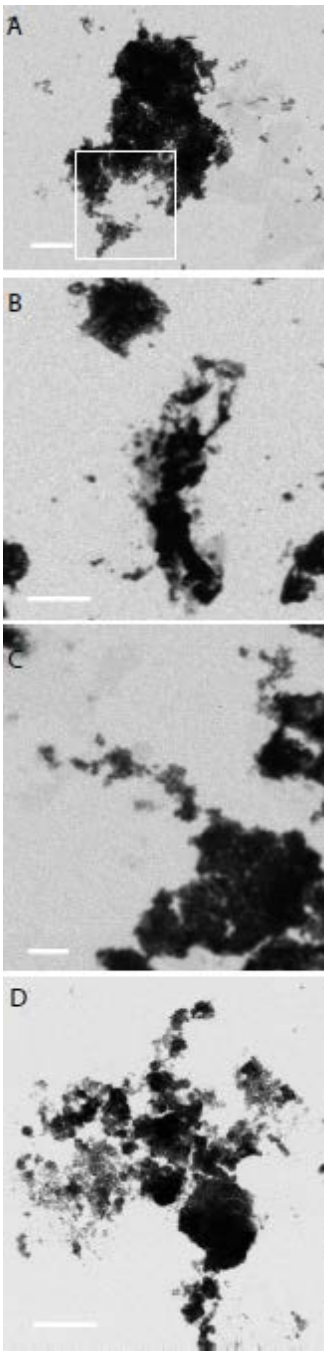

Figure 2.5: Carbon images collected for SUPR30-50, SUPR26-15m, and SUPR22-0.5m showing the distribution of C on the silicon nitride windows. **(A)** C image collected from SUPR30 -50m at 288.6eV; scale bar is 5µm; region in white box has optical density = 2.13 (see figure 2.6) **(B)** C image collected from SUPR26 – 15m at 280eV; scale bar is 5µm; **(C)** C image collected from SUPR26 – 15m at 288.5eV; scale bar is 2µm; **(D)** C image collected from SUPR22 – 0.5m at 340eV; scale bar is 10µm.

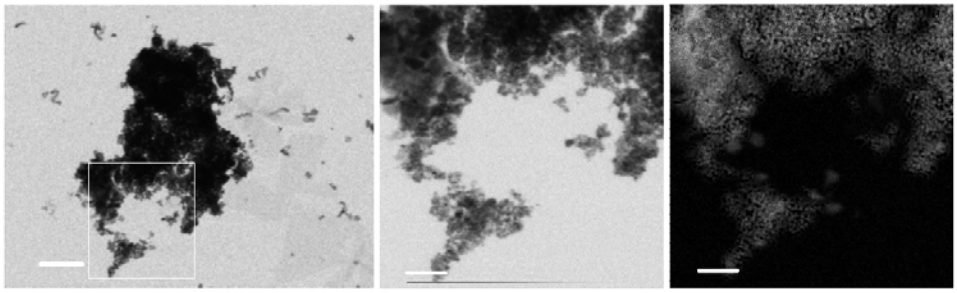

Figure 2.6: **(A)** Carbon image collected from SUPR30 -50m at 288.6eV; scale bar is 5µm (see figure 7); **(B)** Carbon map from white box in image on left; **(C)** Carbon map for image on left; optical density = 2.13.

Table 2.1. Von Damm summary table for the dive/cast, sample elevation (m), volume of seawater filtered (L), vent temperature maximum (°C), sample temperature (°C), Fe concentration as measured by ICP-MS (µmol/kg seawater)[a], and unique sample identifier for samples, and beamline used for Fe and S is XANES[b] analyses.

Dive/Cast	Fe (µmol/kg)	Unique Identifier	Fe XANES	S XANES	C STXM	Fe STXM
J2-614	0.17	SUPR05	10.3.2	10.3.2[c] 13-ID-E[d] 2-ID-B[d]	5.3.2.2[e]	-
J2-614	0.12	SUPR03	-	13-ID-E 2-ID-B	5.3.2.2[e]	-
J2-614	0.18	SUPR11	10.3.2	10.3.2 13-ID-E 2-ID-B	5.3.2.2[e]	5.3.2.2[e]
CTD10	0.03	SUPR57	10.3.2 13-ID-E	10.3.2 13-ID-E	5.3.2.2[e]	5.3.2.2[e]
CTD10	0.06	SUPR58	10.3.2	10.3.2	-	-

a. Fe concentration was measured using ICP-MS (Breier et al., 2014).

b. X-ray Absorption Near Edge Structure (XANES).

c. Advanced Light Source beamline 10.3.2.

d. Advanced Photon Source beamline 13-ID-E and beamline 2-ID-B.

e. Advanced Light Source beamline 5.3.2.2

Table 2.2. Beebe Vents site summary table for the dive/cast, sample elevation (m), volume of seawater filtered (L), vent temperature maximum (°C), sample temperature (°C), Fe concentration as measured by ICP-MS (µmol/kg seawater)[a], and unique sample identifier for samples, and beamline used for Fe and S is XANES[b] analyses.

Dive/Cast	Fe (µmol/kg)	Unique Identifier	Fe 1s XANES	S 1s XANES	C STXM
J2-615	-	SUPR44	-	-	5.3.2.2[e]
J2-615	0.74	SUPR30	10.3.2	10.3.2[c] 13-ID-E[d]	5.3.2.2[e]
J2-615	0.73	SUPR28	-	13-ID-E	-
J2-615	3.84	SUPR26	-	13-ID-E	-
J2-615	5.38	SUPR24	-	13-ID-E	-
J2-615	716	SUPR22	10.3.2	10.3.2 13-ID-E	5.3.2.2[e]

a. Fe concentration was measured using ICP-MS (Breier et al., 2014).

b. X-ray Absorption Near Edge Structure (XANES).

c. Advanced Light Source beamline 10.3.2.

d. Advanced Photon Source beamline 13-ID-E.

e. Advanced Light Source beamline 5.3.2.2.

Table 2.3: Carbon moieties assigned for C 1s X-ray Absorption Near Edge Structure spectra for Von Damm hydrothermal particles.

Sample	Vent elevation (m)	Region	1s → π* unsaturated or aromatic C (C = C)[a]	1s → π* (C = O) Amide (peptide bond)[a]	1s → π* (C = O) Amide (peptide bond) Carboxyl, ester[a]	1s-3p/ σ* (C-OH, alcohol)[b,c]
SUPR57	37	1-3	285.2	288.2		
SUPR11	8	1,3	285.2		288.5	
		2	285.2			289.4
SUPR05	1	1-3	285.2	288.2		
SUPR03	1	1-2	285.2	288.2		
		3	285.2			289.4
Chitin[b,c]				288.2		289.4
Lipid[a]					288.5	289.5
BSA[a]			285.2	288.2		288.5
Alginate[a]			285.2		288.5	

a. Chan et al., 2011
b. Cody et al., 2009
c. Solomon et al., 2009

Table 2.4: Carbon moieties assigned for C 1s X-ray Absorption Near Edge Structure spectra for Beebe particles.

Sample	Vent elevation (m)	Region	1s → π* unsaturated or aromatic C (C = C)[a]	1s → π* (C = O) Amide (peptide bond)[a]	1s → π* (C = O) Amide (peptide bond) Carboxyl, ester[a]	1s-3p/ σ* (C-OH, alcohol)[b,c]
SUPR44	APB	1,3	285.2	288.2		
	APB	2	285.2		288.5	
SUPR30	50	1,3-4	285.2		288.5	
		2	285.2			289.4
SUPR30	50	1-4	285.2		288.5	
SUPR26	15	1				
SUPR22	0.5	1	285.2			
		2-3	285.5			
		4	285.2			
Lipid[a]					288.5	289.5
BSA[a]			285.2	288.2	288.5	
Alginate[a]			285.2		288.5	
Calcite[d]						

a. Chan et al., 2011
b. Cody et al., 2009
c. Solomon et al., 2009
d. Toner et al., 2009

SUPPLEMENTAL FIGURES

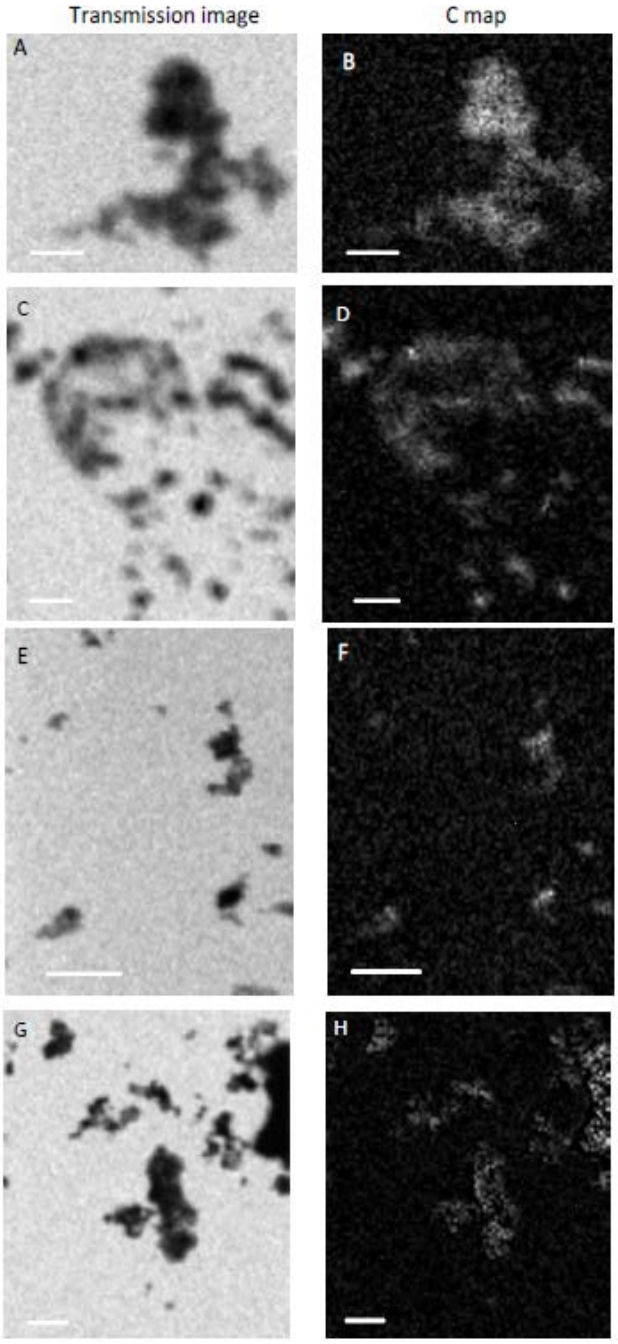

Supplemental figure 2.1: **(A)** STXM image recorded at C 1s edge (288.6 eV) from region 1 of SUPR22; scale bar is 1µm. **(B)** Carbon distribution map for **(A)**; optical density = 0.733; **(C)** STXM image recorded at C 1s edge (288.6 eV) from region 2 of SUPR22; scale bar is 5 µm; **(D)** carbon distribution map for **(C)** optical density = 0.988; **(E)** STXM image recorded at C 1s edge (288.6 eV) from region 3 of SUPR22; scale bar is 5µm; **(F)** carbon distribution map for **(E)**; optical density = 0.882; **(G)** STXM image recorded at C 1s edge (288.6 eV) from region1 of SUPR22; Scale bar is 5µm; **(H)** Carbon distribution map for **(G)**;optical density = 1.31.

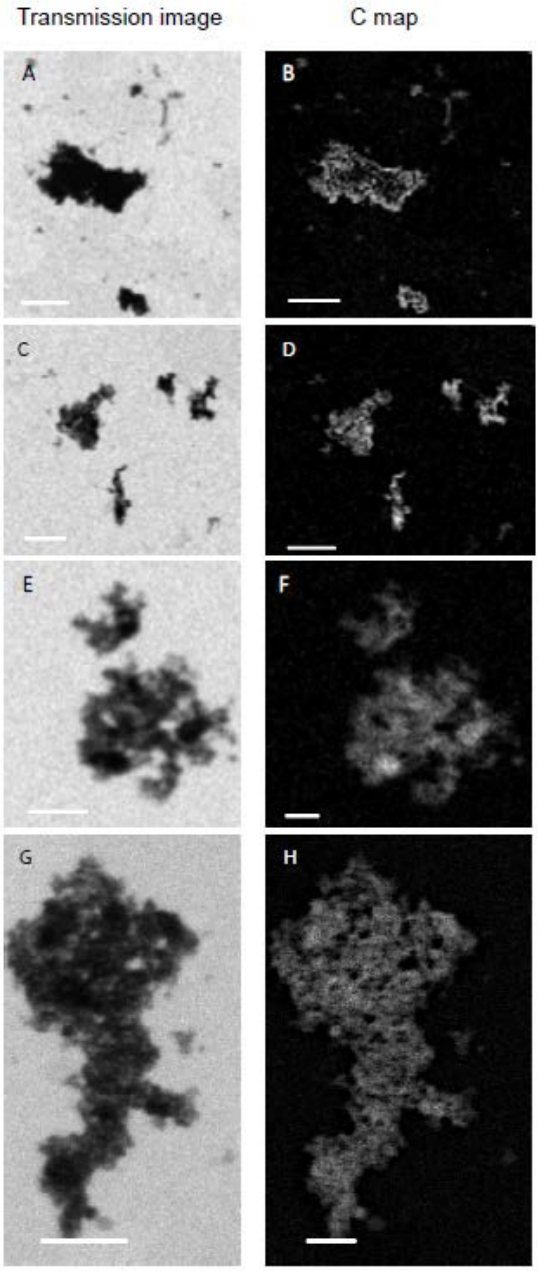

Supplemental figure 2.2: C STXM images for SUPR30-50m. (A) STXM image recorded at C 1s edge (288.6 eV) from region 1 of SUPR30; scale bar is 5µm. (B) Carbon distribution map for (A); optical density = 2.03; (C) STXM image recorded at C 1s edge (288.6 eV) from region 2 of SUPR30; scale bar is 5 µm; (D) carbon distribution map for (C) optical density = 1.58; (E) STXM image recorded at C 1s edge (288.6 eV) from region 3 of SUPR30; scale bar is 2µm; (F) carbon distribution map for (E); optical density = 1.71; (G) STXM image recorded at C 1s edge (288.6 eV) from region 5 of SUPR30; Scale bar is 2µm; (H) Carbon distribution map for (G);optical density = 2.33.

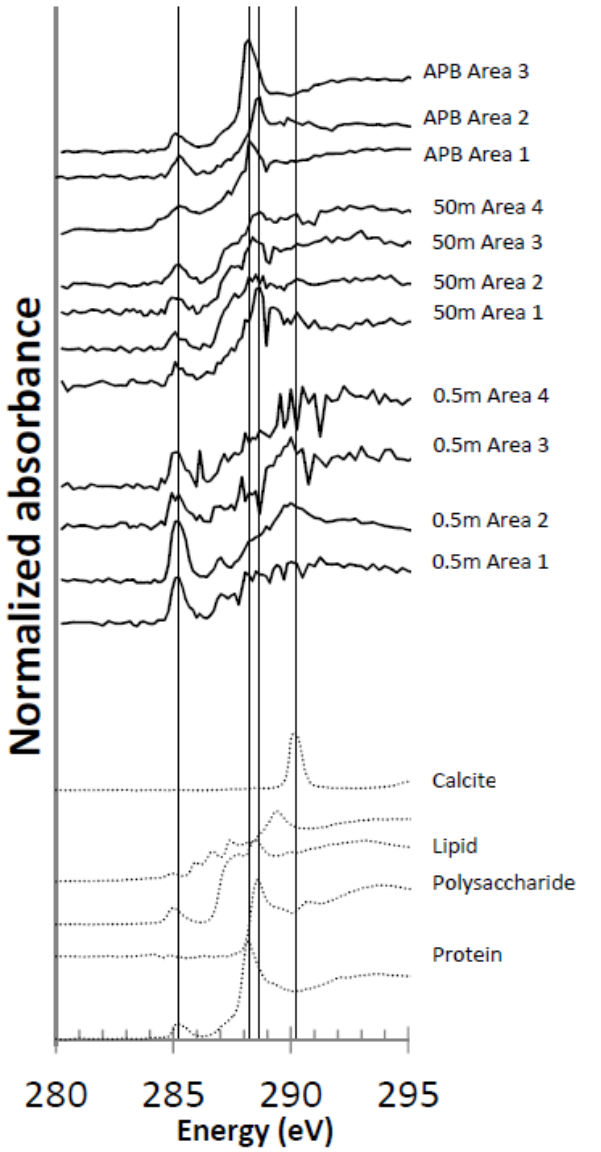

Supplemental figure 2.3: Carbon 1s XANES collected from SUPR22, SUPR30, SUPR44, and SUPR44-APB that show biomolecular signatures. Spectra shown with reference spectra for calcite, lipids, polysaccharides, and protein.

CHAPTER 3

Sulfur 1s X-ray absorption near edge structure (XANES) spectroscopy and chemical mapping of particles and aggregates from Von Damm and Beebe Vents

1. SYNOPSIS

Hydrothermally derived sulfur (S) is an important energy source for chemosynthesis in support of vent primary producers and symbionts. Here we investigate the sulfur (S) chemistry of buoyant plume particles from the Von Damm hydrothermal mound and Beebe Vents, Mid-Cayman Rise, Caribbean Sea. Buoyant hydrothermal plume particles were collected at four elevations above the main Von Damm vent (1m, 8m, 37m, 812m above the vent orifice) and six elevations above the Beebe Vents (0.5m, 5m, 15m, 30m, 50m, APB) using ROV Jason, novel in situ filtration (> 0.2 μm) equipment, and careful shipboard preservation of samples. Sulfur chemistry was measured for particles and aggregates using microprobe S 1s X-ray absorption near edge structure (XANES) spectroscopy and microprobe X-ray fluorescence (XRF) chemical mapping.

Overall, our study reveals a chemically complex suite of particulate S in the physically hydrodynamic plume environments at Von Damm. The S XANES reveal the buoyant plume particles at both sites exhibit a wide variety of S moietites spanning oxidation-reduction (redox) states from S (-2) to S (+6). Phases detected include metal sulfides, inorganic sulfate, and elemental S. Von Damm exhibits a high abundance of organic S -bearing functionalities such as thiol, organic monosulfides, organic disulfides, and ester sulfate. The range of particulate S species observed in the buoyant plume suggest a wide variety of microbial and chemical processes occur in the rising fluids at Von Damm. Comparatively, Beebe Vents buoyant plume particles were composed mainly of iron-rich, strongly reduced (oxidation indices ≤ 1) inorganic S-bearing minerals (metal sulfides). In the first 30m of the rising plume, organic S moieties remain in low abundance, compared to Von Damm. The high concentration of strongly reduced metal sulfides and low

concentration of organic S moieties indicates the Beebe Vents geochemistry is influenced primarily by inorganic processes in the first 30m of the plume.

2. INTRODUCTION

The speciation of S is a key determinant of its reactivity in natural systems (Vairavamurthy, 1993, 1998; Prietzel et al., 2003). Previous S speciation data from hydrothermal systems is based on sequential extraction methods and S isotopic evaluation of minerals collected from chimney structures and fluids samples (Alt et al., 1993; Shanks, 2001; Rouxel et al., 2008; McDermott et al., 2015). Based on these previous investigations, sources of S to hydrothermal systems include: (1) host rocks; (2) sulfide derived from sulfate reduction by bacterial or thermochemical reduction of seawater-derived sulfate; (3) magmatic volatiles; and, (4) sedimentary pyrite and organic-derived S (McDermott et al., 2015, and references therein).

Elevated concentrations of reduced chemical species provide chemical disequilibia in hydrothermal plumes that have the potential to provide energy for microbial primary productivity in hydrothermal vent fluids (German and Seyfried, 2014, and references therein). Microorganisms play a critical role in S cycling from reduced (H2S) to oxidized (SO42-) forms (Findlay et al., 2016). Based on community-wide analyses of genes from plumes and background deep-sea samples, metagenomic data show that S oxidation genes (soxABCDXYZ, apr, sat, sor, rdsr, fcc, and sqr) are the most abundant and diverse form of chemolithoautotrophy in hydrothermal plumes (Anantharman et al., 2016). Microbial S oxidation occurs through several steps and involves oxygen (O2), Fe, and nitrate (NO32-) as potential electron acceptors and H2S, elemental S (S0), and thiosulfate (S2O3-) as potential electron donors (Zopfi et al., 2004). Elemental S and polysulfides are important components of microbial S oxidation (Findlay et al., 2014; Luther et al., 2001; Luther, 1991; Luther, 1990; Luther, 1986). Microorganisms rarely contain all genes needed to convert hydrogen sulfide (H2S) completely to SO42- and it is likely they exchange metabolic intermediates (Anantharaman et al. 2016).

The rising plume fluids at Von Damm and Beebe Vents are a dynamic biogeochemical reaction zone, where S has the potential to be cycled through biotic and abiotic reactions. Known sources of S to the rising plume at Von Damm include H2S and organosulfur compounds (McDermott, 2014; Reeves et al., 2014). Methanethiol (CH3SH), a simply alkyl thiol, in the Von Damm fluids is derived from abiotic decomposition of biomass and biologically derived compounds in the subsurface (Reeves et al., 2014). In the rising plume environment, elevated CH4, H2, and H2S could provide energy for methanotrophs, hydrogen oxidizers, and S oxidizers (McDermott et al,. 2015a; Reed et al., 2015). Sulfur - oxidizing Epsilonproteobacteria Sulfurimonas and Gammaproteobacteria SUP05 have been identified in the plume (Breier et al., 2014; German et al., 2010).

The speciation of S within particles is related to the chemical reactivity of the materials in question, and XANES is a useful tool for the detection of both speciation and distribution of S within particles (Prietzel et al., 2003). Historically, speciation has required applications that use sequential extraction methods (Prietzel et al., 2003 and references therein). For example, acid votile and chromium reducible sulfide (AVS/CRS) were measured to detect S0 and nanoparticulate S0 in concentrations of up to 33µM in first meter of rising hydrothermal plume at the Trans-Atlantic Geotravers (TAG) vent site along the Mid-Atlantic Ridge (Findlay et al., 2014). The XANES method has been established as a nondestructive method for investigating forms of S present in particles (Vairavamurthy, 1994, 1998; Prietzel et al., 2003). The technique has been proven effective at classifying organosulfur compounds such as thiols, organic sulfides, disulfides, polysulfides, and thiophene (Vairavamurthy, 1994; Zeng et al., 2013). Recently, XANES was used to detect the speciation and distribution of S from within hydrothermal plume particles at the submicron scale in particles from the East Pacific Rise (Breier et al., 2013).

The XANES spectroscopy method serves as a non-destructive and element-sensitive technique for the speciation and distribution of particulate S within S-bearing minerals

(Vairamurthy et al., 1997; Manceau and Nagy, 2012).

To apply a Linear Combination Fitting (LCF) method to the XANES data, a robust S reference database was developed that includes all the dominant S species likely present (Manceau and Nagy, 2012). The database presented here includes inorganic S compounds (e.g., pyrite, bornite, chalcopyrite, covellite, elemental S, and polysulfides) and organic S compounds (e.g., sulfoxide, sulfonate, and ester sulfate).

To overcome strong geochemical gradients, rapid entrainment of near bottom seawater, and turbulent conditions that prevail within buoyant hydrothermal plumes, our approach was to use a novel in situ filtration device, the SUspended Particle Rosette (SUPR) sampler, deployed with the Remotely Operated Vehicle ROV JASON (to collect particles from the buoyant plume in a profile above VD-1; Breier et al. 2014). Particles were investigated using particle-specific, synchrotron-radiation X-ray microprobe analysis of the original filter-bound particles. The synchrotron observations of chemical speciation were complemented with bulk geochemical quantification of elements.

Both datasets will be useful in deciphering the activity of plume microbial communities based on metagenomics sequencing. Based on our S 1s XANES observations, Beebe Vents chemistry is dominated mainly by inorganic S-bearing sulfides. These observations are consistent with reports of basalt hosted vent systems. We observed a large diversity of S species in the Von Damm samples. These observations are consistent with reports of substantial microbial processing of the vent fluids prior to venting, as well as an abundance of S redox intermediates in the buoyant plume. The results demonstrate the non-equilibrium status of particles within buoyant plumes, reveal a complex suite of particulate redox intermediates within the buoyant plume, and describe the net effect of buoyant plume processes on the particulate S chemistry of vents.

3. METHODS

Site descriptions are in CHAPTER 1, SECTION 2. Description of sample collection and anaerobic sample preparation is in CHAPTER 2, SECTION 3.

3.1 Sulfur sols preparation

In our experiments, S8nano was prepared by the dilution of saturated elemental S in methanol (S-MeOH) with water (Steudel 2003), with a ratio of S-MeOH:H2O for the S8nano varying from 1:35 (S8nano135R) to 1:6 (S8nano16R) (see table 2 column 'Base Filename' and supplemental figure Fig.3.1). Reference S 1s XANES spectra were acquired for S8nano on beamline SXRMB at the CLS. The S8nano is composed of very small droplets of liquid S "sols" (or S rich compounds) (Steudel 2003) or nanomicrocrystalline S particles (Pasteris et al., 2001) of a hydrophobic character (Garcia Jr and Druschel, 2014). These "sols" are coarsened via nucleation, aggregation and Ostwald ripening processes (Garcia Jr and Druschel, 2014), to turn into α-S8, the thermodynamically most stable form of S in ambient conditions.

3.2 Acquisition of Sulfur reference spectra

Reference S 1s X-ray absorption near edge structure (XANES) spectra were acquired for bornite (Cu5FeS4), chalcopyrite (CuFeS2), covellite (CuS), potassium tetrathionate (K2S4062-), nanoparticulate elemental S (S8nano16R and S8nano135R), and sodium tetrasulfide (Na2S4) in total electron yield (TEY) on beamlines 06B1-1 Soft X-ray Microcharacterization Beamline (SXRMB) at the Canadian Light Source (CLS) (Saskatoon, CA).

S reference spectra were gathered for 1-Amino-2-naphthol-4-sulfonic acid (ANSA) (-RSO3-), cysteine (-RSH), homocysteic acid (-RSO3-), methionine (-RSH), methionine sulfoxide (-RSOR), sodium dodecyl sulfate (SDS) (-ROSO3-), sulfanilamide (-RSRO2), and aromatic 2-thiophenecarboxylic acid (-RSR-) (Zeng et al., 2013).

Yongfeng Hu (personal communication) donated spectra for aromatic benzothiophene (C4H8S). Previously published spectra for L-cystine (-RSSR-), elemental S S(0), greigite (Fe3S4), mackinawite ((Fe,Ni)1 + xSx), pyrite (FeS2), and sodium sulfite (Na2SO3) (Burton et al., 2009; Manceau and Nagy, 2012) were also used (Table 3.1 and Figure 3.2).

To avoid inconsistencies due to choice of standard, all reference spectra were collected after calibration of the monochromator energy using the mineral gypsum (CaSO4H2O) with the 'white line' set to 2482.74 eV. See the APPENDIX for this chapter for the description of calculations made in order to assign oxidation indices to S compounds based on the positon of the white line peak of the main S 1s, or K-edge, absorption edge (Manceau & Nagy, 2012; Prietzel 2012; Vairavamurthy, 1998, 1993, 1995; Zeng et al. 2013). The following S-bearing functional groups were binned together because the XANES spectra did not allow us to differentiate these three sets of the standards (see Figure 3.2): (1) methionine and cysteine; (2) greigite and mackinawite; (3) chalcopyrite and bornite; and, (4) ANSA, homocysteic acid, and sulfone. The following S-bearing functional groups were binned together because the XANES spectra did not allow us to differentiate these three sets of the standards: (1) methionine and cysteine; (2) greigite and mackinawite; (3) chalcopyrite and bornite; and, (4) ANSA, homocysteic acid, and sulfone.

3.3 Assigning oxidation index values for sulfur compounds

Kunzl (1932) was one of the first to use Mosely plots to describe a linear relationship between an element's 1s absorption peak position and valence state based on XANES. Since then, "Kunzl's rule" has been demonstrated many times by others (Mande and Sarpe, 1982; Bart, 1986). Experimental studies involving S XANES have shown a correlation between the intensity of the white line peak of the main S 1s, or K-edge, absorption edge, and oxidation state (Manceau & Nagy, 2012; Prietzel 2012; Vairavamurthy, 1998, 1993; Zeng et al. 2013).

Sulfur XANES can be especially useful for determining the oxidation state of oxyanions of sulfur (e.g., sulfate) because oxygen has a strong electron withdrawing capabilities. Vairavamurthy used Kunzl's rule to assign new oxidation states for thiosulfate (Vairavamurthy et al. 1993) and a sulfoxylate ion (Vairavamurthy et al. 1995). In both studies, a plot for the energy position of the white-line peak for the S 1s absorption edge (in electron volts, eV) versus formal oxidation state for a series of inorganic sulfur compounds (having no ambiguity regarding assignment of the sulfur oxidation state by the traditional method) was used to show a very good linear correlation between peak energy and sulfur speciation.

Vairavamurthy (1998) also used the technique to verify the oxidation state of sulfur in different types of complex organic molecules for which there are irregularities and uncertainties in assigning oxidation state values using the traditional models (Pauling, 1970; Jorgensen, 1969; Hilderbrand & Powell, 1964). Because the XANES-based values differ considerably from conventionally determined oxidation states for most sulfur compounds, Vairavamurthy assigned a new term 'oxidation index' to describe them.

The Vairavamurthy approach, based on Kunzl's rule, to determine sulfur oxidation indices for reference spectra in our database for which the oxidation state was not easily assigned using the traditional model for ionic compound. To do so, a Moseley plot for inorganic compounds (bornite, chalcopyrite, pyrite, S0, sulfite, gypsum) and organic S compounds (homocysteic acid, ANSA, and ester sulfate) with well-known oxidation index values was developed. The S XANES reference spectra were carefully calibrated to a common energy scale, and the energy at which the absorption edge appears is plotted against the oxidation index value for the compound (i.e. valence state assigned using the traditional model for ionic compounds). Cystine, sodium polysulfide, potassium tetrathionate have two different sulfur oxidation states; therefore, a single oxidation index for the material is not possible. For list of absorption peak energies and oxidation indices for each of the S species see Table 3.2 and Figure 3.3. Based on the Moseley plot S-

bearing functional groups were binned into four distinct groups (Figure 3.3):

(1) Strongly reduced (oxidation index ≤ 1). Copper (Cu) Fe monosulfide (greigite (Fe3S4) and mackinawite (Fe, Ni + xS)), Cu sulfide (Cu5FeS2 and CuFeS2), Fe disulfide (FeS2), polysulfide (Na2S4 and K2SO42-), organic disulfide (-RSSR-), thiol (-RSH), α-S8, S8nano16R and S8nano135R, -RSH, and thiophene (-RSO3- and C4H8S);
(2) Weakly reduced (1 < oxidation index < 4). Na2SO3, polysulfide (K2SO42-), and sulfoxide (-RSOR);
(3) Weakly oxidized (4 ≤ oxidation index < 6). Sulfanilamide (-RSRO2), and sulfonate (-RSO3- and -RSO3-);
(4) Strongly oxidized (oxidation index = 6). Ester sulfate (-ROSO3-), inorganic sulfate (CaSO4H2O).

The Moseley plot indicates a positive linear relationship between the energy in electron volts (eV) of the main absorption peak and the oxidation index (valence state) of the S in the compound. For the Beebe Vents dataset, the weakly reduced (sulfite and polysulfides) and weakly oxidized (sulfonate) groups were binned together and called "intermediate and polysulfides."

3.4 Sulfur micro-probe X-ray absorption spectroscopy

The speciation of S in plume particles was measured by synchrotron radiation S 1s XANES at the X-ray microprobe beamline 10.3.2 (Advanced Light Source, Lawrence Berkeley National Laboratory, Berkeley, CA, USA) (Marcus et al., 2004) and the X-ray microprobe beamline 13-ID-E at GeoSoilEnviroCARS (Advanced Photon Source, Argonne National Laboratory, Argonne, IL, USA) (Newville et al., 1999). Additional S 1s XANES spectra were collected at a finer spatial scale at the 2-ID-B beamline (Advanced Photon Source, Argonne National Laboratory, IL) (McNulty et al. 1996).

At all three X-ray microprobes, the sample was raster-scanned through a micro-focused

X-ray beam of monochromatic light to produce elemental maps using X-ray fluorescence (XRF). At 10.3.2, fluorescence was detected using seven-element Ge solid-state or silicon drift diode fluorescence detectors (the Vortex detector in May 2012, the Amptek in January 2013, and the Canberra in November 2013). At 13-ID-E, fluorescence was detected under He flow using a silicon drift Vortex fluorescence detector (August 2013). At 2-ID-B, fluorescence was detected under He flow with a low energy silicon drift diode detector (Ketek). The XRF maps collected at 10.3.2 were deadtime corrected, registered, and combined into a single composite. Counts per pixel were determined using custom beamline software using a normalization setting "none."

At all three instruments, using composite XRF map as a guide, XANES spectra were collected at particular locations within the mapped area, i.e. point observations (Toner et al., 2014). All sample spectra were pre-edge subtracted and post-edge normalized to the edge jump value of 1 using the software ATHENA (Ravel and Newville, 2005). The XANES spectra were fit with linear combination fitting (LCF) of reference spectra to define the range of S (Table 3.1) species present. Normalized spectra were fitted with linear combinations of reference spectra using a custom 10.3.2 Labview-based freeware program (Marcus et al. 2004). The fit quality was evaluated with the normalized sum-of-squares (NSS) parameter, and the addition of a new component was justified when NSS decreased by at least 10%.

Sulfur-bearing functional groups were identified using LCF of S XANES spectra with a suite of S reference spectra (Figure 3.1-3.3; Tables 3.1and 3.2). To measure species abundance, a "speciation mapping" method was developed for the Mid-Cayman Rise samples. The goal was to query large numbers of points within the sample to enable representative and quantitative sampling. The point S XANES observations were used to identify incident energies, spanning the S 1s absorption edges, at which S species present had measurable differences in absorption. The ability to distinguish among S species was estimated by an error calculation that accounted for: 1) total S fluorescence counts; 2) the dwell time per pixel; and 3) the incident energies chosen using custom beamline

software. The composite XRF dataset was fit by LCF with reference spectra along with a background spectrum from a sample blank (XRF tape and Mylar X-ray film) using custom beamline 10.3.2 software.

For S, the speciation mapping approach was developed by expanding on the method of Zeng et al. 2013. To make maps that represented various S species multi-energy maps were acquired by XRF at nine energies [2450(pre-edge), 2470, 2471.73, 2472.6 2481.5, 2478, 2481.5, 2482.74, and 2540 (post-edge)] to create a composite dataset with S 1s absorption profile at each of the ~300,000 pixel queried.

In summary, the investigation of particles on filters requires a sequence of analyses: (1) X-ray fluorescence (XRF) mapping to observe the spatial distribution of S and other particle-forming elements ; (2) point observations of S speciation by S 1s point XANES and LCF with reference spectra to define the range of Fe and S species present; (3) selection of incident X-ray energies for "speciation mapping" as informed by XANES data to measure Fe and S species of interest at every pixel within the area of interest; (4) LCF of speciation map to extract the mol fraction of S species present; and, (5) estimate mol % error for S species using S fluorescence counts, dwell time, and reference spectra used in LCF.

4. RESULTS

4.1 Von Damm Sulfur point XANES

Sulfur 1s XANES spectra were collected for Von Damm for the following samples: VD-2, SUPR11-8m, and SUPR57-37, and VD-1 (Table 2.1). The spectra were fit using linear combinations of S reference spectra (Table 3.1). The fits for each S 1s XANES experimental spectrum were divided into a proportion of reference spectra that is equal to 1 (see supplemental tables 3.1 - 3.4). The S spectra for the each of the four elevations are displayed with the reference spectra that best fit the data (see figures 3.4 - 3.9). The

results of the LCF results are reported as bar charts and binned into S categories based on their oxidation index, and separated again based on whether they were organic and inorganic (Figure 3.10-3.11). The LCF results are summarized in Table 3.3 and Figure 3.11. The best fit components were interpreted as broad categories of S-bearing inorganic (Tables 3.4) and organic (Tables 3.5) functional groups.

Sulfur-bearing functional groups observed in the Von Damm span strongly reduced (-2) to strongly oxidized (+6) S categories (Figures 3.4 – 3.11). Variation in the abundance of oxidation indices at the four elevations are reported as mol % S on a per atom basis (Table 3.3-3.5; Figures 3.11-3.12). A wide variety of organic and inorganic S-bearing functional groups are found at every elevation examined. In general, chemically reduced S emerges from the large vent at the base of the mound (oxidation index < 1) and as fluids rise to 37 m above the vent, the S particles become more chemically oxidized (Figures 3.11f and 3.12). A variety of intermediate redox (sulfite, polysulfide, sulfoxide, sulfone, and sulfonate) and strongly reduced organic (thiol, organic mono- and di-sulfide, and thiophene), species are present within the buoyant plume. However, they do not reveal a strong spatial trend with respect to plume elevation (Figure 3.10c-e).

Strongly reduced inorganic species are highest in concentration in the near-vent samples (Table 3.4; Figure 3.11f). Metal sulfides are present at all plume elevations and decrease from ~ 30 mol% at 1 m (SUPR03 and SUPR05) to ~ 10 mol% at 37m. In contrast, certain strongly reduced organic species, such as thiols, increase with plume height (Figure3.11e; Tables 3.4). Inorganic S species with intermediate oxidation indices (sulfite, sulfoxide, and polysulfide) and strongly reduced inorganic elemental S and nanoparticulate S are only detected in two samples: the base of the main vent, SUPR05-1m, and SUPR11-8m. Organic species with intermediate oxidation indices (sulfone, sulfonate) are detected in every sample, and are highest in the small vent at the top of the mound (SUPR03-1m; see figure 3.12) and lowest in the large vent at the base of the mound (SUPR05-1m) (Table 3.5; Figure 3.11d).

Inorganic and organic sulfate species (ester sulfate) are found at every plume elevation. Overall, these sulfate groups are the most abundant S species detected at 37m (Tables 3.2-3.4). The concentration of sulfate-bearing particles generally increases with plume height. Chemical mapping results confirm the results from the S XANES in terms of S species detected and mol% S (Fig.S3.12-3.14). The variation in the abundance of oxidation indices at the two elevations are reported in mol% S (Table 3.6).

Chemical mapping was used to check the representativeness of the point-XANES results. In general, the chemical mapping agrees well with the point-XANES observations of SUPR05-1m. The chemical map reveals pyrite is spread across the filter as small particles (<3μm) and spots 6-9 contain pyrite (Figure 3.13). The copper iron sulfide is in larger clusters associated with spots 6 and 8 and agrees well with the XANES data. Sulfite, sulfate and inorganic sulfate, elemental S, organic disulfide are also diffusely distributed across the filter in all spots (6-9) and also correlates with the XANES data.

The chemical map for SUPR11-8m agrees well for the XANES for spot 13 and 14 (Figure 3.14). The maps reveals sulfite, nanoparticulate S, and ester sulfate are distributed across the filter. This includes the presence of both elemental S and nanoparticulate S. However, the XANES fits do not indicate thiophene and pyrite as a good fit but the chemical map does.

The concentration of S-bearing functionalities based on S chemical mapping of SUPR05-1m and SUPR11-8m are represented by bar charts (Figure 3.15). The mol% S results from both the point-by-point observations (Figures 3.11-3.12 and table 3.3) and the chemical maps (Figure 3.15) indicate that the point-by-point observations are representative of the species of S present within the particles found in the SUPR05-1m and SUPR11-8m samples. Trends are similar between both datasets for the strongly reduced inorganic elemental S and metal sulfides (Figures 3.11-3.12f and 3.15f). Datasets are also similar for sulfite (Figures 3.11-3.12c and Figure 3.15c), inorganic sulfate (Figures 3.11-3.12b and 3.15b), and ester sulfate (Figures 3.11-3.12a and 3.15a).

4.2 Von Damm particle morphology and elemental distribution

4.2.1 Buoyant plume at 1 m (SUPR05 VD-1)

Based on XRF and S chemical mapping of particles on filters at beamline ALS 10.3.2 and APS 2-ID-B, the large vent at the base of the mound (SUPR05-1m) has S mineral grains that range in size from < 3µm to ~10µm in diameter (Figure 3.13; Fig.S3.1-3.6). The chemical mapping (Figure 3.12) of SUPR05-1m reveals that pyrite is spread across the filter as small particles (<3µm) and copper iron sulfide is in larger clusters associated with intermediately oxidized sulfite. Strongly reduced organic disulfide and strongly oxidized sulfate (organic ester sulfate and inorganic sulfate) are also diffusely distributed across the filter.

4.2.2 Buoyant plume at 8 m (SUPR11)

The XRF and S chemical mapping for SUPR11-8m also reveal S mineral grains that range in size from < 3µm to ~10µm in diameter (Figure 3.13; Fig.S3.7-3.11). The chemical mapping (Figure 3.13) of the 8m sample reveals that strongly reduced thiophene, elemental S, and pyrite cluster together (~3µm in diameter) on the filter with both intermediately oxidized species (sulfite) and strongly oxidized inorganic sulfate. Also, nanoparticulate S is not co-located with elemental S; the nanoparticulate S forms clusters around the elemental S. Ester sulfate appears as particles (<3µm) spread across the entire 200µm2 area. With 2-ID-B, cells were imaged in the SUPR11-8m sample and also determine the cells (Fig.S3.11) contain sulfate and homocysteic acid (Figure 3.9).

4.2.3 Buoyant plume at 37 m (SUPR57)

Based on XRF maps from both 10.3.2 and 13-ID-E, the SUPR57-37m sample has S mineral grains are < 3µm (Fig.S3.12-3.15).

4.2.4 Buoyant plume at 815 m (SUPR58)

Based on an XRF map from13-ID-E, the SUPR58-815m sample has S mineral grains are < 1µm (Fig.S3.16).

4.2.5 Buoyant plume at 1 m (SUPR03 VD-2)

Based on XRF maps from both 13-ID-E and 2-ID-B, the SUPR03-1m sample has S mineral grains are < 3µm (Fig.S3.16-3.19).

4.3 Beebe Sulfur point XANES

Sulfur 1s XANES spectra were collected for the following samples: SUPR22-0.5m (98oC), SUPR24-5m (8oC), SUPR26-15m (6oC), SUPR28-30m (4 oC), and SUPR30-50m (4 oC) (Table 2.2). Sulfur-bearing functional groups observed in the Beebe plume span strongly reduced (-2) to strongly oxidized (+6) S categories (Figures 3.16-3.18). Variation in the abundance of oxidation indices at the four elevations are reported as mol % S on a per atom basis (Figure 3.19-3.20). The linear combination fits (LCF) for each S 1s XANES experimental spectrum were divided into a proportion of reference spectra that is equal to 1 (see supplemental tables, Tables S3.5-3.9).

The S spectra for the each of the four elevations are displayed with the reference spectra that best fit the data (Figures 3.15-3.17). The results of the LCF results are reported in mol% S on a per atom basis, binned into S categories based on their oxidation index, and reported based on organic and inorganic S categories. The binned LCF results are summarized in Table 3.7. Then, the best fit components were also interpreted as broad categories of S-bearing inorganic (Table 3.8) and organic (Table 3.9) functional groups using the reference standard properties reported in Table 3.2.

Sulfur 1s XANES reveal organosulfur species are less abundant than inorganic species. Sulfur-bearing phases in decreasing abundance include: (1) Cu Fe sulfides; (2) Fe

monosulfides; (3) Inorganic sulfate; (4) pyrite; (5) elemental S; (6) ester sulfate; (7) polysulfides; (8) thiol and organic monosulfides; (9) sulfonate; (10) sulfone; and, (11) sulfite. The S XANES data indicate the presence of a wide variety of sulfide particles (Fig.S3.15-3.19; Table 3.7-3.8; Table.S.3.5-3.9). These include Cu Fe sulfides, Cu sulfides, and pyrite (Fig.S3.15-3.19; Table.S3.5-3.9). Based on S XANES, the sulfides at base of the plume (SUPR22-0.5m, and SUPR24-5m) are comprised of mackinawite, greigite, and pyrite (Fig.S3.15 and 3.18; Table.S3.5-3.6).

In general, particles with chemically reduced S emerge from the vent (oxidation index < 1) and as fluids rise to 50m above the vent, the S-bearing particles remain reduced. The hydrothermal vent particles are dominated by strongly reduced inorganic S (metal sulfides and elemental S) and strongly oxidized inorganic S (inorganic sulfate) (Fig.S3.18). Beebe fluids from 0.5m above the vent were primarily iron disulfide (pyrite) and iron monosulfide (greigite and mackinawite) (TableS.3.5). As the fluids reached 50m, metal sulfides remain in high abundance (65mol%), and inorganic sulfate and elemental S decrease (Table 3.7 and 3.8; Figures 3.18). In contrast, certain strongly reduced organic species, such as thiols, and strongly oxidized organic species, ester sulfate, increase with plume height (Figure 3.18).

Sulfur moieties with intermediate oxidation indices (sulfone, sulfonate, and sulfite) and polysulfides are in low abundance in the 0.5m, 30m, and 50m samples (Figure 3.19). Polysulfides are also in low abundance (<8mol%) and are only present in 0.5 sample (SUPR22) and 50m sample (SUPR30) (Fig.S3.19). Throughout the plume, organic S moieities are in much lower abundance than inorganic moieities (<11mol%) (Tables 3.7-3.9; Fig.S3.18-3.19).

Chemical mapping results confirm the results from the S XANES in terms of S species detected and mol% S. The variation in the abundance of oxidation indices at the two elevations are reported in mol% S (Figures 3.23-24).

4.4 Beebe particle morphology and elemental distribution

4.4.1 Buoyant plume at 0.5m (SUPR22)

Based on XRF and S chemical mapping of particles on filters at beamline ALS 10.3.2 and APS 13-ID-E, SUPR22-0.5m has S-bearing particles and aggregates that range in size from < 3µm to ~10µm in diameter (Figure 3.20; Fig.S3..20-3.23). The chemical mapping (Figure 3.21) of SUPR22-0.5m reveals that pyrite, nanoparticulate elemental S, mackinawite, and inorganic sulfate are dominant S-bearing minerals on the filter and appear as large clusters (>10µm). Elemental S, sulfanilamide and sulfite are also diffusely distributed across the filter in small clusters (<1µm).

4.4.2 Buoyant plume at 50m (SUPR30)

The XRF maps of SUPR30-50m also reveal S mineral grains that range in size from < 3 µm to ~10µm in diameter (Figure 3.21; Fig.S3.24-3.26). The chemical mapping (Figure 3.21) of the 50m sample reveals that strongly reduced inorganic S moieties cluster together (~3 µm in diameter) on the filter with both intermediately oxidized species (sulfite) and strongly oxidized inorganic sulfate. Polysulfide, nanoparticulate S, inorganic sulfate, SDS, and sulfite appears as particles that are clustered together (<3 µm). Whereas, greigite and chalcopyrite are diffusely spread across the entire 200µm2 area.

4.4.4 Buoyant plume at 5m (SUPR24), 15m (SUPR26), and 30m (SUPR28)

The XRF maps from 13-ID-E reveal particles in the SUPR24 -5m (Fig.S27), SUPR26-15m (Fig.S28), and SUPR28-30m (Fig.S29), elevations are <3 µm to ~10 µm in diameter. Salt crystals are seen on the silicon nitride window for SUPR28-30m (Fig.S29) and SUPR26-15m (Fig.S28).

5. DISCUSSION

5.1 Sources of S and organic C into the buoyant plume from the subsurface at Von Damm

The subsurface serves a source of H2S, organic C, and metal sulfides to the rising buoyant plume at Von Damm. Sources of S to the Von Damm fluids from the subsurface to endmember fluids have been investigated by others and include H2S (McDermott, 2014). In general, the sub-seafloor environment of hydrothermal vents is a known source for H2S and metal sulfides (e.g., pyrite, chalcopyrite, troilite) to buoyant plume fluids (Ono et al., 2007; Yucel et al. 2011; McDermott et al. 2015a). So, we postulate that metal sulfides are also being produced in the subsurface at Von Damm. Microbial communities in the following generas Methanothermococcus, Archaeoglobus and Sovum are found in the subsurface at Von Damm (Reveillaud et al., 2016). Their cellular material and metabolic biproducts are likely contributing to organic carbon and S from biomass to the subsurface and subsequent near vent samples. These sources of S and organic C in the subsurface are important because it is likely organic C in the subsurface reacts with H2S to generate thiols, organosulfur, and polysulfides (Werne et al., 2004). It has been determined that the CH3SH within the endmembers fluids at Von Damm is derived from abiotic thermal decomposition of preexisting biomass and biological derived compounds (Reeves et al., 2014). The subsurface is also a source of abiotic organic carbon, including species such as CH4 and ethane (C2H6) (McDermott et al., 2015b). Microbial communities in the subsurface are also likely oxidizing S to make intermediately and strongly oxidized S species.

Our S 1s XANES and chemical mapping data reveal a decrease of reduced metal sulfides in the near vent samples (Figures 3.11-3.12 and 3.15). This suggests metal sulfides are formed in the Von Damm fluids either in the subsurface or as the fluids emerge into the deep ocean. The presence of strongly reduced organic S (thiols, organic mono- and disulfides) in the near vent samples (Figure 3.11e and 3.12) indicate that S species react with organic material (abiotic in origin or bioproducts of microbial processes) in the

subsurface, before the fluids emerge. The presence of intermediate and oxidized S species (sulfonate, sulfone, and ester sulfate) as well as elemental S, a known intermediate for S oxidation processes, in the first meter of the rising vent fluids also indicate that microbial processes and chemical oxidation occur in the subsurface or in the near vent samples (Figure 3.11c-d and Fig.315c-d).

5.2 Physical mixing and entrainment processes at Von Damm

As hydrothermal vent fluids rise from the subsurface they are immediately physically mixed with deep ocean seawater (Lupton et al., 1985; Reed et al., 2015). Entrainment of deep ocean waters and re-entrainment of hydrothermal material are processes that dilute vent fluids within the buoyant hydrothermal plume. Dilution occurs at a ratio of 10,000 to 1 (seawater to vent fluid) (Lupton et al., 1985). Entrainment can pull in oxygenated seawater, particles, and microbial communities originating from both the upper water column and background seawater. Microbial communities from the demersal deep ocean background seawater can be entrained as far up as 10m above the seafloor (Reed et al., 2014; 2015). Entrainment also pulls in debris and microbial communities from the host vent site (Estrapa et al., 2016). There is also entrainment of aged particles that reside in the background seawater and the host vent site, including Fe oxyhydroxides (Estrapa et al., 2016; Reed et al., 2015; Bennett et al., 2015; Reed et al., 2014; Sheik et al., 2014; Lupton et al., 1985). Our S 1s XANES suggest that physical entrainment allow for both oxygenated seawater and possibly microbial communities to react with the particles within the Von Damm fluids. By 8m above VD-1, metal sulfides and S0 decrease and S intermediates remain in low abundance (<15 mol%) (Figure 3.11f and 3.12f). By the time the fluids reach 37m above VD-1, all the intermediates are almost gone and sulfates and sulfides are left in high abundance (~20-35 mol%) (Figures 3.11c-d and 3.12). This shift in phases from strongly reduced to oxidized, including the appearance of intermediate phases, suggest turbulent mixing of Von Damm fluids with seawater provide oxic and pH neutral conditions where chemical and biological interactions can occur.

5.3 Transformation of S within the buoyant plume

5.3.1 Sulfur oxidation processes due to metabolism in Von Damm

Entrainment of flocculent material from background seawater also pulls in particulate organic carbon in the Von Damm hydrothermal vent fluids that comes from the surface ocean. The photosynthetic processes likely contribute recalcitrant C that is highly degraded to the plume geochemistry (i.e., marine snow; Bennett et al., 2015). Sulfur can be incorporated into organic compounds to form cyclo-S groups (thiophene) or chains of S such as mono- and di-sulfides (Werne et. al., 2004). It is likely organic C in the plume reacts with S to generate organosulfur compounds.

Microbial populations capable of utilizing mineral substrates in rising hydrothermal plumes, as the fluids rise and laterally spread into the non-buoyant plume, have been characterized previously (Reed et al., 2015; Li et al., 2015; Dick et al., 2009). Previous work demonstrated that Mn-oxidizing microbial communities within the Guaymas Basin hydrothermal plumes and communities such as members of the S-oxidizing ε-proteobacteria SUP05 in the Eastern Lau Spreading Center respond to and alter the geochemical gradients within the buoyant plume (Dick et al., 2009). Sulfur XRF maps show microbial cells in the Von Damm 8m sample (Fig.S11b). Epsilonproteobacteria, known S-and H-oxidizers, are present in both the rising plume and the subsurface at Von Damm (German et al., 2010; Breier et al., 2014; Reveillaud et al., 2016). Sulfur oxidizing communities are likely using SOX or rDSR pathway to generate oxidized forms of S in the rising plume.

The increase in oxidized and intermediate phases and the decrease in reduced sulfides, leads us to hypothesize that biotic reactions occur within the plume and in the surrounding seawater at Von Damm. Sulfur cycling by microbial metabolisms rarely leads to the complete oxidation of sulfide to sulfate and leads to complex mixtures of S intermediates (Anantharaman et al. 2016). It is likely the communities are oxidizing H2S

before using elemental S as an electron donor. A study done with enrichment cultures determined that the rates of denitrification and sulfoxidation for chemolithotrohpic S oxidation with nitrate and oxygen is strongly dependent on the inorganic S compound utilized as an eletcton donor. They determined that thiosulfate and sulfide are more favorable than powered elemental S (bulk αS) (Cardoso et al., 2006).

5.3.2 Reactive intermediates at Von Damm

The shift in phases from reduced to oxidized, suggests biotic and abiotic reactions produce multiple phases of particulate S in the subsurface and within the Von Damm plume. The Von Damm fluids become more oxidized within the first 37m, due to possible (1) microbial oxidation, or; (2) highly reactive particles reacting with oxygenated seawater. The S XANES and chemical mapping data indicate the presence of a wide variety of inorganic and organic S-bearing particles with oxidation indices that span >1 and < 6 (Figures 3.11-3.12 and 3.15). Intermediates include sulfite and polysulfides that are present 1m to 8m above VD-1 (Figures 3.11c and 3.12). As well as sulfoxide that is present (<5 mol%) 8m sample above VD-1 (Figure 3.11c). Sulfonate is present in all of the samples and is highest in the 1m sample above VD-2 (~35 mol%) (Figure 3.11d). Sulfone is in the 8m and 37m sample from above VD-1 (<5 mol%) (Figure 3.11d). The wide variety of S-bearing minerals and functional groups that are intermediately oxidized, within the first 8m, suggest that biogeochemical reactions within the Von Damm fluids include abiotic and biotic chemical reactions with H2S and metal sulfides that occur both in the subsurface and within the rising plume of the Von Damm hydrothermal vent.

5.4 Redox Status of Particles in the Beebe Vents Buoyant Plume

There is an abundance of reduced sulfides in the APB sample (SUPR44). The appearance of elemental S, sulfite, and polysulfides (species of intermediate oxidation indices) in SUPR22-0.5m, SUPR28-30m, and SUPR30-50m suggests that redox processes are active

within the plume, either abiotic or biotic. The known existence of S- and H- oxidizing microbial communities (Reveillaud et al., 2016) indicates biotic processes occur within the diffuse fluids at Beebe. Oxidized S-bearing minerals at higher elevations within include intermediate S-bearing mineral phases (sulfite and polysulfides) and strongly oxidized inorganic sulfate and organic sulfate (ester sulfate) (SUPR 28-30m and SUPR30-50m) (Figures 3.17-3.20) are also an indication of microbial S-oxidation (McCollom, 2000).

The low concentration of organic S-bearing minerals, in the near-vent plume (SUPR22-0.5m up to SUPR28-30m; Figures 3.17-3.20), suggest that the chemistry is controlled by predominately abiotic reactions. Due to the lack of microbial cells or organic C in the SUPR22-0.5m up to SUPR28-30m samples (see CHAPTER 2), these reactions appear to occur quickly and outcompete microbial metabolic processes in the first 30m meters of the rising plume (Yucel et al. 2011; Luther et al., 2001; Findley et al., 2015; Rickard 1997).

6. CONCLUSIONS

We expanded our S reference database and included more metal sulfides and size resolved S sols. Based on XANES perspective, cyclooctasulfur (α-S8) and sols are very similar. Our Moseley plot indicates a positive linear relationship between the eV of the main absorption peak and the valence state of the S in the compound, and the plot helped to bin both the organic and inorganic S-bearing compounds into four categories ranging from reduced (-2) to oxidized (+6). The point-by-point observations and chemical maps reveal similar trends for the strongly reduced inorganic elemental S and metal sulfides, sulfite, and sulfates.

Chemical and biological S oxidation processes and physical entrainment and re-entrainment mixing processes are mixing the reduced (H2S, metal sulfides, S0), intermediate (thiol, organosulfur, polysulfides, and sulfite), and oxidized (ester sulfate

and inorganic sulfate) forms of S among the various elevations within the buoyant plume at Von Damm. The S-bearing particles within the buoyant plume, from bottom to top, decrease in chemically reduced phases. According to our S XANES data, intermediate and oxidized forms of S (i.e., S0, sulfite, sulfate, and polysulfides) begin to form either in the subsurface or as the fluids emerge from the low-temperature VD-1. The intermediate forms of S are detectable within the plume up to 8m above the vent. These S species are an indication that biotic (i.e., SOX or rDSR pathway) S oxidation is occurring in the subsurface and within the plume. These are also evidence of abiotic S oxidation. There might also be entrainment of background seawater S-oxidizing microbial communities and their biomass at the 1m and 8m elevations within the plume. There is a wide range of reactive intermediates in the 8m sample, an indication that oxidation is occurring in the plume or entrainment of oxidized speicies occurs at both the 1m and 8m sample elevations. The top of the plume (37m) contains less variation in S forms, mainly oxidized inorganic and organic sulfate. These forms of S might be exported to the non-buoyant plume and effect the deep-ocean geochemistry.

Overall, our study provides unprecedented spatial and chemical resolution of S-bearing minerals and particulate organosulfur compounds in a dynamic buoyant hydrothermal plume at Von Damm and Beebe Vents. Based on S XANES, we were able to detect, for the first time, a wide variety of particulate inorganic and organic S species at four discreet elevations within the Von Damm rising plume. Even though the fluids are low in metals relative to many deep-sea vents, S-bearing mineral phases are available to participate in both abiotic and biotic chemical reactions.

Chemical changes in the Von Damm hydrothermal plume result from dilution and chemical reactions between the source vent-fluids and the seawater, as well as biotic alteration of minerals and interaction with organic carbon. The C 1s STXM and XANES results in CHAPTER 2 reveal the presence of cellular material and cells in the 1m and 37m samples from the Von Damm fluids. The S XRF map from 2-ID-B also reveals cells in the 8m samples. These data and the known existence of S-oxidizers in the surrounding

seawater also indicate that the wide variety of organic and inorganic S-bearing minerals and moieties are a result of abiotic and biotic chemical processes.

At Beebe Vents, the fluids lack cells and there is a low abundance of organic C in the first 30m of the plume (see CHAPTER 2). Combined with the high concentration of reduced S-bearing minerals, abiotic chemical processes influence the types of S species present in the near-vent particles up to the 30m elevation. Based on the increase in oxidized S-bearing minerals and organic S-bearing moieties 30m and 50m samples, it is likely that diffuse flow microbial communities and ambient seawater communities are entrained in the Beebe Vents hydrothermal plume at 30m above the vent orifice.

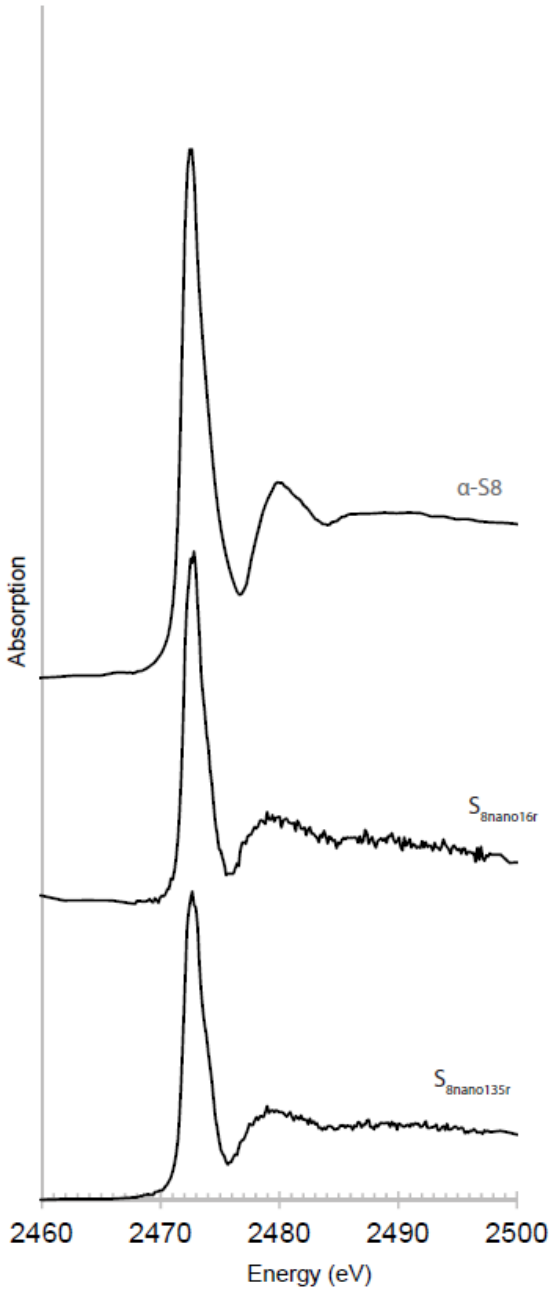

Figure 3.1: Normalized XANES spectra for S_{8nano} prepared by the dilution of saturated elemental sulfur in methanol (S-MeOH) with water (Steudel 2003), with a ratio of S-MeOH:H2O for the S_{8nano} varying from 1:35 to 1:16.

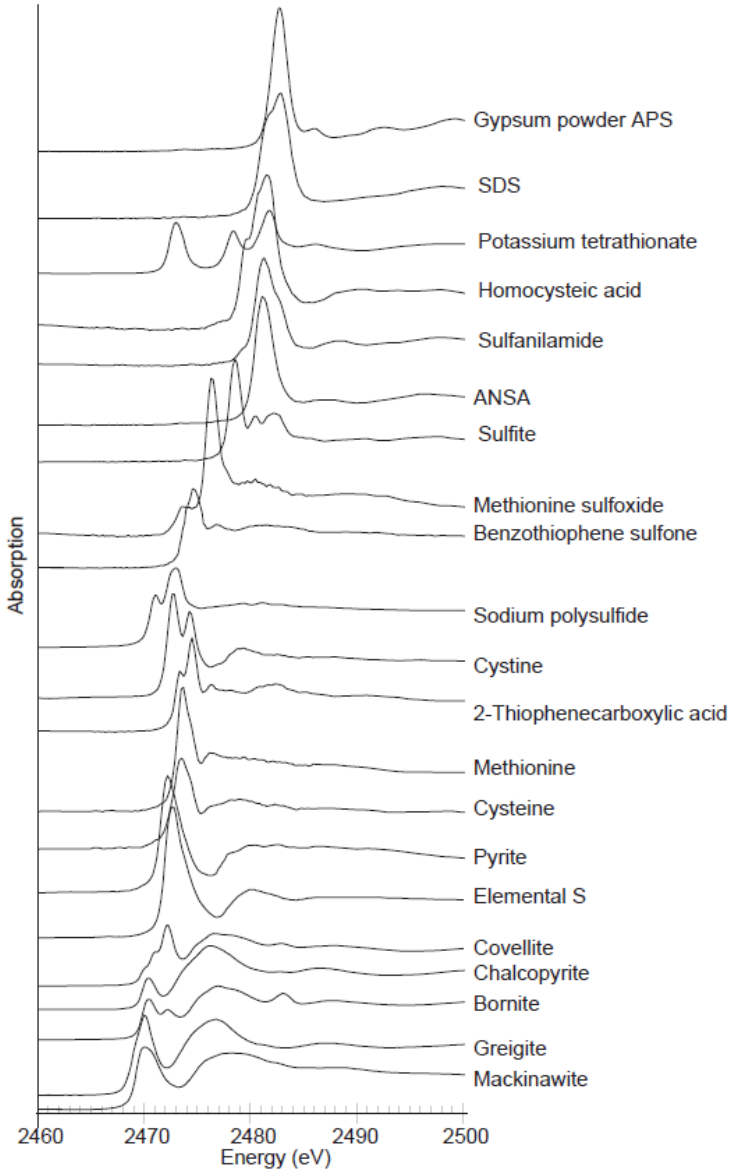

Figure 3.2: Normalized XANES spectra of S reference compounds. Normalized XANES spectra for S8nano can be found in Fig.S3.1.

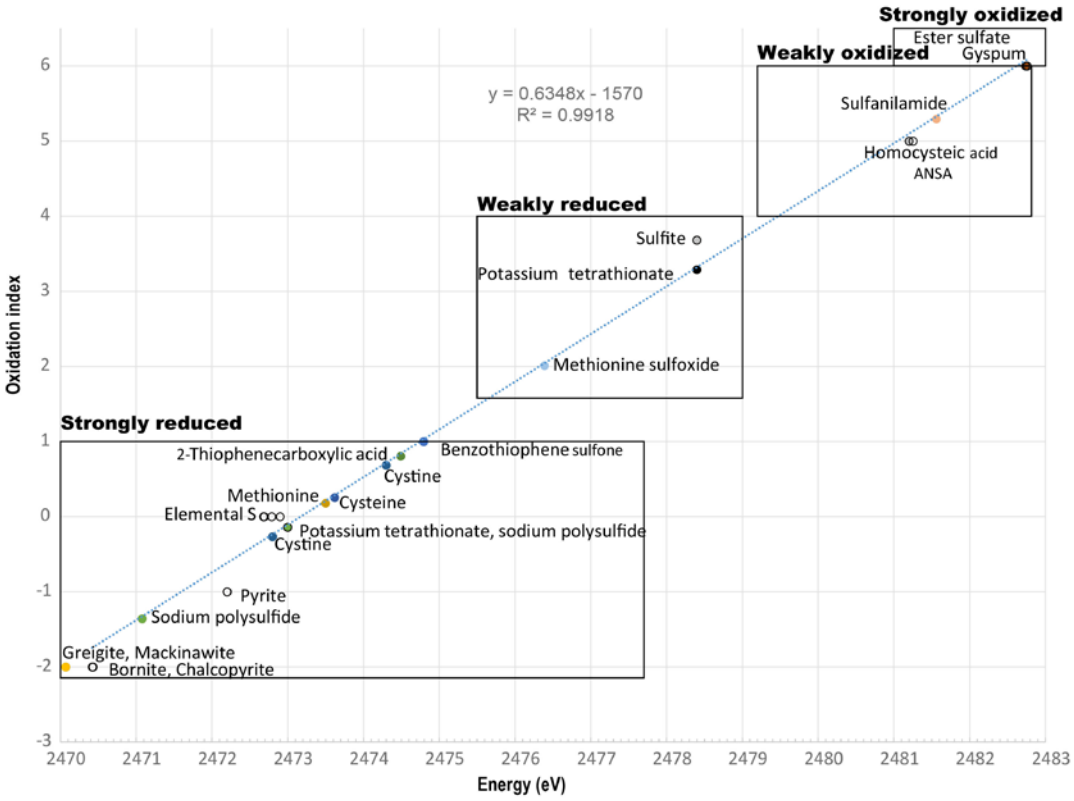

Figure 3.3: Energy (K-edge absorption in eV) of S functionalities with different oxidation indices. Solid line represents linear regression of all data points (R=0.9918). Plot based on data in tables 3.1 and 3.2.

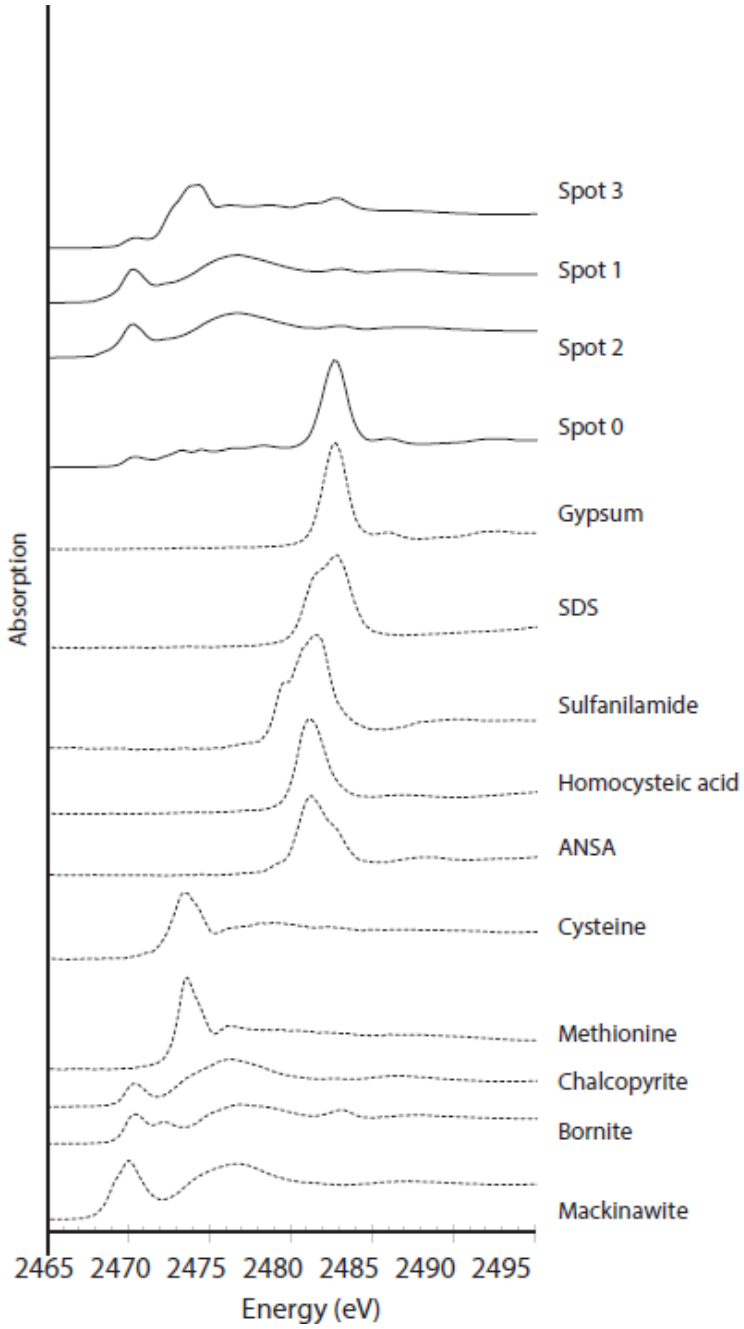

Figure 3.4: Sulfur 1s XANES spectra collected at beamline 13-ID-E displaying the range of S species present in sample SUPR03 collected 1m above Von Damm. The reference spectra (dashed lines) shown are those that created the best LCF results (gypsum, SDS, sulfanilamide, homocysteic acid, ANSA, cysteine, methionine, chalcopyrite, bornite, and mackinwate).

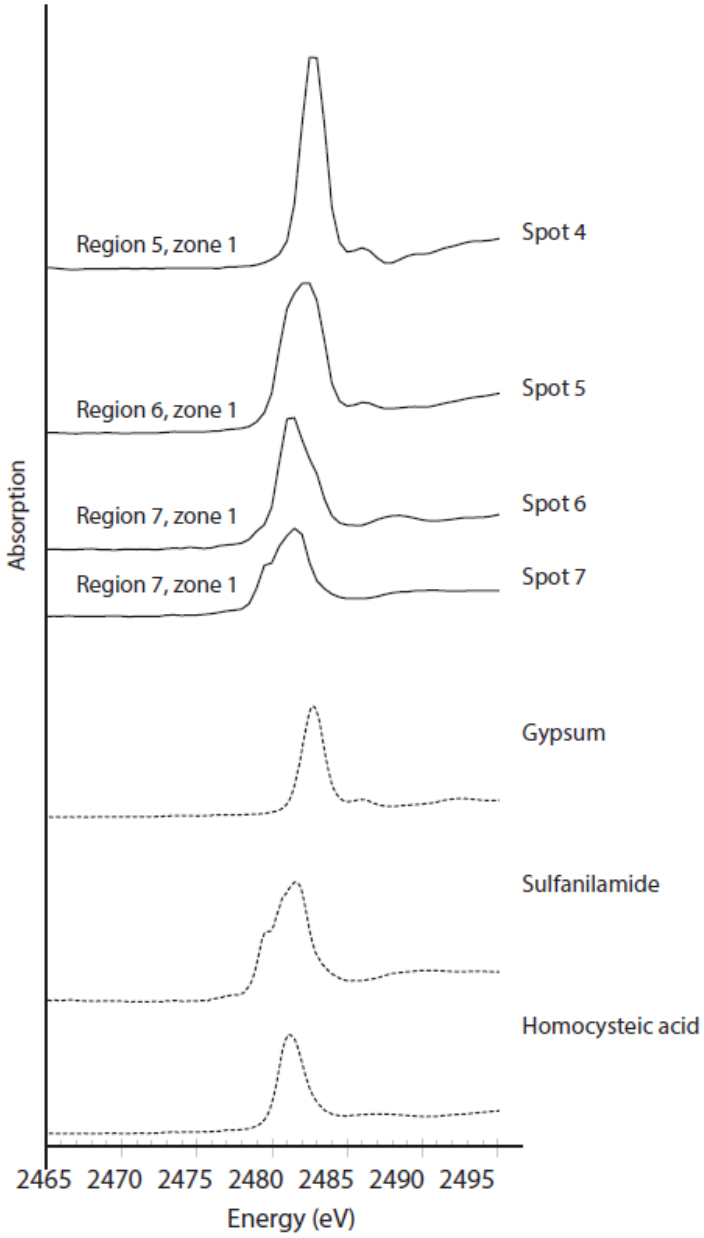

Figure 3.4b: Sulfur 1s XANES spectra collected at beamline 2-ID-B displaying the range of S species present in sample VD-2. The reference spectra (dashed lines) shown are those that created the best LCF results (gypsum, sulfanilamide, and homocysteic acid).

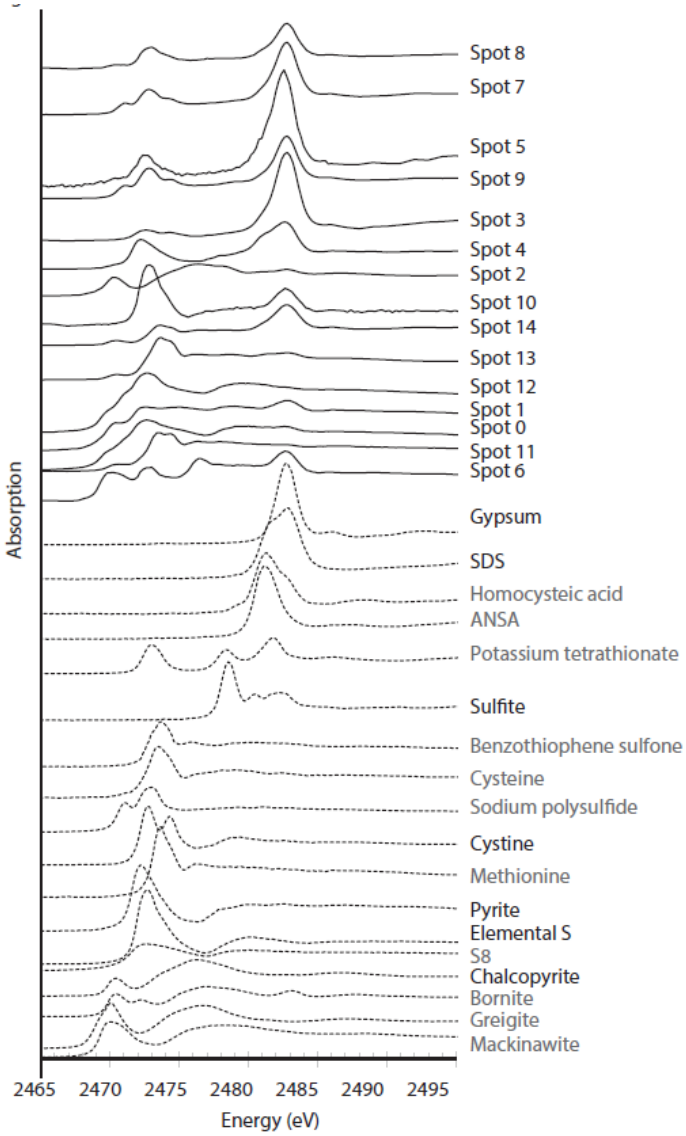

Figure 3.5: Sulfur 1s XANES spectra collected at beamline 10.3.2 and 13-ID-E displaying the range of S species present in sample VD-1 collected 1m above Von Damm. The reference spectra (dashed lines) shown are those that created the best LCF results (gypsum, SDS, sulfanilamide, homocysteic acid, ANSA, potassium tetrathionate, sulfite, benzothiophene sulfone, sulfite, sodium polysulfide, cysteine, methionine, pyrite, elemental S, nanoparticulate S, chalcopyrite, bornite, greigite, and mackinwate). Reference spectra with bold font text are those used to fit the S chemical map (gypsum, SDS, sulfite, cysteine, pyrite, elemental S, and chalcopyrite).

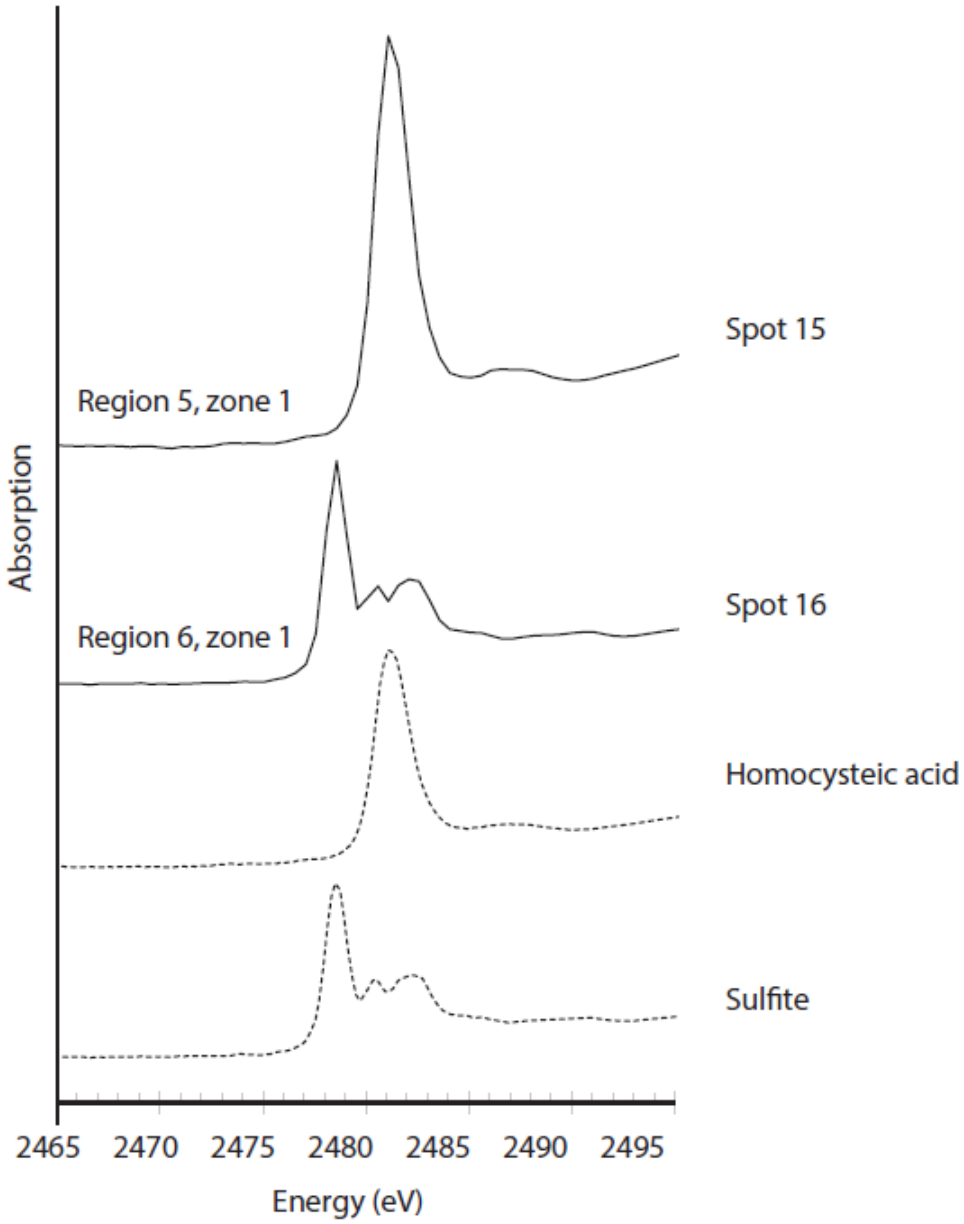

Figure 3.6: Sulfur 1s XANES spectra collected at beamline 2-ID-B displaying the range of S species present in sample VD-1 collected 1m above Von Damm. The reference spectra (dashed lines) shown are those that created the best LCF results (homocysteic acid and sulfite).

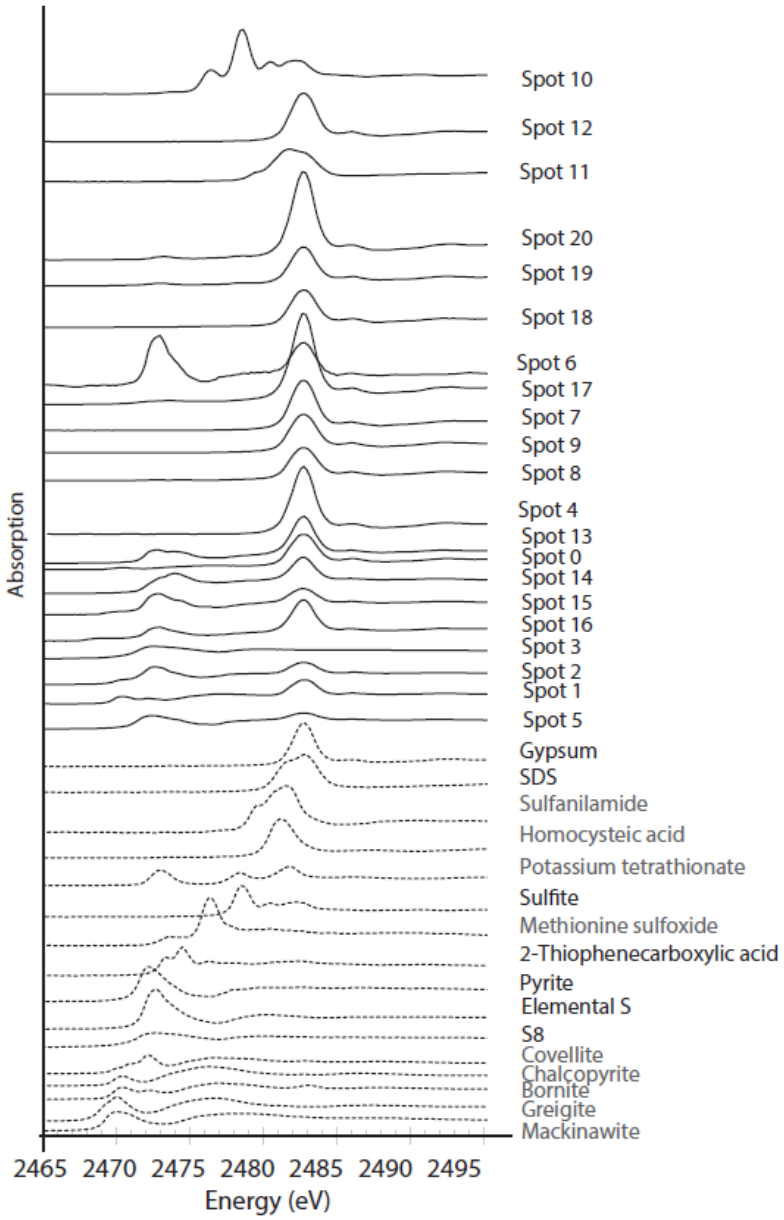

Figure 3.7: Sulfur 1s XANES spectra collected at beamline 10.3.2 and 13-ID-E displaying the range of S species present in sample SUPR11 collected 8m above Von Damm. The reference spectra (dashed lines) shown are those that created the best LCF results (gypsum, SDS, sulfanilamide, homocysteic acid, potassium tetrathionate, sulfite, methionine sulfoxide, 2-thiphenecarboxylic acid, pyrite, elemental S, nanoparticulate S, covellite, chalcopyrite, bornite, greigite, and mackinwate). Reference spectra with bold font text are those used to fit the S chemical map (gypsum, SDS, sulfite, 2-thiophenecarboxylic acid, pyrite, elemental S, and nanoparticulate S).

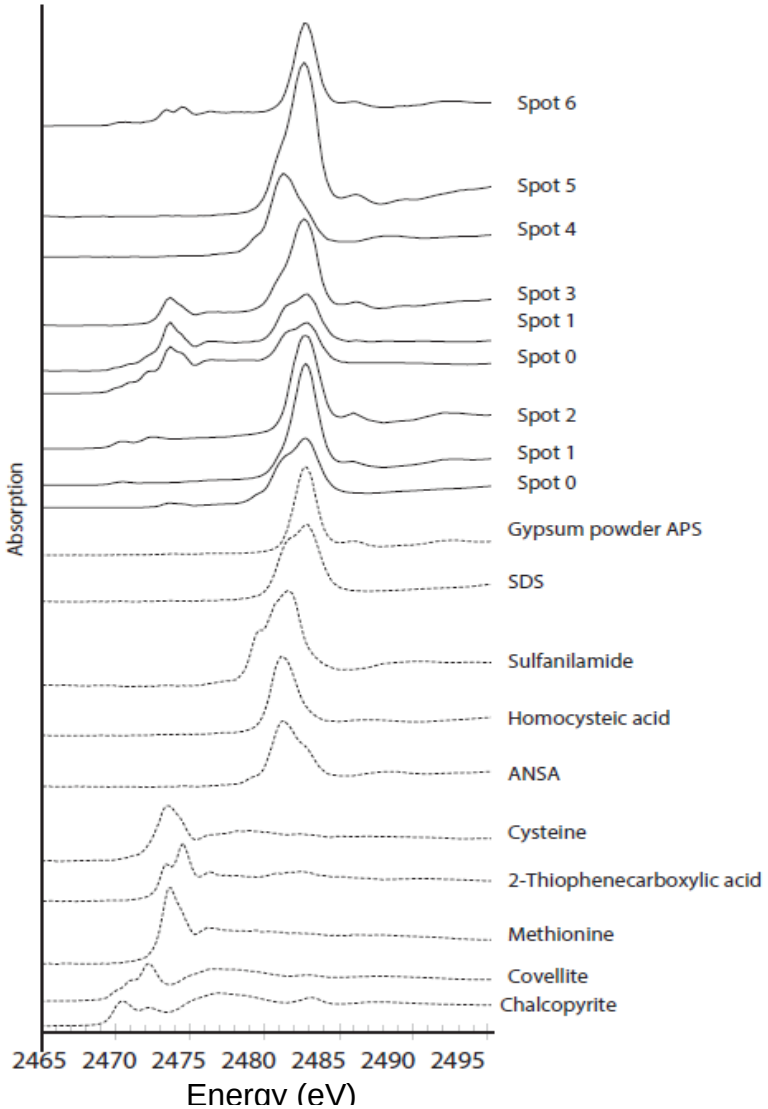

Figure 3.8: Sulfur 1s XANES spectra collected at beamline 2-ID-B displaying the range of S species present in sample SUPR11 collected 8m above Von Damm. The reference spectra (dashed lines) shown are those that created the best LCF results (gypsum and homocysteic acid).

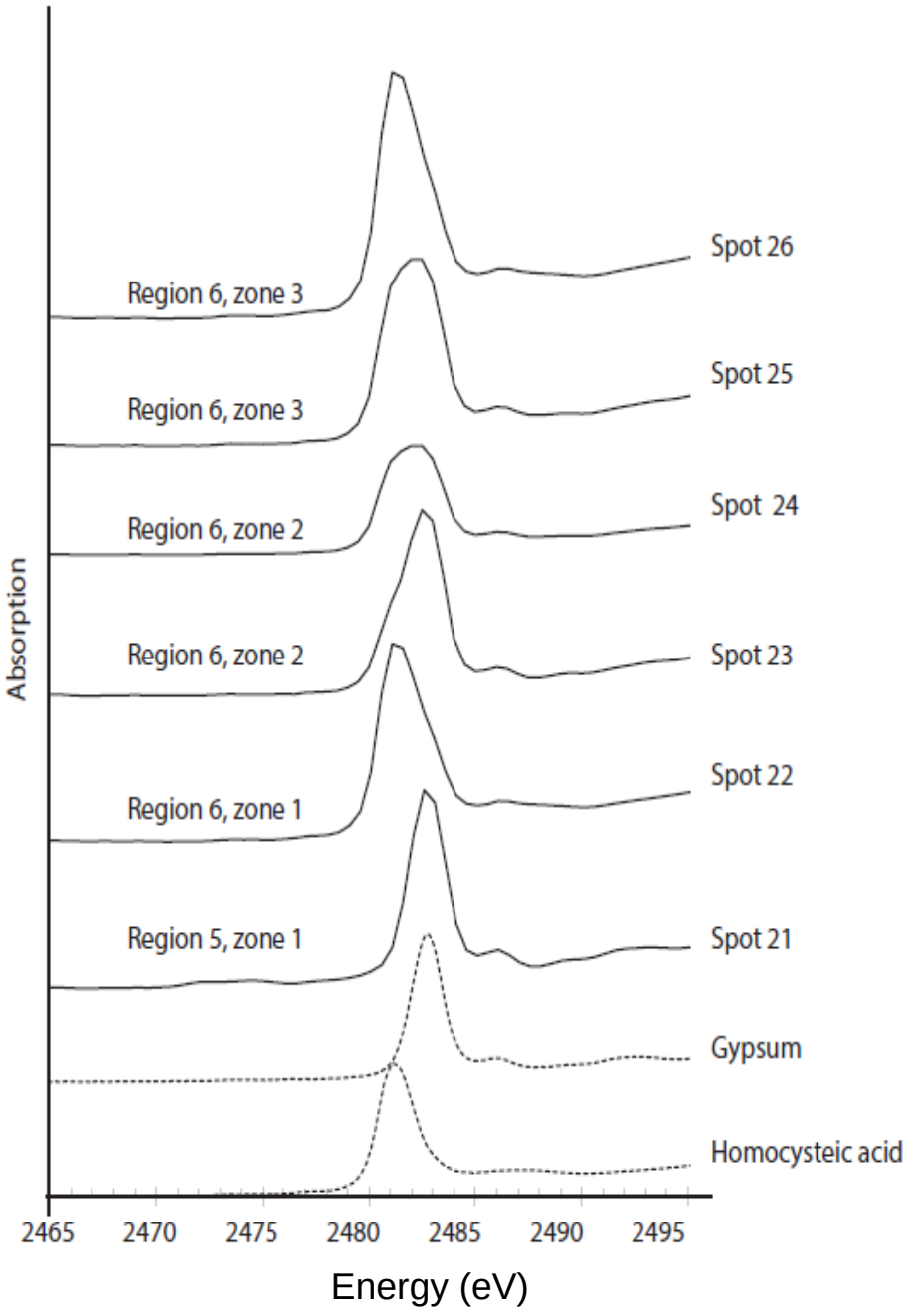

Figure 3.9: Sulfur 1s XANES spectra collected at beamline 2-ID-B displaying the range of S species present in sample SUPR57 collected 37m above Von Damm. The reference spectra (dashed lines) shown are those that created the best LCF results (gypsum, SDS, sulfanilamide, homocysteic acid, 2-thiphenecarboxylic acid, methionine, covellite, and chalcopyrite).

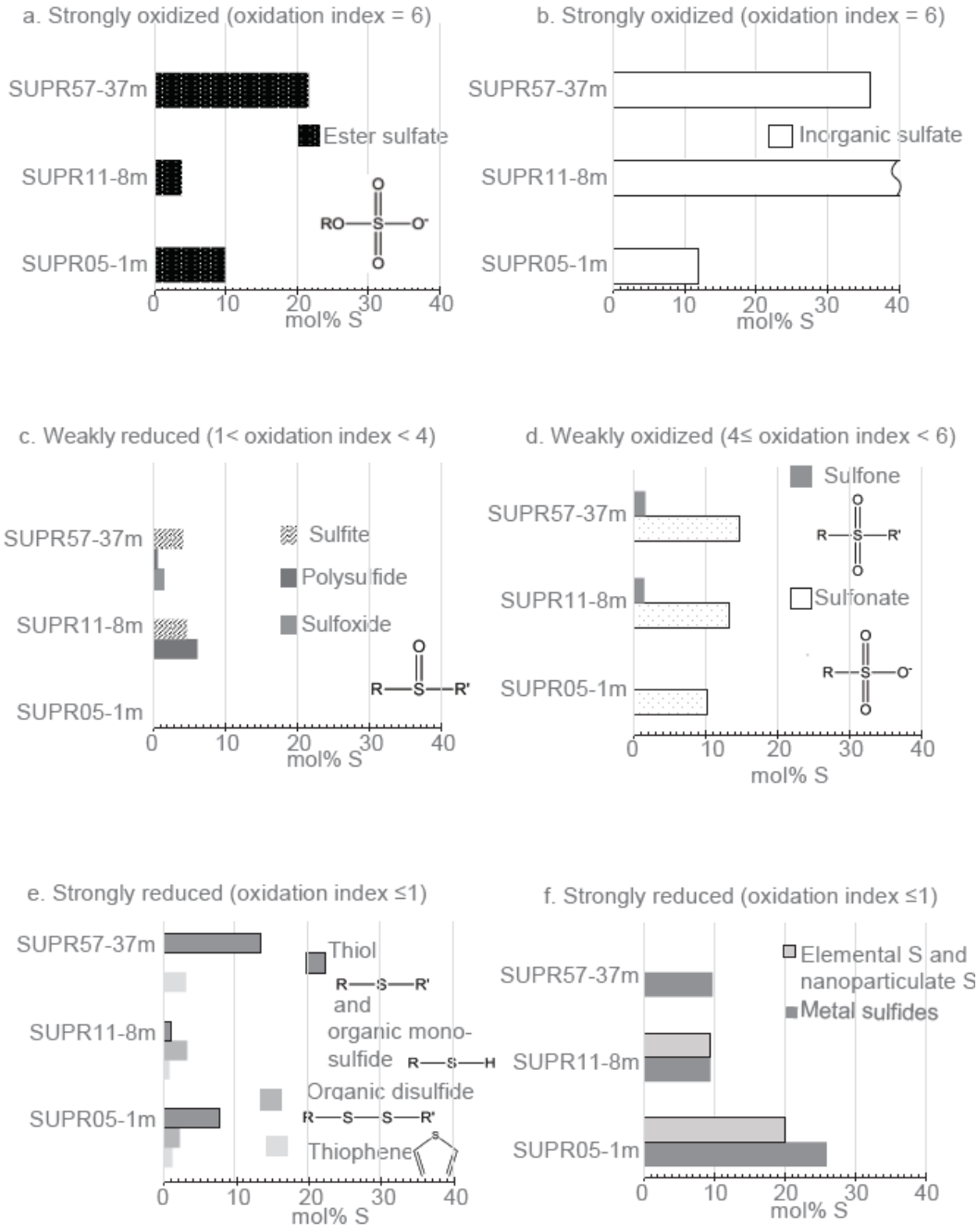

Figure 3.10: Bar charts displaying the S XANES results for SUPR05-1m, SUPR11-8m, and SUPR57-37m in mol% S. (A) strongly oxidized organic moiety, ester sulfate (oxidation index = 6); (B) strongly oxidized inorganic moiety, inorganic sulfate (oxidation index = 6); (C) weakly reduced organic moieties (sulfite, polysulfide, and sulfoxide); (D) weakly oxidized inorganic moieties (sulfone and sulfonate); strongly reduced inorganic moieties (thiol and organic monosulfide, organic disulfide, and thiophene); and, (E) strongly reduced moieites (elemental S and nanoparticulate S and metal sulfide).

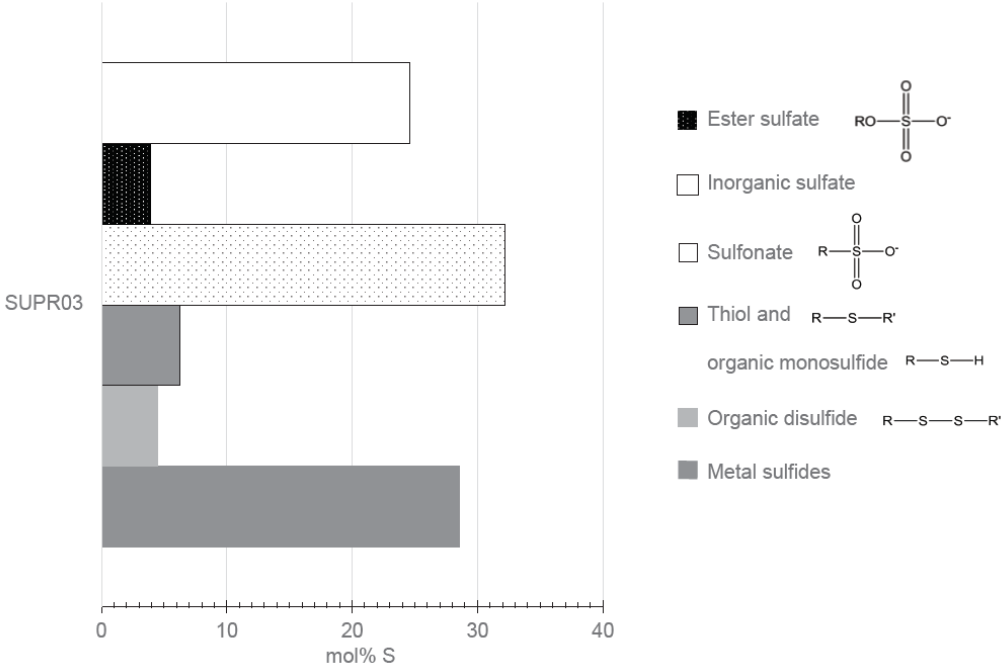

Figure 3.11: Bar charts displaying mol% S based on S 1s XANES results for VD-2.

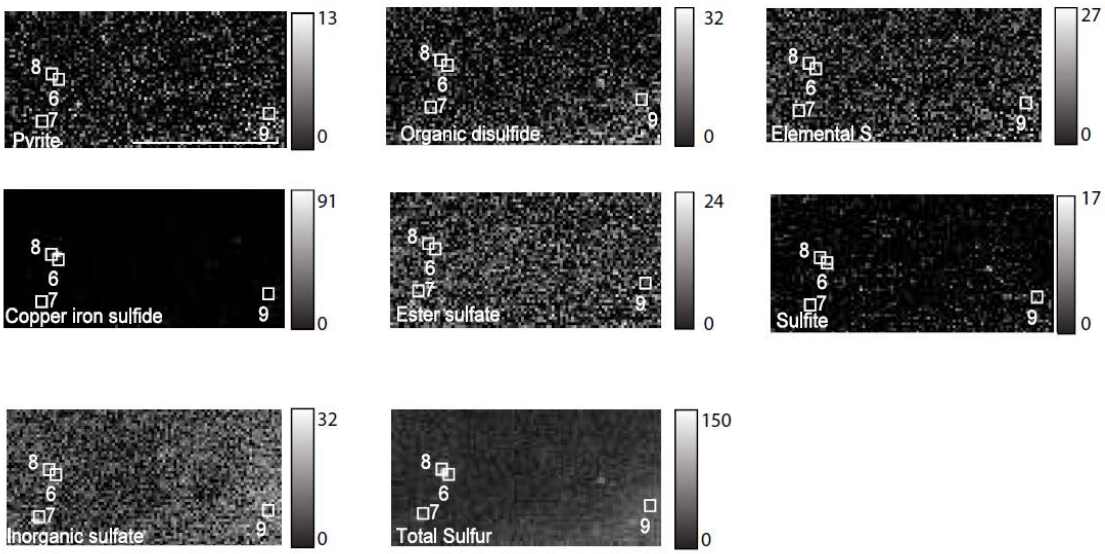

Figure 3.12: VD-1 S chemical mapping results.

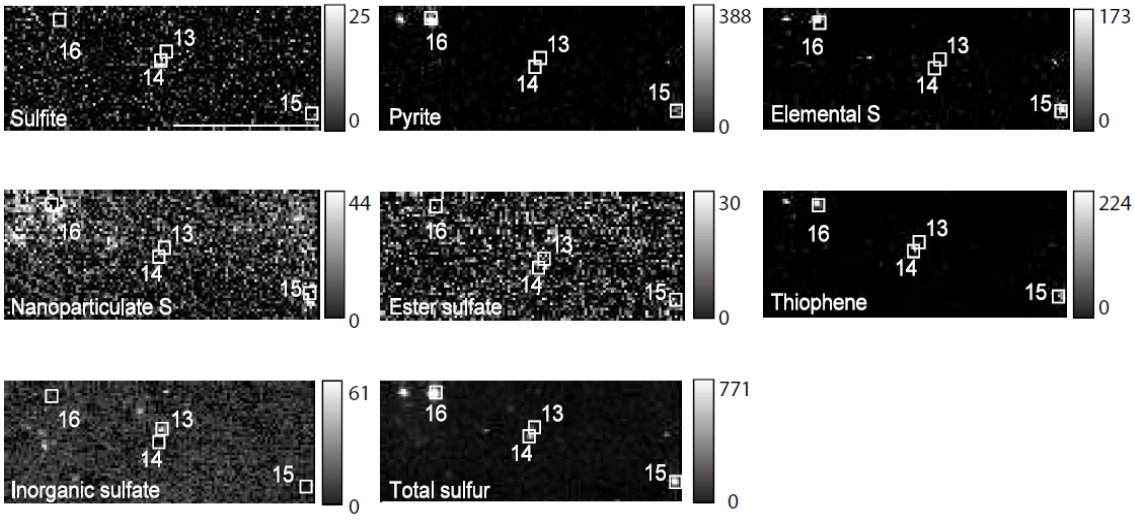

Figure 3.13: SUPR11-8m S chemical mapping results.

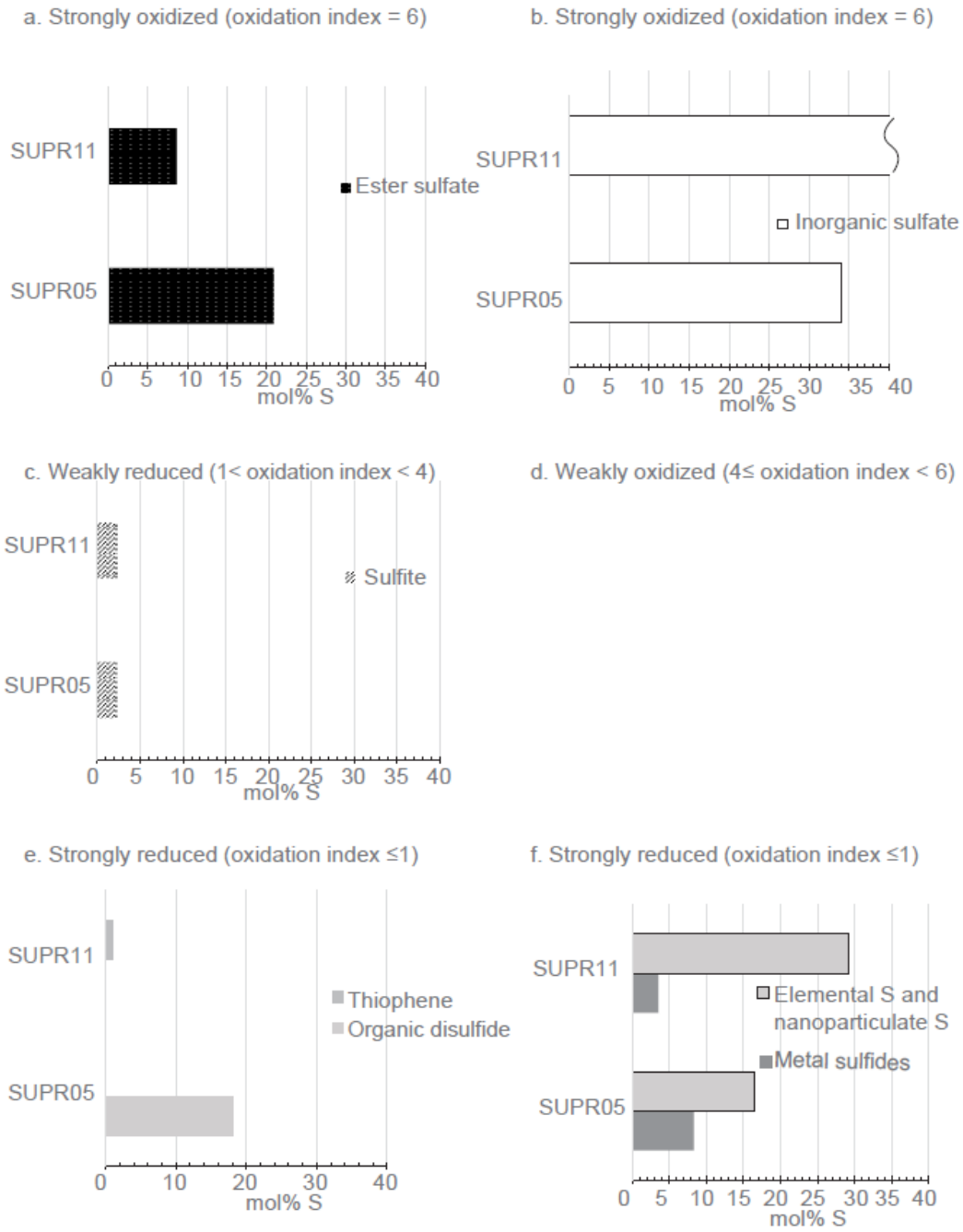

Figure 3.14: Bar chart displaying S chemical map results for Von Damm hydrothermal fluids.

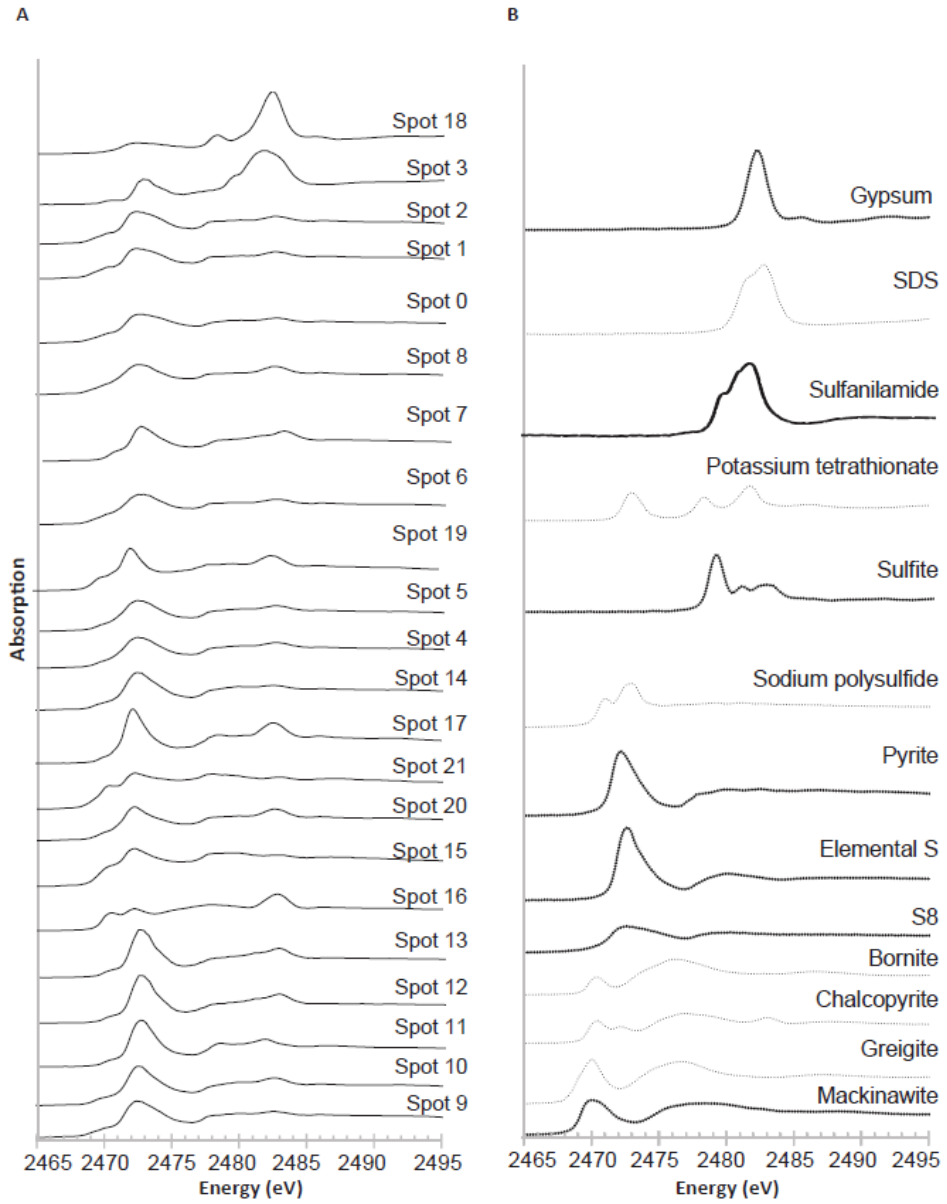

Figure 3.15: Sulfur 1s XANES spectra collected at beamline 10.3.2 and 13-ID-E displaying the range of S species present in sample SUPR22-0.5m. The reference spectra (dashed lines) shown are those that created the best LCF results (gypsum, SDS, sulfanilamide, potassium tetrathionate, sulfite,pyrite, elemental S, nanoparticulate S, chalcopyrite, bornite, greigite, and mackinwate). Reference spectra with bold font text are those used to fit the S chemical map (gypsum, SDS, sulfite, cysteine, pyrite, elemental S, and mackinawite).

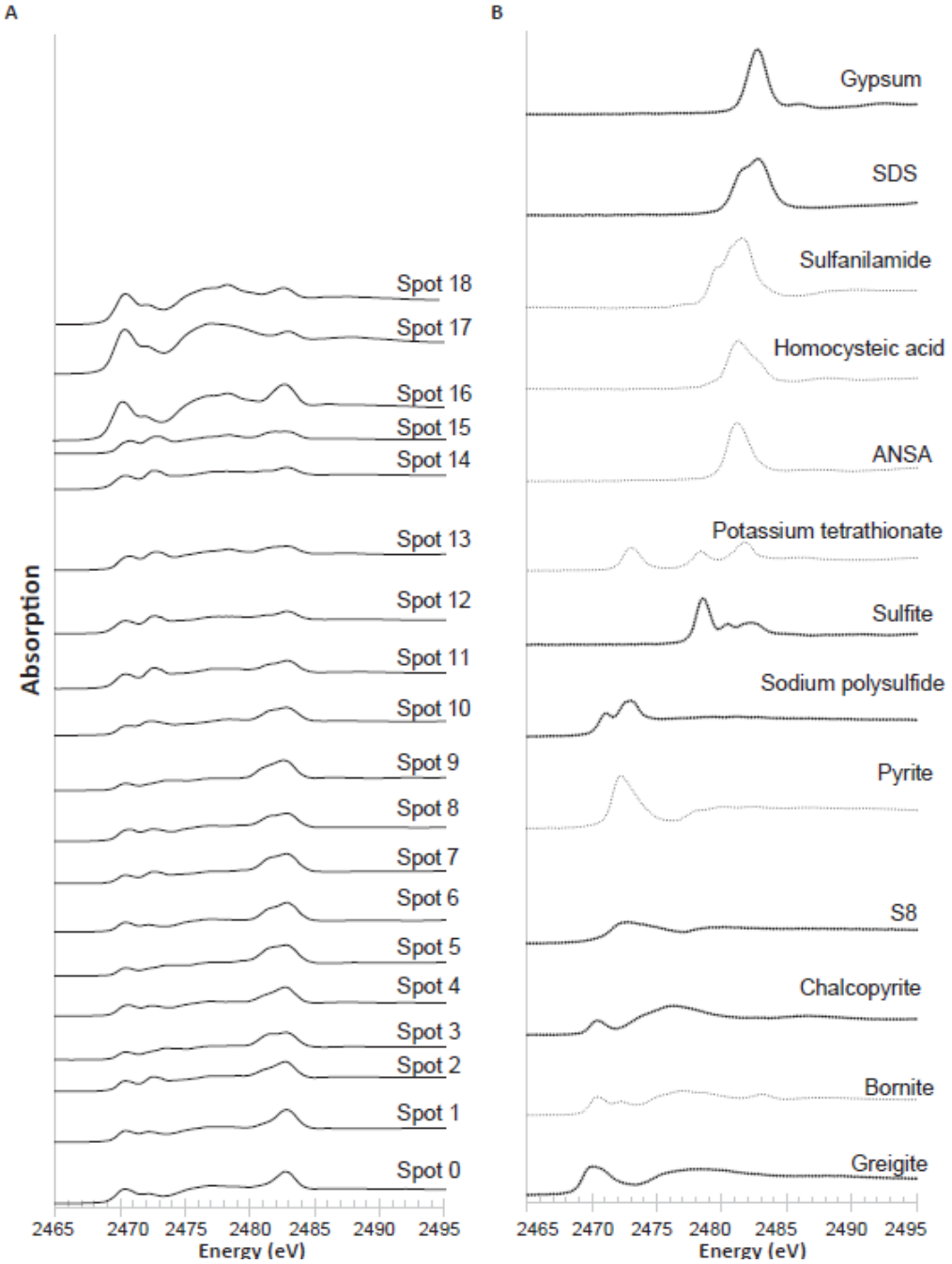

Figure 3.16: Sulfur 1s XANES spectra collected at beamline 10.3.2 and 13-ID-E displaying the range of S species present in sample SUPR30-50m. The reference spectra (dashed lines) shown are those that created the best LCF results (gypsum, SDS, sulfanilamide, homocysteic acid, ANSA, potassium tetrathionate, sulfite, sodium polysulfide, pyrite, nanoparticulate S, chalcopyrite, bornite, and greigite). Reference spectra with bold font text are those used to fit the S chemical map (gypsum, SDS, sulfite, greigite, pyrite, elemental S, and chalcopyrite).

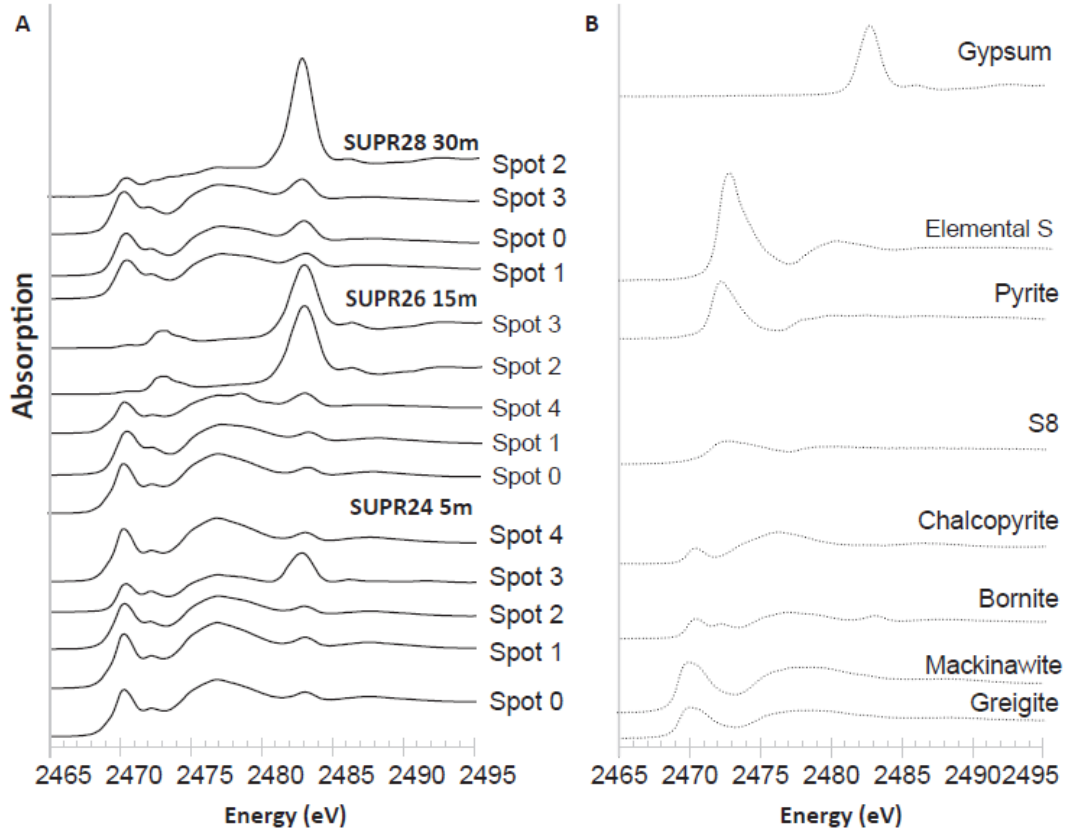

Figure 3.17: Sulfur 1s XANES spectra collected at beamline 13-ID-E displaying the range of S species present in sample SUPR24-5m. The reference spectra (dashed lines) shown are those that created the best LCF results (gypsum, chalcopyrite, greigite, and mackinwate). Sulfur 1s XANES spectra collected at beamline 13-ID-E displaying the range of S species present in sample SUPR26-15m. The reference spectra (dashed lines) shown are those that created the best LCF results (pyrite, elemental S, nanoparticulate S, chalcopyrite, greigite, bornite, and mackinwate). Sulfur 1s XANES spectra collected at beamline 13-ID-E displaying the range of S species present in sample SUPR28-30m. The reference spectra (dashed lines) shown are those that created the best LCF results (gypsum, nanoparticulate S, chalcopyrite, bornite, greigite, and mackinwate).

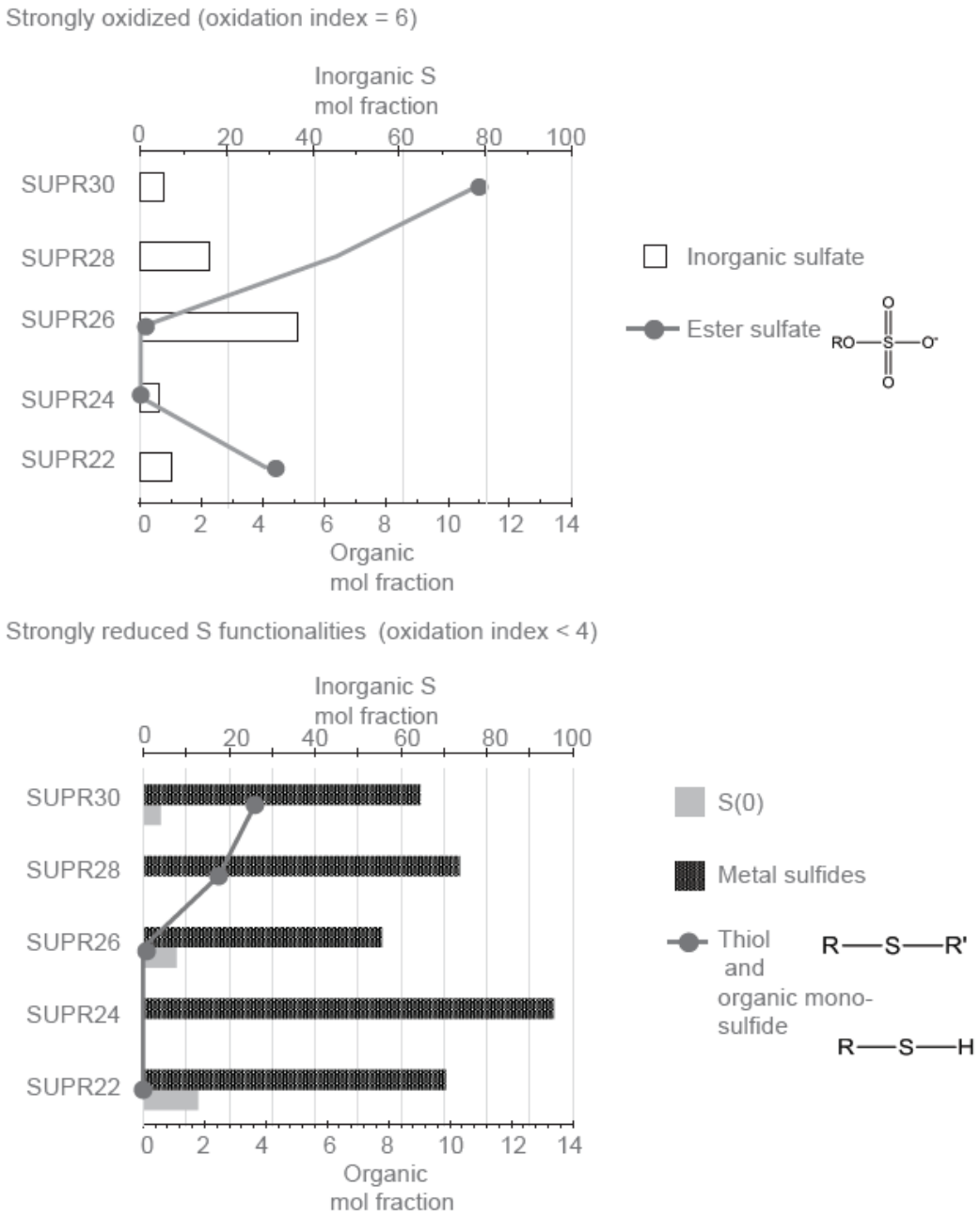

Figure 3.18: Bar charts displaying the S XANES results for SUPR22-0.5m, SUPR24-5m, SUPR26-15m, SUPR28-30m, and SUPR30-50m in mol% S. (A) strongly oxidized organic moiety, ester sulfate (oxidation index = 6) and strongly oxidized inorganic moiety, inorganic sulfate (oxidation index = 6); (B) strongly reduced inorganic moieties (thiol and organic monosulfide).

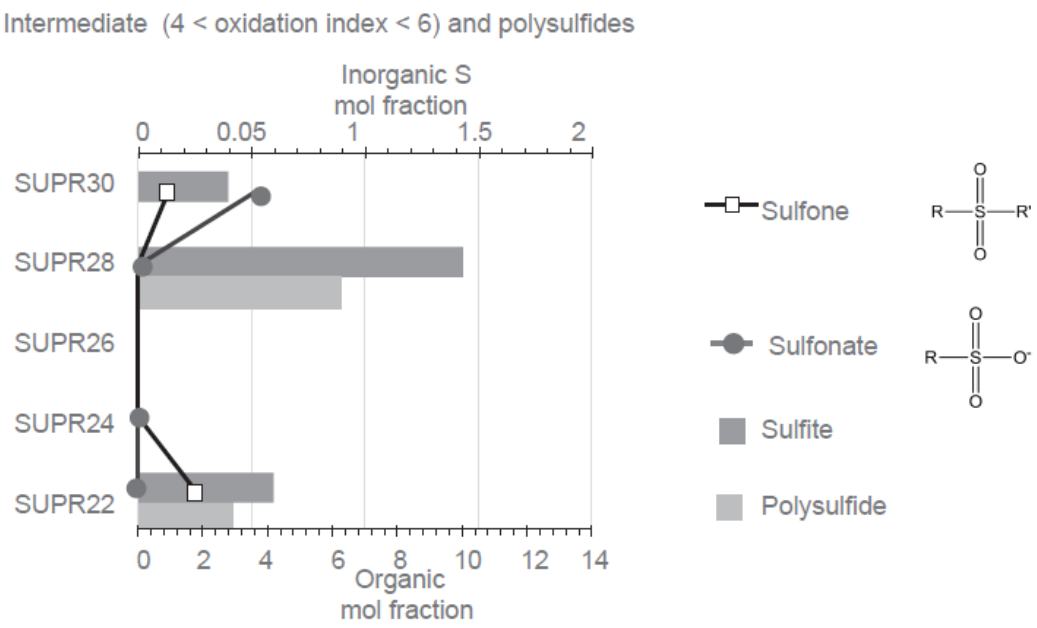

Figure 3.19: Bar charts displaying the S XANES results for SUPR22-0.5m, SUPR24-5m, SUPR26-15m, SUPR28-30m, and SUPR30-50m in mol% S. (A) intermediately oxidized organic moieties (sulfone and sulfonate) and inorganic moieties (sulfite) (4< oxidation index <6) and polysulfides.

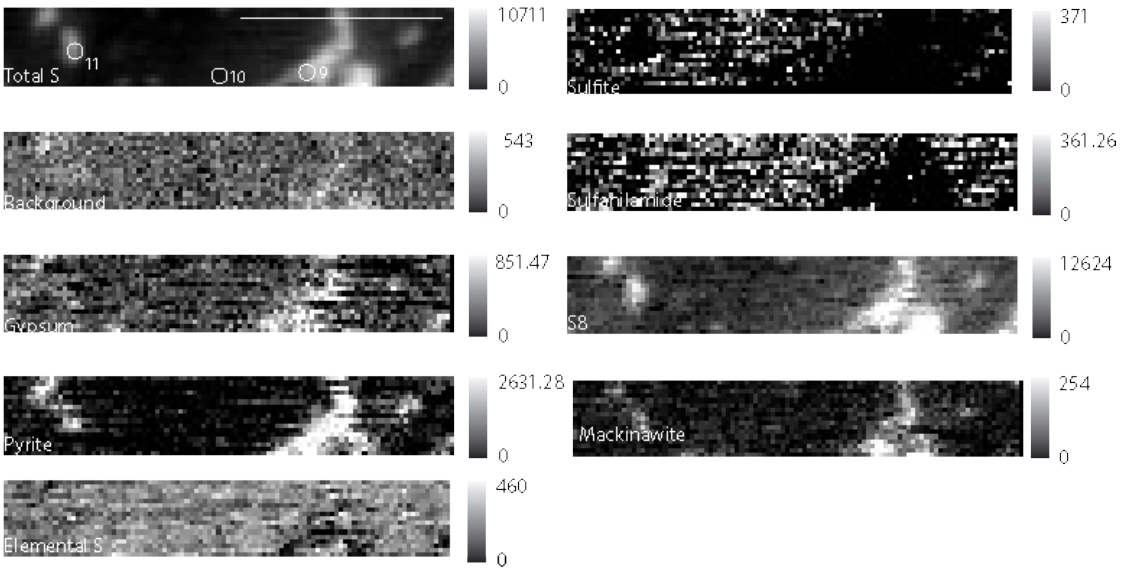

Figure 3.20: Sulfur chemical map for SUPR22-0.5m. Spots 9-11 were analyzed for S 1s XANES. Map was best fit by sulfite, sulfanilamide, gypsum, nanoparticulate S, pyrite, mackinawite, and elemental S.

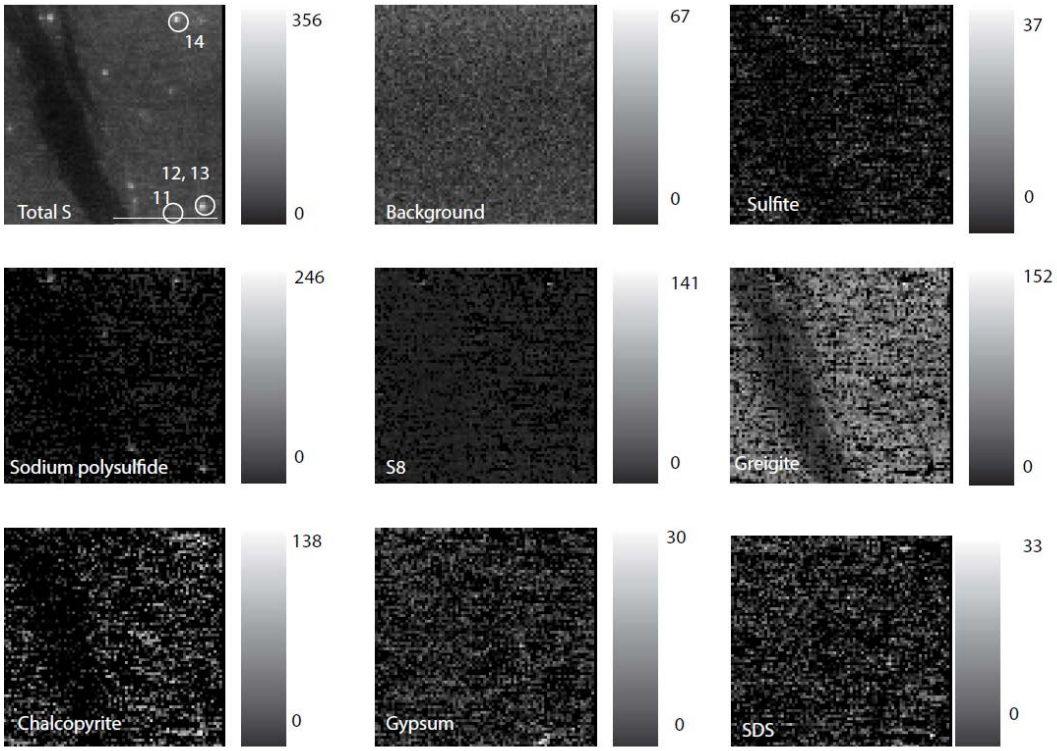

Figure 3.21: Sulfur chemical map for SUPR30-50m. Spots 11-14 were analyzed for S 1s XANES. Map was best fit by sulfite, sodium polysulfide, nanoparticulate S, greigite, chalcopyrite, gypsum, and SDS.

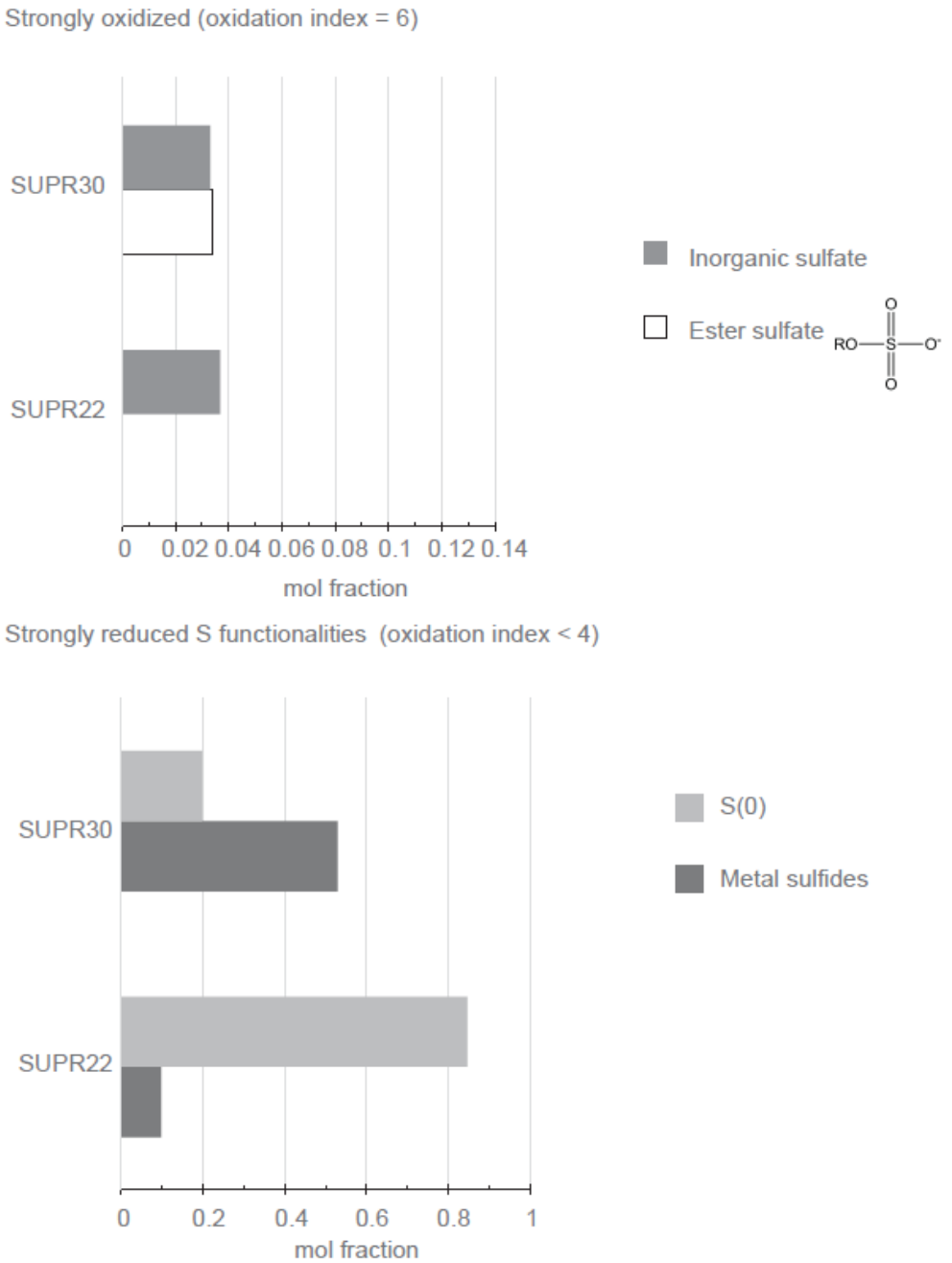

Figure 3.22: Bar charts displaying results for S chemical map for SUPR22-0.5m and SUPR30-50m. Maps were best fit by sulfite, sulfone (sulfanilamide), gypsum, ester sulfate, nanoparticulate S, elemental S, metal sulfides (pyrite, mackinawite, greigite, chalcopyrite, bornite), and polysulfide.

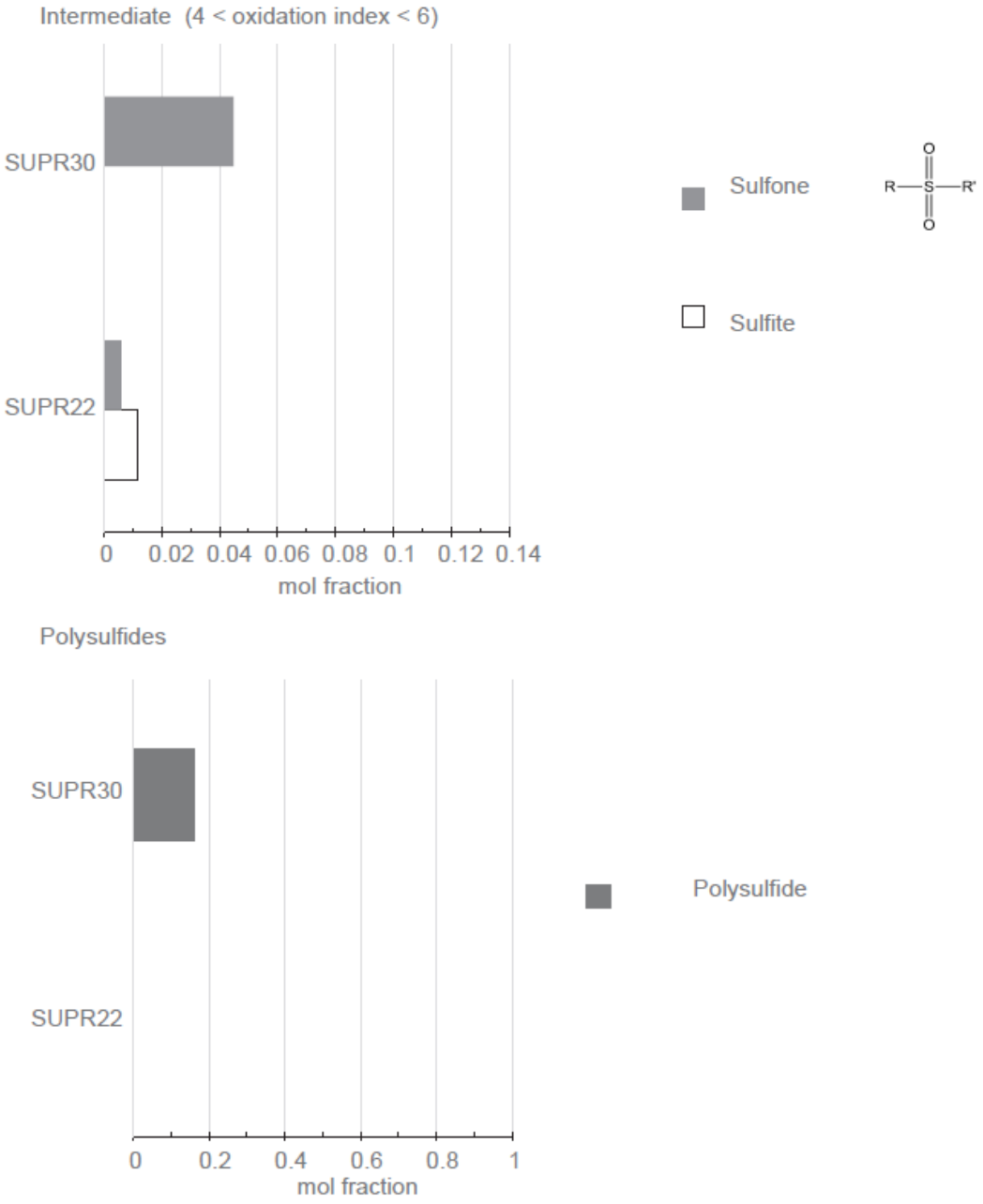

Figure 3.23: Bar charts displaying results for S chemical map for SUPR22-0.5m and SUPR30-50m. Maps were best fit by sulfite, sulfone (sulfanilamide), gypsum, ester sulfate, nanoparticulate S, elemental S, metal sulfides (pyrite, mackinawite, greigite, chalcopyrite, bornite), and polysulfide.

Table 3.1: Table lists the reference file name, compound, functional group, formula, oxidation index, and energy (K-edge absorption in eV) for each S reference.

Base Filename	Compound	Functional Group	Formula	Oxidation index	Energy (eV)
ANSA_ALS[a]	1-amino-2-naphthol-4-sulfonic acid (ANSA)	Sulfonate	RSO_3-	5	2481.25
Benzo_thiophene_CLS[b]	Benzothiophene	Thiophene	C_4H_8S	1	2474.8
Bornite_CLS_TEY[c]_May_2015	Bornite	Copper iron sulfide	Cu_5FeS_4	-2	2470.42
Chalcopyrite_CLS_TEY_May_2015	Chalcopyrite	Copper iron sulfide	$CuFeS_2$	-2	2472.68
Covellite_CLS_TEY	Covellite	Copper sulfide	CuS	-1	2472.20
Cysteine_ALS	Cysteine	Thiol	CSH	0.2	2473.50
Cysteine_APS[d]_TEY	Cysteine	Thiol	CSH	0.2	2473.50
Cysteine_CLS_ambient	Cysteine	Thiol	CSH	0.2	2473.50
Cysteine_CLS_TEY	Cysteine	Thiol	CSH	0.2	2473.50
Cysteine_CLS_TEY_May_2015	Cysteine	Thiol	CSH	0.2	2473.50
Cystine_ALS	Cystine	Organic disulfide	RSSR	-0.3/0.7	2472.80
Cystine_APS_TEY	Cystine	Organic disulfide	RSSR	-0.3/0.7	2472.80
Cystine_CLS_ambient	Cystine	Organic disulfide	RSSR	-0.3/0.7	2472.80
Cystine_CLS_TEY	Cystine	Organic disulfide	RSSR	-0.3/0.7	2472.80
Elemental_sulfur_ALS	Elemental Sulfur	Elemental Sulfur	S	0	2472.68
Greigite_ALS	Greigite	Iron monosulfide	Fe_3S_4	-2	2470.07
gypsum powder_APS_TEY	Gypsum	Inorganic sulfate	$CaSO_4H_2O$	6	2482.74
gypsum_CLS_TEY	Gypsum	Inorganic sulfate	$CaSO_4H_2O$	6	2482.74
Gypsum_ALS_TEY	Gypsum	Inorganic sulfate	$CaSO_4H_2O$	6	2482.74
Gypsum_CLS_Fotios[e]	Gypsum	Inorganic sulfate	$CaSO_4H_2O$	6	2482.74
Homocysteic_acid_ALS	Homocysteic acid	Sulfonate	RSO_3-	5	2481.20
Mackinawite_ALS	Mackinawite	Iron monosulfide	(Fe,Ni)1 + xS	-2	2470.07

Methionine_ALS	Methionine	Organic monosulfide	RSH	0.3	2473.62
Methionine_APS_TEY	Methionine	Organic monosulfide	RSH	0.3	2473.62
Methionine_CLS_TEY	Methionine	Organic monosulfide	RSH	0.3	2473.62
Methionine_CLS_TEY_May_2015	Methionine	Organic monosulfide	RSH	0.3	2473.62
Methionine_sulfoxide_ALS	Sulfoxide	Sulfoxide	RSOR	2	2476.4
Methionine_sulfoxide_CLS_TEY	Sulfoxide	Sulfoxide	RSOR	2	2476.4
Potassium_tetrathionate_CLS_TEY	Polysulfide	Polysulfide	S5062-	-0.1/3.3	2473/ 2478.7
Pyrite_ALS	Pyrite	Iron disulfide	FeS_2	-1	2472.20
Pyrite_CLS	Pyrite	Iron disulfide	FeS_2	-1	2472.20
Pyrite_YF_CLS	Pyrite	Iron disulfide	FeS_2	-1	2472.20
S8[f]_Raffo[g]_CLS_ambient[h]	Elemental Sulfur	Elemental Sulfur	S	0	2472.68
S8nano_135R[i]_CLS_ambient	Elemental Sulfur	Elemental Sulfur	S	0	2472.90
S8nano_16R[j]_centrifuged_CLS_ambient	Elemental Sulfur	Elemental Sulfur	S	0	2472.69
S8nano_16R_CLS_ambient	Elemental Sulfur	Elemental Sulfur	S	0	2472.79
SDS_ALS	Sodium dodecyl sulfate	Ester sulfate	$ROSO_3$-	6	2482.76
SDS_CLS_TEY	Sodium dodecyl sulfate	Ester sulfate	$ROSO_3$-	6	2482.76
SDS_YF_CLS	Sodium dodecyl sulfate	Ester sulfate	$ROSO_3$-	6	2482.76
sodium_polysulfide_CLS_TEY	Polysulfide	Polysulfide	Na_2S_4	-1.4/-0.1	2471.08/2473
Sulfanilamide_ALS	Sulfanilamide	Sulfanilamide	$RSRO_2$	5.3	2473
Sulfite_ALS	Sulfite	Sulfite	SO_3^{2-}	3.68	2481.56
thiophene_APS_TEY	2-Thiophenecarboxylic acid	Thiophene	RSR	1	2474.49
Thiophenecarboxylic_acid_ALS	2-Thiophenecarboxylic acid	Thiophene	RSR	1	2474.49

a. Spectra was collected at the Advanced Light Source (ALS)
b. Spectra was collected at the Canadian Light Source (CLS)
c. Spectra was collected in Total Electron Yield (TEY) mode
d. Spectra was collected at the Advanced Photon Source (APS)
e. Spectra was collected by Fotios Kafantaris (Indiana University Purdue University Indianapolis)
f. Cyclo-octasulfur

g. Raffo sols (formed by the acidification of thiosulfate or polysulfide by adding sulfuric acid)
h. Spectroscopy was run under ambient conditions
i. 135R (1mL S saturated methanol in 35 mL water)
j. 16R (1mL S saturated methanol in 6mL water)

Table 3.2: Table listing the compound, assigned functional group, formula, energy (1s or K-edge absorption in eV), oxidation index, and reference for S reference database. The absorption energy was calculated for greigite, mackinawite, and benzothiophene based on known oxidation index. Oxidation index values were calculated for potassium tetrathionate, sodium polysulfide, cystine, cysteine, methionine, 2-thiophenecarboxylic acid, methionine sulfoxide, and sulfanilamide based on the absorption energy.

Compound	Functional group	Formula	Energy (eV)	Oxidation index	Reference
Bornite	Copper iron sulfide	Cu_5FeS_4	2470.42	-2	Goh 2006
Chalcopyrite	Copper iron sulfide	$CuFeS_2$	2472.68	-2	Goh 2006
Covellite	Copper sulfide	CuS	2472.2	-1	Pearce 2006
Pyrite	Iron disulfide	FeS_2	2472.2	-1	Zeng 2013
Elemental Sulfur	Elemental Sulfur	S	2472.68	0	Zeng 2013
S8_Raffo_CLS_ambient	Elemental Sulfur	S	2472.68	0	this paper
S8nano_16R_centrifuged_CLS_ambient	Elemental Sulfur	S	2472.69	0	this paper
S8nano_16R_CLS_ambient	Elemental Sulfur	S	2472.79	0	this paper
S8nano_135R_CLS_ambient	Elemental Sulfur	S	2472.9	0	this paper
Sulfite	Sulfite	SO_3^{2-}	2478.4	3.68	Zeng 2013
Homocysteic acid	Sulfonate	RSO_3^-	2481.2	5	Zeng 2013
1-amino-2-naphthol-4-sulfonic acid (ANSA)	Sulfonate	RSO_3^-	2481.25	5	Zeng 2013
Gypsum	Inorganic sulfate	$CaSO_4H_2O$	2482.74	6	Zeng 2013
Sodium dodecyl sulfate	Ester sulfate	$ROSO_3^-$	2482.76	6	Zeng 2013
White line calculation					
Greigite	Iron sulfide	Fe_3S_4	2470.07	-2	this paper
Mackinawite	Iron monosulfide	(Fe Ni)1 + xS	2470.07	-2	Todd et al. 2003
Benzothiophene	Benzothiophene	C_4H_8S	2474.8	1	Furman et al.
Oxidation index calculation					
Potassium tetrathionate	Potassium tetrathionate	$S_50_6^{2-}$	2473	-0.14	this paper
Potassium tetrathionate	Potassium tetrathionate	$S_50_6^{2-}$	2478.4	3.29	this paper
Potassium tetrathionate	Potassium tetrathionate	$S_50_6^{2-}$	2481.9	5.51	this paper
Sodium polysulfide	Sodium polysulfide	Na_2S_4	2471.08	-1.36	this paper
Sodium polysulfide	Sodium polysulfide	Na_2S_4	2473	-0.14	this paper

Cystine	Organic disulfide	RSSR	2472.8	-0.27	this paper
Cystine	Organic disulfide	RSSR	2474.3	0.69	this paper
Cysteine	Thiol	RSH	2473.5	0.18	this paper
Methionine	Organic monsulfide	RSH	2473.62	0.25	this paper
2-Thiophenecarboxylic acid	Thiophene	RSR	2474.49	0.81	this paper
Methionine sulfoxide	Sulfoxide	RSOR	2476.39	2.01	this paper
Sulfanilamide	Sulfone	$RSRO_2$	2481.56	5.29	this paper

Table 3.3**.** Linear combination fit results for S 1s XANES data for Von Damm in units of mol % S-standard on a per atom basis. Sulfur moieties and oxidation indices for each S-standard are listed in Table 2.

Category	SUPR03	SUPR05	SUPR11	SUPR57
Copper iron sulfide	21.87	16.94	4.75	1.79
Copper sulfide	-	-	0.12	7.96
Elemental Sulfur	-	4.82	1.94	-
Nanoparticulate S	-	15.26	7.55	-
Pyrite	-	3.15	3.52	-
Ester sulfate	3.94	9.85	3.84	21.62
Inorganic sulfate	24.61	12.02	51.32	35.97
Iron monosulfide	6.70	5.89	1.08	-
Organic disulfide	4.49	2.19	3.19	-
Methionine and cysteine	6.24	7.62	0.90	13.24
Polysulfide	-	6.13	0.66	-
Sulfite	-	4.72	4.19	-
ANSA and homocysteic acid	32.15	10.28	13.32	14.77
Sulfanilamide	-	-	1.44	1.61
Thiophene	-	1.14	0.75	3.04
Sulfoxide	-	-	1.42	-

Table 3.4: Table with concentration of inorganic S-bearing functional groups (mol%) identified at Von Damm using S 1s XANES at the four plume elevations. Categories include strongly reduced, weakly reduced, and strongly oxidized.

	Strongly reduced			**Weakly reduced**			**Strongly oxidized**
Category	Metal sulfides	Elemental S	Nano particulate S	Polysulfide	Sulfoxide	Sulfite	Inorganic sulfate
SUPR57	10	-	-	-	-	-	36
SUPR11	9.5	1.9	7.6	0.7	1.4	4.2	51
SUPR05	26	4.8	15	6.1		4.7	12
SUPR03	29	-	-	-	-	-	25

Table 3.5: Organic S-moieties from Von Damm reported as mol % S on a per atom basis.

	Strongly reduced			**Weakly oxidized**		**Strongly oxidized**
Category	Organic disulfide	Thiophene	Thiol and organic monosulfide	Sulfonate	Sulfone	Ester sulfate
SUPR57	-	3.0	13	15	1.6	22
SUPR11	3.2	0.8	0.9	13	1.4	3.8
SUPR05	2.2	1.1	7.6	10	-	10
SUPR03	4.5	-	6.2	32	-	3.9

Table 3.6: Concentration of S functionalities (mol% S on a per atom basis) identified using chemical mapping of Von Damm.

Category	SUPR05	SUPR11
Copper iron sulfide	0.53	-
Elemental S	16.41	1.98
Nanoparticulate S	-	27.29
Pyrite	7.77	3.53
Inorganic sulfate	34.07	55.13
Organic disulfide	18.01	-
Ester sulfate	20.90	8.64
Sulfite	2.32	2.36
Thiophene	-	1.05

Table 3.7: Linear combination fit results for S 1s XANES data for Beebe in units of mol % S-standard on a per atom basis. Sulfur moieties and oxidation indices for each S-standard are listed in Table 2.

Category	SUPR22	SUPR24	SUPR26	SUPR28	SUPR30
Strongly reduced inorganic					
Copper iron sulfide	10	0.69	40	56	53
Copper sulfide	4	-	-	-	-
Elemental Sulfur	13	-	8	-	4
Pyrite	46	-	-	-	2
Iron monosulfide	11	27	16	18	10
Strongly reduced organic					
Thiol and organic monosulfide	-	-	-	2	4
Intermediate organic					
Sulfonate	-	-	-	-	4
Sulfone	2	-	-	-	1
Polysulfide					
Polysulfide	3	-	-	-	6
Intermediate inorganic					
Sulfite	1	-	-	1	-
Strongly oxidized organic					
Ester sulfate	4	-	-	6	11
Strongly oxidized inorganic					
Inorganic sulfate	7		37	16	5

Table 3.8: Table with concentration of inorganic S-bearing functional groups (mol%) identified using S 1s XANES from Beebe at the four plume elevations. Categories include strongly reduced, weakly reduced, and strongly oxidized.

	Strongly reduced		**Polysulfide**	**Weakly reduced**		**Strongly oxidized**
Category	Metal sulfides	S(0)	Polysulfide	Sulfoxide	Sulfite	Inorganic sulfate
SUPR30	65	4	6	-	-	5
SUPR28	74	-	-	-	1	16
SUPR26	56	8	-	-	-	37
SUPR24	96	-	-	-	-	4
SUPR22	71	13	3	-	1	7

Table 3.9: Organic S-moieties from Beebe reported as mol % S on a per atom basis.

	Strongly reduced			**Weakly oxidized**		**Strongly oxidized**
Category	Organic disulfide	Thiophene	Thiol and organic monosulfide	Sulfonate	Sulfone	Ester sulfate
SUPR30	-	-	4	4	1	11
SUPR28	-	-	2	-	-	6
SUPR26	-	-	-	-	-	-
SUPR24	-	-	-	-	-	-
SUPR22	-	-	-	-	2	4

SUPPLEMTNAL FIGURES

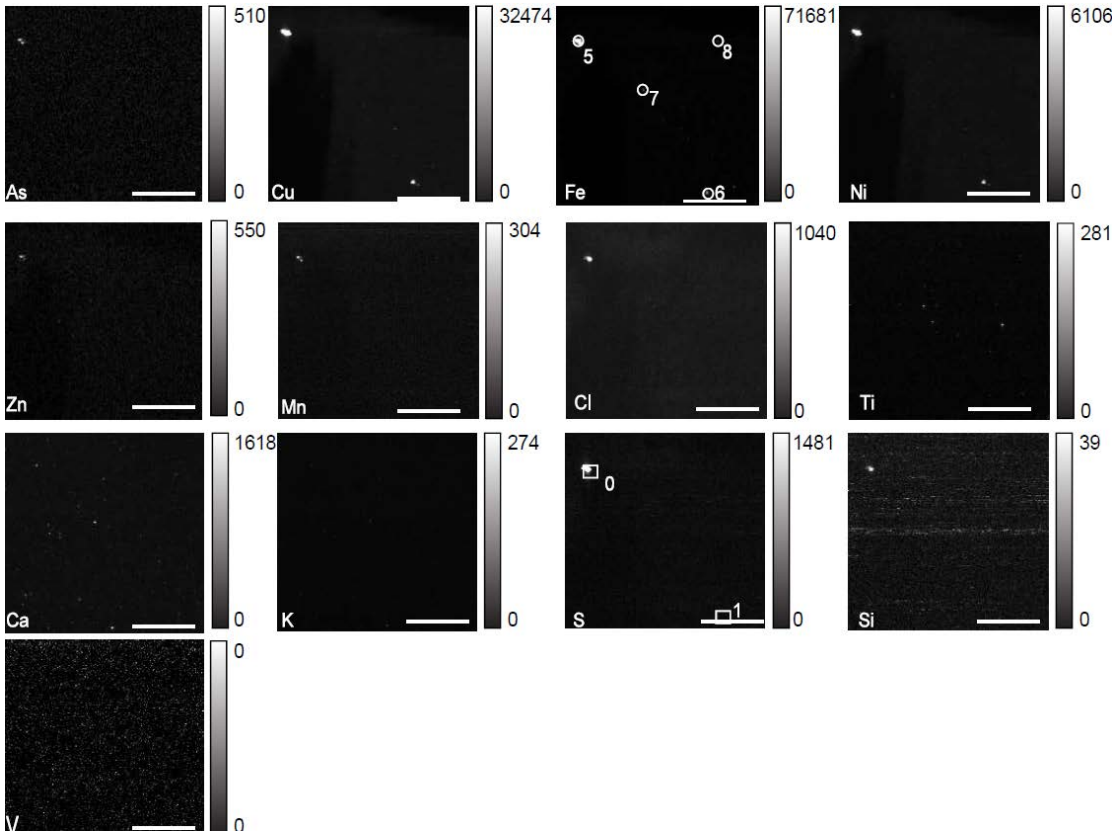

Supplemental figure 3.1: X-ray fluorescence maps for SUPR05-1m collected at ALS beamline 10.3.2. Four spots (spots 5-8) were investigated for Fe 1s XANES. Two spots (0-1) were investigated for S 1s XANES. Maps were for 1000µm X 1000µm area, with 5µm step, and 100ms dwell, at E=7000eV. Scale bar is 300µm.

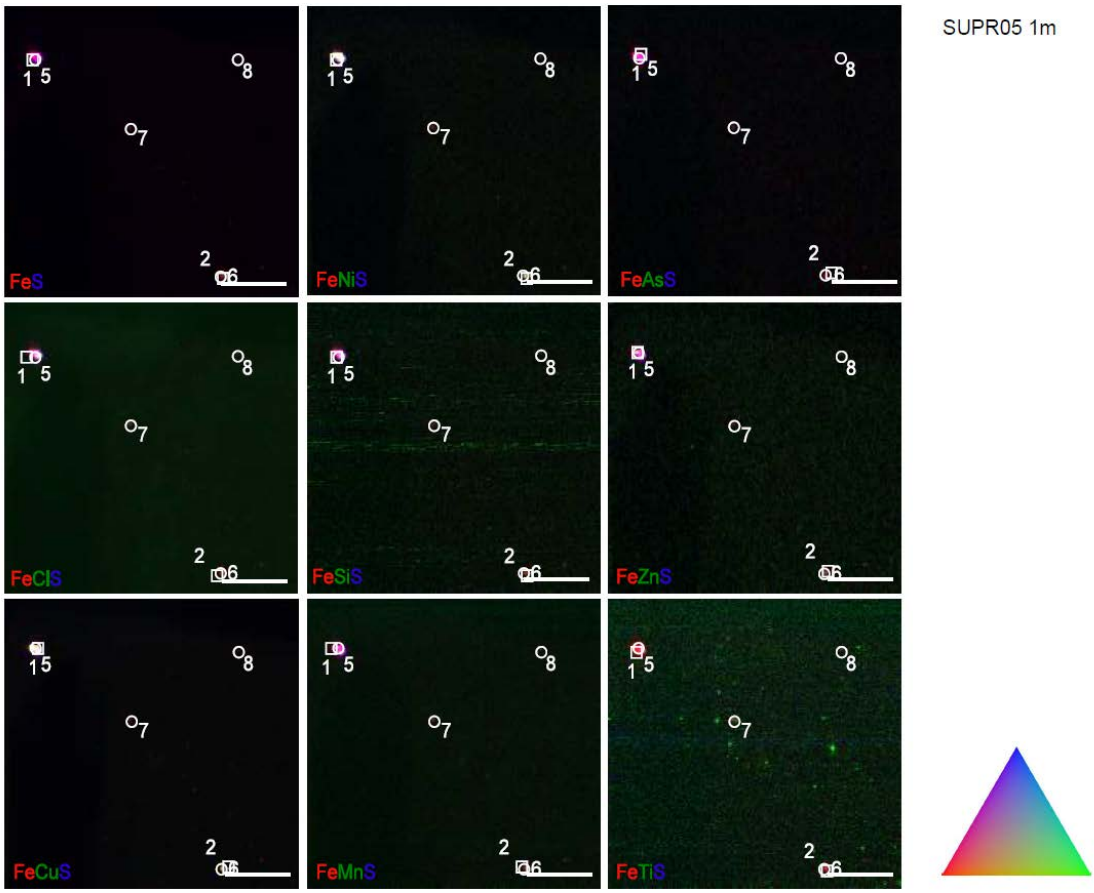

Supplemental figure 3.2: X-ray fluorescence correlation maps for XRF maps in figure 3.1.

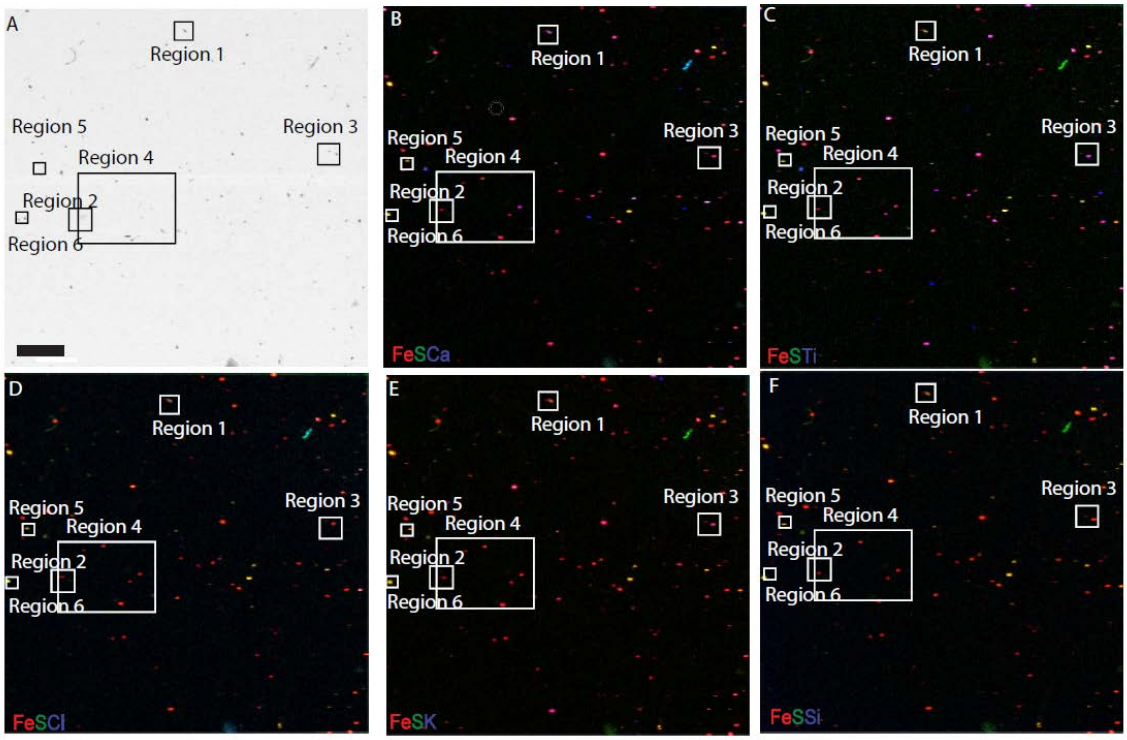

Supplemental figure 3.3: Scanning Transmission X-ray Microscopy and XRF images of sample SUPR05-1m silicon nitride window sample preparation. **(a)** Map collected at 5.3.2.2. Map was completed on a 1mm^2 area with a 10µm step, 4ms dwell, at E=288eV. Scale bar is 100 µm. Regions 1-5 represent areas that were assessed for C and S XAS (Table XX). Regions 1-3 were analyzed for C XANES at 5.3.2.2 (Table XX; Figure XX). Region 4 was analyzed for S 1s XANES at 13-ID-E. Regions 5-6 were analyzed at 2-ID-B. **(b-g)** XRF maps collected at 13-ID-E. Maps were completed on a 1mm^2 area with a 3µm step, 50ms dwell, at E=7500eV.

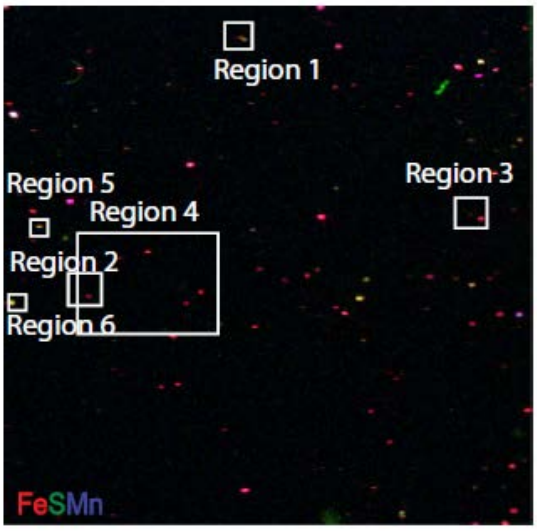

Supplemental figure 3.4: X-ray fluorescence images of sample SUPR05 (1m) silicon nitride window sample preparation. XRF map collected at 13-ID-E. Map was completed on a 1mm^2 area with a 3µm step, 50ms dwell, at E=7500eV.

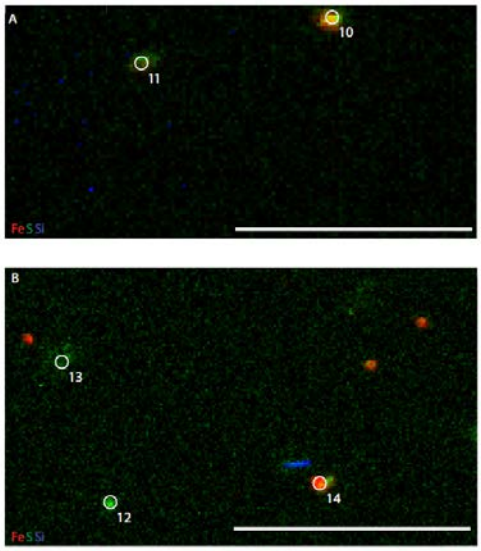

Supplemental figure 3.5: X-ray Fluorescence map for SUPR05-1m region 4. Map and S 1s XANES were collected at 13-ID-E. **(a)** Circles represent where S 1s XANES were collected for spots 10 and 11. Map was for a 200µm X 100 µm area with a 1µm step, 80ms dwell, at E=2500eV. Scale bar is 100µm. **(b)** Circles represent where S 1s XANES were collected for spots 12-14. Map was for a 200µm X 60 µm area with a 1µm step, 80ms dwell, at E=2500eV. Scale bar is 100µm.

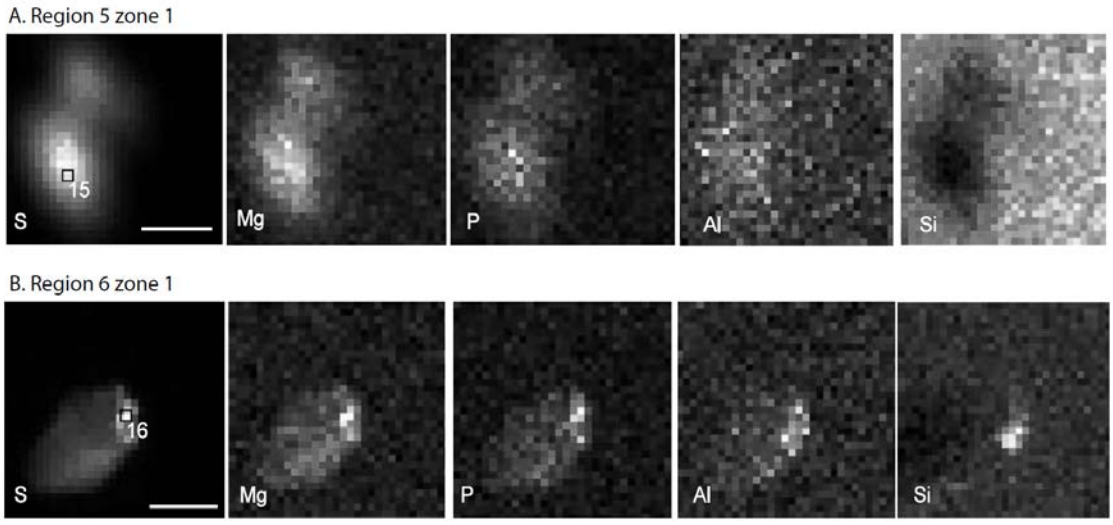

Supplemental figure 3.6: X-ray Fluorescence maps collected at 2-ID-B for SUPR05-1m. Two regions (regions 5 and 6) were investigated with XRF maps and S 1s XANES. **(a)** region 5, E =2490eV, 3 µm scale bar; homocysteic acid was identified in a particle ~3µm in diameter in region 5 (spot 15); and, **(b)** region 6 E = 2490eV, 30 µm scale bar; sulfite in region 6 in a particle ~3µm in diameter (spot 16).

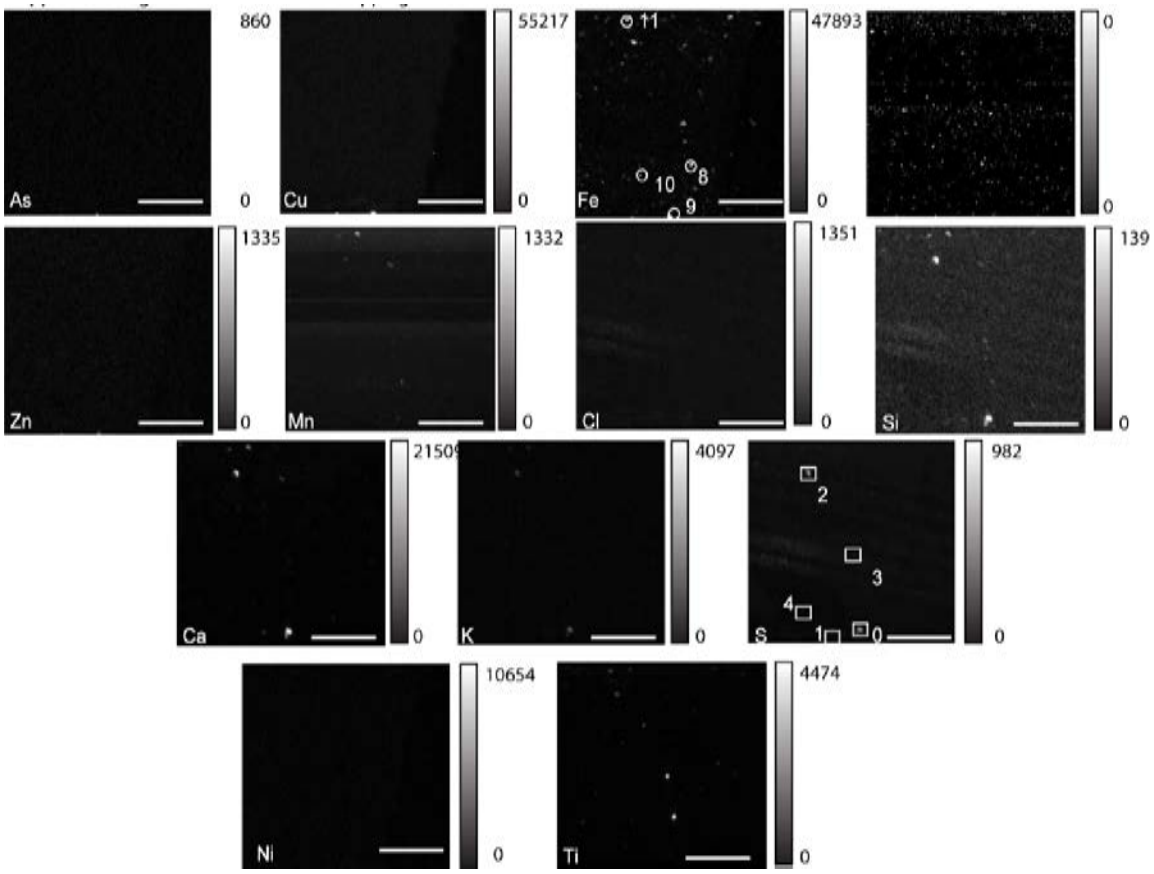

Supplemental figure 3.7: X-ray fluorescence maps for SUPR11-8m collected at ALS beamline 10.3.2. Four spots (spots 8-11) were investigated for Fe 1s XANES. Five spots (0-4) were investigated for S 1s XANES. Maps were for 1000µm X 1000µm area, with 5µm step, and 100ms dwell, at E=7000eV. Scale bar is 300µm.

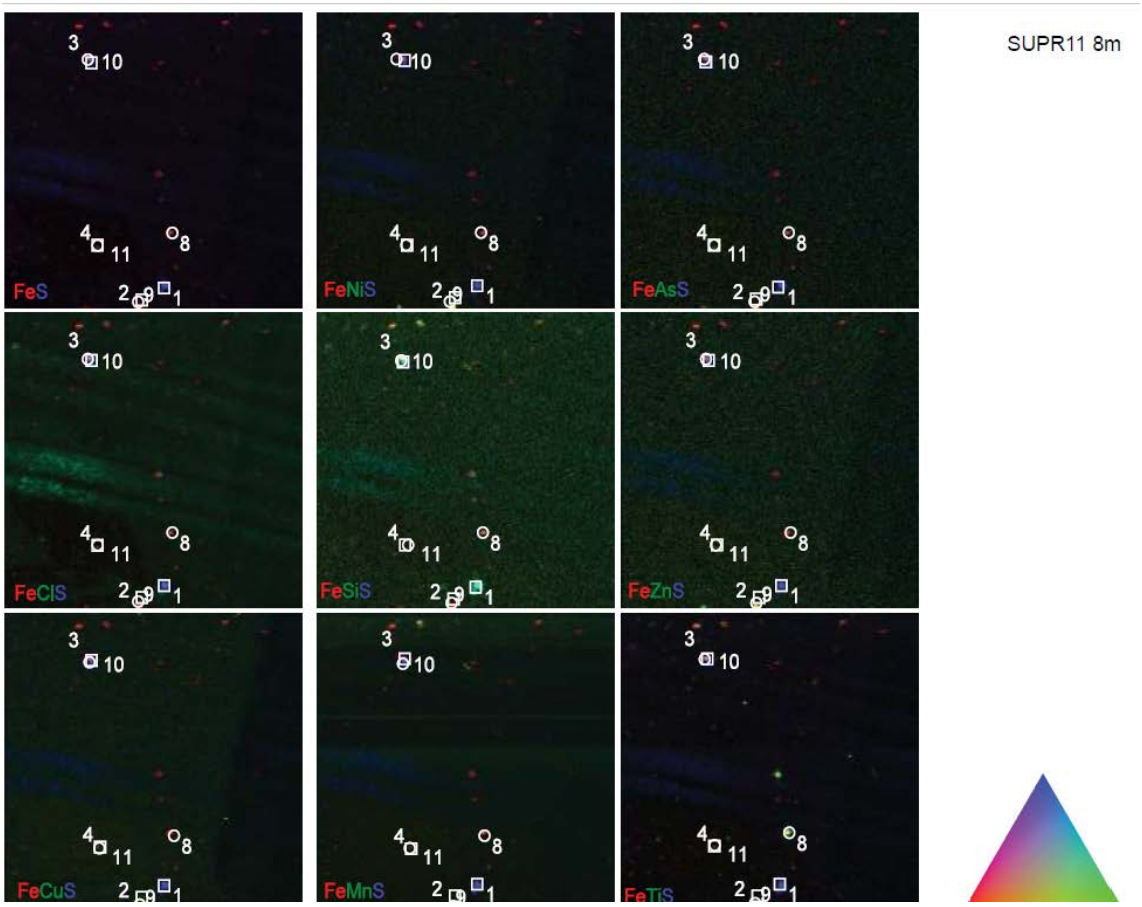

Supplemental figure 3.8: X-ray fluorescence correlation maps for XRF maps in figure 3.7.

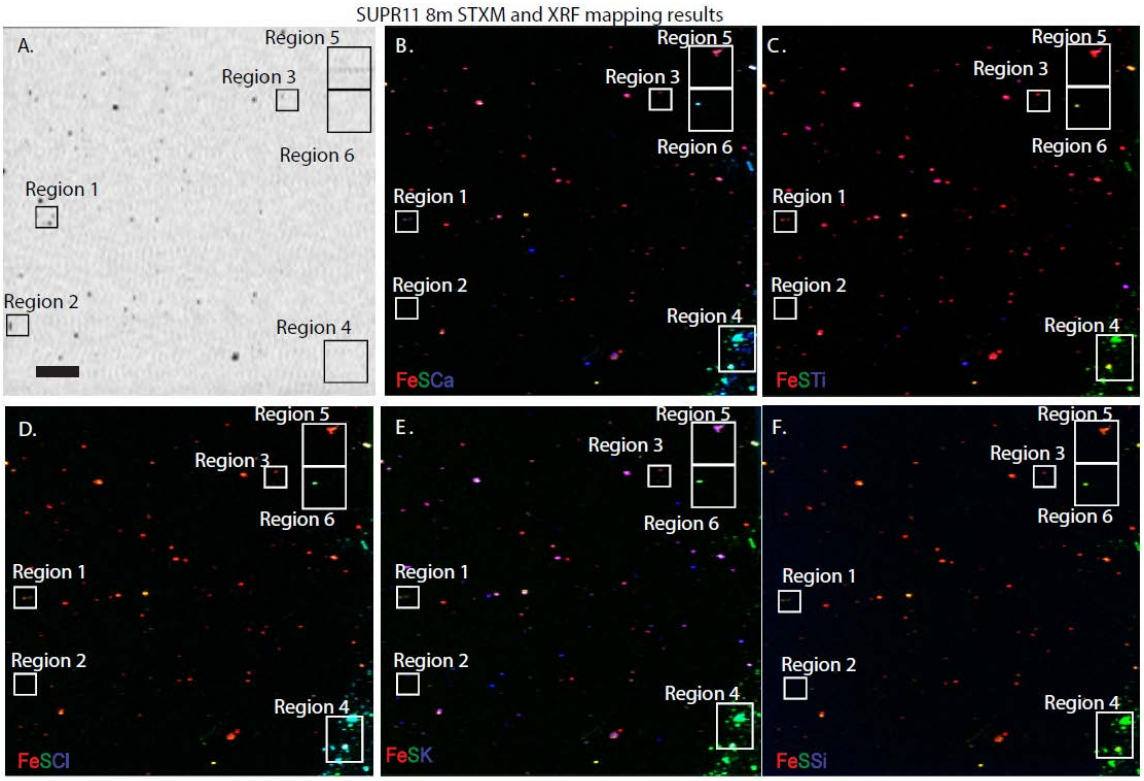

Supplemental figure 3.9: Scanning Transmission X-ray Microscopy and XRF images of sample SUPR11-8m silicon nitride window sample preparation. **(a)** Map collected at 5.3.2.2. Map was completed on a 1mm^2 area with a 10µm step, 4ms dwell, at E=288eV. Scale bar is 100 µm. Regions 1- 6 represent areas that were assessed for C and S XAS. Regions 1-3 were analyzed for C XANES at 5.3.2.2 (Table 2.3; Figure 2.10). Region 4 was analyzed for S 1s XANES at 13-ID-E (Table 2.3; Figure 2.10). **(b-g)** XRF maps collected at 13-ID-E. Maps were completed on a 1mm^2 area with a 3µm step, 50ms dwell, at E=7500eV.

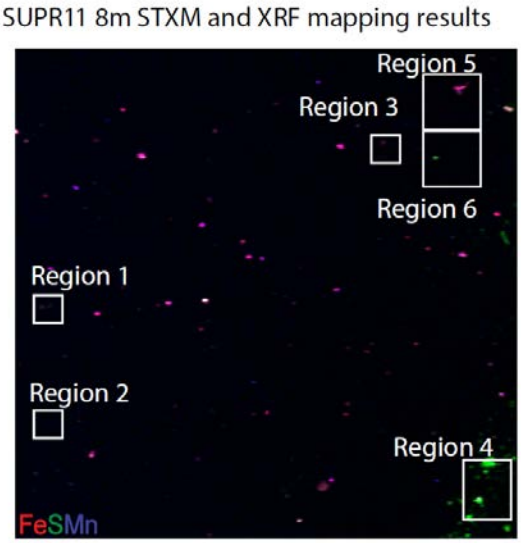

Supplemental figure 3.10: X-ray fluorescence map collected at 13-ID-E. Map was completed on a 1mm^2 area with a 3µm step, 50ms dwell, at E=7500eV.

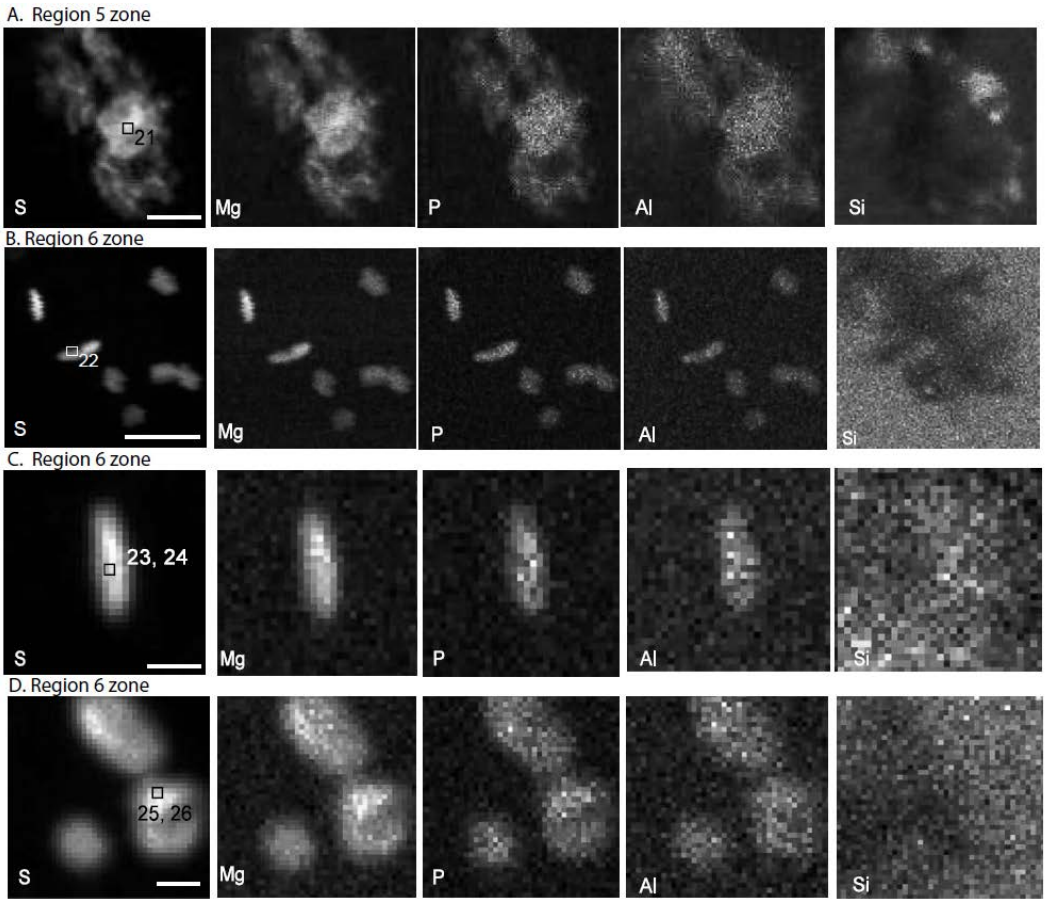

Supplemental figure 3.11: X-ray Fluorescence map collected at 2-ID-B for SUPR11-8m. Two regions (regions 5 and 6) were investigated with XRF maps and S 1s XANES; **(a)** region 5, zone 1, E =2490eV, 3 µm scale bar; cluster of particles is ~6µm across. Sulfur 1s XANES revealed the cluster contains inorganic sulfate. Three zones were assessed in region 6. **(b)** region 6, zone 1, E = 2490eV, 3 µm scale bar; Zones 1 and 2 contain cells ~1µm long, and S 1s XANES within the cells revealed that the cells contain inorganic sulfate and homocysetic acid. **(c)** region 6, zone 2, E = 2490eV, 1 µm scale bar; **(d)** region 6, zone 3, E = 2490eV, 1 µm scale bar; zone 3 has three ~1µm in diameter particles and S 1s XANES from one of the particles identified inorganic sulfate and homocysteic acid.

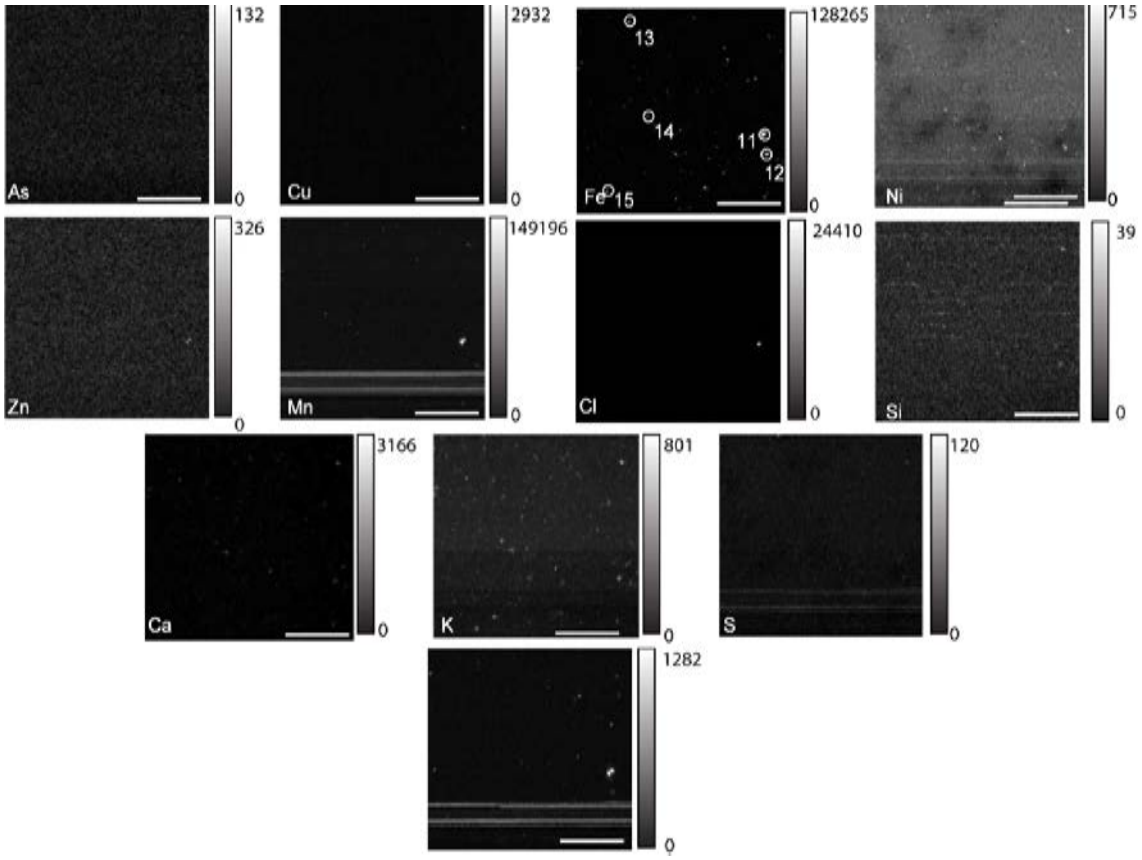

Supplemental figure 3.12: X-ray fluorescence maps for SUPR57 (37m) collected at ALS beamline 10.3.2. Five spots (spots 11-15) were investigated for Fe 1s XANES. Maps were for 1000µm X 1000µm area, with 5µm step, and 100ms dwell, at E=7000eV. Scale bar is 300µm.

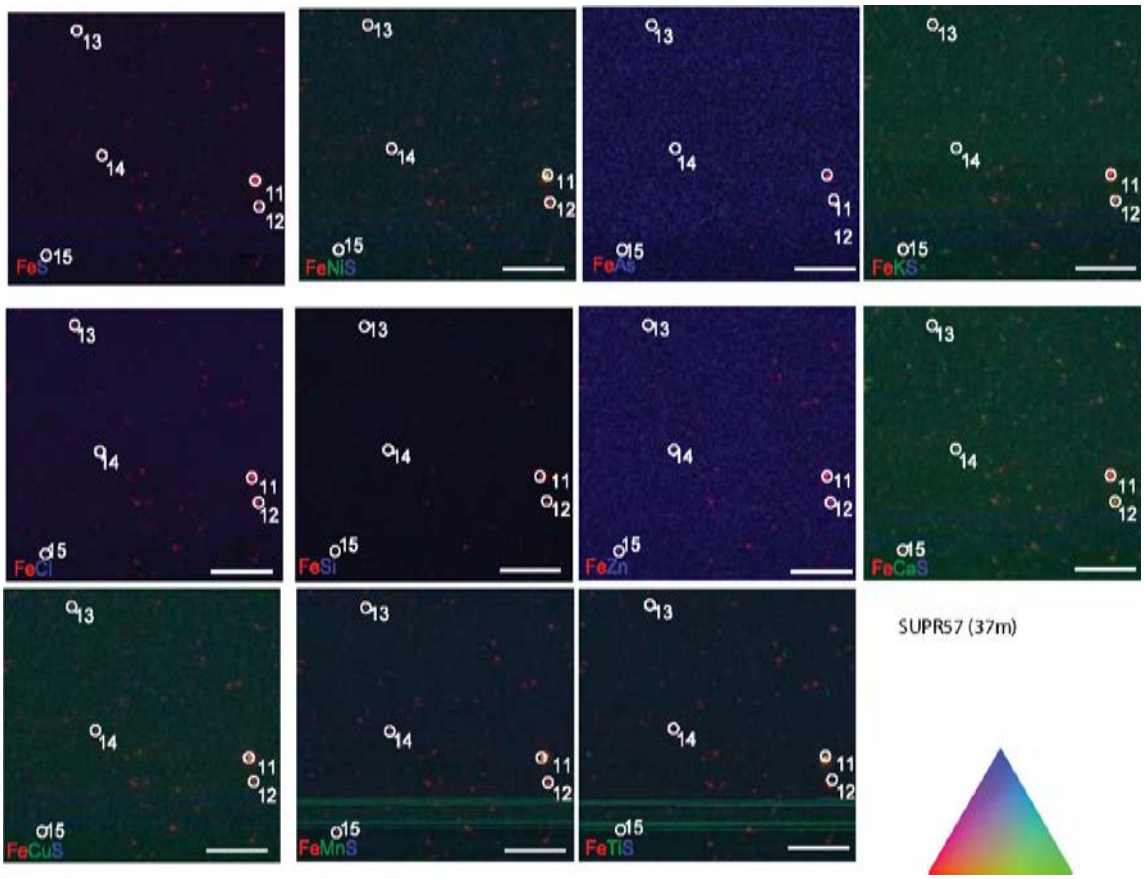

Supplemental figure 3.13: XRF correlation maps for maps in supplemental figure 3.12.

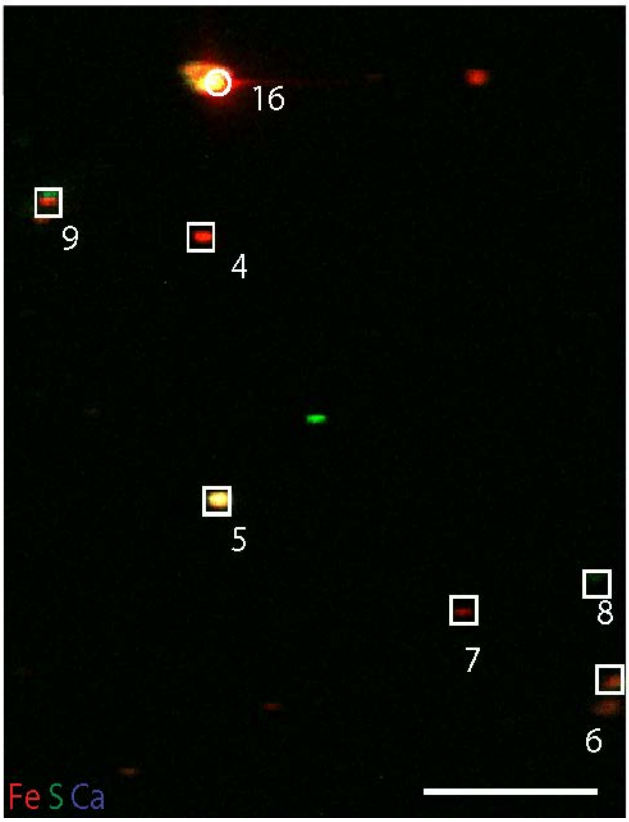

Supplemental figure 3.15: X-ray Fluorescence map for SUPR57 (37m) region 4. Map and S 1s XANES were collected at 13-ID-E. Squares represent where S 1s XANES were collected for spots 0-6. Circle represents where Fe 1s XANES were collected for spot 16.Map was for a 400µm X 500 µm area with a 1µm step, 50ms dwell, at E=7500eV. Scale bar is 100µm.

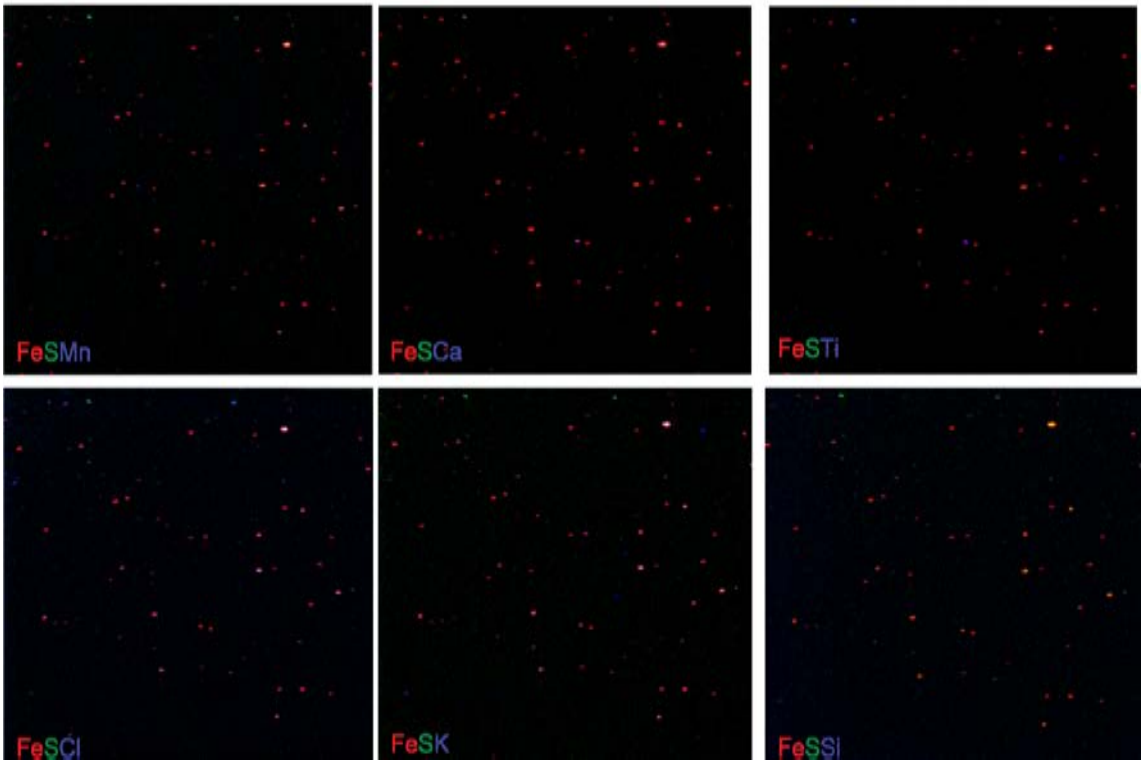

Supplemental figure 3.16: X-ray Fluorescence map for SUPR58 (815m). XRF maps collected at 13-ID-E. Maps were completed on a 1mm^2 area with a 3µm step, 50ms dwell, at E=7500eV.

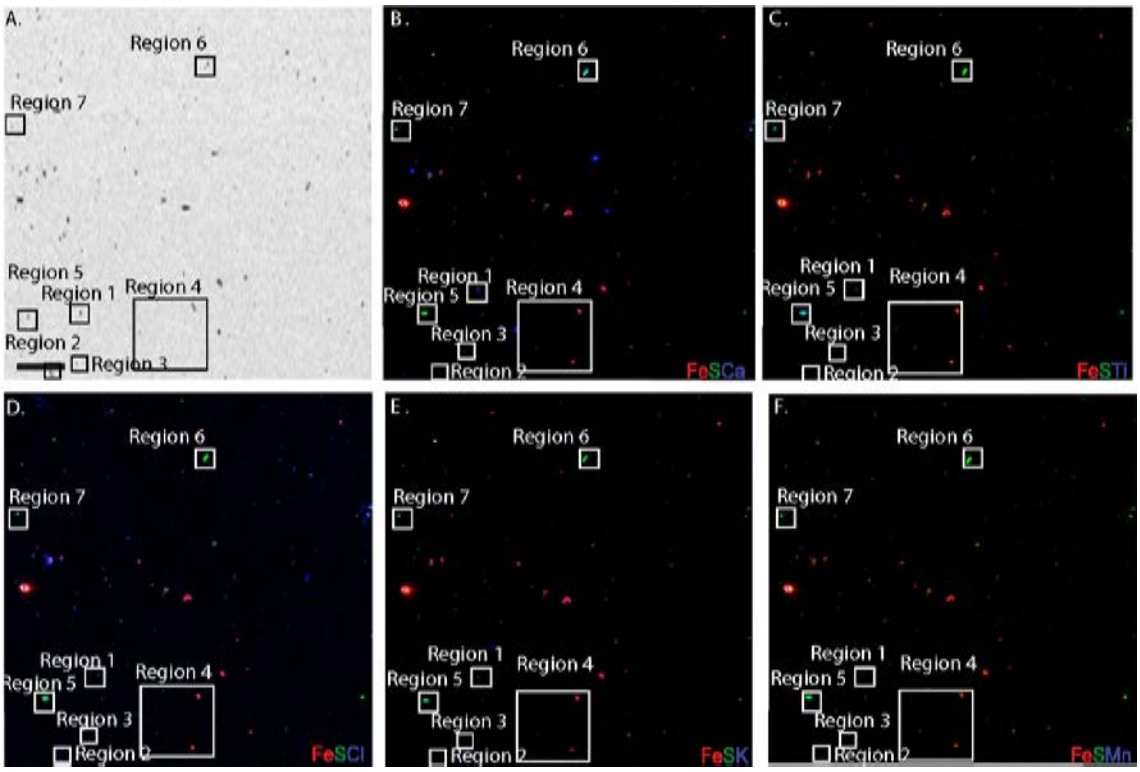

Supplemental figure 3.17: Scanning Transmission X-ray Microscopy and XRF images of sample SUPR03-1m silicon nitride window sample preparation. (a) Map collected at 5.3.2.2. Map was completed on a 1mm2 area with a 10µm step, 4ms dwell, at E=288eV. Scale bar is 100 µm. Regions 1-7 represent areas that were assessed for C and S XAS. Regions 1-3 were analyzed at 5.3.2.2. Region 4 was analyzed at 13-ID-E. Regions 5-7 were analyzed at 2-ID-B. (b-f) XRF maps collected at 13-ID-E. Maps were completed on a 1mm2 area with a 3µm step, 20ms dwell, at E=7500eV.

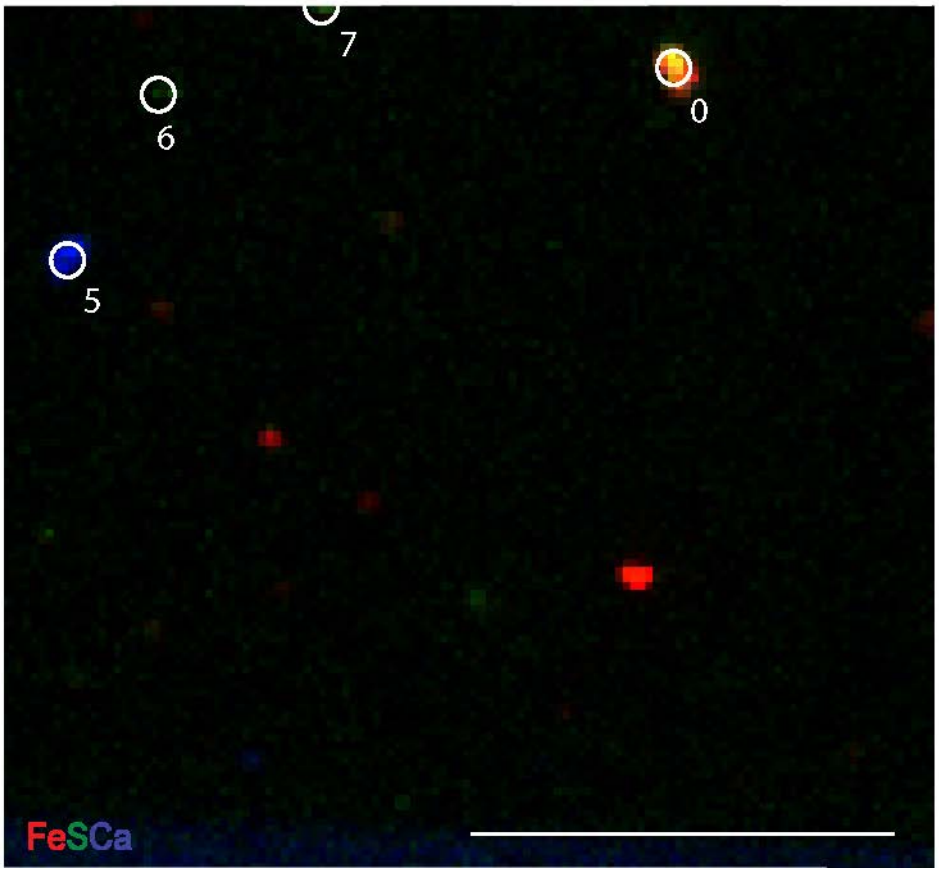

Supplemental figure 3.18: X-ray Fluorescence map for SUPR03-1m region 4. Map and S 1s XANES were collected at 13-ID-E. Circles represent where S 1s XANES were collected for spot 0, and 5-7. Map was for a 200μm^2 area with a 2μm step, 80ms dwell, at E=2500eV. Scale bar is 100μm.

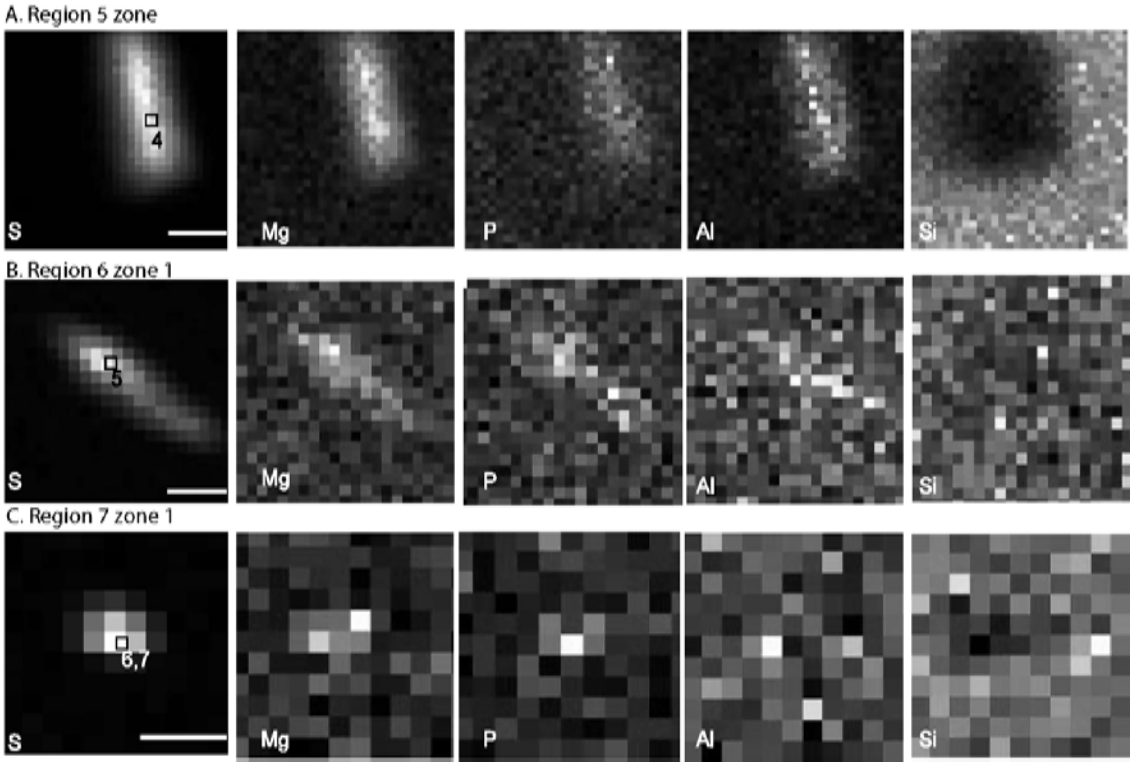

Supplemental figure 3.19: X-ray Fluorescence maps collected at 2-ID-B for SUPR03-1m. Three regions (regions 5, 6, and 7) were investigated with XRF maps and assessed for S 1s XANES. **(a)** region 5, E =2490eV, 3µm scale bar; particle ~6µm long. Sulfur 1s XANES (spot 4) in region 5 determined the presence of inorganic sulfate. **(b)** region 6, E = 2490eV, 3µm scale bar; particle is ~6µm long and S 1s XANES (spot 5) within the S-rich particle determined it was comprised of inorganic sulfate and homocysteic acid. **(c)** region 7, E = 2490eV, 2 µm; particle is ~1µm in diameter and two S 1s XANES (spots 6 and 7) within the S-rich particle determined it was comprised of inorganic sulfate, homocysteic acid, and sulfanilamide.

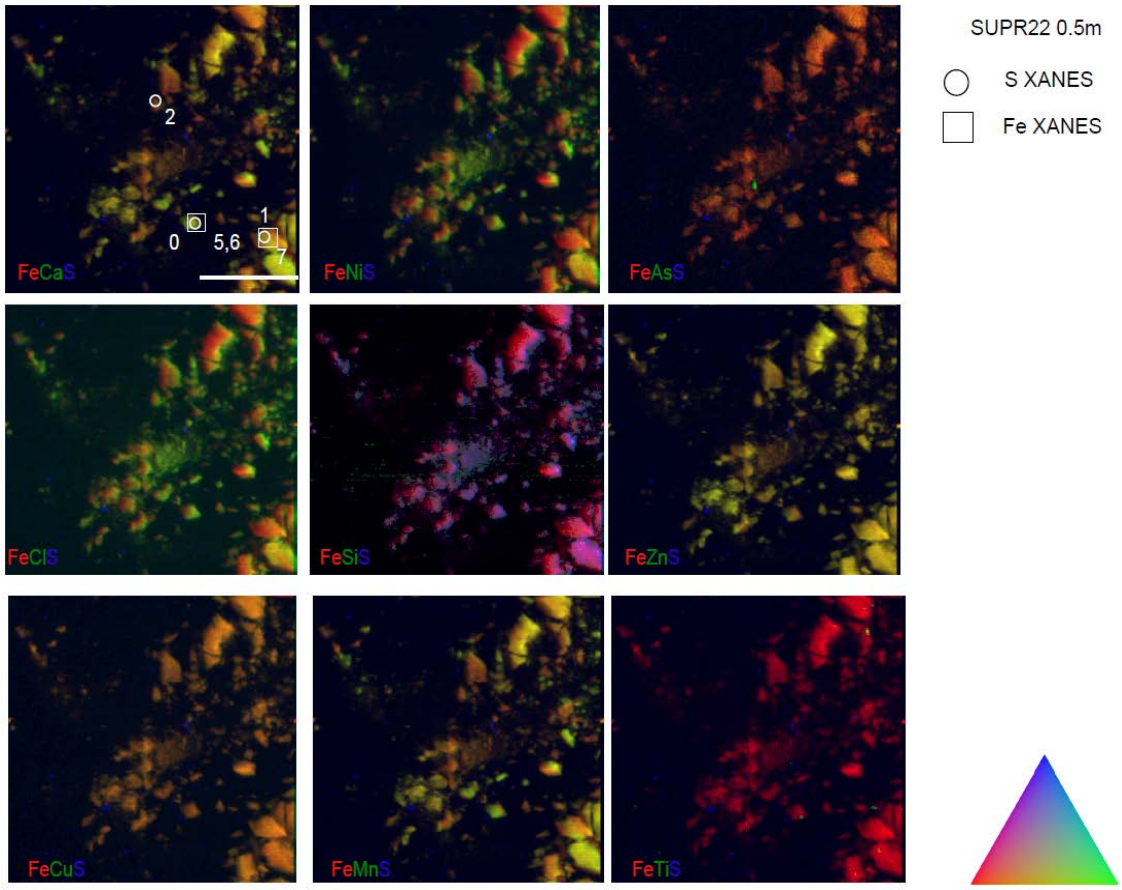

Supplemental Figure 3.20: X-ray fluorescence maps for SUPR22-0.5m collected at ALS beamline 10.3.2. Three spots (spots 6,7 and 8) were investigated for Fe 1s XANES (squares). Three spots (0-2) were investigated for S 1s XANES (circles). Maps were for 1000µm X 1000µm area, with 10µm step, and 100ms dwell, Scale bar is 300µm.

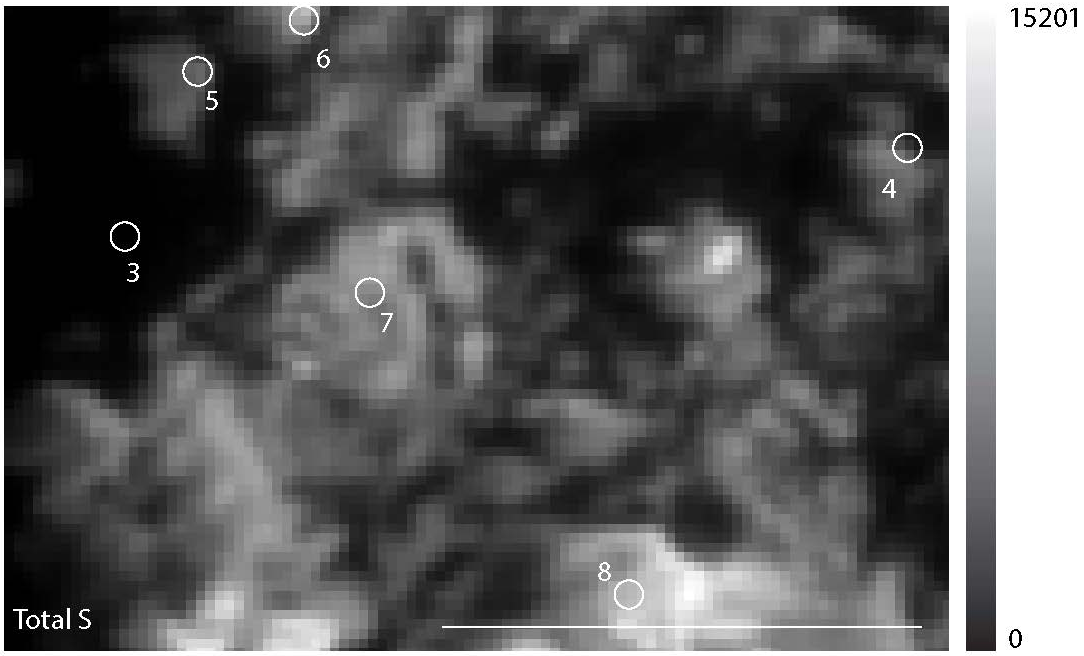

Supplemental Figure 3.21: X-ray fluorescence maps for SUPR22-0.5m collected at ALS beamline 10.3.2. Spots 3-8 were analyzed for S 1s XANES. Map was collected for 530µm X 350µm area, with 5µm step, and 500ms dwell, E = 2520eV, scale bar is 100µm.

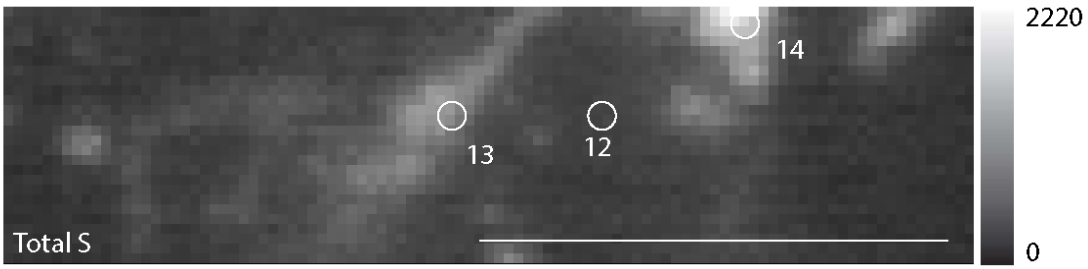

Supplemental Figure 3.22: X-ray fluorescence maps for SUPR22-0.5m collected at ALS beamline 10.3.2. Spot 12-14 were analyzed for S 1s XANES. Map was collected for 3000µm X 2000µm area, with 5µm step, and 500ms dwell, E = 2520eV, scale bar is 100µm.

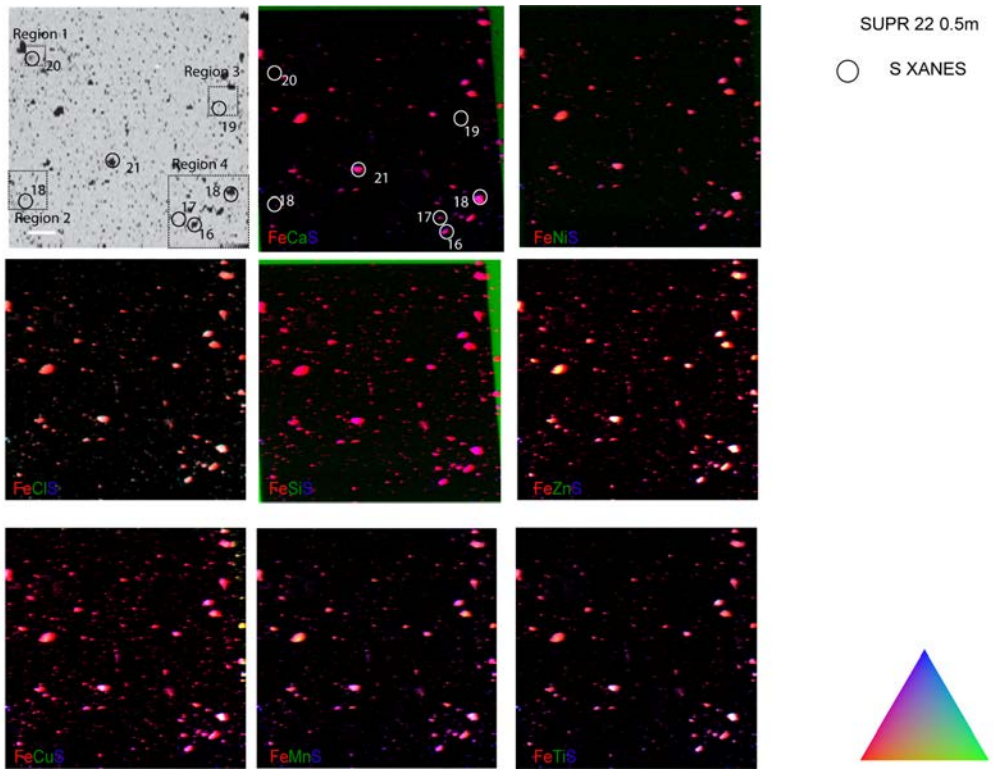

Supplemental figure 3.23: Scanning Transmission X-ray Microscopy and XRF images of sample SUPR22-0.5m silicon nitride window sample preparation. **(a)** Map collected at 5.3.2.2. Map was completed on a 1mm^2 area with a 10µm step, 4ms dwell, at E=288.5eV. Scale bar is 100 µm. Regions 1-4 represent areas that were assessed for C and S XAS. Regions 1-4 were analyzed at 5.3.2.2 for C STXM and XANES. Sulfur XAS data was collected at 13-ID-E; **(b-i)** XRF maps collected at 13-ID-E. Maps were completed on a 1mm^2 area with a 2µm step, 20ms dwell, at E=2500eV.

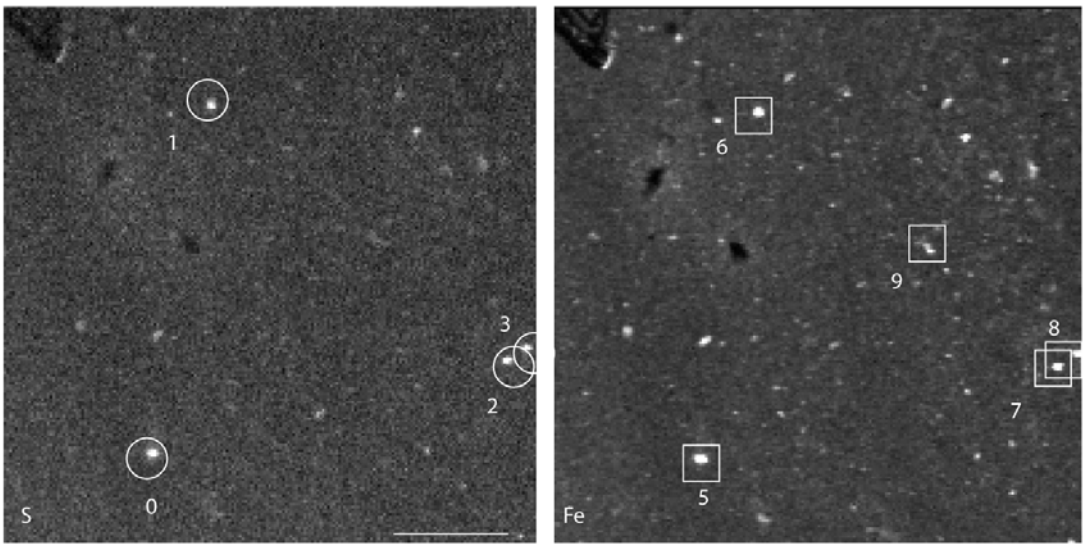

Supplemental figure 3.24: X-ray fluorescence maps for SUPR30-50m collected at ALS beamline 10.3.2. Five spots (spots 5-9) were investigated for Fe 1s XANES (squares). Four spots (0-1) were investigated for S 1s XANES (circles). Maps were for 1000µm X 1000µm area, with 5µm step, and 100ms dwell, at E=7000eV. Scale bar is 300µm.

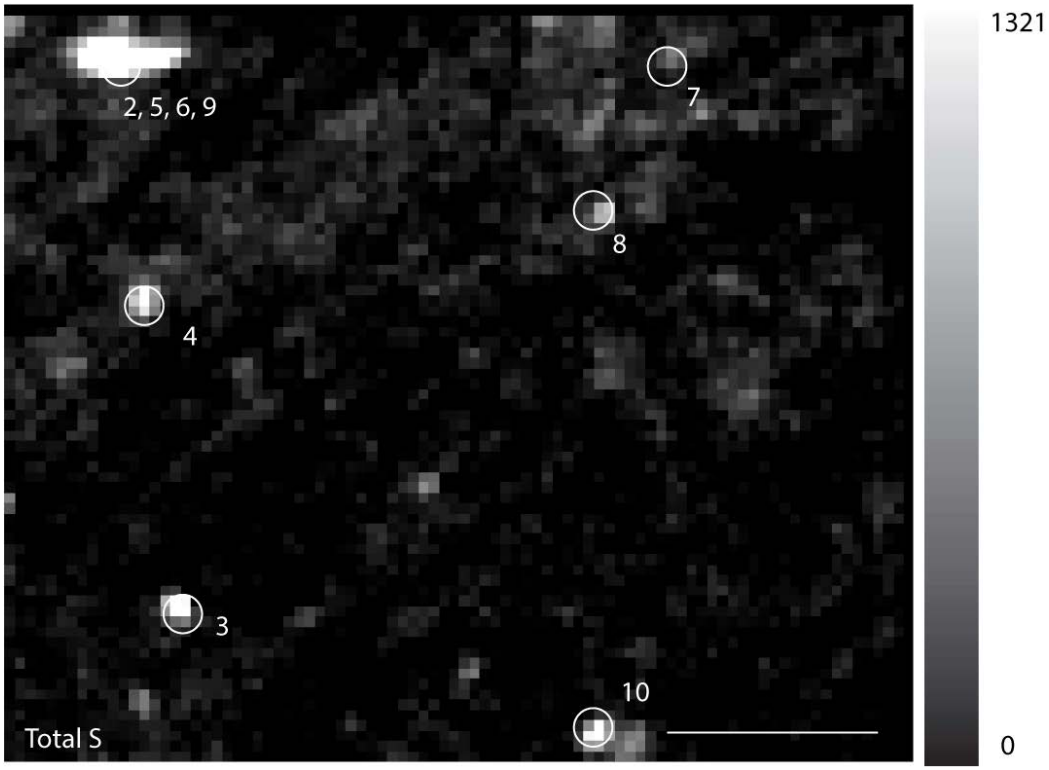

Supplemental figure 3.25: X-ray fluorescence maps for SUPR30-50m collected at ALS beamline v10.3.2. Spots 2-10 were analyzed for S 1s XANES. Map was collected for 500µm X 400µm area, with 5µm step, and 500ms dwell, E = 2520eV, scale bar is 100µm.

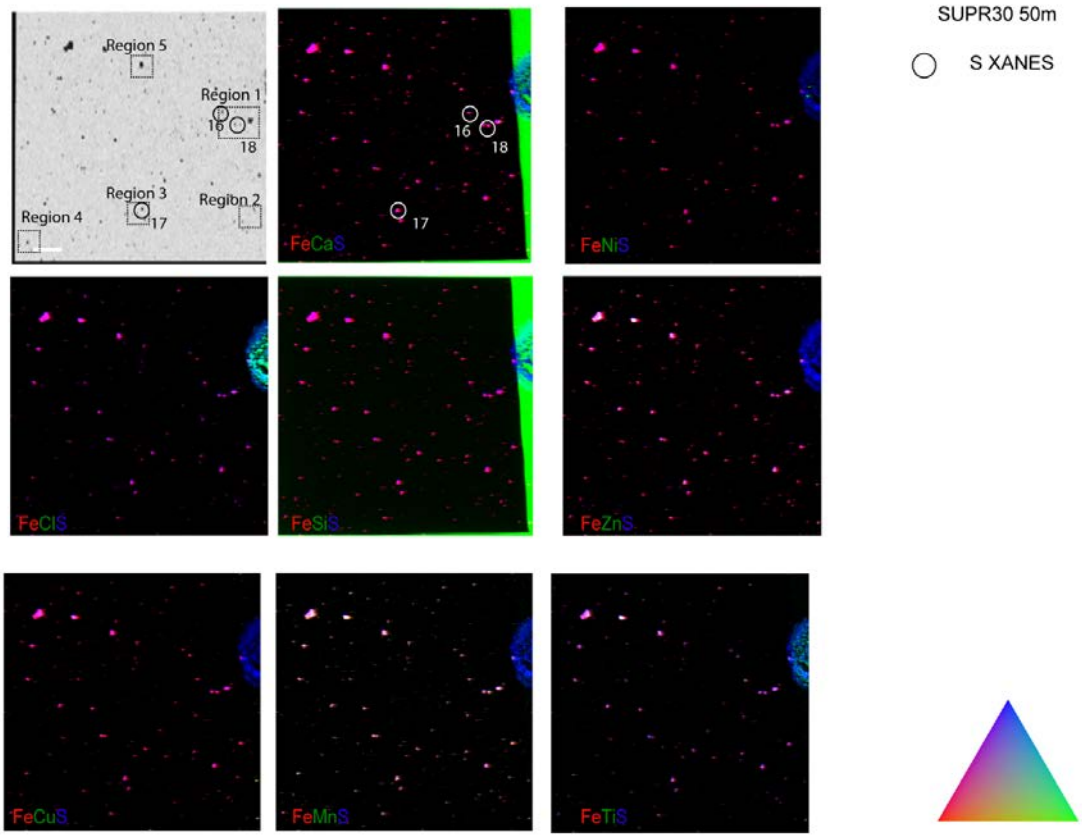

Supplemental figure 3.26: Scanning Transmission X-ray Microscopy and XRF images of sample SUPR30-50m silicon nitride window sample preparation. **(a)** Map collected at 5.3.2.2. Map was completed on a 1mm^2 area with a 10µm step, 4ms dwell, at E=288eV. Scale bar is 100 µm. Regions 1-5 were analyzed at 5.3.2.2. Regions 1 and 3 were analyzed at 13-ID-E. **(b-f)** XRF maps collected at 13-ID-E. Maps were completed on a 1mm^2 area with a 2µm step, 20ms dwell, at E=2500eV.

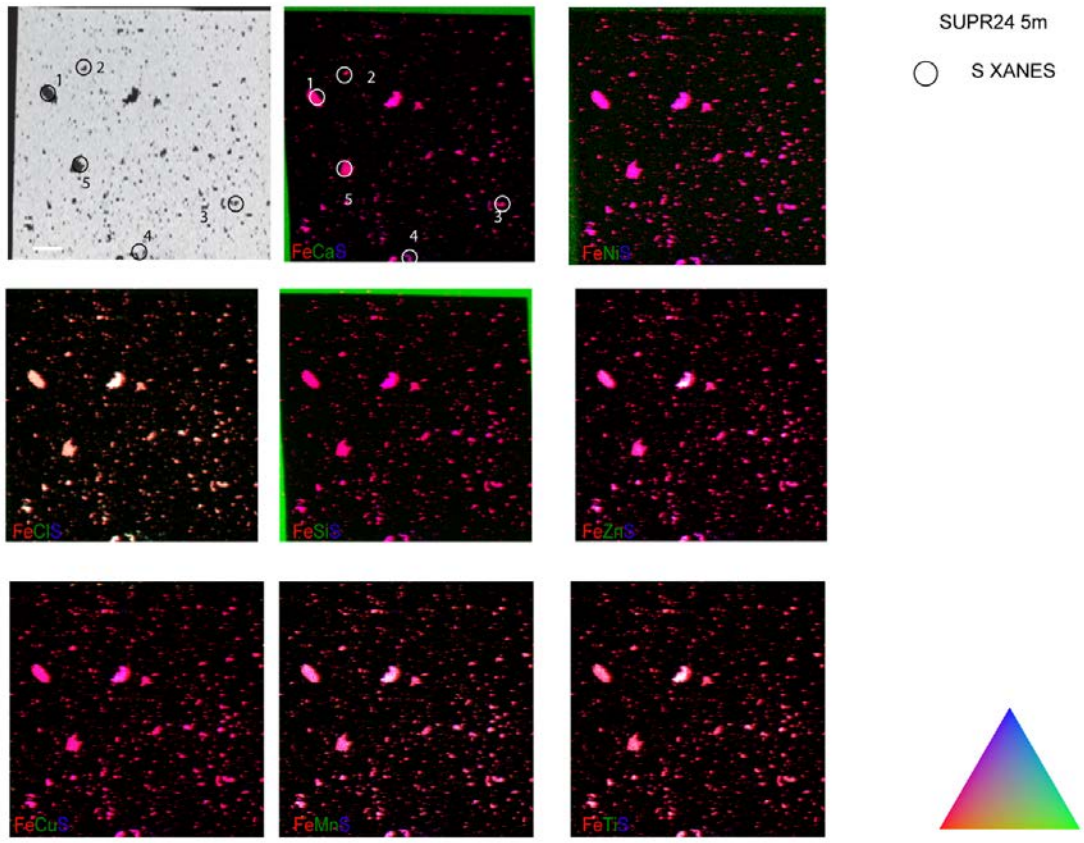

Supplemental figure 3.27: Scanning Transmission X-ray Microscopy and XRF images of sample SUPR24-5m silicon nitride window sample preparation. **(a)** Map collected at 5.3.2.2. Map was completed on a 1mm^2 area with a 10µm step, 4ms dwell, at E=288eV. Scale bar is 100 µm. Spots 1-5 were analyzed for S XANES at 13-ID-E. **(b-f)** XRF maps collected at 13-ID-E. Maps were completed on a 1mm^2 area with a 3µm step, 20ms dwell, at E=2500eV.

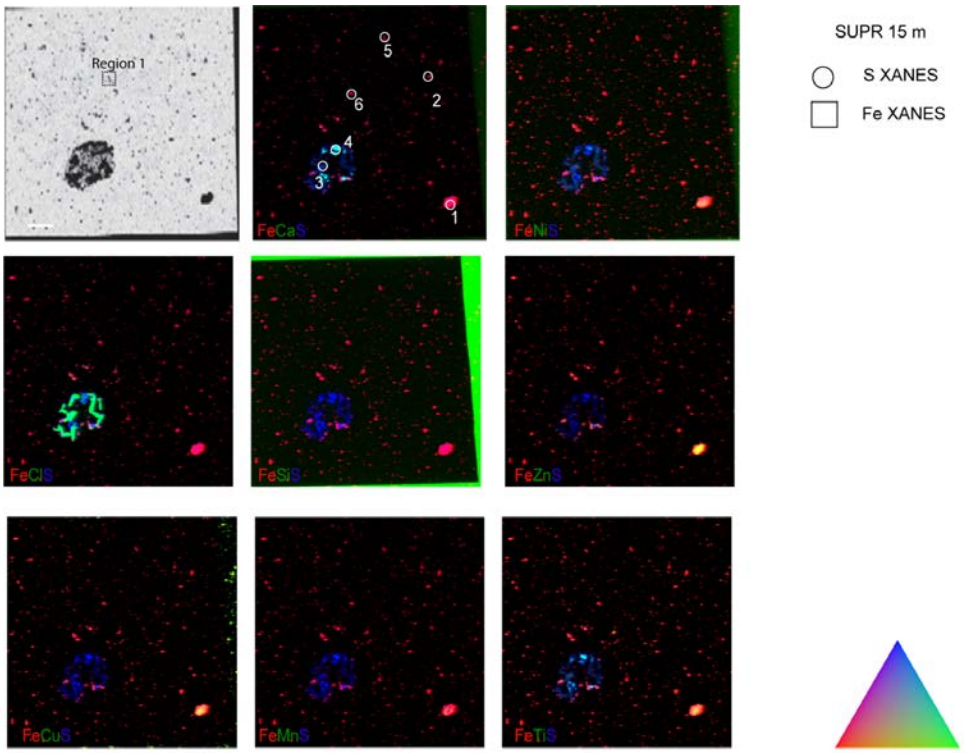

Supplemental figure 3.28: Scanning Transmission X-ray Microscopy and XRF images of sample SUPR24-15m silicon nitride window sample preparation. **(a)** Map collected at 5.3.2.2. Map was completed on a 1mm^2 area with a 10µm step, 4ms dwell, at E=288.6eV. Scale bar is 100 µm. Region 1 was analyzed at 5.3.2.2. Spots 1-5 were analyzed at 13-ID-E. **(b-f)** XRF maps collected at 13-ID-E. Maps were completed on a 1mm^2 area with a 2µm step, 20ms dwell, at E=2500eV

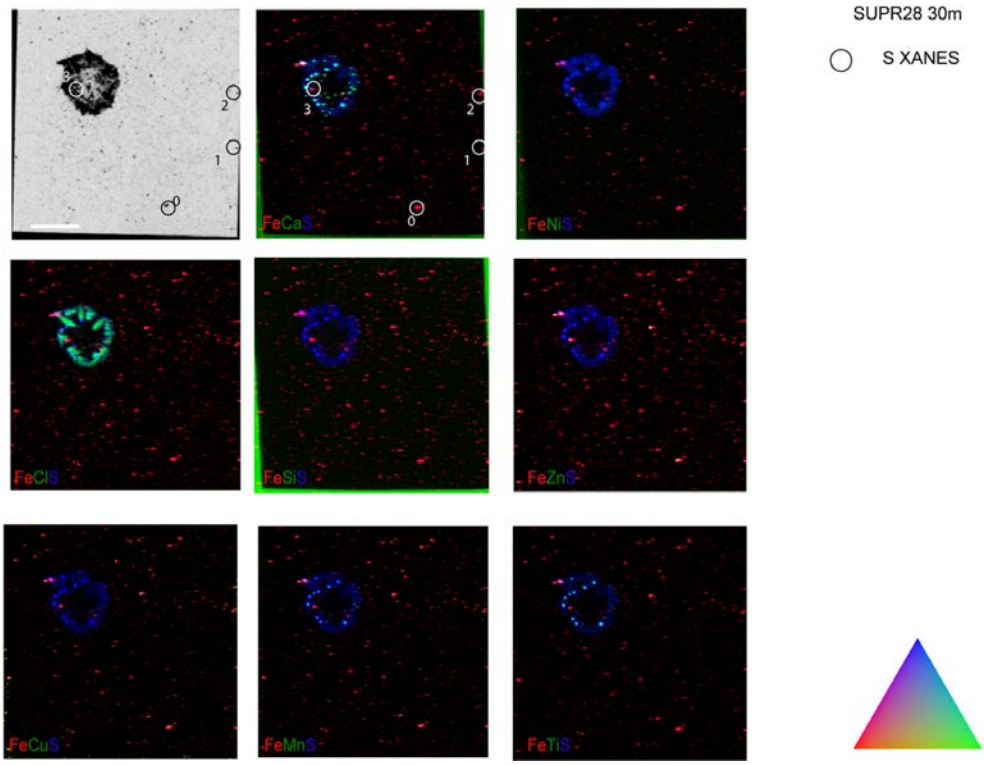

Supplemental figure 3.29: Scanning Transmission X-ray Microscopy and XRF images of sample SUPR28-30m silicon nitride window sample preparation. **(a)** Map collected at 5.3.2.2. Map was completed on a 1mm^2 area with a 10µm step, 4ms dwell, at E=288eV. Scale bar is 100 µm. Spots 1-4 were analyzed for S XANES at 13-ID-E. **(b-f)** XRF maps collected at 13-ID-E. Maps were completed on a 1mm^2 area with a 2µm step, 20ms dwell, at E=2500eV.

SUPPLEMENTAL TABLES

Supplemental table 3.1: Table lists the spot name and the region of the silicon nitride window where S 1s XANES were collected for SUPR03 (1m). The proportion (P), the component (C), sum, and NSS($X10^{-4}$) for the LCF results are listed. The elements detected by XRF mapping are also listed. As well as the beamline used to collect spectra. The sum of component fractions was not constrained to one and varied between 0.89 and 1.28. The spectra were determined best fit by the following reference spectra: (1) strongly reduced Fe monosulfide (mackinawite), Cu Fe sulfide (chalcopyrite and bornite), methionine, thiol (cysteine), and organic disulfide (cysteine); (2) weakly oxidized sulfanilamide, sulfonate (homocysteic acid); and, strongly oxidized ester sulfate (SDS), and inorganic sulfate (gypsum).

Spot	Region	P1	C1	P2	C2	P3	C3	P4	C4	sum	NSS ($X10^{-4}$)	Elements	Beamline
0	4	0.27	Chalcopyrite	0.16	Cysteine	0.56	Gypsum	0.14	SDS	1.13	37	Fe,S	APS 13-ID-E
1	4	0.23	Bornite	0.35	Chalcopyrite	0.32	Mackinawite	0	None	0.90	201	Ca	APS 13-ID-E
2	4	0.34	Bornite	0.36	Chalcopyrite	0.25	Mackinawite	0	None	0.95	196	S	APS 13-ID-E
3	4	0.33	Bornite	0.38	Cystine	0.37	Methionine	0.20	SDS	1.28	72	S	APS 13-ID-E
4	5	0.89	Gypsum	0	None	0	None	0	None	0.89	4650	S, Mg, P, Al, Ti	APS 2-ID-B
5	6	0.41	Gypsum	0.84	Homocysteic acid	0	None	0	None	1.25	882	S, Ca, Fe, Mg, P	APS 2-ID-B
6	7	0.24	Gypsum	0.92	Homocysteic acid	0	None	0	None	1.16	334	S, Mg, P, Ti	APS 2-ID-B
7	7	1	Sulfanilamide	0	Homocysteic acid	0	None	0	None	1	3110	S, Ti	APS 2-ID-B

Supplemental table 3.2: Table lists the spot name and the region of the silicon nitride window where S 1s XANES were collected for SUPR05 (1m). The proportion (P), the component (C), sum, and NSS($X10^{-4}$) for the LCF results are listed. The elements detected by XRF mapping are also listed. As well as the beamline used to collect spectra.The sum of component fractions was not constrained to one and varied between 0.78 and 1.35. Seventeen point XANES were collected for SUPR05. The spectra were determined best fit by the following reference spectra: (1) strongly reduced elemental S (elemental S, nanoparticulate S), Fe disulfide (pyrite), copper iron sulfide (chalcopyrite and bornite), iron monosulfide (greigite and mackinawite), methionine, thiol (cysteine), polysulfide (sodium polysulfide and potassium tetrathionate), organic disulfide (cystine), and thiophene (benzothiophene sulfone); (2) weakly reduced sulfite; (3) weakly oxidized sulfonate (ANSA and homocysteic acid); and, (4) strongly oxidized ester sulfate (sodium dodecyl sulfate) and inorganic sulfate (gypsum). Fe 1s XANES spot 5 correlates with S 1s XANES spot 0. Fe XANES 1s spot 6 correlates with S 1s XANES spot 1.

Spot	Region	P1	C1	P2	C2	P3	C3	P4	C4	sum	NSS ($X10^{-4}$)	Elements	Beamline
0	-	0.17	Greigite	0.01	Gypsum	0.73	S8_raffo	0.08	Sodium polysulfide	0.98	11.4	Fe, S, Si, Cl, Ni, As, Zn, Cu, Mn	ALS 10.3.2
1	-	0.16	Chalcopyrite	0.07	Gypsum	0.14	Mackinawite	0.62	S8_raffo	0.99	16.3	Fe, Ni, Cu	ALS 10.3.2
2	-	0.20	Greigite	0.12	Pyrite	0.54	S8_raffo	0.18	Sodium polysulfide	1.04	14.6		ALS 10.3.2
3	-	0.22	Cystine	0.29	Gypsum	0.05	Pyrite	0.44	SDS	1.01	28		ALS 10.3.2
4	-	0.23	ANSA	0.09	Bornite	0.12	Gypsum	0.37	Pyrite	0.81	17.1		ALS 10.3.2
5	-	0.26	Elemental S	0.13	Greigite	0.28	Gypsum	0.17	Homocysteic acid	0.83	51.4		ALS 10.3.2
6	-	0.46	Chalcopyrite	0.13	Mackinawite	0.081	S8_16r	0.15	SDS	0.82	42		ALS 10.3.2
7	-	0.15	Cystine	0.35	Gypsum	0.21	SDS	0.38	Sodium polysulfide	1.12	101		ALS 10.3.2
8	-	0.16	Bornite	0.19	Gypsum	0.19	S8_135r	0.24	SDS	0.78	152		ALS

													10.3.2
9	-	0.25	Chalcopyrite	0.30	Gypsum	0.31	S8_16r	0.22	SDS	1.09	68.4		ALS 10.3.2
10	4	0.78	Bornite	0.23	Mackinawite	0.08	K tetrathionate	0.09	SDS	1.18	34	Fe, Si	APS 13-ID-E
11	4	0.19	Benzothiophene	0.31	Bornite	0.54	Cysteine	0.09	K tetrathionate	1.14	26.5	Fe, Si	APS 13-ID-E
12	4	0.27	Bornite	0.44	Methionine	0.12	S8_135r	0.09	SDS	0.93	83.4	Fe, Si	APS 13-ID-E
13	4	0.21	Bornite	0.31	Cysteine	0.23	Gypsum	0.19	SDS	0.94	102	Si	APS 13-ID-E
14	4	0.17	Bornite	0.56	Elemental S	0.19	Gypsum	0.23	K tetrathionate	1.16	124	S, Mg, P, Al, Fe, Si	APS 13-ID-E
15	5, zone 1	1.35	Homocysteic acid	0	None	0	None	0	None	1.35	2260	S, Mg, P, Al, Si, Fe, S	APS 2-ID-B
16	6, zone 1	0.80	Sulfite	0	None	0	None	0	None	0.8	5710	Fe, S	APS 2-ID-B

Supplemental table 3.3: Table lists the spot name and the region of the silicon nitride window where S 1s XANES were collected for SUPR11 (8m). The proportion (P), the component (C), sum, and NSS(X10-4) for the LCF results are listed. The elements detected by XRF mapping are also listed; as well as the beamline used to collect spectra. The sum of component fractions was not constrained to one and varied between 0.78 and 1.59. The spectra were determined best fit by the following reference spectra: (1) strongly reduced thiophene (2-Thiophencarboxylic acid), polysulfide (potassium tetrathionate), iron sulfide (pyrite), elemental S (elemental S and nanoparticulate S),copper iron sulfide (chalcopyrite and bornite), copper sulfide (covellite), iron monosulfide (greigite and mackinawite), organic disulfide (cystine), and methionine; (2) weakly reduced sulfoxide (methionine sulfoxide), and sulfite; (3) weakly oxidized sulfanilamide, sulfonate (homocysteic acid); and, (4) strongly oxidized inorganic sulfate (gypsum), ester sulfate (SDS).

Spot	Region	P1	C1	P2	C2	P3	C3	P4	C4	sum	NSS ($X10^{-4}$)	Elements	Beamline
0	-	0.17	Bornite	0.87	Gypsum	0	None	0	None	1.04	735	S, Si, Ca, K	ALS 10.3.2
1	-	0.44	Chalcopyrite	0.42	Gypsum	0	None	0	None	0.86	252	Fe, Ni, Cu	ALS 10.3.2
2	-	0.19	Chalcopyrite	0.32	Gypsum	0.38	Pyrite	0.2	S8_16r	1.09	85.5	Fe, Si, Ti	ALS 10.3.2
3	-	0.26	Chalcopyrite	0.16	Gypsum	0.18	S8_135r	0.18	SDS	0.78	169	Si, Ti, Fe	ALS 10.3.2
4	-	0.98	Gypsum	0	None	0	None	0	None	0.99	1710	Fe	ALS 10.3.2
5	-	0.09	Cystine	0.21	Gypsum	0.61	Pyrite	0	None	0.92	39.5		ALS 10.3.2
6	-	0.34	Gypsum	0.97	S8_135r	0	None	0	None	1.31	2850		ALS 10.3.2
7	-	1	Gypsum	0.28	Gypsum	0	None	0	None	0.89	52		ALS 10.3.2
8	-	0.05	Cystine	0.86	Gypsum	0	None	0	None	0.91	103		ALS 10.3.2
9	-	1.02	Gypsum	0	None	0	None	0	None	1.02	206		ALS 10.3.2
10	-	0.4	Sulfoxide	1.18	Sulfite	0	None	0	None	1.59	3560		ALS

													10.3.2
11	-	0.51	SDS	0.41	Sulfanilamide	0	None	0	None	0.91	770		ALS 10.3.2
12	-	0.88	Gypsum	0.16	Gypsum	0	None	0	None	1.04	181		ALS 10.3.2
13	-	0.23	Bornite	0.465	Gypsum	0.24	S8_135r	0.40	SDS	1.34	112		ALS 10.3.2
14	-	0.75	Cystine	0.26	Gypsum	0.25	Methionine	0	None	1.27	97.7		ALS 10.3.2
15	-	0.55	Elemental S	0.14	Greigite	0.40	Gypsum	0.21	Thiophene	1.31	91.9		ALS 10.3.2
16	-	0.506	Gypsum	0.16	Mackinawite	0.55	S8_16r	0	None	1.22	120		ALS 10.3.2
17	4	0.59	Gypsum	0.24	Gypsum	0	None	0	None	0.83	30.2		APS 13-ID-E
18	4	0.05	Bornite	0.79	Gypsum	0.08	Gypsum	0	None	0.92	35.6		APS 13-ID-E
19	4	0.03	Covellite	0.51	Gypsum	0.30	Gypsum	0.11	Potassium tetrathionate	0.95	19.4		APS 13-ID-E
20	4	0.31	Gypsum	0.59	Gypsum	0.08	Potassium tetrathionate	0	None	0.98	25.2	Si, S, Cl, Ca, Fe	APS 13-ID-E
21	5, zone 1	0.94	Gypsum	0	None	0	None	0	None	0.94	240	Si, Cl, K, Ca, Ti, Fe	APS 2-ID-B
22	6, zone 1	0.16	Gypsum	1.1	Homocysteic acid	0	None	0	None	1.26	770	Si, S, Cl, K, Ca, Ti , Fe	APS 2-ID-B
23	6, zone 2	0.48	Gypsum	0.39	Homocysteic acid	0	None	0	None	0.87	382	Si, S, Cl, K, Ca, Ti , Fe	APS 2-ID-B
24	6, zone 2	0.22	Gypsum	0.46	Homocysteic acid	0	None	0	None	0.69	529	Si, S, Cl, K, Ca, Ti , Fe	APS 2-ID-B

25	6, zone 3	0.39	Gypsum	0.79	Homocysteic acid	0	None	0	None	1.16	847	Si, S, Cl, K, Ca, Ti , Fe	APS 2-ID-B
26	6, zone 3	0.15	Gypsum	1.02	Homocysteic acid	0	None	0	None	1.17	517	Si, S, Cl, K, Ca, Ti , Fe	APS 2-ID-B

Supplemental table 3.4: Table lists the spot name and the region of the silicon nitride window where S 1s XANES were collected for SUPR57 (37m). The proportion (P), the component (C), sum, and NSS($X10^{-4}$) for the LCF results are listed. The elements detected by XRF mapping are also listed; as well as the beamline used to collect spectra. Nine point XANES were collected for SUPR57 (supplemental table 12). The sum of component fractions was not constrained to one and varied between 0.94 and 1.64. The spectra were determined best fit by the following reference spectra: (1) strongly reduced Cu Fe sulfide (chalcopyrite), Cu sulfide (covellite), methionine, thiol (cysteine), and thiophene (2-Thiophencarboxylic acid); (2) weakly oxidized sulfanilamide and sulfonate (ANSA and homocysteic acid); and, (3) strongly oxidized ester sulfate (SDS) and inorganic sulfate (gypsum).

Spot	Region	P1	C1	P2	C2	P3	C3	P4	C4	sum	NSS ($X10^{-4}$)	Elements	Beamline
0	-	0.05	Methionine	0.86	SDS	0.18	Sulfanilamide	0	None	1.1	82.8		ALS 10.3.2
1	-	0.09	Chalcopyrite	0.27	Gypsum	0.53	Gypsum	0.47	SDS	1.37	27.6		ALS 10.3.2
2	-	0.28	Covellite	1.36	Gypsum	0	None	0	None	1.64	167		ALS 10.3.2
3	4	0.39	Covellite	0.48	Methionine	0.49	SDS	0	None	1.37	192	Fe, Si	APS 13-ID-E
4	4	0.22	Covellite	0.58	Methionine	0.58	SDS	0	None	1.38	211	Si, S, Cl, K, Ca, Fe	APS 13-ID-E
5	4	0.43	Gypsum	0.25	Homocysteic acid	0.36	Methionine	0	None	1.05	106	Si, S, Cl, Ti	APS 13-ID-E
6	4	0.94	ANSA	0	None	0	None	0	None	0.94	514	Si, S, Cl, K, Ca, Fe	APS 13-ID-E
7	4	0.68	Gypsum	0.45	Homocysteic acid	0	None	0	None	1.14	311	Si	APS 13-ID-E
8	4	0.11	Chalcopyrite	0.74	Gypsum	0.34	Thiophene	0	None	1.19	119	Si	APS 13-ID-E

Supplemental table 3.5: Table lists the spot name and the region of the silicon nitride window where S 1s XANES were collected for SUPR22 (0.5m). The proportion (P), the component (C), sum, and NSS($X10^{-4}$) for the LCF results are listed. The elements detected by XRF mapping are also listed. As well as the beamline used to collect spectra.

Spot	Region	P1	C1	P2	C2	P3	C3	P4	C4	sum	NSS ($X10^{-4}$)	Elements	Beamline
0		0.08	Gypsum	0.23	Mackinawite	0.76	Pyrite	0	None	1.08	22		10.3.2
1		0.1	Gypsum	0.2	Mackinawite	0.55	Pyrite	0.27	S8nano 16r centrifuged cls ambient	1.12	22		10.3.2
2		0.08	Gypsum	0.21	Mackinawite	0.84	Pyrite	0	None	1.13	29		10.3.2
3		0.2	Bornite	0.27	S8nano 16r cls ambient	0.41	SDS	0.42	Sulfanilamide	1.3	42		10.3.2
4		0.14	Greigite	0.07	Gypsum	0.68	Pyrite	0.11	Sodium polysulfide	1	14		10.3.2
5		0.07	Gypsum	0.2	Mackinawite	0.61	Pyrite	0.15	Sodium polysulfide	1.03	20		10.3.2
6		0.26	Chalcopyrite	0.2	Pyrite	0.42	Pyrite	0.13	SDS	1.01	32		10.3.2
7		0.12	Gypsum	0.18	Mackinawite	0.57	Pyrite	0.17	Sodium polysulfide	1.04	25		10.3.2
8		0.06	Gypsum	0.15	Mackinawite	0.34	Pyrite	0.56	S8 raffo cls ambient	1.1	17		10.3.2
9		0.2	Elemental S	0.14	Greigite	0.05	Gypsum	0.65	Pyrite	1.03	24		10.3.2
10		0.2	Chalcopyrite	0.28	Pyrite	0.31	s8nano 16r cls	0.15	SDS	0.94	41		10.3.2

							ambient						
11		0.19	Chalcopyrite	0.28	Pyrite	0.31	s8nano 16r cls ambient	0.15	SDS	0.93	29		10.3.2
12		0.18	Chalcopyrite	0.28	Elemental S	0.25	Potassium tetrathionate	0.27	Pyrite	0.98	27		10.3.2
13		0.31	Elemental S	0.17	Greigite	0.1	Gypsum	0.48	Pyrite	1.06	52		10.3.2
14		0.12	Elemental S	0.06	Gypsum	0.17	Mackinawite	0.74	Pyrite	1.09	21		10.3.2
15	4	0.28	Chalcopyrite	0.25	Greigite	0.72	Pyrite	0	None	1.25	11	Fe,S,Cl,Zn, Cu, Mn, Ti	13-ID-E
16	4	0.61	Chalcopyrite	0.17	Gypsum	0.26	Pyrite	0	None	1.03	50	Fe,S,Cl,Zn, Cu, Mn, Ti	13-ID-E
17	4	0.33	Covellite	0.18	Gypsum	0.49	Pyrite	0.04	Sulfite	1.05	13	Fe,S,Cl,Zn, Cu, Mn, Ti	13-ID-E
18	2	0.29	Gypsum	0.37	S8 raffo cls ambient	0.11	SDS	0.1	Sulfite	0.87	30	Fe,S,Cl,Zn, Cu, Mn, Ti	13-ID-E
19	3	0.3	Covellite	0.24	Greigite	0.14	Gypsum	0.32	Pyrite	1	15	Fe,S,Cl,Zn, Cu, Mn, Ti	13-ID-E
20	1	0.2	Covellite	0.09	Greigite	0.12	Gypsum	0.61	Pyrite	1.02	11	Fe,S,Cl,Zn, Cu, Mn, Ti	13-ID-E
21		0.37	Chalcopyrite	0.28	Mackinawite	0.64	Pyrite	0	None	1.29	16	Fe,S,Cl,Zn, Cu, Mn, Ti	13-ID-E

Supplemental table 3.6: Table lists the spot name and the region of the silicon nitride window where S 1s XANES were collected for SUPR24 (5m). The proportion (P), the component (C), sum, and NSS($X10^{-4}$) for the LCF results are listed.

Spot	P1	C1	P2	C2	P3	C3	P4	C4	sum	NSS (x10-4)	Beamline
0	0.88	Chalcopyrite	0.37	Mackinawite	0	None	0	None	1.25	89.4	13-ID-E
1	1	Chalcopyrite	0.45	Mackinawite	0	None	0	None	1.45	66	13-ID-E
2	0.78	Chalcopyrite	0.25	Greigite	0.18	Mackinawite	0	None	1.2	49	13-ID-E
3	0.82	Chalcopyrite	0.28	Gypsum	0	None	0	None	1.1	90	13-ID-E
4	0.95	Chalcopyrite	0.46	Mackinawite	0	None	0	None	1.4	95	13-ID-E

Supplemental table 3.7: Table lists the spot name and the region of the silicon nitride window where S 1s XANES were collected for SUPR26 (15m). The proportion (P), the component (C), sum, and NSS($X10^{-4}$) for the LCF results are listed. The elements detected by XRF mapping are also listed. As well as the beamline used to collect spectra.

Spot	P1	C1	P2	C2	P3	C3	P4	C4	sum	NSS ($X10^{-4}$)	Elements	Beamline
1	0.84	Chalcopyrite	0.42	Mackinawite	0	None	0	None	1.26	106	Fe	13-ID-E
2	0.76	Chalcopyrite	0.36	Greigite	0	None	0	None	1.12	68	Fe	13-ID-E
3	0.2	Bornite	1.17	Gypsum	0.25	S8nano 16r cls ambient	0.42	SDS	2.04	36	Fe	13-ID-E
4	0.1	Bornite	0.58	Gypsum	0.13	S8nano 16r cls ambient	0.21	SDS	1.01	36	Fe	13-ID-E
5	0.11	Bornite	0.56	Gypsum	0.12	S8nano 16r cls ambient	0.17	SDS	0.96	56	Fe	13-ID-E
6	0.54	Chalcopyrite	0.05	Gypsum	0.26	Mackinawite	0.04	Sulfite	0.89	42	Fe	13-ID-E

Supplemental table 3.8: Table lists the spot name and the region of the silicon nitride window where S 1s XANES were collected for SUPR28 (30m). The proportion (P), the component (C), sum, and NSS($X10^{-4}$) for the LCF results are listed. The elements detected by XRF mapping are also listed. As well as the beamline used to collect spectra.

Spot	P1	C1	P2	C2	P3	C3	P4	C4	sum	NSS ($X10^{-4}$)	Beamline
0	0.69	Chalcopyrite	0.33	Greigie	0.08	Gypsum	0	None	1.1	71	13-ID-E
1	0.79	Chalcopyrite	0.34	Greigie	0.07	Gypsum	0	None	1.2	56	13-ID-E
2	0.7	Chalcopyrite	0.09	Gypsum	0.21	Mackinawite	0.07	Sulfite	1.08	48	13-ID-E
3	0.54	Chalcopyrite	0.12	Cysteine	0.54	Gypsum	0.31	SDS	1.52	47	13-ID-E

Supplemental table 3.9: Table lists the spot name and the region of the silicon nitride window where S 1s XANES were collected for SUPR30 (50m). The proportion (P), the component (C), sum, and NSS($X10^{-4}$) for the LCF results are listed. The elements detected by XRF mapping are also listed. As well as the beamline used to collect spectra.

Spot	P1	C1	P2	C2	P3	C3	P4	C4	sum	NSS (x10-4)	Elements	Beamline
0	0.57	Chalcopyrite	0.06	Gypsum	0.07	Pyrite	0.2	SDS	0.9	28		10.3.2
1	0.04	ANSA	0.56	Chalcopyrite	0.15	Greigite	0.17	Gypsum	0.94	18		10.3.2
2	0.09	ANSA	0.39	Chalcopyrite	0.19	Cysteine	0.18	SDS	0.85	10		10.3.2
3	0.13	ANSA	0.54	Chalcopyrite	0.11	Gypsum	0.11	s8nano 16r cls	0.89	15		10.3.2
4	0.12	ANSA	0.49	Chalcopyrite	0.11	Gypsum	0.11	Sodium polysulfide	0.84	15		10.3.2
5	0.4	Chalcopyrite	0.16	Cysteine	0.26	SDS	0.08	Sulfanilamide	0.9	21		10.3.2
6	0.35	Chalcopyrite	0.14	Cysteine	0.14	Gypsum	0.13	Homocysteic acid	0.76	12		10.3.2
7	0.42	Chalcopyrite	0.1	s8nano 16r	0.28	SDS	0.04	Sulfanilamide	0.83	13		10.3.2
8	0.48	Chalcopyrite	0.2	SDS	0.17	Sodium polysulfide	0.05	Sulfanilamide	0.9	16		10.3.2
9	0.37	Chalcopyrite	0.15	Cysteine	0.16	Gypsum	0.14	Homocysteic acid	0.81	14		10.3.2
10	0.44	Chalcopyrite	0.08	Potassium tetrathionate	0.21	Pyrite	0.2	SDS	0.93	19		10.3.2
11	0.54	Chalcopyrite	0.16	Greigite	0.18	s8nano 16r cls	0.16	SDS	1.04	33		10.3.2
12	0.42	Chalcopyrite	0.19	Greigite	0.16	s8nano 16r cls	0.14	SDS	0.91	47		10.3.2
13	0.56	Chalcopyrite	0.17	Potassium tetrathionate	0.1	SDS	0.2	Sodium polysulfide	1.04	47		10.3.2

14	0.41	Chalcopyrite	0.23	greigite	0.17	s8nano 16r cls	0.12	SDS	0.92	42		10.3.2
15	0.47	Chalcopyrite	0.15	Potassium tetrathionate	0.08	SDS	0.22	Sodium polysulfide	0.92	43		10.3.2
16	0.63	Chalcopyrite	0.35	Greigite	0.17	Gypsum	0.03	Sulfite	1.17	23	Fe, S, Zn, Mn, Ti	13-ID-E
17	0.18	Bornite	0.47	Chalcopyrite	0.47	Greigite	0	None	1.12	43	Fe, S, Zn, Mn, Ti	13-ID-E
18	0.57	Chalcopyrite	0.24	Greigite	0.04	Gypsum	0.04	Sulfite	0.89	34	Fe, S, Zn, Mn, Ti	13-ID-E

APPENDIX

1. TESTING "S BY WEIGHT" APPROACH WITH ANALYSIS OF STANDARD MIXTURES

When we collect XANES data, the X-rays are penetrating a volume of material that is composed of a mixture of compounds. The absorption of the sample is the sum of the absorption due to volume of each separate compound. We examined the validity of the XANES method for analysis of 4 test mixtures prepared with sodium dodecyl sulfate, cystine, methionine, and cysteine (Table 1A). The approach involved preparing mixtures, collecting the spectra (CLS SXRMB), normalizing the spectra, and fitting the data.

Our normalization procedure gives spectra proportional to the absorption per atom of sulfur, not per cubic centimeter of material. In order to calculate the percentage that each volume of material contributes to the LCF spectra, we did the following conversion:

(1) We calculated the percentage of sulfur, by weight, each compound contributes by dividing the molecular weight of S (32 g/mol) by the molecular weight of the compound (e.g., Sodium dodecyl sulfate is 11% S by weight; Table 2A);
(2) We converted the density of each compound to mol per cubic centimeter (e.g., sodium dodecyl sulfate is 0.004 mol/cm^3; Table 2);
(3) Then, we multiplied density (mol/cm^3) by the percentage of S contributed by the compound, to get mol of sulfur per cubic centimeter of the compound (e.g., sodium dodecyl sulfate has 0.0004 mol S/cm^3; Table 2A);
(4) Then, based on the moles of compound we added to the mixture, we took the ratio of the compound to the total moles of S contributed by the mixture to obtain the percentage of S contributed from each compound (e.g., Mixture 1 has 14% sodium dodecyl sulfate; Table 2A).

1.1 Results for test mixtures

Four mixtures were measured. Calculation and LCF results for mixture 1 (sodium dodecyl sulfate, methionine sulfoxide, and cystine) are found in Table 2A and Figure 1A. Based on the calculations, mixture 1 should be 1.2% sodium dodecyl sulfate, 47% methionine sulfoxide, and 38.8% cystine. Based on LCF results, the compound is 85.5% sodium dodecyl sulfate, 39.7% methionine sulfoxide, and 8.3% cystine (Table 1A).

Calculation and LCF results for mixture 2 (cysteine and methionine) are found in table 3 and figure 12. Based on the calculations, mixture 2 should be 1.2% sodium dodecyl sulfate, 47% methionine sulfoxide, and 38.8% cystine. Based on LCF results, the compound is 85.5% sodium dodecyl sulfate, 39.7% methionine sulfoxide, and 8.3% cystine (Table 1A).

Calculation and LCF results for mixture 3 (cystine, cysteine and 2-thiophenecarboxylic acid) are found in table 4 and figure 12. Based on the calculation, the mixtures should be 8.5% cystine, 57.5% cysteine, and 34% 2-thiophenecarboxylic acid. Based on LCF results, the compound is 120% cysteine (Table 1A).

Calculation and LCF results for mixture 4 (cystine, cysteine, 2-thiophenecarboxylic acid, and sodium dodecyl sulfate) are found in table 5 and figure 12. Based on the calculation, the mixtures should be 10% cystine, 68% cysteine, 18% 2-thiophenecarboxylic acid, and 4% sodium dodecyl sulfate. Based on LCF results, the compound is 18.7% cysteine, 28.9% 2-thiophenecarboxylic acid, and 90.7% sodium dodecyl sulfate (Table 1A).

1.2 Conclusion for test mixtures

The calculated and LCF fit results for all four mixtures were inconclusive. We hypothesize the experiments were inclusive due to a lack of proper density values for methione and 2-thiophenecarboxylic acid. For future experiments, the density of each of these compounds would need to be determined in order to compare the datasets.

2. USING SULFUR 1S XANES TO MEASURE OXIDATION INDEX FOR POLYSULFIDES

In CHAPTER 3, S 1s XANES were used to determine the oxidation index of S compounds. Kunzl (1932) was one of the first to suggest a linear relationship between an element's X-ray absorption K-edge absorption (white line) and valence based on X-ray absorption experimental data. Kunzl used Moseley plots to compare the K-absorption edges of oxides. Moseley plots were developed to show that the frequency of the strongest characteristic line emitted by an element increases systematically as its atomic number Z increases. The frequency of a spectral line is given by:

$$\nu = R_\infty c(M/+m) Z^2 (1/n^2_f - 1/n^2_i),$$

where R is the Rydberg constant for an atom of infinite mass. One Rydberg unit of energy, expressed in terms of electron volts, is 13.605 eV ($109757 \cdot 1\ cm^{-1}$), and n_i and n_f are the principal quantum numbers of the initial and final states of the atom involved in the transition. M is electron mass, M is nucleus mass.

Guided by Bohr's theory, Moseley plotted $(\nu / R)^{1/2}$ of the measured K line against Z. He obtained a straight line that could be expressed as:

$$(\nu / R) K_\alpha^{1/2} = 0.874 (Z - 1.13)$$ (Moseley law)

Kunzl used Moseley plots to state that energy levels of elements, bound to oxygen, with atomic numbers 10 to 28 are independent of the atomic number, and depend only on valency. Kunzl's rule is valid for monoatomic species where the charges in atomic charge density, represented by edge shifts, can be equated unambiguously to formal oxidation state (Kunzl, 1932; Bart, 1986; Mande and Sarpe, 1982). Atoms in polyatomic ions and in molecules that are not fully ionic cause deviations from the Kunzl's rule because of factors such as covalent bonding.

Vairavamurthy used Kunzl's rule to assign new oxidation states for thiosulfate (Vairavamurthy et al. 1993) and a sulfoxylate ion (Vairavamurthy et al. 1995). In both studies, a plot for white-line maximum (in electron volts) versus formal oxidation state

for a series of inorganic sulfur compounds (having no ambiguity regarding assignment of the sulfur oxidation state by the traditional method) was used to show a very good linear correlation between peak energy and sulfur speciation. Because XANES-based values differ considerably from conventionally determined oxidation states for most sulfur compounds, Vairavamurthy uses the new term 'oxidation index' to describe them.

2.1. Vairamurthy approach for determining oxidation indices

We used the Vairavamurthy approach, based on Kunzl's rule, to determine sulfur oxidation index for potassium tetrathionate ($S_4O_6^{2-}$) using S 1s XANES spectroscopy (Figure 2A). The linear regression line in Figure 3.3 was used to calculate the average oxidation index values for the S functionalities found within the potassium tetrathionate compound.

Based on S 1s XANES, we see peaks at 2473, 2478.4, and 2481.9eV (Figure 3.2). These correlate with oxidation index values of -0.1 and +3.3 and +5.4 for the first, second, and third peaks (Figures 2A-3Aa). However, tetrathionate should only have 2 S environments, and should only have 2 S 1s K-edge peaks, and therefore only 2 oxidation indices at +0.5 and -1.6 (see figure 3Ab). We hypothesize that the third peak can be attributed to impurities in the tetrathionate powder. The powder likely has both penta- and tetrathionate. The 5 S environments (see figure 3Ab) in pentathionate would provide 3 S 1s K-edge signals. To test this hypothesis, we need to perform X-ray Diffraction of the tetrathionate powder that was used for this experiment.

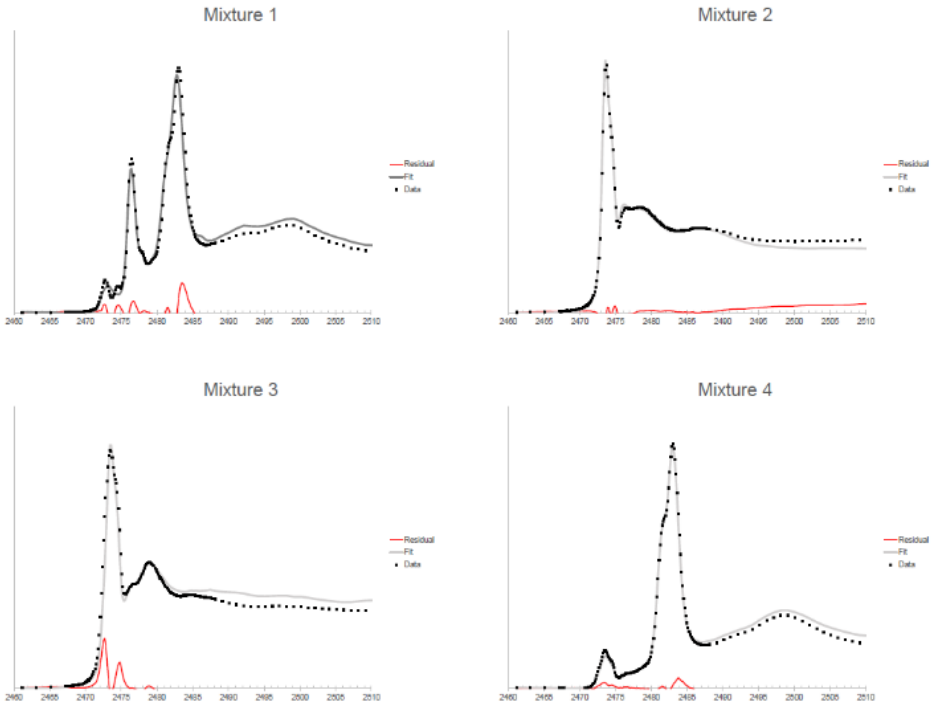

Figure 1A: Sulfur 1s XANES spectra for mixtures 1-4 plotted with fits in tables 2-5.

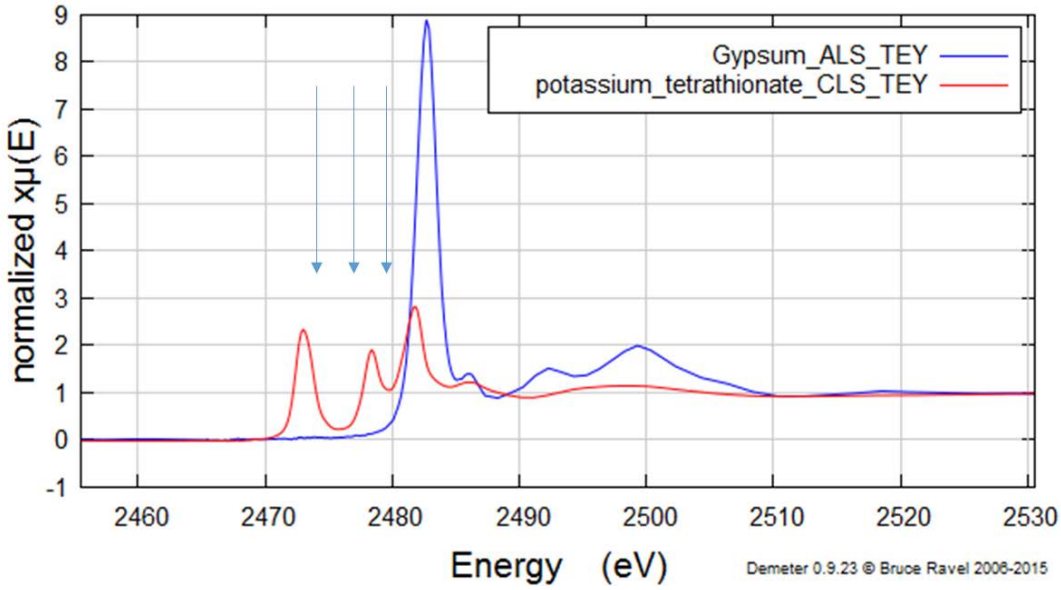

Figure 2A: Sulfur 1s XANES spectrum for potassium tetrathionate plotted with our reference spectra for sulfate (gypsum). The arrows designate peaks at 2473, 2478.4, and 2481.9eV.

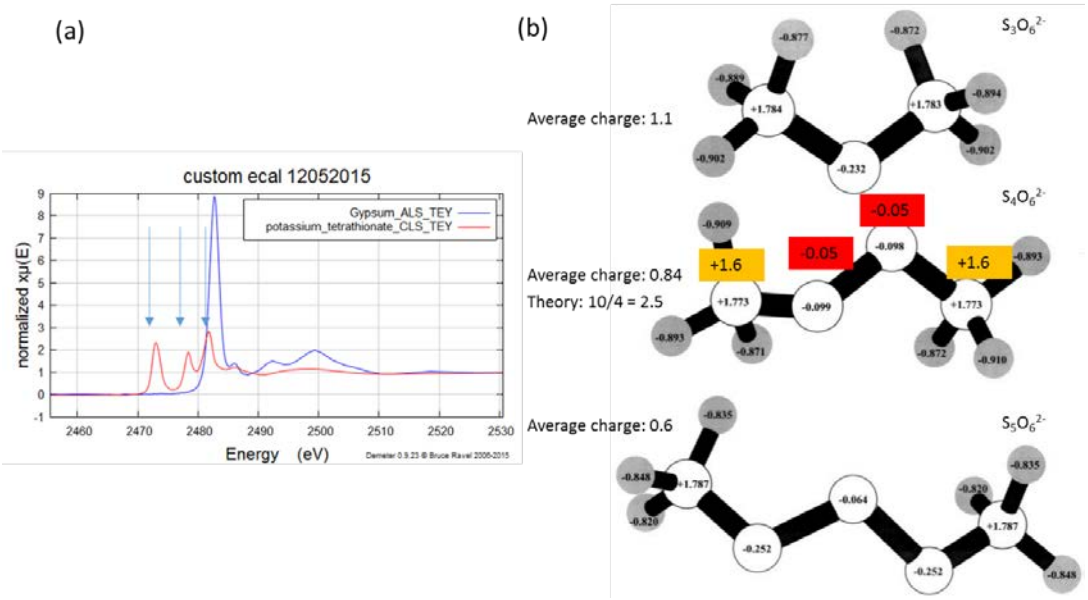

Figure 3A: Sulfur 1s XANES spectra shown with arrows (a) at 2473, 2478.4, and 2481.9eV. These correlate with oxidation index values of -0.1 and +3.3 and +5.4 for the first, second, and third peaks. Arrows indicate oxidation index values assigned for the three peaks observed (-0.1, +3.3, and +5.5, respectively). The third peak could be oxidation of the compound, or the spectra is also including some S3O62- impurities in the sample; (b) models for S3O62-,S4O62- and ,S5O62-. The average charge on each molecule is +1.1, +2.5, and +0.6, respectively. We've labeled the oxidation index values we calculated and where we predict the charges will reside.

Table 1A: Calculations for mixture 1 (sodium dodecyl sulfate, methionine sulfoxide, and cystine). We calculated the percentage of sulfur, by weight, each compound contributes by dividing the molecular weight of S (32g/mol) by the molecular weight of the compound. We converted the density to mol per cubic centimeter. Then, we multiplied density by the percentage of S contributed by the compound, to get mol of sulfur per cubic centimeter of the compound. Then, based on the moles of compound we added to the mixture, we took the ratio of the compound to the total moles of S contributed by the mixture to obtain the percentage of S contributed from each compound. Based on the calculation, the mixtures should be 1.2% sodium dodecyl sulfate, 47% methionine sulfoxide, and 38.8% cystine. Based on LCF results, the compound is 85.5% sodium dodecyl sulfate, 39.7% methionine sulfoxide, and 8.3% cystine.

Compound	**MW**	**D (g/ cm^3)**	**D (mol/ cm^3)**	**%S**	**molS/ cm^3**	**Mixture 1 (mol)**	**P mixture 1**	**%mol S/ cm^3**	**LCF**
Sodium dodecyl sulfate	288.38	1.01	0.004	11	0.0004	0.000060	0.31	14.24	85.5
Methionine sulfoxide	165.21	1*	0.006	19	0.0012	0.000066	0.33	47	39.7
Cystine	240.29	1.68	0.007	13	0.0009	0.000069	0.35	38.8	8.3

Table 2A: Calculations for mixture 2 (cysteine and methionine). We calculated the percentage of sulfur, by weight, each compound contributes by dividing the molecular weight of S (32g/mol) by the molecular weight of the compound. We converted the density to mol per cubic centimeter. Then, we multiplied density (mol/cm^3) by the percentage of S contributed by the compound, to get mol of sulfur per cubic centimeter of the compound. Then, based on the moles of compound we added to the mixture, we took the ratio of the compound to the total moles of S contributed by the mixture to obtain the percentage of S contributed from each compound. Based on the calculation, the mixtures should be 86.6% cysteine and 13.4% methionine. Based on LCF results, the compound is 37.2% cysteine and 65.4% methionine.

Compound	**MW**	**D (g/cm^3)**	**D mol/ cm^3**	**%S**	**molS/ cm^3**	**Mixture 2 (mol)**	**P mixture 1**	**%molS / cm^3**	**LCF**
Cysteine	121.16	1.5	0.012	26	0.003	0.0006	0.79	86.6	37.2
Methionine	149.21	1.34	0.009	21	0.002	0.0002	0.21	13.4	65.4

Table 3A: Calculations for mixture 3 (cystine, cysteine and 2-thiophenecarboxylic acid). We calculated the percentage of sulfur, by weight, each compound contributes by dividing the molecular weight of S (32g/mol) by the molecular weight of the compound. We converted the density of each compound to mol per cubic centimeter. Then, we multiplied density (mol/cm^3) by the percentage of S contributed by the compound, to get mol of sulfur per cubic centimeter of the compound. Then, based on the moles of compound we added to the mixture, we took the ratio of the compound to the total moles of S contributed by the mixture to obtain the percentage of S contributed from each compound. Based on the calculation, the mixtures should be 8.5% cystine, 57.5% cysteine, and 34% 2-thiophenecarboxylic acid. Based on LCF results, the compound is 120% cysteine.

Compound	**MW**	**D (g/cm^3)**	**D mol/ cm^3**	**%S**	**molS/ cm^3**	**Mixture 2 (mol)**	**P mixture 1**	**%molS/ cm^3**	**LCF**
Cystine	240.29	1.68	0.007	13	0.0009	0.00009	0.13	8.5	-
Cysteine	121.16	1.5	0.012	26	0.003	0.00008	0.26	57.5	120
2-thiophenecarboxylic acid	128.15	1*	0.008	25	0.002	0.0002	0.25	34	-

Table 4A: Calculations for mixture 4 (cystine, cysteine, 2-thiophenecarboxylic acid, and sodium dodecyl sulfate). We calculated the percentage of sulfur, by weight, each compound contributes by dividing the molecular weight of S (32g/mol) by the molecular weight of the compound. We converted the density of each compound to mol per cubic centimeter. Then, we multiplied density (mol/cm^3) by the percentage of S contributed by the compound, to get mol of sulfur per cubic centimeter of the compound. Then, based on the moles of compound we added to the mixture, we took the ratio of the compound to the total moles of S contributed by the mixture to obtain the percentage of S contributed from each compound. Based on the calculation, the mixtures should be 10% cystine, 68% cysteine, 18% 2-thiophenecarboxylic acid, and 4% sodium dodecyl sulfate. Based on LCF results, the compound is 18.7% cysteine, 28.9% 2-thiophenecarboxylic acid, and 90.7% sodium dodecyl sulfate.

Compound	**MW**	**D (g/cm^3)**	**D mol/ cm^3**	**%S**	**molS/ cm^3**	**Mixture 2 (mol)**	**P mixture 1**	**%molS/ cm^3**	**LCF**
Cystine	240.29	1.68	0.007	13	0.0009	0.00009	0.17	10	-
Cysteine	121.16	1.5	0.012	26	0.003	0.0002	0.33	68	18.7
2-thiophenecarboxylic acid	128.15	1*	0.008	25	0.002	0.0002	0.36	18	28.9
Sodium dodecyl sulfate	288.38	1.01	0.004	11	0.0004	0.00007	0.14	4	90.7

CHAPTER 4

Iron 1s X-ray absorption near edge structure (XANES) spectroscopy of the particles within the buoyant plumes at Von Damm and Beebe Vents

1. SYNOPSIS

Here we investigate the iron (Fe) in Fe-bearing minerals from particles collected within the rising plume of the Von Damm hydrothermal mound and Beebe Vents site, Mid-Cayman Rise, Caribbean Sea. By describing the phases of Fe minerals in the buoyant plumes at the submicron scale, this research aimed describe the Fe particle chemistry of two chemical diverse vents. Beebe Vents plume fluids emerge at 398 ^{o}C, enriched in dFe (6700 mmol/L) and H_2S (12 ± 2mmol/L). Von Damm Fluids are cooler (226 ^{o}C), Fe depleted (dFe =5.7-450 µmol/L) and H_2S rich (3.24 mmol/L). Hydrothermal plume particles from four elevations above the Von Damm vent (VD-1, 8m, 37m, 812m above the vent) as well as two elevations above the Beebe Vents site (0.5m and 50m) were analyzed. The study successfully measured the particle size (<3 µm to 100 µm) and composition of Fe-rich particulates within the Von Damm and Beebe Vents. We investigated pFe collected on 0.2µm filters. The Fe speciation was assessed using: (1) microprobe Fe 1s X-ray absorption near edge structure (XANES) spectroscopy, and (2) XRF Fe chemical mapping. X-ray Fluorescence maps were also used to describe the distribution of As, V, Ni, Cu, Fe, Ni, Zn, Mn, Cl, Ti, Ca, S, and Si within particles filtered in situ, as well as characterize particle size and distribution. Chemical mapping and Fe XANES reveal similar trends in Fe-bearing mineral phases. The trends suggest the diversity of Fe-bearing minerals are formed from chemical processes within the plume and are pulled in from physical entrainment processes. The plume particles primarily consist of sulfides and Fe oxyhydroxides. There were also low concentrations of Fe (II) oxides, silicates, and Fe (III) phyllosilicates. The presence of silicates could be evidence for either allochtonous or autochonous silicate-forming processes in the rising plume.

1. INTRODUCTION

Iron is the 4th most abundant element on earth and it is an important element for biological and geochemical processes. Examining the Fe budget of the world's oceans became a major scientific endeavor over 30 years ago (Holland, 1984). Sources of Fe to the ocean (e.g., rivers, groundwater, and diagenetic fluids) have been measured and investigated (Gordon et al., 1982).

The impact that hydrothermal plumes could have on the whole ocean biogeochemical budget has been an active source of research since the discovery of hydrothermal vents in the 1970's (Dasch et al., 1971; Edmond et al., 1979; Mottl et al., 1983; Kadko et al., 1993, 1986/1987; Kadko et al., 1994; German et al., 1991; German and Seyfried, 2014, and references therein).

To understand how plumes might be a source of Fe to the deep ocean, first the source and evolution of plumes needed to be understood. With only a few samples from the Galapagos, Edmond and colleagues (1979) developed the first research study where hydrothermal fluids as a significant source of Fe to the deep ocean was presented. To properly test the dynamic processes within plumes, Lupton and others (1998) deployed a neutrally buoyant plume drifter that monitored a plume. From Lupton and others (1998), researchers began to postulate how hydrothermal plumes rise >100m, over timescales of 1 hour and the composition of fluids is diluted by seawater by ~10,000:1 as the fluids reach neutrally buoyant height.

The fate of Fe in a hydrothermal plume begins with the 2 stage process of building sulfide chimneys at the ocean floor. Stage 1 growth is the precipitation of porous anhydrite walls and fine inclusions of sulfide minerals grow at the seafloor (Tivey, 2007; Yücel et al., 2011; Breier et al., 2014; German and Seyfried, 2014, and references therein). In stage II, the precipitation of anhydrite and Cu-Fe bearing sulfide minerals occurs. The fluids produce sulfide minerals (pyrite (FeS_2), chalcopyrite ($FeCuS_2$), troilite

(FeS)) because Fe, S, and Cu react within the vent conduit and at the vent orifice (Tivey, 2007; Ono et al., 2007; Yücel, et al., 2011; Syverson et al., 2013; Mcdermott et al., 2015). Once fluids have exited the chimney, and Fe(II) reaches oxygenated seawater, it is oxidized to Fe(III) in first few meters (~3.3 hours) (Field and Sherrel, 2000). Rapid cooling and dilution as well as an increase in pH and oxygen concentration leads to the precipitation of Fe oxyhydroxides (Mottl and McConachy, 1990). The rate of dissolved Fe(II) oxidation in hydrothermal plumes is influenced by the redox conditions prevailing within the local ambient water column. (Field and Sherrell, 2000; Millero, 2001).

The expectation for the precipitation of Fe-bearing minerals at fluids emitting from Von Damm differs from Beebe Vents. Both are located in oxygen-rich (200µmol/kg) seawater, both are H2S rich. However, Von Damm is Fe depleted (pFe = 0.32- 0.03 µmol/kg) and Beebe Vents is Fe-rich (pFe =5.38- 0.73 µmol/kg). Von Damm should contain less Fe-rich particles and Beebe Vents more Fe-rich particles.

Presently, there is growing evidence for the far field export of hydrothermally sourced Fe to the deep ocean (Bennet et al., 2008; Toner et al., 2009; Yucel et al., 2011; Carazzo et al., 2013; Saito et al, 2013; Fitzsimmons et al., 2014; Rouxel et al., 2016). For Fe to be transported from hydrothermal plumes, Fe first needs to be stabilized. Currently, three key processes known to preserve and transport Fe away from buoyant plumes: (1) organic C complexation and the formation of Fe complexes and Fe colloids with dissolved and Particulate Organic Carbon (POC) (Bennett et al., 2008; Toner et al., 2009); (2) production of nanoparticulate pyrite (Yucel et al., 2011; Gartman et al., 2014); (3) and metal uptake by microbial communities (Li et al., 2014) (Rouxel et al., 2016). The size distribution of Fe (soluble < colloidal < particulate) is also important because dFe fractions can have an impact on the bioavailable and residence time of Fe (Fitzsimmons and Boyle, 2000).

The Fe XANES techniques used in this chapter have proven useful for the characterization of Fe speciation for particulate Fe samples collected from the ocean and

deep-sea hydrothermal vents (Lam et al., 2006; Toner et al., 2009; Breier et al., 2012; Li et al., 2014, 2015). For this study, we have investigated particulate Fe collected on 0.2µm filters. Using Fe 1s XANES and chemical mapping, this research aimed to understand the processes that control the Fe chemistry of the Von Damm and Beebe Vents by describing the variety of Fe minerals in the buoyant plumes at the submicron scale.

3. METHODS

Site descriptions are in CHAPTER 1, SECTION 2. Description of **sample collection** and **anaerobic sample preparation** is in CHAPTER 2, SECTION 3.

3.1 Iron micro-probe X-ray absorption spectroscopy

The speciation of Fe in plume particles was measured by synchrotron radiation Fe 1s XANES at the X-ray microprobe beamline 10.3.2, Advanced Light Source, Lawrence Berkeley National Laboratory, Berkeley, CA, USA (Marcus et al., 2004) and the X-ray microprobe beamline 13-ID-E at GeoSoilEnviroCARS, Advanced Photon Source, Argonne National Laboratory, Argonne, IL, USA (Newville, 1999).

At both X-ray microprobes, the sample was raster-scanned through a micro-focused X-ray beam of monochromatic light to produce elemental maps using X-ray fluorescence (XRF). At 10.3.2, fluorescence was detected using seven-element Ge solid-state or silicon drift diode fluorescence detectors (the Vortex detector in May 2012, the Amptek in January 2013, and the Canberra in November 2013). At 13-ID-E, fluorescence was detected using a silicon drift Vortex fluorescence detector (April 2014).

At both instruments, using composite XRF map as a guide, XANES spectra were collected at particular locations within the mapped area, i.e. point observation (Toner et al., 2014). All sample spectra were pre-edge subtracted and post-edge normalized to the edge jump value of 1 using the software *ATHENA* (Ravel and Newville, 2005). The

XANES spectra were fit with linear combination fitting (LCF) of reference spectra to define the range of Fe (Table 4.1) species present. Normalized spectra were fitted with linear combinations of reference spectra using a custom 10.3.2 Labview-based freeware program (Marcus et al. 2004). The fit quality was evaluated with the normalized sum-of-squares (NSS) parameter, and the addition of a new component was justified when NSS decreased by at least 10%.

Fit results for Fe 1s XANES are interpreted and reported as broad categories of Fe-bearing minerals. Reference materials include sulfides, silicates, an Fe(II) oxide, and Fe(III) oxyhydroxides (Table 4.1). This approach is taken because Fe 1s XANES are diagnostic for some minerals, such as pyrite (FeS_2), but not all minerals. For example, Fe 1s XANES for ferrihydrite ($Fe^{3+}{}_5HO_8 \cdot 4H_2O$) is poorly distinguished from goethite (α-FeOOH). The results of the LCF are reported in mol% of Fe.

To measure species abundance, a "speciation mapping" method was developed for the Mid-Cayman Rise samples (Toner et al. 2014). The goal was to query large numbers of points within the sample to enable representative and quantitative sampling. The point Fe XANES observations were used to identify incident energies, spanning both the Fe 1s absorption edges, at which the Fe species present had measurable differences in absorption. The ability to distinguish among Fe species was estimated by an error calculation that accounted for: 1) total Fe fluorescence counts; 2) the dwell time per pixel; and 3) the incident energies chosen using custom beamline software. The composite XRF dataset was fit by LCF with reference spectra along with a background spectrum from a sample blank (XRF tape and Mylar X-ray film) using custom beamline 10.3.2 software. A speciation mapping approach was developed from the method of Toner et al. 2012. The XRF maps were collected at eight incident energies [7110 (pre-edge), 7113.3, 7120.9, 7125, 7127.5, 7129.2, 7132.5, and 7350 (post-edge eV)] to create a composite dataset with an Fe 1s absorption profile at each of the ~ 100,000 pixels queried. Speciation maps were fit using a linear combination approach with reference spectra chosen from the point XANES survey of the sample using published approaches

developed for hydrothermal materials (Toner et al., 2012; Breier et al., 2012). The chemical maps were fit with up to 7 reference spectra at a time and the final fits were those that produced a normalized mean-square error closest to 0.

4. RESULTS

4.1 Iron-bearing mineral phases present in particles from the Von Damm plume and their abundance captured by Fe 1s XANES

Iron 1s XANES spectra were collected for the following elevations within the Von Damm buoyant plume at 1m, 8m, 37m, and 812m (sample names and details are located in Table 2.1). The spectra were fit with reference spectra from reference materials (Table 4.1). The Fe spectra for the each of the four elevations are displayed with the reference spectra that best fit the data (Fig.4.1-4.4; Tables S4.1-4.4). The results of the LCF are reported in mol% Fe on a per atom basis (mol% Fe-bearing minerals in particles collected on filter) in Table 4.2 and Figure 4.5.

Based on ICP-MS of the particles, the pFe concentration decreases within the buoyant plume as a function of elevation (Table 2.1; Figure 4.5). Based on the Fe XANES fits, Fe-bearing plume particles consist primarily of sulfides (pyrite and cubanite), silicates (almandine, hornblende, lizardite, richteriate, roedderite, and chlorite), and Fe oxyhydroxides (Figures 4.1-4.4; Table 4.2; Table.S4.1-4.4).

Silicates were significant portion of the Fe-bearing minerals in each of the samples (13-37mol%). Iron(II)-bearing phase (Mauna basalt glass, hercynite, and $FeSO_4$) and an Fe(III) pyllosilicate (STX clay) were also detected within the plume (Figure 4.5 and Table 4.2). The Fe(III) pyllosilicate (STX clay) was the second most abundant phase in the 37m (28mol%) and the third most abundant phase in the APB sample (13mol%) (Figure 4.5 and Table 4.2). The Fe(II)-bearing phases are less abundant than all other phases in the samples (<7mol%) (Figure 4.5 and Table 4.2).

According to XANES results, sulfides (pyrite and cubanite) were present in all the samples, excluding the APB (Figure 4.1-4.5 and Table 4.2). The concentrations were highest in the near vent sample (41mol% Fe sulfide in particles collected on filter in the 1m sample, based on 9 point observations) and decreased with plume height (11mol% in the 37m sample, based on 17 point observations) (Figure 4.5; Table 4.2; Table.S4.1 and 4.3).

The XANES data reveal that the APB (812m above the vent orifice) particles contain Fe-bearing minerals that contain Fe(0) (Fe foil and Metglass) in spot 1 (Figure 4.4 and 4.9). These data were neglected because it is unlikely that Fe(0) is in the plume (personal communication Chip Breier). The data were removed from the final XANES results (Table 4.2; Figure 4.5).

4.2 Ground truth for XANES using chemical mapping of particles from the Von Damm plume

4.2.1 Presence-absence of Fe-bearing mineral phases using both techniques

The chemical mapping results ground truth the Fe XANES for presence-absence of minerals at each elevation. For example, Fe(III) phyllosilicates are present in all the samples using both techniques. Specifically, if we look at the VD-1 sample, XANES reveal that at spots 1 and 3 the particles contain Fe(III) phyllosilicates (Table.S 4.1, Figure 4.6) and chemical mapping also reveals the presence of Fe(III) phyllosilicates (Figure 4.6) in spots 0, 1, 3 (Figures 4.1 and 4.6; Table.S 4.1).

Both the Fe chemical maps and XANES reveal sulfides are present in all samples, excluding the APB. For the 8m sample, based upon both the XANES and chemical map, particles contain sulfides in spots 5 and 6 (Fig.S 4.2). For the 1m and 37m samples, chemical maps did not verify sulfides in the same spots as the XANES point

observations. For example, in the 1m sample particles in spot 2 contain sulfides (Table.S4.1), and per the chemical map for the 1m sample (Figure 4.6), sulfides are present in other particles, but not at spot 2. Sulfides were also not verified in spots 0-4 in the 37 sample (Figure 4.8). Sulfides were present in other particles on the filter for the 8m sample (Figure 4.8). Based on both XANES and chemical mapping, there were no sulfides or Fe(II)-bearing phase (Figure 4.10; Table 4.3) in the APB sample. (see section 4.2 for a more detailed comparison of all samples).

4.2.2 Variation in the concentration of Fe-bearing mineral phases using XANES and chemical mapping

The concentration of Fe-bearing minerals varies between the two techniques but the trends captured remain similar. Specifically, per chemical mapping, the mol% of sulfide varies between the two techniques, but the trend of increasing sulfides in the plume remains similar (Figures 4.5 and 4.10 and Table 4.2-4.3). Sulfide is lower in the 1m sample (28 mol%), compared to XANES (41 mol%). In the 8m sample, sulfide is only 9 mol% in the 8m sample compared to 15 mol% with XANES (Figure 4.5 and 4.10; Tables 4.2-4.3). Chemical maps also reveal sulfide material increases again in the 37m sample and the value is twice (22 mol%) as high as the results from 11 point observations made with XANES (Figure 4.5 and 4.10; Tables 4.2-4.3). Also see section 4.2 for detailed comparison of all samples.

4.3 Detailed comparison of XANES and chemical mapping

4.3.1 Comparison of XANES and chemical mapping for VD-1 (SUPR05- 1m)

Nine point observations were made with Fe 1s XANES for the 1m sample. Approximately 160,000 pixels were queried using Fe chemical mapping (Figure 4.6). The Fe 1s XANES spots 0-4 were analyzed at the same beamtime that the Fe chemical map was collected (Figure 4.6). Spot 4-8 were collected at a previous beamtime (see

Fig.S3.1). All XANES observations were used to help determine which Fe reference spectra should be used to fit the Fe chemical map. Based on the XANES data, the Fe-bearing mineral phases in decreasing abundance include sulfides, silicates, Fe(III)oxyhydroxides, Fe(III) phyllosilicates, and Fe(II) oxides + salts + glasses. Based on the chemical map, the Fe-bearing phases in decreasing abundance include Fe(III)phyllosilicate, Fe(III)oxyhydroxides, sulfides, silicates, and Fe(II) oxides + salts + glasses.

Sulfides: The XANES revealed that sulfides were highest (42 mol%) (pyrite and cubanite) in the 1m sample (Table 4.2; Table.S 4.1; Figures 4.1 and 4.5). The Fe chemical mapping did not verify the presence of sulfides at spot 2, where XANES identified the presence of pyrite (Figure 4.6; Table. S4.1). Although, other particles that were not analyzed via Fe 1s XANES did contain sulfides (pyrite and cubanite), and account for 28 mol% of the Fe-bearing particles on the filter. The concentration is less than the concentration based on the XANES data (42 mol%) (Table 4.3; Figure 4.10).

Silicates: Silicates were also abundant (28 mol%) (almandine, hornblende, lizardite, richterite, roedderite, and chlorite) (Table 4.2; Table.S 4.1; Figures 4.1 and 4.5). For chemical mapping, almandine and chlorite were used to fit maps for silicates, and silicates were verified at spots where XANES also identified silicate minerals (spots 0, 1, 2,3, and 4) (Figure 4.6; Table.S 4.1). For the chemical mapping results, silicates account for 34 mol% of the Fe-bearing particles on the filter. The concentration is more than the concentration based on the XANES data (8 mol%) (Table 4.3; Figure 4.10).

Fe(III)oxyhydroxide: The XANES reveal Fe(III) oxyhydroxides were also abundant (22 mol% and include ferrihydrite, akageneite, lepidocrocite, and goethite) (Table 4.2; Figures 4.1 and 4.5). The Fe chemical mapping verified the presence of Fe(III) oxyhydroxides in spots 0 and 1 (Figure 4.6; Table.S 4.1). The Fe(III)oxyhydroxides account for 28 mol% of the Fe-bearing particles on the filter. The concentration is more than the concentration based on the XANES data (22 mol%) (Table 4.3; Figure 4.10).

Fe(III)phyllosilicate: The XANES reveal an Fe (III)phyllosilicate (STX clay) was also abundant (8 mol%) (Table 4.2; Figures 4.1 and 4.5). The Fe chemical mapping verified the presence of the same Fe(III)phyllosilicate in spots 1 and 3 (Figure 4.6; Table.S 4.1). The Fe (III) phyllosilicate accounts for 34mol% of the Fe-bearing particles on the filter. The concentration is more than the concentration based on the XANES data (8 mol%) (Table 4.3; Figure 4.10).

Fe(II) oxides + salts + glasses: The XANES reveal Fe (II) oxides + salts + glasses (Mauna Loa basalt glass) were present (1 mol%) (Table 4.2; Figures 4.1 and 4.5). The Fe chemical mapping did verify the presence of Fe(II) oxides + salts + glasses at spot 2, where XANES did not identify the presence of Fe(II) oxides + salts + glasses (Figure 4.6; Table. S4.1). The Fe(II) oxides + salts + glasses account for 3mol% of the Fe-bearing particles on the filter. The concentration is more than the concentration based on the XANES data (1 mol%) (Table 4.3; Figure 4.10).

4.3.2 Comparison of XANES and chemical mapping for SUPR11- 8m

Twelve point observations were made with Fe 1s XANES for the 8m sample (Table.S4.2). Approximately 200,000 pixels were queried using Fe chemical mapping (Figure 4.7). The Fe 1s XANES spots 0-7 were analyzed at the same beamtime that the Fe chemical map was collected (Figure 4.7). Spot 8-11 were collected at a previous beamtime (see Fig.S3.7). All XANES observations were used to help determine which Fe reference spectra should be used to fit the Fe chemical map. Based on the XANES data, the Fe-bearing mineral phases in decreasing abundance include Fe(III) oxyhydroxides, silicates, sulfides, Fe (III) phyllosilicates, and Fe(II) oxides + salts + glasses. Based on the chemical map, the Fe-bearing phases in decreasing abundance include silicates, Fe (III)phyllosilicate, Fe (III)oxyhydroxides, sulfides, and do not contain Fe (II) oxides + salts + glasses.

Sulfides: The XANES revealed that sulfides were the third most abundant phase (15mol%) (pyrite and cubanite) in the 1m sample (Table 4.2; Table.S 4.2; Figures 4.2 and 4.7). The Fe XANES identified sulfides in spots 0, 1, 5, 6, and 7 (Table.S 4.2; Figures 4.2 and 4.7). The chemical mapping verified the presence of sulfides at spot 5 and 6 (Figure 4.7; Table. S4.2). The concentration of sulfides identified using chemical mapping (9 mol%) is less than the concentration based on the XANES data (15 mol%) (Table 4.3; Figures 4.5, 4.7, and 4.10).

Silicates: Silicates were the most abundant Fe-bearing mineral phase (51 mol%) (including hornblende, richterite, and chlorite) (Table 4.2; Table.S 4.2; Figures 4.2 and 4.5). For chemical mapping hornblende, richterite, and chlorite were used to fit maps for silicates, and silicates were verified at spots where XANES also identified silicate minerals (spots 0- 7) (Figure 4.7; Table.S 4.2). Silicates account for 51 mol% of the Fe-bearing particles on the filter. The concentration is more than the concentration based on the XANES data (26 mol%) (Table 4.3; Figure 4.10).

Fe(III)oxyhydroxide: The XANES reveal Fe(III) oxyhydroxides were the third most abundant Fe-bearing mineral phase (16mol%) (including akaganeite) (Table 4.2; Table.S 4.2; Figures 4.2 and 4.7). The Fe chemical mapping verified the presence of Fe(III) oxyhydroxide (akageneite) in spot 0 (Figure 4.7; Table.S 4.2). The concentration of akageneite is less than the concentration based on the XANES data (43 mol%) (Table 4.3; Figure 4.10).

Fe (III)phyllosilicate: The XANES reveal an Fe (III)phyllosilicate (STX clay) in the particles on the filter (9 mol%) (Table 4.2; Table.S 4.2; Figures 4.2 and 4.7). The Fe chemical mapping verified the presence of the same Fe(III)phyllosilicate in spots 4 and 5 (Figure 4.7; Table.S 4.2). The Fe(III) phyllosilicate accounts for 23 mol% of the Fe-bearing particles on the filter. The concentration is more than the concentration based on the XANES data (9 mol%) (Table 4.3; Figure 4.10).

Fe (II) oxides + salts + glasses: The XANES reveal Fe(II) oxides + salts + glasses ($FeSO_4$) were present (7 mol%) (Table 4.2; Table.S 4.2; Figures 4.2 and 4.7). The Fe chemical mapping did not verify the presence of $FeSO_4$ at spot 2, where XANES identified the presence of $FeSO_4$ (Figure 4.6; Table. S4.2).

4.3.3 Comparison of XANES and chemical mapping for SUPR57- 37m

Seventeen point observations were made with Fe 1s XANES for the 37m sample (Table.S4.3). Approximately 60,000 pixels were queried using Fe chemical mapping (Figure 4.8). The Fe 1s XANES spots 0-10 were analyzed at the same beamtime that the Fe chemical map was collected (Figure 4.8). Spot 11-16 were collected at a previous beamtime (see Fig.S3.8). All XANES observations were used to help determine which Fe reference spectra should be used to fit the Fe chemical map. Based on the XANES data, the Fe-bearing mineral phases in decreasing abundance include Fe(III)oxyhydroxides, Fe(III) phyllosilicates, silicates, sulfides, and Fe (II) oxides + salts + glasses. Based on the chemical map, the Fe-bearing phases in decreasing abundance include silicates, Fe(III)phyllosilicate, sulfides, Fe (III) oxyhydroxides, and Fe (II) oxides + salts + glasses.

Sulfides: The XANES revealed that sulfides were in the particles on the filter (11 mol%) (pyrite, cubanite, pentlandite, and FeS) in the 1m sample (Table 4.2; Table.S 4.3; Figures 4.3 and 4.5). The Fe XANES identified sulfides in spots 11, 14-16 (Table.S 4.3; Fig.S3.12). The chemical mapping did not verify the presence of sulfides at spots 0-10 of the chemical map (Figure 4.8). The concentration of sulfides (using pyrite and cubanite) identified using chemical mapping (22 mol%) is more than the concentration based on the XANES data (11 mol%) (Table 4.3; Figure 4.10).

Silicates: Silicates were the third most abundant Fe-bearing mineral phase (13mol%) (including lizardite, hornblende, richterite, and chlorite) (Table 4.2; Table.S 4.3; Figures 4.3 and 4.5). For chemical mapping hornblende, richterite, and chlorite were used to fit maps for silicates, and silicates were verified at spots where XANES also identified

silicate minerals (spots 0, 1, 2, 5, and 8) (Figure 4.8; Table.S 4.3). Silicates account for 34mol% of the Fe-bearing particles on the filter. The concentration is more than the concentration based on the XANES data (13 mol%) (Table 4.3; Figure 4.10).

Fe (III) oxyhydroxide: The XANES reveal Fe(III) oxyhydroxides were the most abundant Fe-bearing mineral phase (44mol%) (including akageneite, ferrihydrite, and toner biogenic oxide) (Table 4.2; Table.S 4.3; Figures 4.3 and 4.5). The Fe chemical mapping verified the presence of Fe(III) oxyhydroxide (goethite) was 20mol% of the Fe-bearing minerals in the particles and verified the presence of goethite in spot 4 (Figure 4.8; Table.S 4.2). The concentration of goethite is less than the concentration based on the XANES data (44mol%) (Table 4.3; Figure 4.10).

Fe (III) phyllosilicate: The XANES reveal an Fe(III)phyllosilicate (STX clay) in the particles on the filter (28mol%) (Table 4.2; Table.S 4.3; Figures 4.3 and 4.5). The Fe chemical mapping verified the presence of the same Fe(III)phyllosilicate in spots 0, 2, 5-8, and 10 (Figure 4.8; Table.S 4.3). The Fe(III) phyllosilicate accounts for 23mol% of the Fe-bearing particles on the filter. The concentration is less than the concentration based on the XANES data (28 mol%) (Table 4.3; Figure 4.10).

Fe (II) oxides + salts + glasses: The XANES reveal Fe(II) oxides + salts + glasses (Hercynite) was present in spot 4 (4 mol%) (Table 4.2; Table.S 4.3; Figures 4.3, 4.5, and 4.8). The Fe chemical mapping did not verify the presence Hercynite in spot 4, where XANES identified the presence of Hercynite (Figure 4.8; Table. S4.3). However, the Hercynite accounts for 2 mol% of the Fe-bearing minerals within particles on the filter (Table 4.3; Figure 4.10).

4.3.4 Comparison of XANES and chemical mapping for SUPR58- 812m

Four point observations were made with Fe 1s XANES for the APB (812m above the vent orifice) sample (Table.S4.4). Approximately 160,000 pixels were queried using Fe

chemical mapping (Figure 4.9). The Fe 1s XANES spots 0-3 were analyzed at the same beamtime that the Fe chemical map was collected (Figure 4.9). Based on the XANES data, the Fe-bearing mineral phases in decreasing abundance include Fe (III) oxyhydroxides, silicates, Fe (III) phyllosilicates, with no sulfides, and no Fe (II) oxides + salts + glasses. Based on the chemical map, the Fe-bearing phases in decreasing abundance include silicates, Fe (III) oxyhydroxides, Fe (III) phyllosilicate, with no sulfides, and no Fe (II) oxides + salts + glasses.

Sulfides: The XANES and chemical map reveal that no sulfides were in the particles on the filter (Table 4.2; Table.S 4.4; Figures 4.4, 4.5, 4.9, and 4.10).

Silicates: The XANES data reveal silicates as the second most abundant Fe-bearing mineral phase (37 mol%) (including hornblende, richterite, biotite, and pigeonite) (Table 4.2; Table.S 4.4; Figures 4.4 and 4.5). For chemical mapping biotite, pigeonite, and richterite were used to fit maps for silicates, and silicates were verified at spots where XANES also identified silicate minerals (spots 0, 2, and 3) (Figure 4.9; Table.S 4.4). Silicates account for 46mol% of the Fe-bearing particles on the filter. The concentration is more than the concentration based on the XANES data (37 mol%) (Table 4.3; Figure 4.10).

Fe (III) oxyhydroxide: The XANES reveal Fe(III) oxyhydroxides were the most abundant Fe-bearing mineral phase (50 mol%) (including akageneite and a ferrihydrite/goethite mix) (Table 4.2; Table.S 4.4; Figures 4.4 and 4.5). The Fe chemical map was fit with goethite. The map verified the presence of Fe(III) oxyhydroxide (goethite) in spots 0 and 2 (Figure 4.9). The concentration of goethite is less (31 mol%) than the concentration based on the XANES data (50mol%) (Table 4.3; Figure 4.10).

Fe (III) phyllosilicate: The XANES reveal an Fe (III) phyllosilicate (STX clay) in the particles on the filter (13mol%) (Table 4.2; Table.S 4.4; Figures 4.4 and 4.5). The Fe chemical mapping verified the presence of the same Fe(III)phyllosilicate in spot 2 (Figure

4.9; Table.S 4.4). The Fe(III) phyllosilicate accounts for 23 mol% of the Fe-bearing particles on the filter. The concentration is more than the concentration based on the XANES data (13mol%) (Table 4.3; Figure 4.10).

Fe (II) oxides + salts + glasses: The XANES and chemical map reveal that no sulfides were in the particles on the filter (Table 4.2; Table.S 4.4; Figures 4.4, 4.5, 4.9, and 4.10).

4.4 Particle morphology, correlation of Fe and S 1s XANES, and elemental distribution of Von Damm

Based on XRF and Fe chemical mapping of particles, SUPR05-1m contains Fe mineral grains ranging in size from < 3 µm to 10µm in diameter (Figure 4.6; Fig.S3.1-3.2), while the SUPR11-8m has Fe mineral grains ranging from < 3 µm to 50 µm in diameter (Figure 4.7; Fig.S3.7-3.8). Based on XRF maps SUPR57-37 Fe-bearing grains are smaller than any other segment of the buoyant plume (< 3µm to 5µm; Figure 4.8; Fig.S3.11-3.12). Based on the Fe chemical mapping, the above plume background Fe-bearing particles (SUPR58-APB) range in size from <3 µm to 5 µm (Figure 4.9; Fig.S3.15).

4.4.1 Elemental distribution and correlation of Fe and S 1s XANES of particles in SUPR05-1m

The As, V, Ni, Cu, Fe, Ni, Zn, Mn, Cl, Ti, Ca, S, and Si distributions within the particles and aggregates were determined by XRF mapping (Fig.S3.1-3.2). Iron 1s XANES were collected for spots 0-4 at ALS beamline 10.3.2 using Fe chemical maps, without additional XRF mapping. Four spots (spots 5 - 8) were investigated with Fe 1s XANES and XRF mapping at ALS beamline 10.3.2 (Fig.S3.1-3.2).

The Fe 1s XANES for spot 5 correlate with S 1s XANES for spot 0 (Fig.S3.1-3.2). Spot 5 XRF maps show Fe, S, Si, Cl, Ni, As, Zn, Cu and Mn associated with what Fe and S 1s

XANES identified as sulfides (Table.S4.1; Fig.S3.1-3.2). Spot 5 S 1s XANES for spot 0 show greigite, inorganic sulfate, elemental S, and sodium polysulfide.

Fe XANES 1s spot 6 correlates with S 1s XANES spot 1(Fig.S3.1-3.2). Spot 6 shows Fe, Ni, and Cu associated with Fe sulfides. The S 1s XANES for spot 1 show chalcopyrite, inorganic sulfate, mackinawite, and nanoparticulate S. Spot 7 Fe 1s XANES show Fe associated with Fe oxyhydroxides and Fe silicates, and no S 1s XANES were collected for Fe 1s XANES spot 7.

4.4.2 Elemental distribution and correlation of Fe and S 1s XANES of particles in SUPR11-8m

Four spots (8-11) were investigated for Fe 1s XANES at ALS beamline 10.3.2 and As, V, Ni, Cu, Fe, Ni, Zn, Mn, Cl, Ti, Ca, S, and Si distributions within the particles and aggregates were determined by XRF mapping (Figure 4.7; Fig.S3.7-3.8; Table.S4.2). Fe 1s XANES were collected at Spots 0-7 when Fe chemical maps were collected, without additional XRF mapping. Sulfur 1s XANES spots 1, 2, and 4 correlate with Fe 1s XANES spots 9, 10, and 11 (Fig.S3.7-3.8). Sulfur 1s XANES spots 5-16 were investigated for S 1s XANES when S chemical maps were collected, without additional XRF mapping.

The Fe 1s XANES and XRF maps determined chlorite, hematite, and psuedobrookite were associated with Si, Ti, and Fe at spot 8. Spot 9 shows Fe, Ni, Zn, and Cu associated with cubanite and pyrite. Spot 10 shows akaganeite, augite, and richterite in association with Fe, Ti, and Si. Spot 11 shows chlorite, ferrihydrite and STX clay associated with Fe.

Both Fe and S 1s XANES revealed sulfides in particles for spot 1. S 1s XANES for spot 1 show chalcopyrite and inorganic sulfate associated with Fe, Ni, and Cu (Table.S4.2). The Fe 1s XANES for spot 1 reveal cubanite and pyrite (Table.S4.2).

The Fe and S 1s XANES do not reveal the same mineral phases for S 1s XANES spot 2. The particles in S 1s XANES for spot 2 (Fe 1s XANES spot 11) show chalcopyrite, inorganic sulfate, pyrite, and elemental S associated with Fe, Si, and Ti (Table.S4.2). The Fe 1s XANES reveal chlorite, ferrihydrite, and STX clay (Table.S4.2).

The Fe and S 1s XANES do not reveal the same mineral phases for S 1s XANES spot 4 (Fe 1s XANES spot 8). The S 1s XANES show inorganic sulfate associated with Fe. The Fe 1s XANES reveal chlorite, hematite, and psuedobrookite (Table.S4.2).

4.4.3 Elemental distribution and correlation of Fe and S 1s XANES of particles in SUPR57-37m

The As, V, Ni, Cu, Fe, Ni, Zn, Mn, Cl, Ti, Ca, S, and Si distributions within the particles and aggregates were determined by XRF mapping (Figures 4.8 and Fig.S3.12-3.13). Five spots (spots 11-15) were investigated for Fe 1s XANES and XRF mapping at ALS beamline 10.3.2. The Fe 1s XANES for spots 0-10 were collected at beamline 10.3.2 when Fe chemical maps were collected (Figure 4.8), without additional XRF mapping.

Spot 11 shows cubanite and pyrite associated with Fe, Ni, Zn, Mn, Ti, Ca, K, and Cu (Table.S4.3). Spot 12 shows chlorite, ferrihydrite, and Fe(III) phyllosilicate associated with Fe, Ca, K, and Cu (Table.S4.3). Spot 13 shows chlorite, richterite, and Fe(III) phyllosilicate associated with Fe (Table.S4.3). Spot 14 shows ferrihydrite and pyrite associated with Fe and Ca. Spot 15 shows Fe sulfide, Fe(III) phyllosilicate, and biogenic oxide associated with Ca and K. One spot (spot 16) was investigated for Fe 1s XANES and XRF mapping at beamline APS 13-ID-E (Table.S4.3). Spot 16 shows pentlandite and an Fe(III) phyllosilicate associated with Fe and Si (Table.S4.3; Fig.S3.15).

4.4.4 Elemental distribution and correlation of Fe and S 1s XANES of particles in SUPR58-APB (812m above the vent orifice)

The As, V, Ni, Cu, Fe, Ni, Zn, Mn, Cl, Ti, Ca, S, and Si distributions within the particles and aggregates were not analyzed by XRF mapping for the APB (812m above the vent orifice) sample.

4.5 Iron-bearing mineral phases present in particles from the Beebe Vents plume and their abundance captured by Fe 1s XANES

Iron 1s XANES spectra were collected 0.5m and 50m above the Beebe Vents (sample names and details are located in Table 2.1). The spectra were fit with reference spectra from reference materials (Table 4.1). The Fe spectra for the each of the four elevations are displayed with the reference spectra that best fit the data (Fig.4.11; Tables 4.4-4.5 and S4.5-4.6). The results of the LCF are reported in mol% Fe on a per atom basis (mol% Fe-bearing minerals in particles collected on filter) in Table 4.4-4.5 and Figure 4.12.

Based on ICP-MS of the particles, the pFe concentration decreases within the buoyant plume as a function of elevation (personal communication, Chip Breier, Table 2.1; Figure 4.12). Based on the Fe XANES fits, Fe-bearing plume particles consist primarily of sulfides (pyrite, FeS, troilite, pentlandite, and cubanite) and Fe oxyhydroxides (Fe std 100 ffh, Ferrihydrite 6l fendorf, Toner_biogenic_oxide, Greenrust SO_4, and lepidocrocite) (Figure 4.12 and Table.S4.5-4.6). There were also spectra that fit best with Fe(II) oxides (psuedobrookite), a silicate (richterite), an Fe (III) phyllosilicate (STX clay), and native Fe (haxonite) (for formulas see table 4.1) (Figure 4.12; Table 4.4; Table.S4.5-4.6).

Reduced Fe-bearing mineral phases were observed in both samples. According to XANES results, sulfide concentrations were highest in the near vent sample (94mol% Fe sulfide in particles collected on the filter in the 0.5m sample, based on 12 point observations) and decreased with plume height (47mol% in the 50m sample, based on 10 point observations) (Figure 4.12; Table 4.4; Table.S 4.5-4.6). Fe(II) oxides (Pseudobrookite) were also observed in the 0.5m sample in spot 11 (Table.S4.5) The Fe(II) were not observed in the 50m sample (Table.S4.6).

The XANES data reveal that particles in the 0.5m sample contain Fe-bearing minerals that contain Fe(0) (Haxonite) in spot 9 (Figure 4.13; Table.S4.5). These data were neglected because it is unlikely that Fe(0) is in the plume (personal communication Chip Breier). The data were removed from the final XANES results (Table 4.4; Figure 4.12). Originally, there was a high concentration of Fe(III) (Fe(III) oxyhydroxides and Fe(III) carbonate) in the 0.5m sample is due to our sample handling (Fig.S4.4; Table.S4.5 and 4.7). Therefore, the Fe(III) and native Fe signals in the 0.5m sample were considered background and removed from the XANES and Fe chemical mapping results (Table 4.4; Figure 4.12).

4.6 Ground truth for XANES using chemical mapping of particles from the Beebe Vents plume

4.6.1 Presence-absence of Fe-bearing mineral phases using both techniques

The chemical mapping results ground truth the Fe XANES for presence-absence of minerals at each elevation. For example, Fe(III) oxyhydroxides are present in the 0.5m sample in spots 8, 9, 10, and 11 (Table.S4.5); the chemical map revealed the presence of Fe(III) oxyhydroxides at these spots (4.13). Silicates were present in the 50m sample in spots 0 and 1 with XANES (Table.S4.6); the chemical map revealed the presence of silicates at these spots as well (Figure 4.14). Sulfides are also present in the 50m sample at spots 0, 1, and 2; the chemical map also revealed the presence of sulfides at these spots (Figure 4.14).

4.6.2 Variation in the concentration of Fe-bearing mineral phases using both techniques

After removing Fe (III) and Fe (0), the concentration of Fe-bearing minerals is comparable between the two techniques. Specifically, per chemical mapping, the mol%

of sulfide is very close in the 0.5m sample (100 mol%), compared to XANES (96 mol%) (Figure 4.12 and 4.15; Tables 4.4-4.5).

The same is true for sulfides in the 50m sample. The XANES reveal a high concentration of sulfides (47 mol%) and the value is close to the chemical map (46 mol%) (Figures 4.12 and 4.15; Tables 4.5 and Table.S4.6).

The concentration of silicates and Fe(III) oxyhydroxides are variable for the 50m sample. The silicates were lower with XANES (3 mol%) than with the chemical map (32 mol%) (Figures 4.12 and 4.15; Tables 4.5 and Table.S4.6). The Fe(III)oxyhydroxides were higher with XANES (47 mol%) than with the chemical map (15 mol%) (Figures 4.12 and 4.15; Tables 4.5 and Table.S4.6). However, in both datasets, the Fe (III) oxyhydroxides increase, Fe sulfides decreases, and Fe (III) phyllosilicates appear, in the 50m sample (Table 4.4-4.5).

4.7 Detailed comparison of XANES and chemical mapping

4.7.1 Comparison of XANES and chemical mapping for SUPR22- 0.5m

Twelve point observations were made with Fe 1s XANES for the 0.5m sample. Approximately 160,000 pixels were queried using Fe chemical mapping. The Fe 1s XANES spots 8-11 were analyzed at the same beamtime that the Fe chemical map was collected (Figure 4.13). Spot 0-4 (see Fig.S4.1-4.2) and spots 5-7 were collected at a previous beamtime (see Fig.3.20). All XANES observations were used to help determine which Fe reference spectra should be used to fit the Fe chemical map. Based on the XANES data, the Fe-bearing mineral phases in decreasing abundance include sulfides and Fe (II) oxides + salts + glasses. Based on the chemical map, the Fe-bearing phases in decreasing abundance include sulfides, silicates, Fe (III) oxyhydroxides, and Fe (III) phyllosilicate.

Sulfides: The XANES revealed that sulfides were highest (94 mol%) (pyrite and cubanite) in the 0.5m sample (Table 4.4; Table.S 4.5; Figures 4.11 and 4.12). The Fe chemical mapping did not verify the presence of sulfides at spot 8, where XANES identified the presence of cubanite (Figure 4.13; Table. S4.5). Although, other particles that were analyzed via Fe 1s XANES did contain sulfides (pyrite) in particles in spots 10 and 11 on the filter (Figure 4.13).

Silicates: Silicates were not observed with XANES in the 0.5m sample (Table 4.4; Figure 4.12). Silicates were not observed in the 0.5 chemical map (Figure 4.13 and 4.15).

Fe (III) oxyhydroxides and Fe (III) carbonates: The chemical map reveals Fe (III) oxyhydroxides were present in the 0.5m chemical map (Figure 4.13). The Fe (III) present in the 0.5m sample is due to our sample handling (Fig.S4.4; Table.S4.5 and 4.7). Therefore, the Fe (III) signal in the 0.5m sample were considered background and removed from the XANES and Fe chemical mapping results (Table 4.4; Figure 4.12).

Fe (III) phyllosilicate: The XANES reveal no Fe(III)phyllosilicate (STX clay) in the 0.5m sample (Table 4.4; Figures 4.12). The Fe chemical map was not fit with the Fe (III) phyllosilicate reference material (Figure 4.13).

Fe(II) oxides + salts + glasses: The XANES reveal Fe(II) oxides + salts + glasses (psuedobrookite) was present in spot 11 (6mol%) (Figures 4.12; Table 4.4; Table.S4.5; Fig.S4.13). The Fe chemical mapping did not verify the presence of Fe(II) oxides + salts + glasses at spot 11, where XANES did not identify the presence of Fe(II) oxides + salts + glasses (Figure 4.6; Table. S4.1).

4.7.2 Comparison of XANES and chemical mapping for SUPR30- 50m

Ten point observations were made with Fe 1s XANES for the 50m sample. Approximately 60,000 pixels were queried using Fe chemical mapping. The Fe 1s XANES spots 0-4 were analyzed at the same beamtime that the Fe chemical map was collected (Figure 4.14). Spot 5-9 were collected at a previous beamtime (see Fig.S3.24). All XANES observations were used to help determine which Fe reference spectra should be used to fit the Fe chemical map. Based on the XANES data, the Fe-bearing mineral phases in decreasing abundance include sulfides, Fe (III) oxyhydroxides, silicates, and Fe(III) phyllosilicates. Based on the chemical map, the Fe-bearing phases in decreasing abundance include sulfides, silicates, Fe (III) oxyhydroxides, and Fe (III) phyllosilicates

Sulfides: The XANES revealed that sulfides were the third most abundant phase (47 mol%) (pyrite, pyrrhotite, and cubanite) in the 50m sample (Table 4.4; Table.S 4.6; Figure 4.12). The Fe XANES identified sulfides in spots 0, 1, 2, and 3 (Figure 4.14; Table. S4.6). The chemical mapping verified the presence of sulfides at spots 0, 1, and2 (Figure 4.14; Table. S4.6). The concentration of sulfides identified using chemical mapping (46 mol%) is similar to the concentration based on the XANES data (47 mol%) (Tables 4.4 and 4.5; Figures 4.12 and 4.15).

Silicates: Silicates (richterite) were abundant in the 50m chemical map (32mol%) (Table 4.5; Table.S 4.6; Figures 4.14 and 4.15). Silicates were verified at spots 0 and 1 where XANES also identified silicate minerals (Figure 4.14; Table.S 4.6). The concentration is more than the concentration based on the XANES data (3mol%) (Table 4.4; Figure 4.12).

Fe (III) oxyhydroxide: The chemical map reveals Fe(III) oxyhydroxides were abundant in the 50m sample (15 mol% and include ferrihydrite) (Table 4.5; Figures 4.14 and 4.15). The Fe chemical mapping verified the presence of Fe(III) oxyhydroxides in spots 0 and 1 (Figure 4.14; Table.S 4.6).

Fe (III) phyllosilicate: The XANES reveal an Fe(III)phyllosilicate (STX clay) was present in the 50m sample (3 mol%) (Table 4.4; Figures 4.12). The Fe chemical mapping

did not verify the presence of the same Fe (III) phyllosilicate in spots 0, 1, 2, and 3 (Figure 4.14; Table.S 4.6). The Fe(III) phyllosilicate was present in other particles on the filter, not analyzed with Fe1s XANES and accounts for 7 mol% of the Fe-bearing particles on the filter. The concentration is more than the concentration based on the XANES data (3 mol%) (Tables 4.4 and 4.5; Figures 4.12 and 4.15).

Fe(II) oxides + salts + glasses: The XANES reveal Fe (II) oxides + salts + glasses ($FeSO_4$) were not present in the chemical map (Table 4.5; Figures 4.14 and 4.15).

4.8 Particle morphology, correlation of Fe and S 1s XANES, and elemental distribution of of particles in the Beebe Vents

Based on XRF and Fe chemical mapping of particles, SUPR22-0.5m contains Fe mineral grains ranging in size from < 3 µm to 100 µm in diameter (Figure 4.13; Fig.S3.20-3.23). The SUPR30-50m has Fe mineral grains ranging from < 3µm to 50 µm in diameter (Figure 4.14; Fig.S3.24-3.26).

4.8.1 Elemental distribution and correlation of Fe and S 1s XANES of particles in SUPR22-0.5m

The As, V, Ni, Cu, Fe, Ni, Zn, Mn, Cl, Ti, Ca, S, and Si distributions within the particles and aggregates were determined by XRF mapping (Fig.S3.20). Iron 1s XANES were collected for spots 8-11 at ALS beamline 10.3.2 using Fe chemical maps, without additional XRF mapping (Figure 4.13). Four spots (spots 5-7) were investigated with Fe 1s XANES and XRF mapping at ALS beamline 10.3.2 (Fig.S3.20).

The Fe 1s XANES for spot 5,6 correlate with S 1s XANES for spot 0 (Fig.S320). Spots 5,6 and 7 in the XRF maps show Fe, Ca, S, Ni, Cl, Zn, Cu, and Mn. Spots 5 and 6 are associated with Fe 1s Fe XANES identified as sulfides (FeS, pyrite, cubanite) and Fe(III) oxyhydroxides (ferrihydrite and lepidocrocite) (Table.S4.5; Fig.S3.20). Spot 5 S 1s

XANES for spot 0 show gypsum, mackinawite, and pyrite (Table.S3.5). Both Fe and S 1s XANES reveal sulfides at spot 5,6 (S 1s XANES spot 0). Fe XANES 1s for spot 7 reveal and Fe(III) carbonates (coalingite), sulfides (pyrite), and Fe(III)oxyhydroxides (ferrihydrite). The S 1s XANES spot 1(Fig.S3.20) reveal gypsum, mackinawite, pyrite, and nanoparticulate S (Table.S3.5). Both Fe and S 1s XANES reveal sulfides at spot 7 (S 1s XANES spot 1).

4.8.2 Elemental distribution and correlation of Fe and S 1s XANES of particles in SUPR30-50m

The As, V, Ni, Cu, Fe, Ni, Zn, Mn, Cl, Ti, Ca, S, and Si distributions within the particles and aggregates were not determined by XRF mapping.

The Fe and S XANES both reveal sulfides in Fe 1s XANES spot 5 (S 1s XANES spot 0). The Fe 1s XANES observations made at spot 5 correlate with S 1s XANES spot 0. The Fe 1s XANES for spot 5 reveal cubanite, ferrihydrite, and pyrrhotite (Table.S4.6). The S 1s XANES reveal chalcopyrite, gypsum, pyrite, and SDS (Table.S3.9).

The Fe and S XANES both reveal sulfides in Fe 1s XANES spot 6 (S 1s XANES spot 1). The Fe 1s XANES observations made at spot 6 correlate with S 1s XANES spot 1. The Fe 1s XANES for spot 5 reveal cubanite, ferrihydrite, and pyrrhotite (Table.S4.6). The S 1s XANES reveal ANSA, chalcopyrite, greigite, and gypsum (Table.S3.9).

The Fe and S XANES both reveal sulfides in Fe 1s XANES spot 7 (S 1s XANES spot 2).The Fe 1s XANES observations made at spot 7 correlate with S 1s XANES spot 2. The Fe 1s XANES for spot 7 reveal cubanite, ferrihydrite, and pyrite (Table.S4.6). The S 1s XANES reveal ANSA, chalcopyrite, cysteine, and SDS (Table.S3.9).

The Fe and S XANES both reveal sulfides in Fe 1s XANES spot 8 (S 1s XANES spot 3)..The Fe 1s XANES observations made at spot 8 correlate with S 1s XANES spot 3.

The Fe 1s XANES for spot 7 reveal cubanite, ferrihydrite, and pyrite (Table.S4.6). The Fe 1s XANES observations made at spot 8 correlate with S 1s XANES spot 3. The S 1s XANES reveal ANSA, chalcopyrite, gypsum, and nanoparticulate S (Table.S3.9).

5. DISCUSSION

In hydrothermal fluids, inorganic reactions produce H_2S through the reduction of seawater-derived sulfate by Fe^{2+} bearing minerals in basalt (Shanks, 2001). The H_2S can react with $Fe^{2+}_{(aq)}$ to produce iron sulfides (Tivey et al., 1996; Tivey, 2007; McDermott, 2014):

$$Fe^{2+}_{(aq)} + H_2S_{(aq)} \rightarrow FeS_{(s)} + 2H^{+}_{(aq)}$$

Then, the remaining $Fe^{2+}_{(aq)}$ reacts with oxygen to generate Fe oxyhydroxides:

$$Fe^{2+}_{(aq)} + 0.25O_{2(g)} + 2.5H_2O \rightarrow Fe(OH)_{3(s)} + 2H^{+}_{(aq)}$$

These reactions occur quickly and outcompete microbial metabolic processes in the first few meters of the rising plume (Rickard and Luther, 1997; Yücel et al., 2011; Findlay et al., 2014).

Previous research has determined that three inorganic chemical processes transform Fe^{2+} within vent fluids: (1) reactions with sulfur to create sulfide mineral phases (Tivey et al., 1996; Yücel, et al., 2011; Syverson et al., 2013; Mcdermott et al., 2015); (2) oxidation by seawater to form Fe(III) oxyhydroxide minerals (Kadko, 1993; Field and Sherrell, 2000); and, (3) silicate mineral formation (Tivey 2007; Gartman et al., 2014).

5.1 Redox Status of Particles and precipitation of Fe-bearing minerals of Von Damm

We investigated the Fe in Fe-bearing minerals from particles collected along the rising plume at Von Damm (0.5m to 50m above the vent). The Fe XANES and chemical mapping results reveal an increase in oxidized Fe (III) oxyhydroxides. This suggest the fluids become more oxidized within the first 37m, due to possible (1) microbial oxidation, or; (2) highly reactive particles reacting with oxygenated seawater (Figure 4.5). The chemical mapping results capture Fe-bearing silicates and Fe(II) oxides as they emerge from the Von Damm fluids (Figure 4.10). They remain in low concentrations as the plume rises and they decrease in abundance in the background sample. This might be due to the entrainment of minerals that are from the surrounding seawater. The same entrainment processes could be mixing highly reactive reduced species with oxygenated seawater, generating more oxidized forms of Fe-bearing minerals.

5.2 Redox Status of Particles and precipitation of Fe-bearing minerals of Beebe

The Beebe Vents data from 0.5 and 50m above the vent reveal sulfides minerals in the Fe-bearing minerals. Previous X-Ray Diffraction results from Beebe Vents identified Cu-Fe sulfides in chimney samples. The Inductively Coupled Plasma-Optical Emission Spectrometry (ICP-OES) determined a high concentration of Si on the exterior of the chimney structures and high concentrations of Cu on the interior of the chimney structures at Beebe Vents (Webber et al., 2015). Estrada and colleagues (2016) determined that the particles in the Beebe Vents plume are <100μm in diameter and iron-rich.

Similar to the S 1s XANES, the Fe 1s XANES data support the theory that sulfides are formed in the Beebe fluids either in the subsurface (Yücel et al., 2011) or as fluids emerge from the vent. The Fe 1s XANES results also reveal that within the buoyant plume, the particulate Fe species are chemically reduced. Iron-bearing phases in decreasing abundance include: (1) Fe sulfides; (2) Fe (III) oxyhydroxides; (2) Fe (III) carbonates; and, (4) Fe (III) silicates and Fe(II) silicates. The sulfides at the base of the

plume (SUPR22-0.5m) are comprised of pyrite (FeS_2), troilite (FeS), and cubanite ($CuFe_2S_3$) (Figure 4.11; Table.S4.5).

6. CONCLUSIONS

Von Damm fluids are high in dissolved metals, relative to seawater, but endmember abundances of dFe (5.7 to 450 µmol/kg) are low relative to higher-temperature vents fields on the Mid-Atlantic Ride (McDermott, 2014). Despite the low abundance of Fe in Von Damm, we identified several Fe-bearing minerals throughout the rising plume. Several lines of evidence, combined with the Fe results, indicate that the geochemical processes in the rising plumes at Von Damm are controlled by the entrainment of minerals and microbial communities from the host vent as well as the surrounding seawater. The presence of cellular material and cells (CHAPTER 2), the known existence of S-oxidizing microbial communities in the surrounding seawater (German et al., 2010; Breier et al., 2014), and the imaging of cell-like features with XRF maps indicated microbial communities are present in and around the rising plume. The identification of organosulfur and a variety of oxidized and intermediately oxidized S species (CHAPTER 3) indicated oxidation processes occur in the plume, and entrainment processes are likely to mix highly reactive reduced species with oxygenated seawater, generating oxidized forms of both S- and Fe-bearing minerals.

Our Fe 1s XANES results for Beebe Vents verify the presence of high levels of Fe in the rising plume, and we were able to identify sulfides, Fe oxyhydroxides, Fe(II) oxides, silicates, and Fe(III) phyllosilicates within the particles. High concentrations of reduced Fe-bearing minerals and low concentrations of organic S (CHAPTER 3) and organic material (CHAPTER 2) in Beebe Vents indicate inorganic chemical processes occur in the fluids. It also indicates that less mixing with seawater occurs before the plume reaches 50m.

Primary silicates are formed from magma cooling and secondary phyllosilicates are formed from weathering of primary phyllosilicate minerals. The Fe-bearing minerals within the Von Damm and Beebe Vents particles that match silicate reference materials are assumed to be transported into the plume after they were formed in other places (allochtonous), and are not particles that were formed within the plume (autochonous). However, a near bottom background sample was not analyzed. Without a near bottom background sample, for either Von Damm or Beebe Vents, we cannot definitively state that the silicate signal is from entrainment and not from the formation of silicate minerals within the plume.

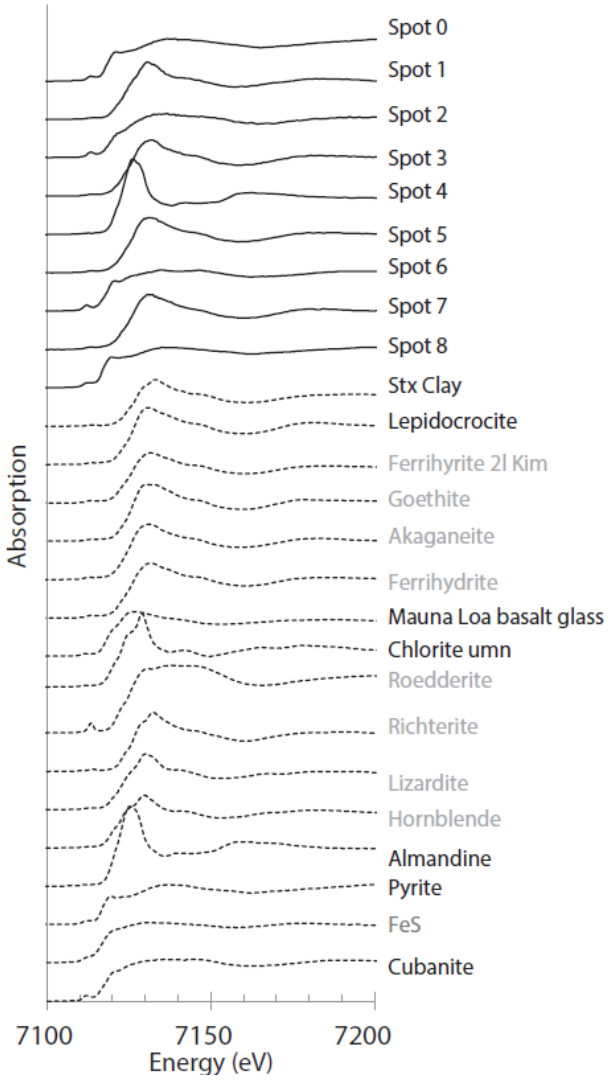

Figure 4.1: Iron 1s XANES spectra displaying the range of Fe species present in sample SUPR05 collected 1m above Von Damm. The reference spectra (dashed lines) shown are those that created the best LCF results (Almandine, hornblende, lizardite, richterite, roedderite, chlorite, cubanite, Mauna Loa basalt glass, FeS, pyrite, ferrihydrite, akaganeite, lepidocrocite, STX clay). Reference spectra with bold font text are those used to fit the Fe chemical map (STX clay, lepidocrocite, Mauna Loa basalt glass, chlorite, almandine, pyrite, and cubanite) (see Table 4.1 for formulas).

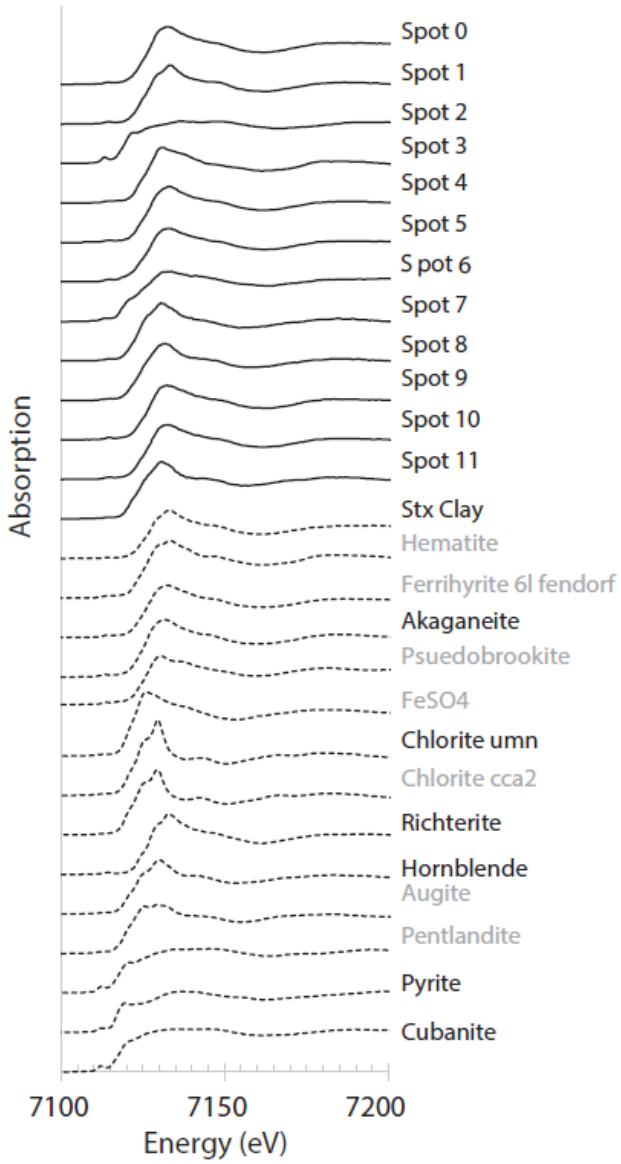

Figure 4.2: Iron 1s XANES spectra displaying the range of Fe species present in sample SUPR11 collected 8m above Von Damm. The reference spectra (dashed lines) shown are those that created the best LCF results (Augite, hornblende, richterite, psuedobrookite, chlorite, cubanite, pentlandite, FeSO4, pyrite, ferrihydrite, akaganeite, hematite, STX clay). Reference spectra with bold font text are those used to fit the Fe chemical map (STX clay, akaganeite, pyrite, cubanite, chlorite, richterite, and hornblende) (see Table 4.1 for formulas).

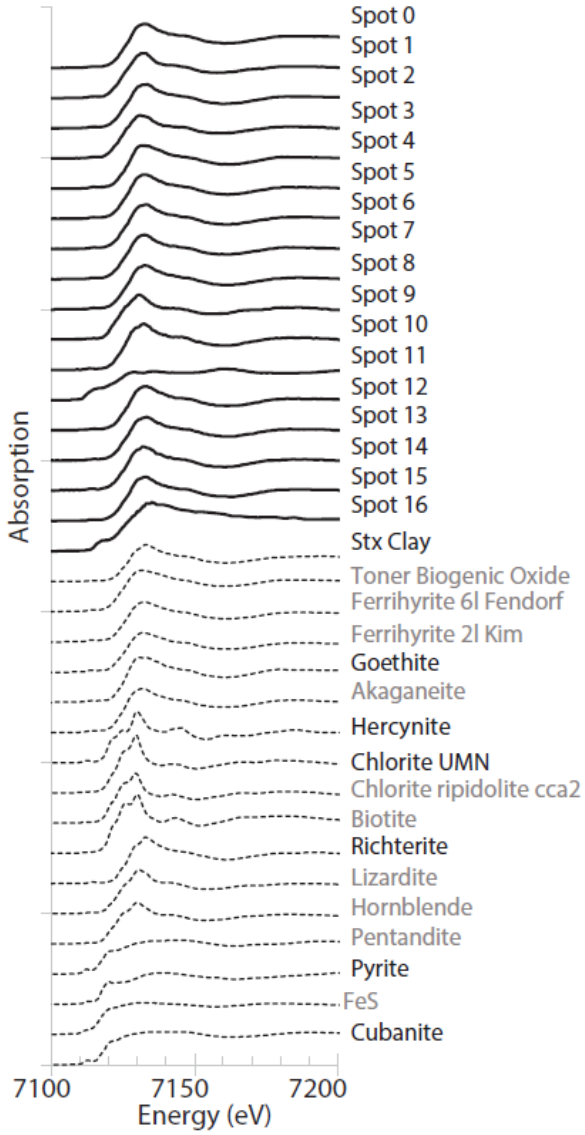

Figure 4.3: Iron 1s XANES spectra displaying the range of Fe species present in sample SUPR57 collected 37m above Von Damm. The reference spectra (dashed lines) shown are those that created the best LCF results (Hornblende, richterite, lizardite, chlorite, hercynite, cubanite, pentlandite, FeS, pyrite, goethite, ferrihydrite, akaganeite, toner biogenic oxide, and STX clay). Reference spectra with bold font text are those used to fit the Fe chemical map (STX clay, goethite, pyrite, cubanite, hercynite, chlorite, and richterite) (see Table 4.1 for formulas).

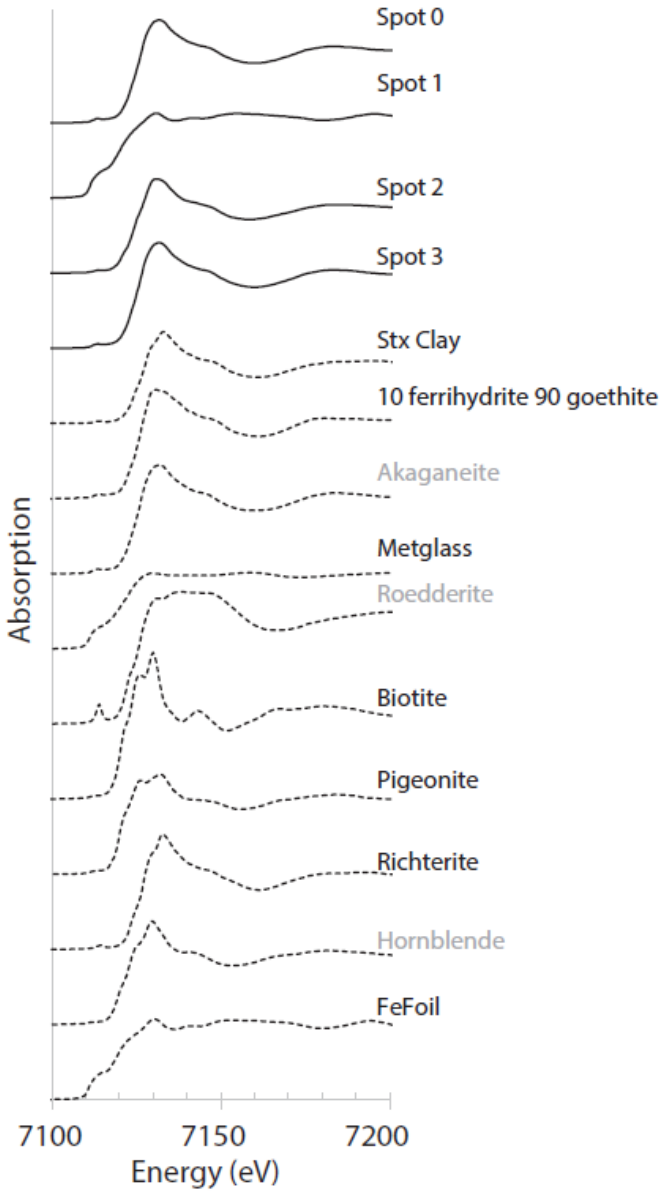

Figure 4.4: Iron 1s XANES spectra displaying the range of Fe species present in sample SUPR58 collected APB above Von Damm. The reference spectra (dashed lines) shown are those that created the best LCF results (Stx Clay, 10ferrihydrite 90 goethite, akaganeite, metglass, roedderite, biotite, pigeonite, richterite, hornblende, and Fe foil). Reference spectra with bold font text are those used to fit the Fe chemical map (STX clay, 10 ferrihydrite 90 goethite, metglass, biotite, pigeonite, richterite, and hornblende) (see Table 4.1 for formulas).

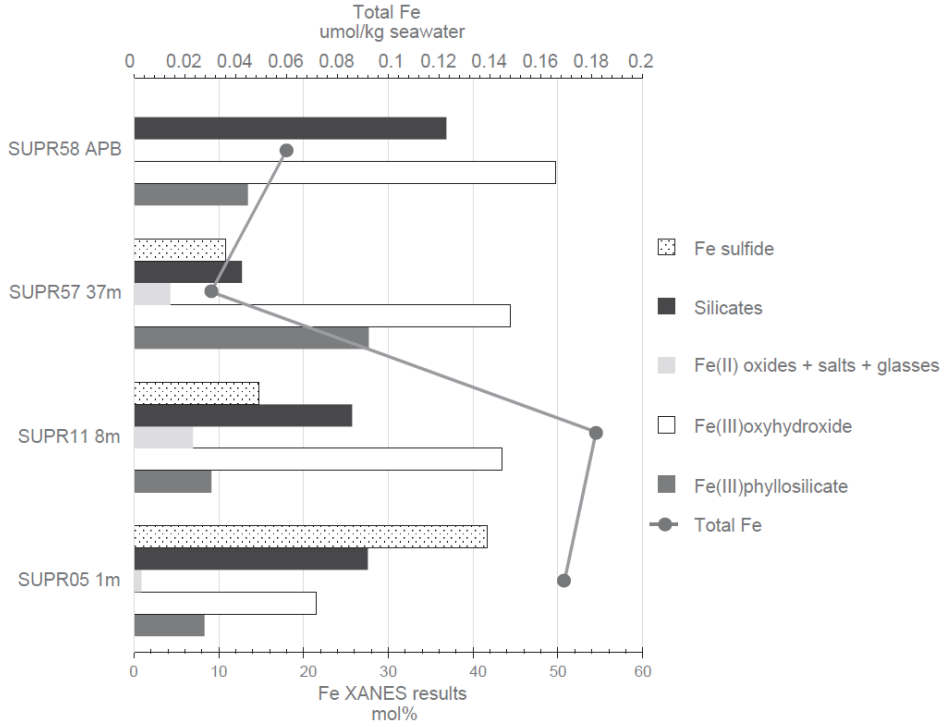

Figure 4.5: Total particulate Fe and Fe XANES results in mol% Fe for Von Damm hydrothermal fluids.

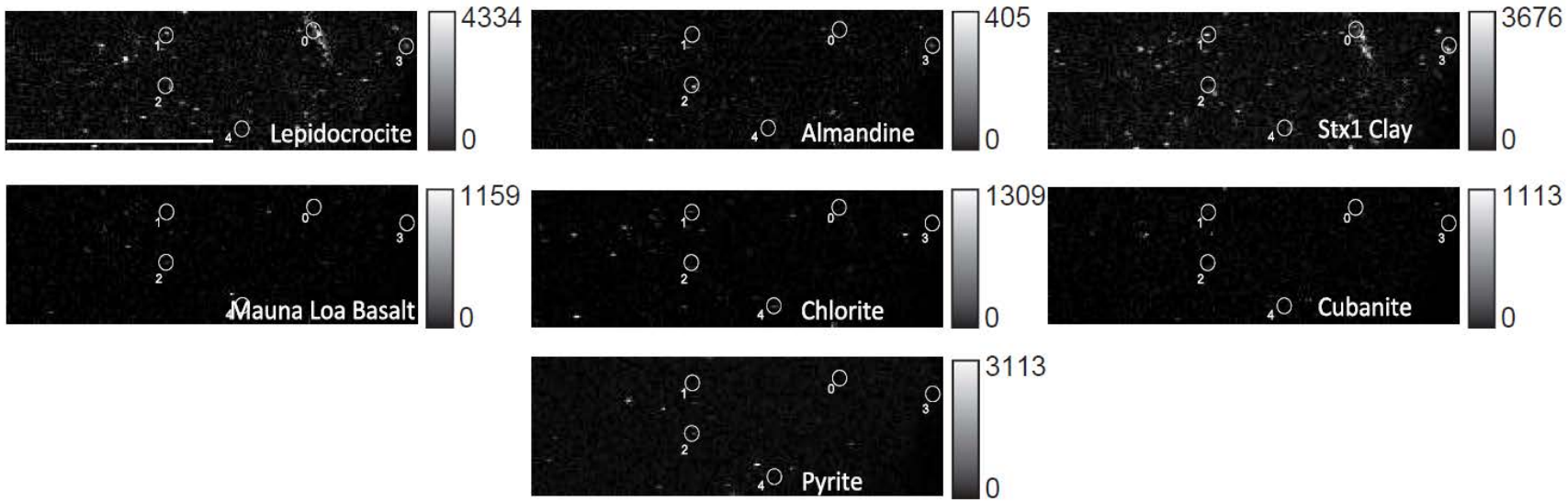

Figure 4.6: Fe chemical map for SUPR05 collected 1m above Von Damm hydrothermal vent. Eight energies (7110, 7113.3, 7120.9, 7125, 7127.5, 7129.2, 7132.5eV) were used and this is a composite of the fit with seven reference spectra (STX clay, lepidocrocite, Mauna Loa basalt glass, chlorite, almandine, pyrite, and cubanite) (see Table 4.1 for formulas). Circles indicate where Fe XANES were collected. Gradient bar represents counts per pixel. Scale bar is 400µm.

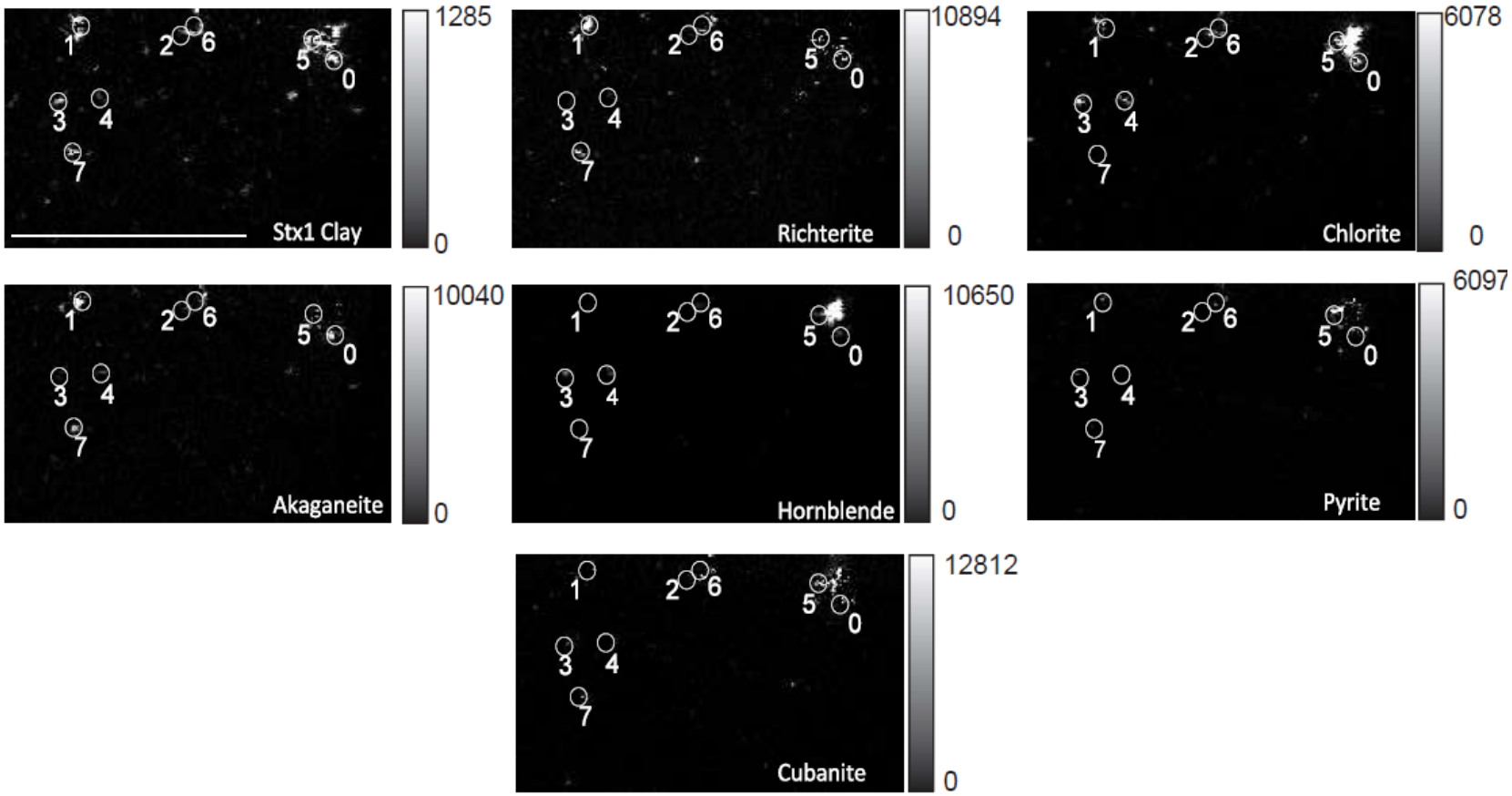

Figure 4.7: Fe chemical map for SUPR11 collected 8m above Von Damm hydrothermal vent. Eight energies (7110, 7113.3, 7120.9, 7125, 7127.5, 7129.2, 7132.5eV) were used and this is a composite of the fit with seven reference spectra (STX clay, akaganeite, hornblende, chlorite r2139, richterite, pyrite, and cubanite) (see Table 4.1 for formulas). Circles indicate where Fe XANES were collected. Gradient bar represents counts per pixel. Scale bar is 400μm.

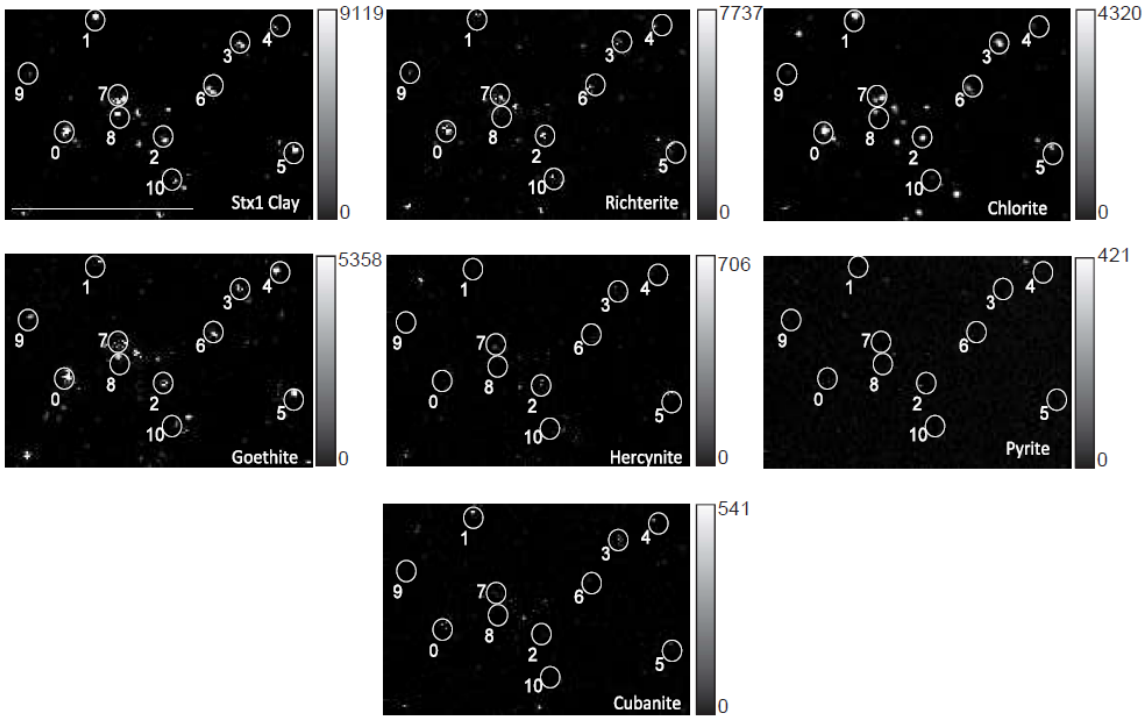

Figure 4.8: Fe chemical map for SUPR57 collected 37m above Von Damm hydrothermal vent. Eight energies (7110, 7113.3, 7120.9, 7125, 7127.5, 7129.2, 7132.5eV) were used and this is a composite of the fit with seven reference spectra (STX clay, 10ferrihydrite 90goethite, hercynite, chlorite r2139, richterite, pyrite, and cubanite) (see Table 4.1 for formulas). Circles indicate where Fe XANES were collected. Gradient bar represents counts per pixel. Scale bar is 200μm.

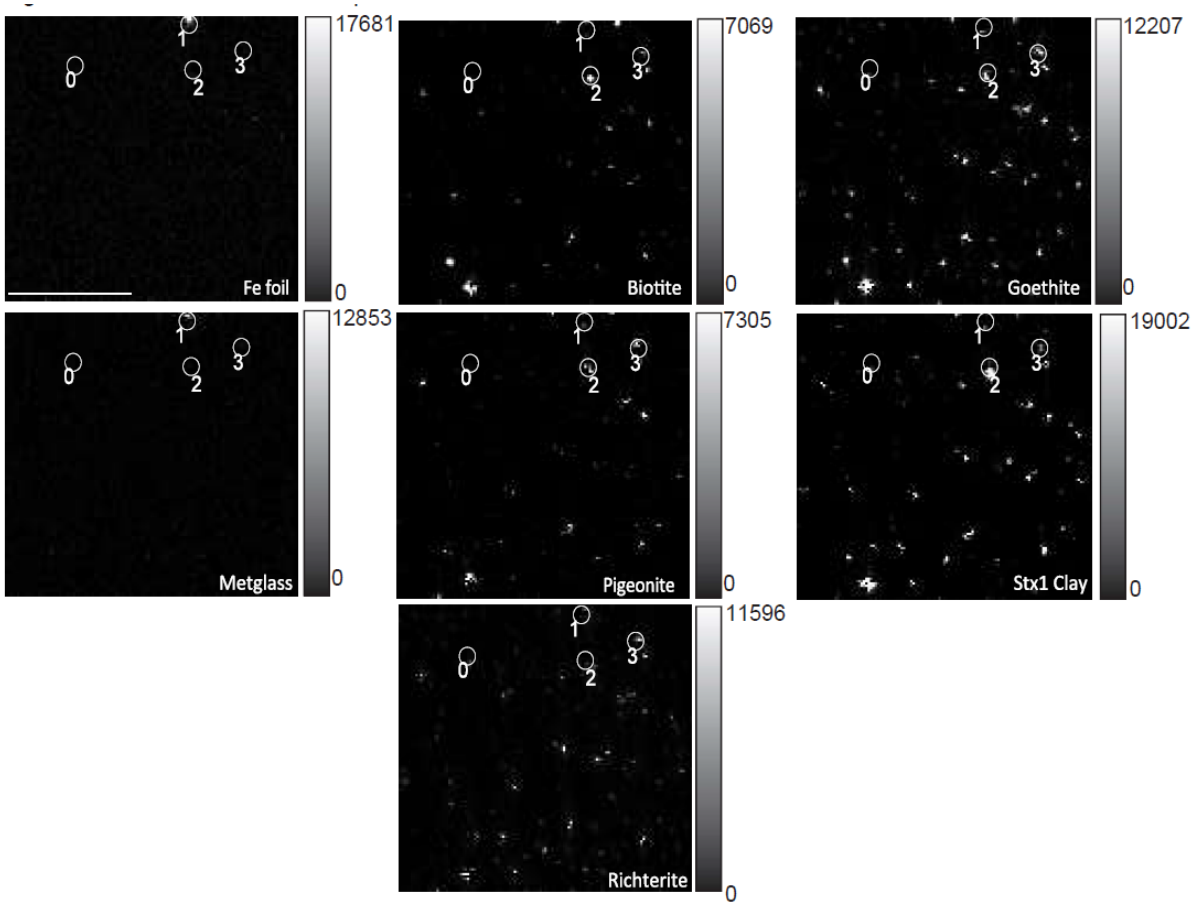

Figure 4.9: Fe chemical map for SUPR58 collected 812m above Von Damm hydrothermal vent. Eight energies (7110, 7113.3, 7120.9, 7125, 7127.5, 7129.2, 7132.5eV) were used and this is a composite of the fit with seven reference spectra (STX clay, goethite, biotite, richterite, pigeonite, metglass, and Fe Foil) (see Table 4.1 for formulas). Circles indicate where Fe XANES were collected. Gradient bar represents counts per pixel. Scale bar is 200μm.

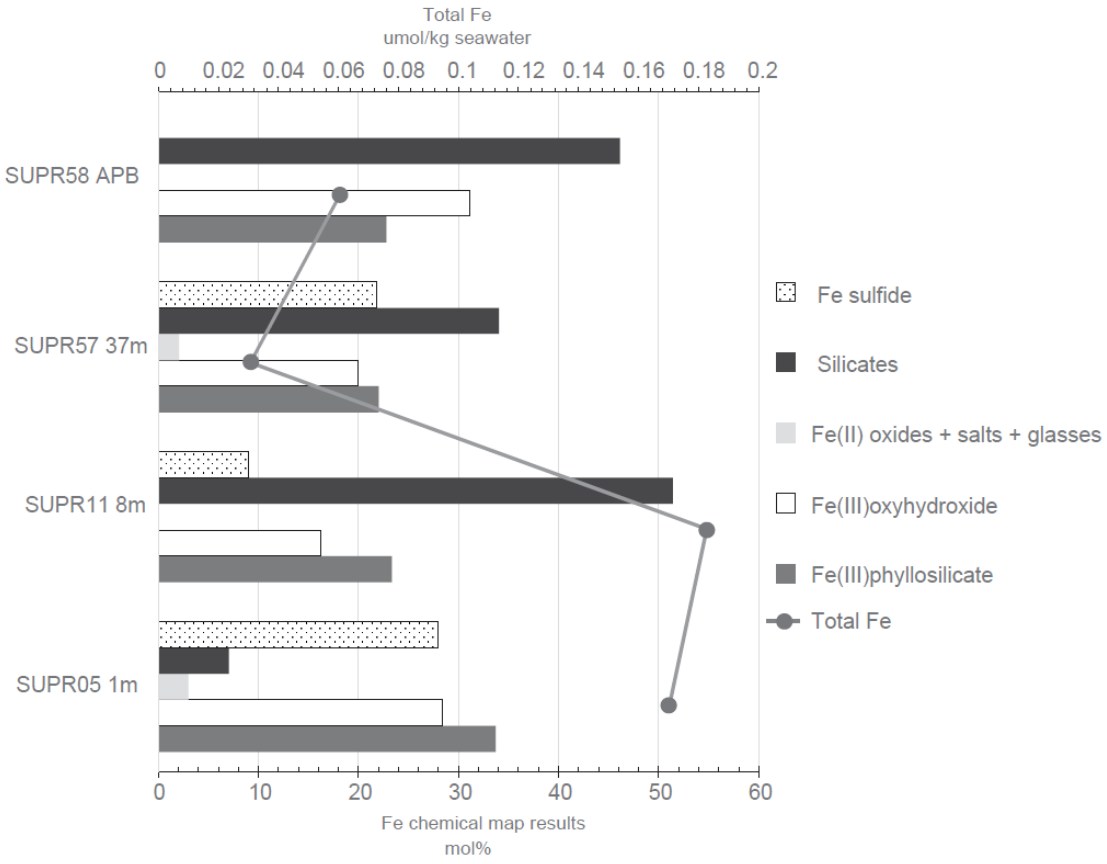

Figure 4.10: Bar chart displaying Fe chemical map results for Von Damm hydrothermal

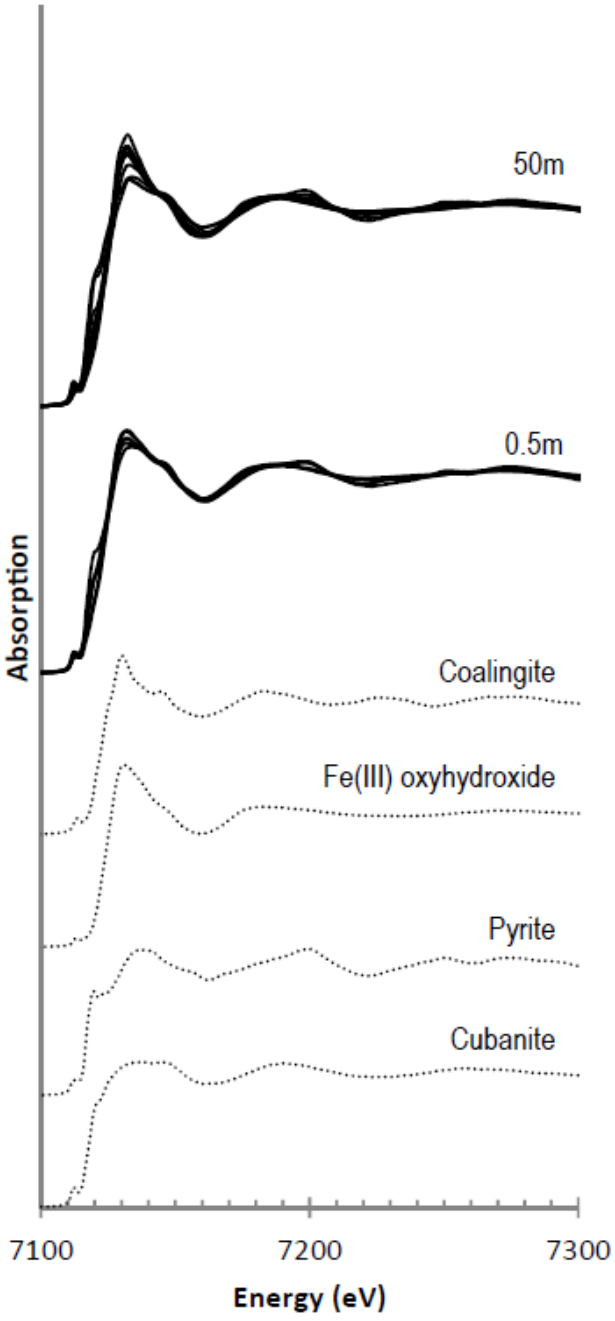

Figure 4.11: Iron 1s XANES spectra displaying Fe species present in sample SUPR22-0.5m and SUPR30-50m. Reference spectra (coalingite, toner biogenic oxide, ferrihydrite, cubanite, FeS, and pyrite) are plotted against spectra from the samples (see Table 4.1 for formulas).

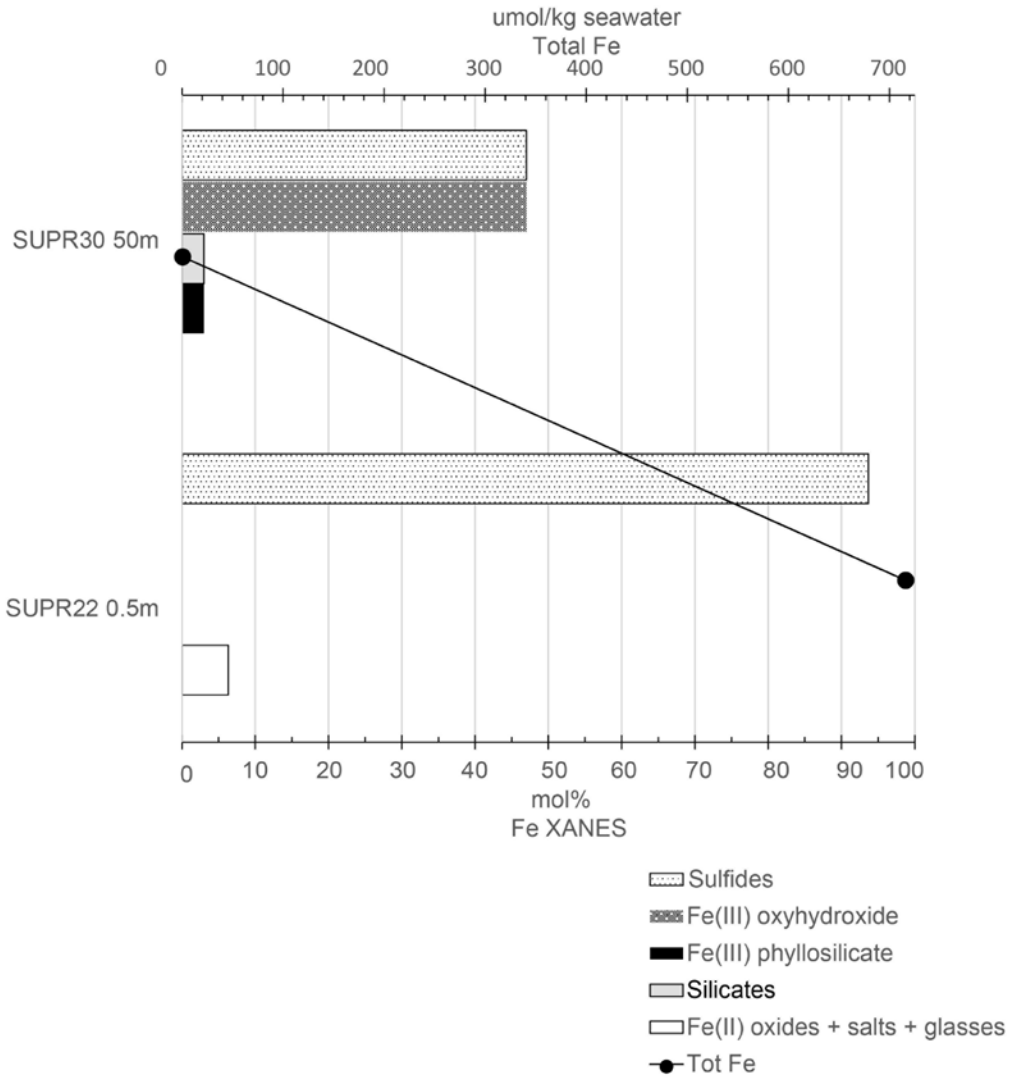

Figure 4.12: Bar chart displaying Fe 1s XANES and total Fe results for Beebe hydrothermal fluids.

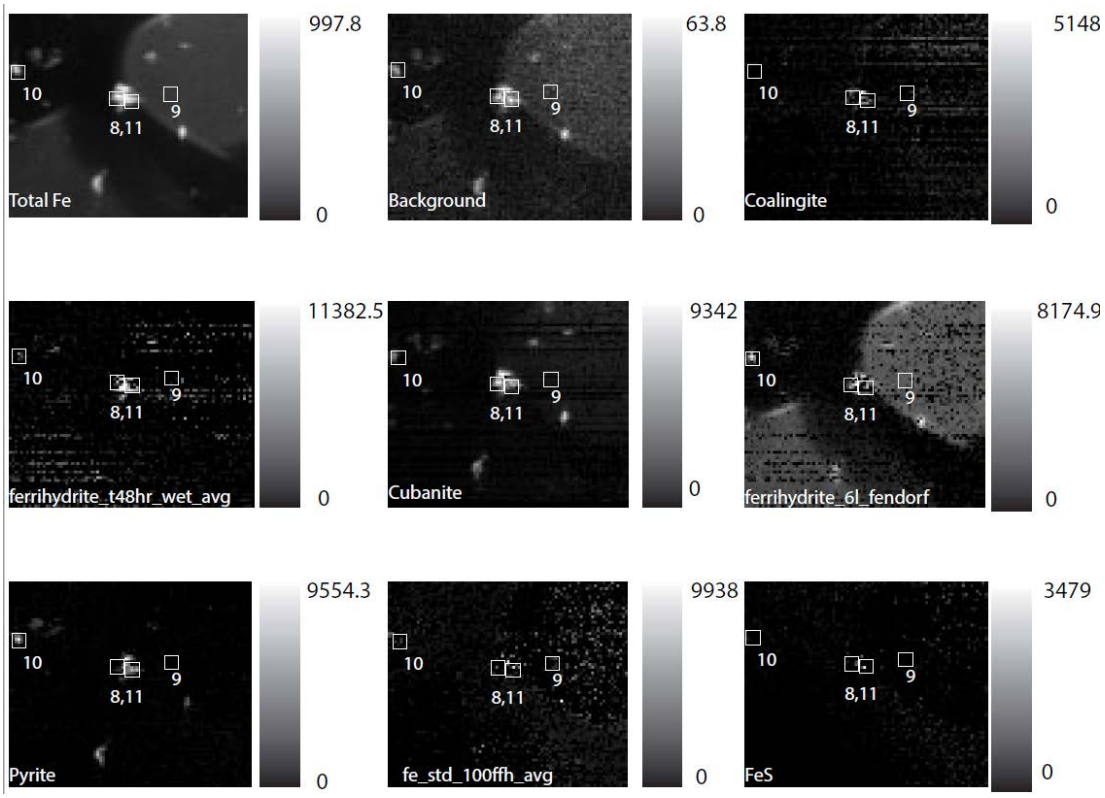

Figure 4.13: Iron chemical map for SUPR22-0.5m. Spots 9-12 were analyzed for Fe 1s XANES. Eight energies (7110, 7113.3, 7120.9, 7125, 7127.5, 7129.2, 7132.5eV) were used and this is a composite of the fit with seven reference spectra. Map was best fit by the following reference spectra: coalingite, ferrihydrite (ferrihydrite_t48r_wet_avg, ferrihydrite_6l_fendorf, fe_std_100ffh_avg), cubanite, pyrite, and FeS (see Table 4.1 for formulas). Scale bar is 200µm

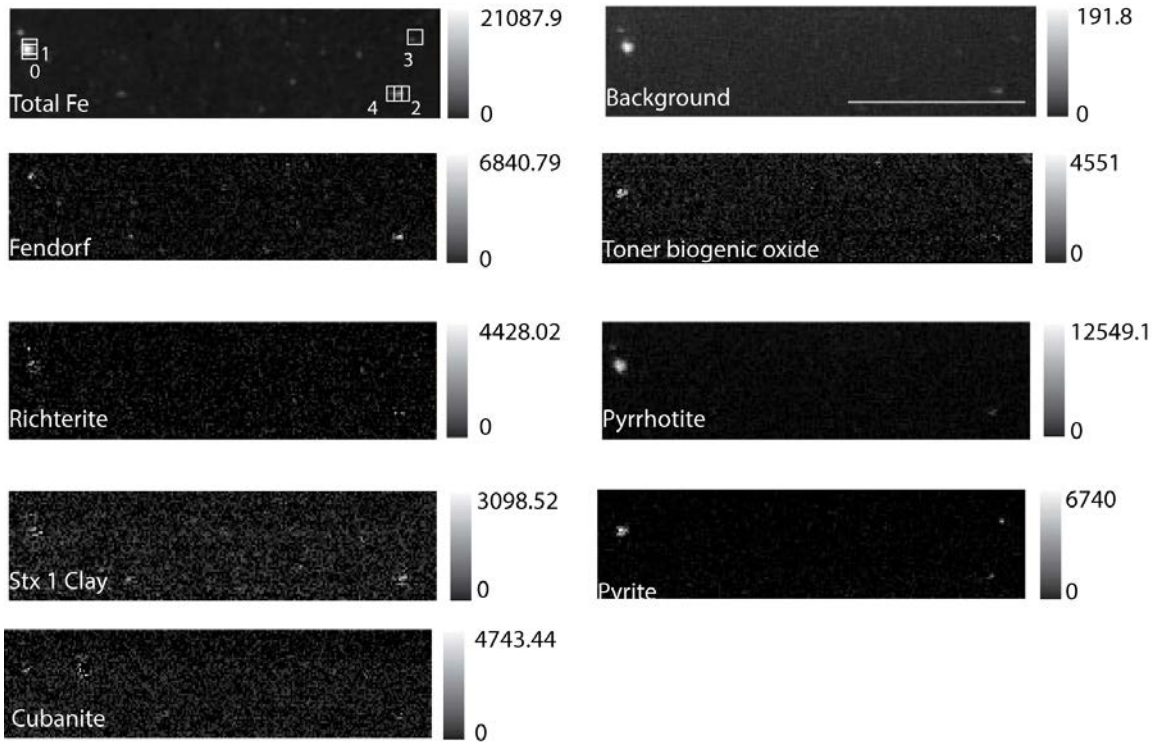

Figure 4.14: Iron chemical map for SUPR30-50m. Scale bar is 300µm. Fe chemical map for SUPR22-0.5m. Eight energies (7110, 7113.3, 7120.9, 7125, 7127.5, 7129.2, 7132.5eV) were used and this is a composite of the fit with seven reference spectra. Spots 0-14 were analyzed for Fe 1s XANES. Map was best fit by the following reference spectra: ferrihydrite_6l_fendorf, toner biogenic oxide, richterite, pyrrhotite, Stx_1_Clay, pyrite, and cubanite (see Table 4.1 for formulas).

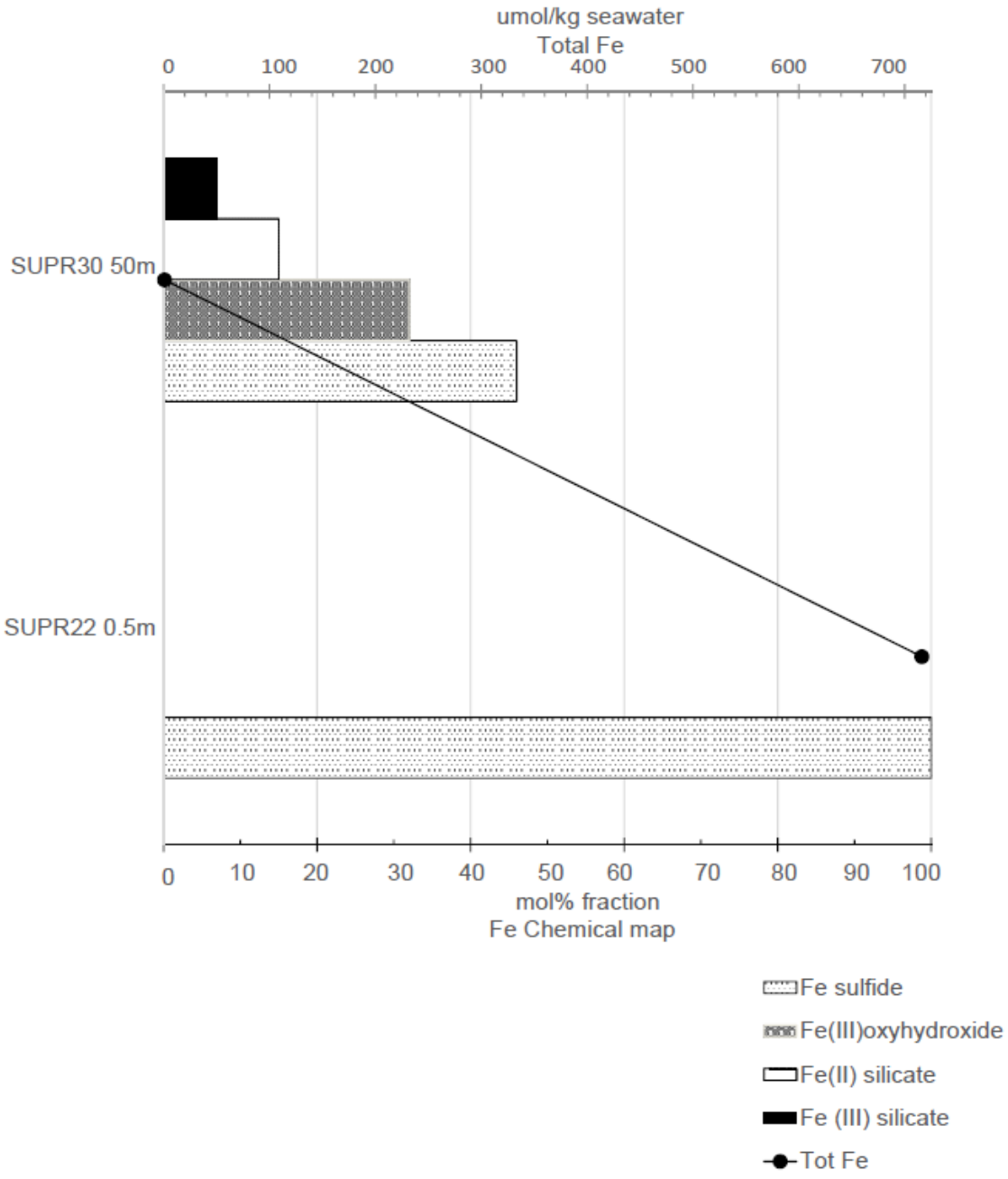

Figure 4.15: Bar chart displaying Fe chemical mapping and total Fe results for Beebe hydrothermal fluids.

Table 4.1: Table lists the reference file name, category, formula, valence state (V), mol of Fe, supplier or source of the compound, the facility (Fac.) spectra was collected, the beamline spetra was collected, the citation for the spectra, and the owner of the compound for each Fe-bearing mineral for categories of Fe-bearing minerals identified in the Von Damm particles.

Reference File name	Category	Formula	V	Source	Fac.	BL	Citation	Owner
Stx 1 Clay	Fe(III) phyllosilicate	$(Ca_{0.27}Na_{0.04}K_{0.01})[Al_{2.41}Fe(II)_{0.09}Mntr Mg_{0.71}Ti_{0.03}][Si_8]20O(OH)_4$	+3	Clay Mineral Society	ALS	10.3.2	O'Day et al., 2004	Matthew Marcus
Lepidocrocite	Fe(III) oxyhydroxide	Y-$Fe^{3+}O(OH)$	+3	Colleen Hansel	SSRL		Marcus et al., 2008	Colleen Hansel
Hematite	Fe(III) oxyhydroxide	$Fe^{3+}{}_2O_3$	+3	Mattew Marcus	ALS	10.3.2	Marcus et al., 2008	Matthew Marcus
Toner_biogenic_oxide	Fe(III) oxyhydroxide	$Fe^{3+}O(OH)$	+3	Brandy Toner	ALS	10.3.2	Toner et al., 2009	Brandy Toner
Ferrihydrite 6l fendorf	Fe(III) oxyhydroxide	$Fe^{3+}{}_5HO_8 4H_2O$	+3		ALS	10.3.2	Marcus et al., 2008	Matthew Marcus
Ferrihydrite 2l kim	Fe(III) oxyhydroxide	$Fe^{3+}{}_5HO_8 4H_2O$	+3	Clara S. Chan	ALS	10.3.2	Marcus et al., 2008	Clara S. Chan
Fe std 100 goe	Fe(III) oxyhydroxide	α-$Fe^{3+}O(OH)$	+3		ALS	10.3.2	Marcus et al., 2008	Matthew Marcus
Akaganeite	Fe(III) oxyhydroxide	β-$Fe^{3+}O(OH)$	+3	Sirine Fakra	ALS	10.3.2	Marcus et al., 2008	Sirine Fakra
Fe std 100 ffh	Fe(III) oxyhydroxide	$Fe^{3+}{}_5HO_8 4H_2O$	+3		ALS	10.3.2	Marcus et al., 2008	Matthew Marcus
Hercynite	Fe(II) oxides + salts + glasses	$Fe^{2+}Al_2O_4$	+2	Glenn A. Waychunas	ALS	10.3.2	Marcus et al., 2008	Matthew Marcus
Greenrust SO_4	Fe(III) oxyhydroxide	$Fe^{2+}4Fe^{3+}2(OH)12SO_4H_2$	+3	Thomas Borch	ALS	10.3.2		Matthew Marcus

		O						
Fe3O4	Fe(III) oxyhydroxide	$Fe^{3+}2Fe^{2+}O_4$	+3	Matt Newville	ALS	10.3.2		Matt Newville
Mauna Loa basalt glass	Fe(II) oxides + salts + glasses	Basalt glass[a]	+2	Matthew Marcus	ALS	10.3.2	Marcus et al., 2008	Matthew Marcus
Psuedobrookite	Fe(II) oxides + salts + glasses	$Fe^{3+}Fe^{2+}0.4Mg0.10.75Fe^{2+}0.25O_5$	+2	Sirine Fakra	ALS	10.3.2	Marcus et al., 2008	Sirine Fakra
FeSO4	Fe(II) oxides + salts + glasses	$FeSO_4$	+2	Clara S. Chan	ALS	10.3.2	Marcus et al., 2008	Clara S. Chan
Chlorite r2139	Silicates	$(Mg,Fe)_3(Si,Al)_4O10(OH)_2(Mg,Fe)_3(OH)_6$	+2/+3	Brandy Toner	ALS	10.3.2	Marcus et al., 2008	Matthew Marcus
Chlorite ripidolite cca2	Silicates	$(Mg,Fe,Al)_6(Si,Al)_4O10(OH)_8$	+2/+3	Jacob Frommer and Andreas Vogelin	ALS	10.3.2	Marcus et al., 2008	Matthew Marcus
Roedderite	Silicates	$Na_{1.5}K_{0.5}Mg_{3.75}Fe^{2+}_{1.25}Si_{12}O_{30}$	+2		ALS	10.3.2	Marcus et al., 2008	Matthew Marcus
Biotite	Silicates	$KMg_{2.5}Fe^{2+}_{0.5}AlSi_3O_{10}(OH)_{1.75}F_{0.25}$	+2	Kent Ross	ALS	10.3.2	Marcus et al., 2008	Matthew Marcus
Lizardite	Silicates	$Mg_{2.9}Fe_{0.1}Si_2O_5(OH)_4$	+2	Freider Klein	ALS	10.3.2	Marcus et al., 2008	Matthew Marcus
Pigeonite	Silicates	$Mg_{1.35}Fe^{2+}_{0.55}Ca_{0.1}Si_2O_6$	+2	Sirine Fakra	ALS	10.3.2	Marcus et al., 2008	Sirine Fakra
Richterite	Silicates	$Na_2CaMg_3Fe^{2+}_2(Si_8O_{22})(OH)_2$	+2	Sirine Fakra	ALS	10.3.2	Marcus et al., 2008	Sirine Fakra
Hornblende	Silicates	$(Ca,Na)_{2-3}(Mg,Fe,Al)_5(Al,Si)_8O_{22}(OH,F)_2$	+2	Thomas Borch	ALS	10.3.2	Marcus et al., 2008	Matthew Marcus
Almandine	Silicates	$Fe^{2+}{}_3Al_2(SiO4)_3$	+2	Glenn A.	ALS	10.3.2	Marcus et al., 2008	Matthew Marcus

				Waychunas				
Augite	Silicates	$Ca_{0.9}Na_{0.1}Mg_{0.9}Fe^{2+}_{0.2}Al_{0.4}Ti_{0.1}Si_{1.9}O_6$	+2	Anna Butterworth	ALS	10.3.2	Marcus et al., 2008	Matthew Marcus
Pentlandite	Fe sulfide	$(Fe,Ni)_9S_8$	+2	Sirine Fakra	ALS	10.3.2	Marcus et al., 2008	Sirine Fakra
Pyrite	Fe sulfide	FeS_2	+2	Sirine Fakra	ALS	10.3.2	Marcus et al., 2008	Sirine Fakra
FeS	Fe sulfide	FeS	+2	Thomas Borch	ALS	10.3.2	Marcus et al., 2008	Matthew Marcus
Cubanite	Fe sulfide	$CuFe^{2+}_2S_3$	+2	Sirine Fakra	ALS	10.3.2	Marcus et al., 2008	Sirine Fakra
Metglass	Native iron	$Fe_{81}B_{13.5}Si_{3.5}C_2$	+2	Matthew Marcus	ALS	10.3.2	Marcus et al., 2008	Matthew Marcus
Haxonite	Native iron	$Fe_{20}Ni_3C_6$	0	Sirine Fakra	ALS	10.3.2	Marcus et al., 2008	Matthew Marcus
FeSi2	Native iron	$FeSi_2$	0	Tonio Buonassisi	ALS	10.3.2	Marcus et al., 2008	Matthew Marcus
FeFoil	Native iron	Fe(0)	0	Sirine Fakra	ALS	10.3.2	Marcus et al., 2008	Sirine Fakra

Table 4.2: Concentration of Fe-bearing phases (mol% Fe on a per atom basis) identified through linear combination fitting of Fe 1s XANES with reference spectra (see Table 4).

Category	SUPR05 1m Fe (mol%)	SUPR11 8m Fe (mol%)	SUPR57 37m Fe (mol%)	SUPR58 APB Fe (mol%)
Fe(III) phyllosilicate	8	9	28	13
Fe(III) oxyhydroxide	22	43	44	50
Fe(II) oxides + salts + glasses	1	7	4	-
Silicates	28	26	13	37
Fe sulfide	42	15	11	-

Table 4.3: Concentration of Fe-bearing phases (mol% Fe on a per atom basis) identified through Fe chemical mapping.

Category	SUPR05 1m Fe (mol%)	SUPR11 8m Fe (mol%)	SUPR57 37m Fe (mol%)	SUPR58 APB Fe (mol%)
Fe(III) phyllosilicate	34	23	22	23
Fe(III) oxyhydroxide	28	16	20	31
Fe(II) oxides + salts + glasses	3	-	2	-
Silicates	7	51	34	46
Fe sulfide	28	9	22	-

Table 4.4: Concentration of Fe-bearing phases (mol% Fe on a per atom basis) identified through linear combination fitting of Fe 1s XANES with reference spectra.

Category	SUPR22 0.5m Fe (mol%)	SUPR30 50m Fe (mol%)
Sulfides	94	47
Silicates	-	3
Fe(II) oxides + salts + glasses	6	-
Fe(III) oxyhydroxides	-	47
Fe(III) phyllosilicate	-	3

Table 4.5: Concentration of Fe-bearing phases (mol% Fe on a per atom basis) identified with Fe chemical mapping.

Category	SUPR22 0.5m Fe (mol%)	SUPR30 50m Fe (mol%)
Sulfides	100	46
Silicates	-	32
Fe(III) oxyhydroxide	-	15
Fe(III) phyllosilicate	-	7

SUPPLEMENTAL FIGURES

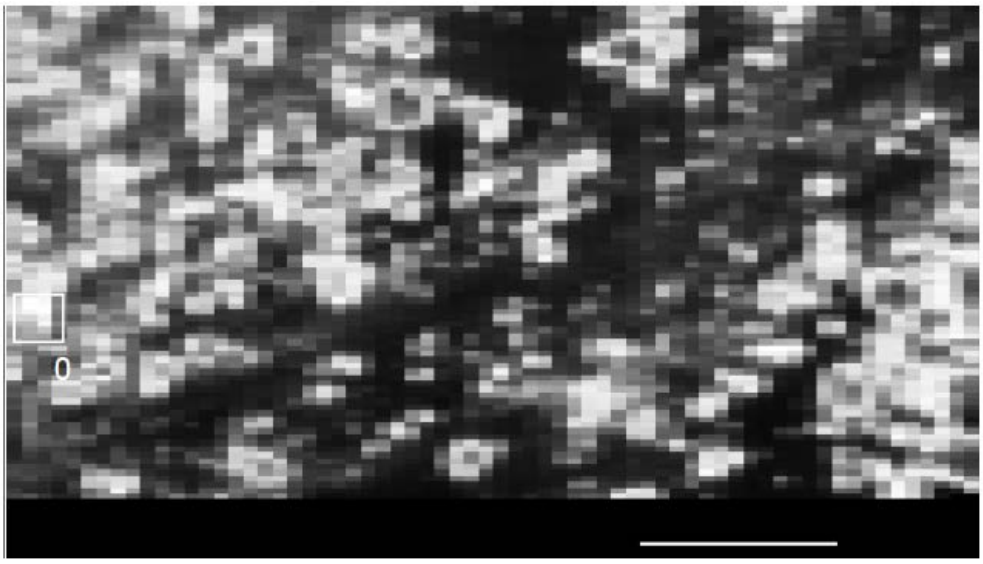

Supplemental figure 4.1: X-ray fluorescence maps for SUPR22-0.5m collected at ALS beamline 10.3.2. Spot 0 were analyzed for Fe 1s XANES. Map was collected for 11350µm X 10800µm area, with 15µm step, and 100ms dwell, E = 10000eV, scale bar is 200µm.

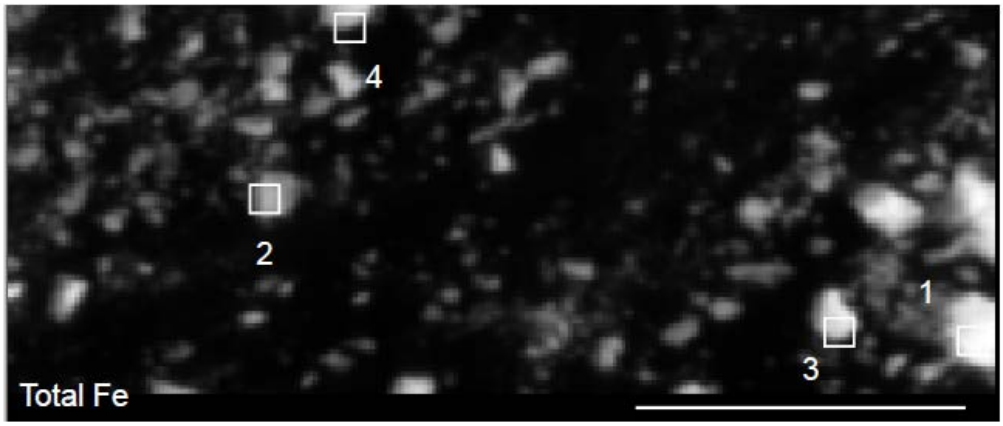

Supplemental figure 4.2: X-ray fluorescence maps for SUPR22-0.5m collected at ALS beamline 10.3.2. Spots 1-4 were analyzed for Fe 1s XANES. Map was collected for 10500µm X 11000µm area, with 4µm step, and 250ms dwell, E = 7350eV, scale bar is 300µm.

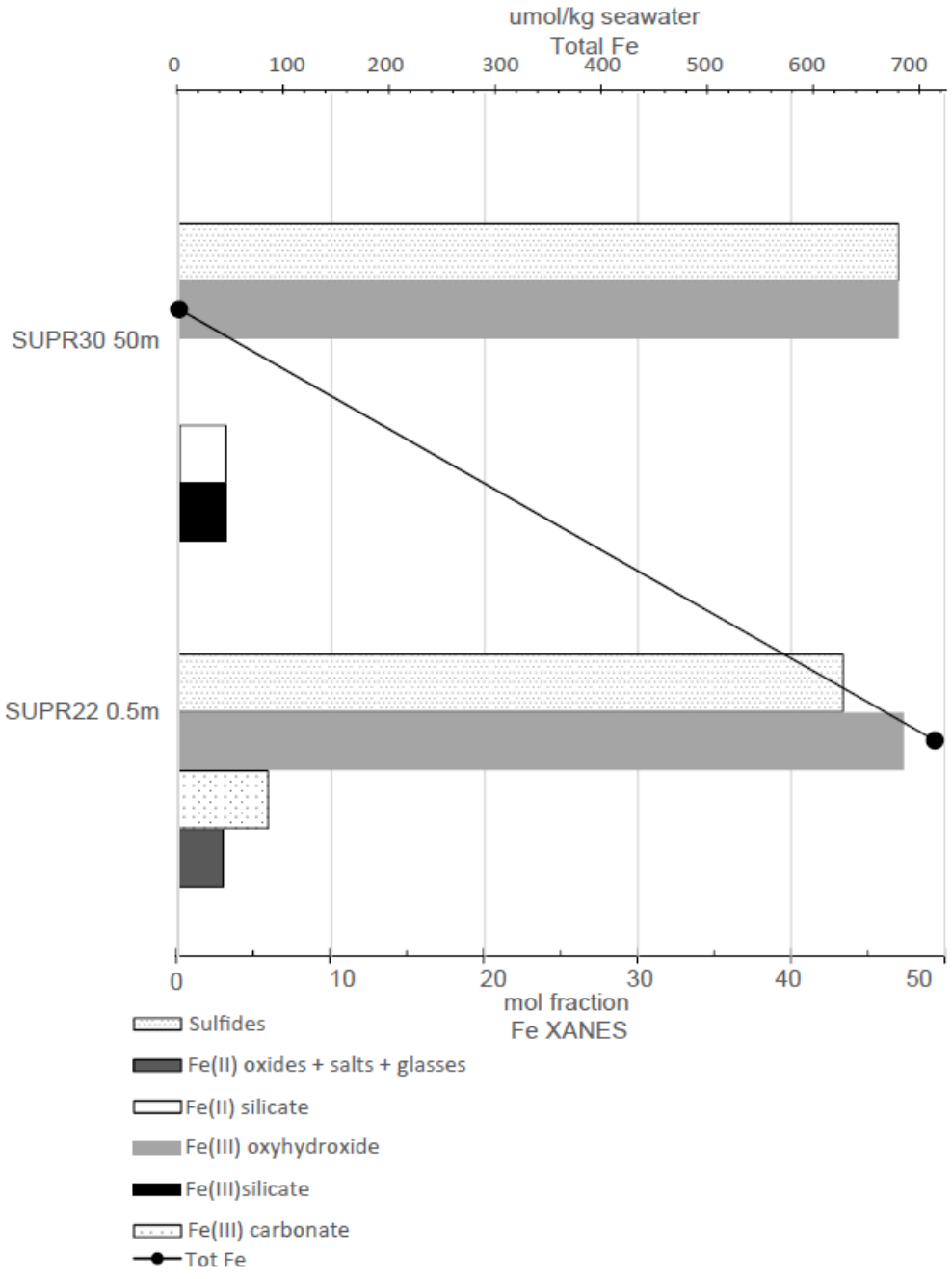

Supplemental figure 4.3: Bar chart displaying Fe 1s XANES and total Fe results for Beebe Vents hydrothermal fluids before background signal was removed.

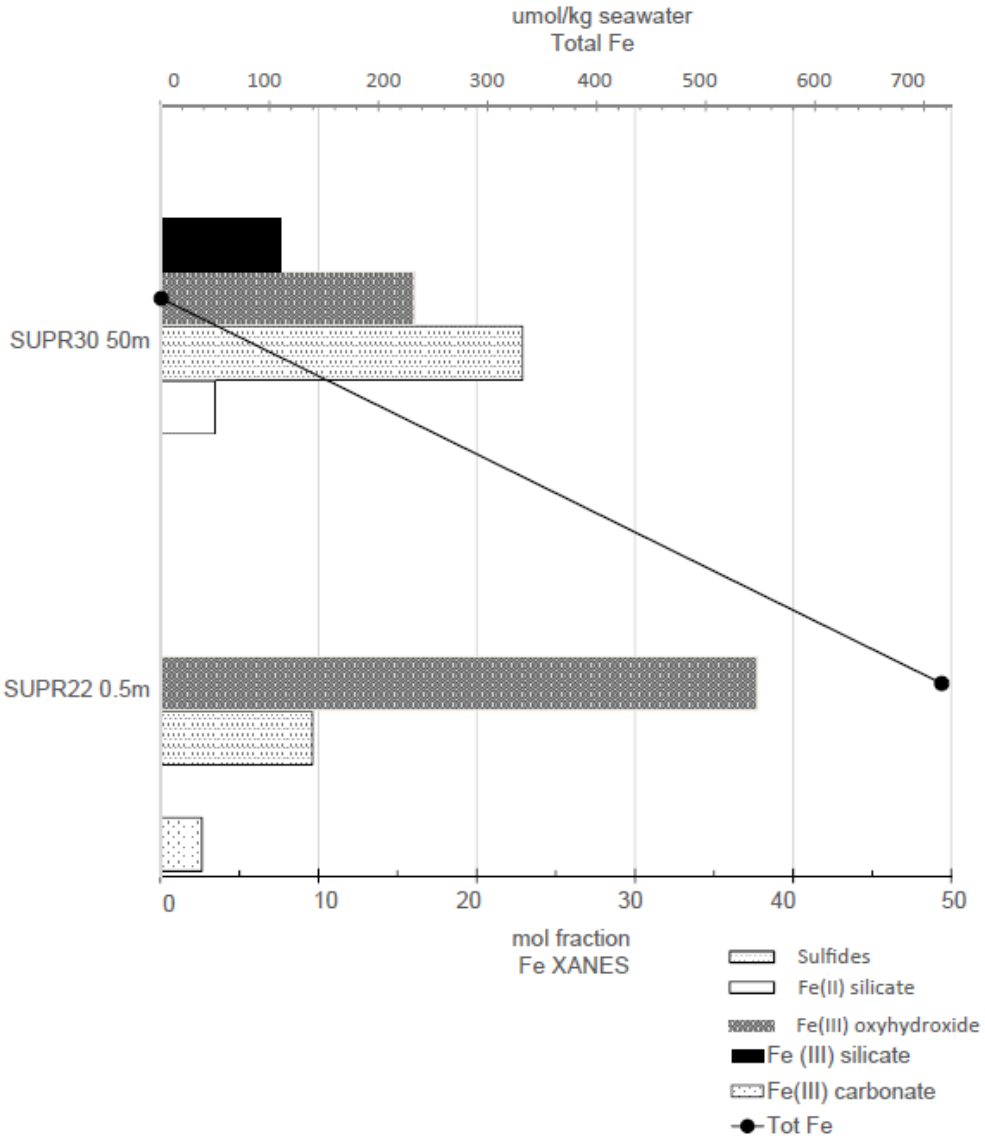

Supplemental figure 4.4: Bar chart displaying Fe chemical mapping and total Fe results for Beebe Vents hydrothermal fluids before the background signal was removed.

SUPPLEMENTAL TABLES

Supplemental table 4.1: Table lists the spot name where Fe 1s XANES were collected for SUPR05 (1m). The proportion (P), the component (C), sum, and NSS(X10-4) for the LCF results are listed. The elements detected by XRF mapping are also listed; as well as the beamline used to collect spectra. Nine XANES spots were analyzed and spectra were fit by the following reference spectra: almandine, hornblende, lizardite, richterite, roedderite, chlorite, cubanite, Mauna Loa basalt glass, FeS, pyrite, ferrihydrite, akaganeite, lepidocrocite, and STX clay. Fe 1s XANES spot 5 correlates with S 1s XANES spot 0. Fe XANES 1s spot 6 correlates with S 1s XANES spot 1.

Spot	P1	C1	P1	C1	P1	C1	sum	NSS ($X10^{-4}$)	Elements	Beamline
0	0.47	Ferrihydrite	0.53	Lepidocrocite	0.08	Mauna Loa Basalt glass	0.99	0.62		ALS 10.3.2
1	0.48	Akaganeite	0.12	Hornblende	0.38	Stx 1 Clay	0.99	0.87		ALS 10.3.2
2	0.77	Cubanite	0.15	Richterite	0.07	Roedderite	0.99	1.74		ALS 10.3.2
3	0.37	Chlorite	0.27	Lizardite	0.36	Stx 1 Clay	1	0.83		ALS 10.3.2
4	0.25	Cubanite	0.7	Pyrite	0.05	Roedderite	1	1		ALS 10.3.2
5	0.26	FeS	0.74	Pyrite	0	None	1	1.07	Fe, Cl, Si, Ni, As, Zn, Cu, Mn	ALS 10.3.2
6	0.98	Cubanite	0	None	0	None	0.98	3.16	Fe, Ni, Cu	ALS 10.3.2
7	0.11	Ferrihydrite 2k kim	0.51	Augite	0.32	Goethite	0.99	0.56	Fe	ALS 10.3.2
8	0.91	Almandine	0.06	FeSi2	0	None	0.97	4.63	Fe	ALS 10.3.2

Supplemental table 4.2: Table lists the spot name where Fe 1s XANES were collected for SUPR11 (8m). The proportion (P), the component (C), sum, and NSS($X10^{-4}$) for the LCF results are listed. The elements detected by XRF mapping are also listed. As well as the beamline used to collect spectra. Twelve XANES spots were analyzed and spectra were fit by the following reference spectra: augite, hornblende, richterite, psuedobrookite, chlorite, cubanite, pentlandite, FeSO4, pyrite, ferrihydrite, akaganeite, hematite, and STX clay.

Spot	P1	C1	P2	C2	P3	C3	sum	NSS (x10-4)	Elements	Beamline
0	0.24	Akaganeite	0.09	Chlorite ripidolite cca2	0.67	Hornblende	1	0.712		ALS 10.3.2
1	0.06	Chlorite ripidolite	0.85	Ferrihydrite 6l fendorf	0.08	Psuedobrookite	1	0.247		ALS 10.3.2
2	0.66	Ferrihydrite 6l fendorf	0.23	Psuedobrookite	0.1	Richterite	1	0.661		ALS 10.3.2
3	0.38	Akaganeite	0.55	Hornblende	0.07	Richterite	1	0.613		ALS 10.3.2
4	0.38	Chlorite ripidolite	0.23	FeSO4	0.38	Stx 1 Clay	1	1.23		ALS 10.3.2
5	0.3	Cubanite	0.38	Pentlandite	0.32	Stx 1 Clay	1	2.87		ALS 10.3.2
6	0.04	Chlorite ripidolite	0.86	Ferrihydrite 6l fendorf	0.09	Pyrite	1	0.266		ALS 10.3.2
7	0.06	Chlorite	0.74	Ferrihydrite 6l fendorf	0.19	Richterite	1	0.256		ALS 10.3.2
8	0.08	Chlorite	0.62	Hematite	0.29	Psuedobrookite	1	2.28	Si, Ti, Fe	ALS 10.3.2
9	0.88	Cubanite	0.11	Pyrite	0	none	1	3.32	Fe, Ni, Zn, Cu	ALS 10.3.2
10	0.34	Akaganeite	0.14	Augite	0.52	Richterite	1	0.91	Fe, Si, Ti	ALS 10.3.2
11	0.12	Chlorite	0.49	Ferrihydrite 6l fendorf	0.39	Stx 1 Clay	1	0.532	Fe	ALS 10.3.2

Supplemental table 4.3: Table lists the spot name and the region of the silicon nitride window where Fe 1s XANES were collected for SUPR57 (37m). The proportion (P), the component (C), sum, and NSS($X10^{-4}$) for the LCF results are listed. The elements detected by XRF mapping are also listed; as well as the beamline used to collect spectra. Seventeen Fe 1s XANES spots were analyzed and spectra were fit by the following reference spectra: hornblende, richterite, lizardite, chlorite, hercynite, cubanite, pentlandite, FeS, pyrite, goethite, ferrihydrite, akaganeite, toner biogenic oxide, and STX 1 clay.

Spot	P1	C1	P2	C2	P3	C3	sum	NSS (x10-4)	Elements	Beamline
0	0.11	Chlorite r2137	0.55	Ferrihydrite 6l fendorf	0.33	Stx 1 Clay	0.99	0.496		ALS 10.3.2
1	0.18	Biotite	0.4	Lizardite	0.42	Richterite	1	0.709		ALS 10.3.2
2	0.15	Chlorite ripidolite cca2	0.41	Ferrihydrite 6l fendorf	0.44	Stx 1 Clay	1	0.584		ALS 10.3.2
3	0.49	Akaganeite	0.51	Hornblende	0	none	1	0.838		ALS 10.3.2
4	0.42	Ferrihydrite 6l fendorf	0.54	Fe std 100 goe	0.02	Hercynite	0.98	0.539		ALS 10.3.2
5	0.1	Chlorite r2137	0.49	Ferrihydrite 6l fendorf	0.4	Stx 1 Clay	0.99	0.627		ALS 10.3.2
6	0.43	Akaganeite	0.14	Hornblende	0.42	Stx 1 Clay	0.99	0.491		ALS 10.3.2
7	0.5	Akaganeite	0.26	Lizardite	0.23	Stx 1 Clay	0.99	0.63		ALS 10.3.2
8	0.12	Chlorite r2139	0.48	Ferrihydrite 6l fendorf	0.4	Stx 1 Clay	0.99	0.552		ALS 10.3.2
9	0.22	Akaganeite	0.23	Biotite	0.55	Hornblende	1	1.13		ALS 10.3.2

10	0.54	Akaganeite	0.45	Stx 1 Clay	0	none	0.99	1.7		ALS 10.3.2
11	0.39	Cubanite	0.6	Pyrite	0	none	0.99	4.24	Fe, Ni, Zn, Mn, Ti, Ca, K, Cu	ALS 10.3.2
12	0.07	Chlorite r2137	0.49	Ferrihydrite 6l fendorf	0.42	Stx 1 Clay	0.99	0.686	Fe, Ca, Cu	ALS 10.3.2
13	0.22	Chlorite r2139	0.42	Richterite	0.35	Stx 1 Clay	0.99	0.886	Fe	ALS 10.3.2
14	0.68	Ferrihydrite 2l kim	0.31	Pyrite		none	1	0.519	Fe, Ca	ALS 10.3.2
15	0.18	FeS	0.32	Stx 1 Clay	0.5	Toner_biogenic_oxide	0.9	0.613	Ca, K	ALS 10.3.2
16	0.37	Pentlandite	0.637	Stx 1 Clay	0	none	1.01	537	Fe, Si	APS 13-ID-E

Supplemental table 4.4: Fe 1s XANES LCF results for SUPR58 (812m). Four XANES spots were analyzed and spectra were fit by the following reference spectra: stx Clay, 10ferrihydrite 90 goethite, akaganeite, metglass, roedderite, biotite, pigeonite, richterite, hornblende, and Fe foil.

Spot	P1	C1	P1	C1	P1	C1	sum	NSS ($X10^{-4}$)
0	0.49	10 ferrihydrite 90 goethite	0.20	Hornblende	0.27	Richterite	0.95	1.47
1	0.69	Fe foil	0.39	Metglass	0	None	1.08	1.25
2	0.28	Akaganeite	0.19	Biotite	0.37	Stx 1 Clay	0.85	1.12
3	0.61	Akaganeite	0.12	Pigeonite	0.25	Richterite	0.98	1.65

Supplemental table 4.5: Table lists the spot name and the region of the silicon nitride window where Fe 1s XANES were collected for SUPR22 (0.5m). The proportion (P), the component (C), sum, and NSS($X10^{-4}$) for the LCF results are listed.

Spot	P1	C1	P2	C2	P3	C3	sum	NSS (x10-4)	Elements
0	0.13	Coalingite	0.5	Fe std 100 ffh	0.37	Pyrite	1	27	Fe, Ca, S, Ni, Cl, Zn, Cu, Mn
1	0.22	Cubanite	0.61	ferri wet	0.16	FeS	0.99	44	Fe, Ca, S, Ni, Cl, Zn, Cu, Mn
2	0.51	Pyrite	0.49	Toner biogenic oxide	0	None	1	50	
3	0.38	Cubanite	0.41	ferri wet	0.19	Lepidocrocite	0.9	35	
4	0.36	Cubanite	0.45	Ferrihydrite 6l fendorf	0.18	Troilite	0.99	31	
5	0.23	Ferrihydrite 6l fendorf	0.33	FeS	0.44	Pyrite	1	51	
6	0.32	Cubanite	0.23	Lepidocrocite	0.44	Pyrite	0.99	45	
7	0.28	Coalingite	0.27	ferri wet	0.45	Pyrite	1	62	
8	0.57	Ferrihydrite_6l_fendorf	0.18	Greenrust_so4	0.24	Pentlandite	0.805	1	
9	0.08	Greenrust_so4	0.11	Haxonite	0.8	Lepidocrocite	0.99	1	
10	0.19	fe3o4	0.4	Lepidocrocite	0.42	Pyrite	1	1	
11	0.29	Coalingite	0.35	Psuedobrookite	0.36	Pyrite	1	1	

Supplemental table 4.6: Table lists the spot name and the region of the silicon nitride window where Fe 1s XANES were collected for SUPR30 (50m). The proportion (P), the component (C), sum, and NSS($X10^{-4}$) for the LCF results are listed.

Spot	P1	C1	P2	C2	P3	C3	sum	NSS (x10-4)
0	0.73	Cubanite	0.11	Pyrrhotite	0.15	Richterite	0.99	0.675
1	0.68	Cubanite	0.15	Pyrrhotite	0.17	Richterite	0.99	0.466
2	0.25	Cubanite	0.65	Ferrihydrite 6l fendorf	0.09	Pyrrhotite	0.99	0.317
3	0.27	Cubanite	0.62	Ferrihydrite 6l fendorf	0.1	Pyrrhotite	0.99	0.79
4	0.28	Cubanite	0.56	Ferrihydrite 6l fendorf	0.16	Pyrrhotite	0.99	0.365
5	0.21	Cubanite	0.67	Fe std 100 ffh	0.11	Pyrrhotite	0.99	0.399
6	0.3	Cubanite	0.56	Ferrihydrite 6l fendorf	0.13	Pyrrhotite	0.99	0.392
7	0.12	Cubanite	0.44	Fe std 100 ffh	0.44	Pyrite	0.99	0.526
8	0.14	Cubanite	0.66	Fe std 100 ffh	0.2	Pyrite	0.99	0.383
9	0.19	FeS	0.29	Stx 1 Clay	0.52	Toner biogenic oxide	0.99	0.507

Supplemental table 4.7: Concentration of Fe-bearing phases (mol% Fe on a per atom basis) identified through linear combination fitting of Fe 1s XANES with reference spectra. This is the data with the Fe(III) species in the 0.5m sample, before they were removed as background signal.

Category	SUPR22 0.5m Fe (mol%)	SUPR30 50m Fe (mol%)
Sulfides	44	47
Fe(II) oxides + salts + glasses	3	-
Fe(II) silicate	-	3
Fe(III) oxyhydroxide	47	47
Fe(III)silicate	-	3
Fe(III) carbonate	6	-

Supplemental table 4.8: Concentration of Fe-bearing phases (mol% Fe on a per atom basis) identified through linear combination fitting of Fe chemical map with reference spectra. This is the data with the Fe(III) species in the 0.5m sample, before they were removed as background signal.

Category	SUPR22 0.5m Fe (mol%)	SUPR30 50m Fe (mol%)
Sulfides	19	45
Fe(II) silicate	-	7
Fe(III) oxyhydroxide	75	32
Fe(III)silicate	-	15
Fe(III) carbonate	5	-

CHAPTER 5

Synthesis of results

1. SYNOPSIS

This study provides fine-scale characterization of the carbon (C), iron (Fe)- and sulfur (S)-particle geochemistry of two hydrothermal plumes located along the ultraslow (15-17 mm/yr full rate) spreading center, the Mid-Cayman Rise. The Mid-Cayman Rise is an ultra-slow spreading ridge located in the Western Caribbean Sea in the Cayman Trough (Rosencrantz and Mann, 1991). In 2009-2010, two hydrogen-rich vent sites were discovered along the Mid-Cayman Rise. Piccard is an basalt-hosted hydrothermal field, situated 800m deeper than any previously reported Mid-Ocean Ridge hydrothermal field, at 4960m below the surface of the ocean (Kinsey and German, 2013; German et al., 2015). The fluids from Beebe, one of three active vents in the Piccard hydrothermal field, are acidic (pH 3.2), sulfide-rich (12.3mM H2S), hydrogen-rich (20.7 mM H2), and methane depleted (0.13 mM CH4) compared to Von Damm (Mcdermott, 2015; Reveillaud et al., 2016) (Figure 1.4a). Von Damm is an ultramafic (peridotite influenced) hydrothermal vent, located 21km away from Beebe. Von Damm is half as deep as the Beebe Vents site (2350m below the surface of the ocean). The fluids are slightly acidic (pH 5.6) with up to 19.2 mM H2 and 2.8 mM CH4 (Reveillaud et al., 2016) (Figure 1.5). Samples were collected with a newly developed instrument, called the SUPR (SUspended Particle Rosette) (Breier et al., 2014). The SUPR was developed for high-precision collection of deep-sea samples, and it also made it possible to collect samples for complementary research efforts. Hydrothermal plume particles from the buoyant plume were collected by in situ filtration at four elevations above the Von Damm vent (1m, 8m,

37m, 812m above the vent orifice) as well as six elevations above the Beebe Vents site (0.5m, 5m, 15m, 30m, 50m, and APB).

The research goals for this study are: (1) interpret the chemical inputs to the base of the buoyant plume; (2) investigate the physical, biological, and chemical processes active within the buoyant plume leading to particle alteration; and, (3) determine if processes in the Mid-Cayman Rise plumes modulate hydrothermal fluxes to the deep ocean. To assess biogeochemical processes occurring within the buoyant hydrothermal plumes S, C, and Fe speciation was measured for particles and aggregates using: (1) microprobe S 1s and Fe 1s X-ray absorption near edge structure (XANES) spectroscopy, (2) microprobe X-ray fluorescence (XRF) chemical mapping, and (3) scanning transmission X-ray microscopy (STXM) based C 1s and Fe 2p XANES. The high resolution spectromicroscopy and X-ray microprobe analyses allowed for the characterization and speciation of nanoparticulate minerals at spatial scales relevant to in situ chemical and microbial processes.

The C data corroborates previous genomic research that has established the presence of microbial communities within the subsurface and the surrounding seawater at Von Damm. Carbon XANES of Von Damm fluids reveal the presence of biomolecules such as proteins, lipids, polysaccharides, and chitin in plume particles. Particles close to the vent are composed of chitin-rich materials from vent shrimp, while protein-rich microbial cells become more abundant in the rising plume. Unlike Von Damm, the Beebe Vents C images, maps, and XANES spectra reveal that the C concentration is low in the Beebe Vents particles.

The S 1s XANES and chemical maps of Von Damm buoyant plume particles reveal a diversity of S-bearing mineral phases, including sulfides. The buoyant plume particles

exhibit a wide variety of inorganic and organic S moieties spanning oxidation-reduction (redox) states from S (-2) to S (+6). Beebe Vents buoyant plume particles were composed mainly of iron-rich, strongly reduced (oxidation indices ≤ 1) inorganic S-bearing minerals (metal sulfides). In the first 30m of the rising plume, organic S moieties remain in low abundance, compared to Von Damm. The high concentration of strongly reduced metal sulfides and low concentration of organic S moieties indicates the Beebe Vents geochemistry is influenced primarily by inorganic processes in the first 30m of the plume.

Hydrothermal venting creates dynamic biogeochemical reactions zones where chemically reduced species, such as iron, into contact with organic matter (Breier et al., 2012). Iron 2p imaging and XANES indicate that nano-particulate Fe minerals are associated with particulate organic C (POC) at the 8m and 37m elevations. These images serve as examples of how Fe-C interactions could potentially serve as significant sources of Fe to the ocean.

2. INTRODUCTION

Research studies for the Mid-Cayman Rise have focused on the microbial metabolic diversity and community composition at the Von Damm and Beebe Vents sites. The Von Damm and Beebe Vents fluids have a greater range of biotic C sources in the Von Damm fluids (Bennett et al., 2015). Previously studied 13δC values indicate POC in Von Damm is influenced by autotrophic metabolic processes (subseafloor) and marine snow (upper water column) (Bennett et al., 2015). Stable C isotope 13δC values indicate POC in Beebe Vents is influenced by the metabolic processes of sulfide and Fe-oxidizing communities, and by the internal S cycle between S-oxidizers and ε- and γ-proteobacteria living symbiotically with the Rimicaris hybisae (Bennett et al., 2015). Energetic

modeling and metagenomic analyses indicate Von Damm and Beebe Vents share similar and dominant H-utilizing genera. These communities are fueled by the high hydrogen environment in both sites (Reveillaud et al., 2016).

Previous studies have focused on how microbial communities active within rising hydrothermal plumes might actively alter the particle composition within the fluids. Microbial populations capable of utilizing mineral substrates in the buoyant plume, as the fluids rise and laterally spread into the non-buoyant plume, have been characterized previously (Li et al., 2015; Anantharaman et al., 2015; Sheik et al., 2014; Dick et al., 2009). Transport time along the rising buoyant plume is short compared to the doubling time of low-temperature, deep-sea microbial populations. On average, transport along rising hydrothermal plumes occurs within 10s of minutes before the fluids reach the non-buoyant plume, and there is ~10 minutes before the fluids exiting the vent orifice are diluted with seawater (Reed et al, 2015). Doubling time for Fe-oxidizing Mariprofundus ferroxydans, in culture, is 12 hours (Emerson et al., 2007) and S- and H-oxidizing ε-proteobacteria Sulfuriomans paravinallae, in culture, is 13-15 hours (Takai et al, 2006).

A mathematical model that combined thermodynamics, growth and reaction kinetics, and transport processes derived from fluid dynamics of the ABE vent field of the Lau Basin demonstrated active metabolic communities within rising hydrothermal plume come from the surrounding seawater (Reed et al., 2015). These communities utilize reduced S in the rising plume. For example, communities such as members of the S-oxidizing ε-proteobacteria SUP05 and SAR324 are ready for growth as they are entrained into the rising plume fluids where reduced sulfur compounds are abundant. Previous work has demonstrated that distinct Mn-oxidizing microbial communities within the Guaymas Basin hydrothermal plumes respond to and alter the geochemical gradients within the buoyant plume (Dick et al., 2009). This study corroborates modeling efforts made by

Reed and others (2015) and observations already made by Dick and others (2009) of alteration plume geochemistry by microbial communities.

3. BIOGEOCHEMISTRY OF VON DAMM

The presence of cells in the C STXM images at 37m, suggest that entrainment of ambient seawater pulls in S-oxidizing microbial communities (SUP05) (Figure 2.2). Microbial inputs in hydrothermal fluids can come from the subseafloor environment, below the vent. In the Mid-Cayman Rise system, those include H- and S-oxidizing communities (Reveillaud et al., 2016). Microbial populations can also come from symbionts living with macrofauna. In the Mid-Cayman Rise, these include S-oxidizers and ε- and γ-proteobacteria living symbiotically with the Rimicaris hybisae (Bennett et al., 2015). Communities can also come from the surrounding seawater. In the Mid-Cayman Rise system, these ambient seawater communities include SUP05 (German et al., 2010; Breier et al., 2014).

Overall, the C 1s STXM and XANES reveal the evolution of organic C in the buoyant plume and the Fe- and S 1s XANES provide insight for the availability of mineral substrates, as well as the presence of altered (oxidized) mineral byproducts. The S-bearing particles in Von Damm include intermediate and oxidized S-bearing functionalities at every elevation. These S-bearing functionalities could be produced by biotic and abiotic S oxidation of sulfides. The presence of cellular material indicates the Fe and S is altered by biotic processes. For example, S XRF maps collected at 2-ID-B for the 8m sample, reveal images of what appear to be cells (Figure 3.11b). The S 1s XANES collected from within the cells, reveal the S associated with the cells is oxidized (gypsum and homocysteic acid) (Figure 3.8). The S XRF maps from 2-ID-B, combined with the C XANES, which reveal the presence of lipids and polysaccharides in the 8m particles

(Figure 2.3b), suggest that microbial processes alter fluid chemistry in the mid-plume environment.

Combined with the C 1s STXM and XANES, the Fe- and S 1s XANES, the data suggest that the Von Damm fluids are influenced by microbial metabolic processes at the 1m, 8m, and 37m intervals. The presence of shrimp detritus, cellular material, and cells at 1m above the vent orifice (Figure 2.3) suggest that biotic processes are generating the intermediate and oxidized S-bearing functionalities (sulfite, polysulfide, ester sulfate, and inorganic sulfate) in the near-vent environment (Figure 3.10). Cellular material and cells in the 37m sample (Figure 2.2i), including oxidized nanoparticulate Fe with cells (Figure 2.2 a-c, k-p), suggest microbial populations continue to alter plume particle geochemistry as the plume reaches the non-buoyant plume.

4. BIOGEOCHEMISTRY OF BEEBE VENTS

The C STXM and X-ray nanomicroprobe images reveal that the C concentration in Beebe Vents are much lower than Von Damm (Figure 2.4-2.6). The C-bearing particles at 0.5m are very low and it is not until the fluids reach 30m, 50m and 1456m within the Beebe Vents plume that C begin to resemble proteins, lipids, and polysaccharides (Fig.S2.3). Transmission images and C maps from Beebe reveal cells only in the SUPR44-APB sample (Figure 2.4). Unlike Von Damm, where POC is rich in cellular material and biomass, the Beebe Vents data suggests that the Beebe plume particle geochemistry is influenced primarily by inorganic processes up to ~30m in the rising plume. Bennett and colleagues (2015) determined that the POC in the Beebe fluids come from the entrainment of flocculent material from background seawater where chemoautotrophic processes contribute to complex organic C molecules, and our findings present imagery that can corroborate the presence of POC in the >30m samples in the Beebe Vents fluids.

The appearance of elemental S, sulfite, and polysulfides (species of intermediate oxidation indices) in the Beebe fluids at 0.5m, 30m, and 50m suggests that redox processes are active within the Beebe Vents plume (Figures 3.18-3.19). Based on the C 1s STXM images, the lack of cells and low abundance of organic C in the first 30m of the plume combined with the high concentration of reduced Fe and S-bearing minerals indicate inorganic chemical processes influence the types of Fe and S species present in the first 30m of the Beebe Vents hydrothermal plume. Oxidized S-bearing minerals in the higher elevations within the plume where microbial organisms can outcompete abiotic processes, include intermediate S-bearing mineral phases (sulfite and polysulfides) and strongly oxidized inorganic sulfate and organic sulfate (ester sulfate). These S-bearing minerals are an indication of entrainment of oxygenated seawater and S-oxidizing microbial communities into the rising plume.

Similar to Von Damm, the organisms are likely entrained from the surrounding seawater and from the host vent (Reed et al, 2015; Reveillaud et al., 2016). Lack of cellular material at 0.5m, compared to the near-vent cellular material at Von Damm, could be due to rapid dilution with seawater at Von Damm, or a lack of subseafloor communities in the Beebe Vents, due to high-temperature subseafloor (predicted to be 452 oC in Beebe Vents; McDermott, 2015) and end-member temperatures (398 oC; McDermott, 2015) (maximum temperature for life is 122 oC (Takai et al., 2008)).

5. THE LEAKY VENTS OF THE MID-CAYMAN RISE

The chemical signals from hydrothermal plumes can be detected thousands of kilometers from their vent source because particles <2 μm are capable of being dispersed within the neutrally buoyant plume into the open ocean (Baker and Massoth, 1987; Walker and

Baker ,1988). Stable minerals, such as pyrite, sphalerite, and chalcopyrite have long residence times in plumes and ocean sediments (Feely et al., 1987). Metal- and sulfur-rich hydrothermal fluids and chimneys support microbial communities (Toner et al, 2012). Synchrotron radiation studies, have proven useful in the characterization of nanoparticulate Fe- and S particles emitted from deep-sea hydrothermal vents (Breier et al., 2012; Toner et al., 2009).

Estrapa and others (2016) and McDermott (2014) determined that the particles within the Beebe Vents are iron-rich and too small to settle in the buoyant plume (<100 µm). The Fe and S 1s XANES, presented here, provide evidence for the presence of sulfides in both the Von Damm and Beebe Vents fluids that are <1 µm to 10 µm. Per Fe and S XAS data, S and Fe species exist in the reduced oxidation state in the Beebe fluids plume up into the APB sample. The presence of abundant reduced sulfides in the Beebe APB sample (SUPR44) corroborates previous data that suggest sulfides and oxidized Fe species remain within the buoyant plume, the far-field plume, and eventually the open ocean (Walker and Baker, 1988; Yücel et al., 2011). The Von Damm plume is not metal rich, and it is hard to consider it an example of an important Fe source to the oceans. The nanoparticulate Fe associated with microbial cells in the C 1s STXM images from the 37m and 11m sample from Von Damm do, however, serve as examples of how Fe-C interactions could potentially serve as significant sources of Fe to the ocean (Toner et al., 2009).

BIBLIOGRAPHY:

Agarwal B.K. (1979) X-ray Spectroscopy, Springer, Berlin Heidelberg, New York.

Alt, J.C., Shanks, W.C., Shanks, Jackson, M.C. (1993) Cyclcing of sulfur in subduction zones: The geochemsitry of sulfur in Mariana Island Arc and back-arc through. *Earth and Planetary Science Letters*. **119**, 477-494.

Alexander P. Webber, Stephen Roberts, Bramley J. Murton and M. R. S. H. (2015) Geology, sulfide geochemistry and supercritical venting at the Beebe Hydrothermal Vent Field, Cayman Trough. *Geochemistry, Geophys. Geosystems*, 2661–2678.

Anantharman, K., Breier, J.A., Dick, G.J. (2016) Metagenomic resolution of microibal functions in deep-sea hydrotheraml plumes across the Eastern Lau Spreading Center, *The ISME Journal*, **10**, 225-239.

Baker, E.T., and Massoth, G.J. (1987) Characteristics of hydrothermal plumes from two vent fields on the Juan de Fuca Ridge, northeast Pacific Ocean. *Earth and Planetary Science Letters.* **85,** 59-73.

Ballard R., Bryan W., Dick H., Emery K., Thompson G., Uchupi E., Davis K. E., De Boer J., Delong S. E. and Fox P. J. (1979) Geological and geophysical investigation of the Midcayman Rise Spreading Center: Initial results and observations. *Maurice Ewing Ser.* **2**, 66–93.

Bart, J.C.J. (1986) Near-Edge X-ray absorption spectroscopy in catalysis. *in Advances in Catalysis*. Vol. 34. 203-296.

Bennett, S.A., Achterberg, E.P., Connelly, D.P., Statham, Fones, G.R. (2008) The distribution and stabilisation of dissolved Fe in deep-sea hydrothermal plumes. Earth and Planetary Science Letters, 270 (3), 157-167.

Bennett S.A., Coleman M., Huber J. a., Reddington E., Kinsey J. C., McIntyre C., Seewald J. S. and German C. R. (2013) Trophic regions of a hydrothermal plume dispersing away from an ultramafic-hosted vent-system: Von Damm vent-site, Mid-Cayman Rise. *Geochemistry, Geophys. Geosystems* **14**, 317–327.

Bennett S. A., Dover C. Van, Breier J. a. and Coleman M. (2015) Effect of depth and vent fluid composition on the carbon sources at two neighboring deep-sea hydrothermal vent fields (Mid-Cayman Rise). *Deep Sea Res. Part I Oceanogr. Res. Pap.* **104**, 122–133.

Bennett, S.A., Hansman, R.L., Sessions, A.L., Nakamura, K., Edwards, K.J. (2011) Tracing iron-fueled microbial carbon production within the hydrothermal plumes at the Loihi seamount. *Geochimica et Cosmochimica Acta*. **75**, 5526-5539.

Bennett, S.A., Statham, P.J., Green, D.R., Bris, N.L., McDermott, J.M., Prado, F., Rouxel, O.J., Von Damm, K., German, C.R. (2012) Dissolved and particulate organic carbon in hydrothermal plumes from the East Pacific Rise, 9^{o}50'N. Deep-sea Research I. 58, 922-931.

Bischoff J. L. and Rosenbauer, R.J. (1987) Phase separation in seafloor geothermal systems; an experimental study of the effects on metal transport. Am J Sci 287, 953-978.

Bischoff J. L. and Dickson F. W. (1975) Seawater-basalt interaction at 200??C and 500

bars: Implications for origin of sea-floor heavy-metal deposits and regulation of seawater chemistry. *Earth Planet. Sci. Lett.* **25**, 385–397.

Boyce, K.C., Cody, G.D., Feser, M., Jacobsen, C., Knoll, A.H., Wirick, S. (2002) Organic chemical differentiation within fossil plant cell walls detected with X-ray spectromicroscopy. *Geology*. **30**, 1039-1042.

Breier J. A, Sheik, C.S, Gomez-Ibanez, D., Sayre-McCord, R.T., Sanger R., Rauch C., Coleman M., Bennett, S.A., Cron, B.R., Li, M., German, C.R., Toner, B.M., Dick, G.J. (2014) A large volume particulate and water multi-sampler with in situ preservation for microbial and biogeochemical studies . Deep-Sea Research I, **94**, 195–206.

Breier J.A.., Toner B. M., Fakra S. C., Marcus M. a., White S. N., Thurnherr a. M. and German C. R. (2012) Sulfur, sulfides, oxides and organic matter aggregated in submarine hydrothermal plumes at 9°50′N East Pacific Rise. *Geochim. Cosmochim. Acta*.

Brindley GW, Brown G (1980) Crystal structures of clay minerals and their X-ray identification.
Mineralogical Society, London

Burton, E.D., Bush, R.T., Sullivan, L.A., Hocking, R.K., Mitchell, D.R.G, Johnston, S.G., Fitzpatrick, R.W., Raven, M., McClure, S., Jang, L.Y. (2009) Iron-Monosulfide Oxidation in Natural Sedimetns: Resolving Microbially Mediated S Transformations Using XANES, Electron Microscopy, an Selective Extractions. *Environmental Science and Technology*, **43**, 3128-3134.

Carazzo, G., Jellinek, A.M., Turchyn, A.V. (2013) The remarkable longevity of submarine plumes: Implications for the hydrothermal input of iron to the deep-ocean. Earth and Planeatry Science Letters, 382, 66-76.

Chan C. S., Stasio G. De, Welch S. a, Fakra S. and Banfield J. F. (2004) Nanocrystal Fibers. *Science*. **303**, 1656-1658.

Chan, C.S., Fakra, S.C., Emerson, D., Fleming, E.J., Edwards, K.J. (2011) Lithotrophic iron-oxidizing bacteria produce organic stalks to control mineral growth implications for biosignature formation. The ISME Journal. **5**, 717-727.

Chung J.-S. and Ice G. (1999) Automated indexing for texture and strain measurement with broad-bandpass x-ray microbeams. *J. Appl. Phys.* **86**, 5249–5255.

Cody, G.D., Brandes, J., Jacobsen, C., Wirick, S. (2009) Soft X-ray induced chemical modification of polysacchradies in vascular plant cell walls. *Journal of Electron Spectroscopy and Related Phenomena.* **170**, 57-64.

Cody G. D., Ade H., Wirick S., Mitchell G. D. and Davis a. (1998) Determination of chemical-structural changes in vitrinite accompanying luminescence alteration using C-NEXAFS analysis. *Org. Geochem.* **28**, 441–455.

Connelly D. P., Copley J. T. P., Murton B. J., Stansfield K., Tyler P. a., German C. R., Dover V., Cindy L., Amon D., Furlong M., Grindlay N., Hayman N., Hühnerbach V., Judge M., Le Bas T., McPhail S., Meier A., Nakamura K., Nye V., Pebody M., Pedersen R. B., Plouviez S., Sands C., Searle R. C., Stevenson P., Taws S. and Wilcox S. (2012) Hydrothermal vent fields and chemosynthetic biota on the world's deepest seafloor spreading centre. *Nat. Commun.* **3**, 620.

Cosmidis J. and Templeton A. S. (2016) Self-assembly of biomorphic carbon/sulfur microstructures in sulfidic environments. *Nat. Commun.* **7**, 12812.

Dasch, E.J. (1971) Isotopic analysis of metalliferous sediment from East Pacific Rise, Earth and Planetary Science Letters, 13, 175-180.

Dick, G.J., Clement, B.G., Webb, S.M., Fodrie, F.J., Bargar, J.R., Tebo, B.M. (2009) Enzymatic microbial Mn(II) oxidation and Mn biooxide production in the Guaymas Basin deep-sea hydrotheraml plume. *Geochemica et Cosmochimica Atca.* **73**, 6517-6530.

Emerson, D., Rentz, J.A., Lilburn, T.G., Davis, R.E., Aldrich, H., Chan, C., Moyer, C.L. (2007) A novel lineage of proteobacteria involved in formation of marine Fe-oxidizing microbial mat communities. PLoS One.

Edmond, J.M., Measures, C., McDuff, R.E., Chan, L.H., Grant, C.B. (1979) Ridge Crest hydrotheraml activity and the balances of major and minor elements in the ocean: The Galapagos data, Earth and PLanetary Science Letters 46, 1-18.

Estrapa, M.L., Breier, J.A., and German, C.R. (2015) Particle dynamics in the rising plume at Piccard Hydrothermal Field, Mid-Cayman Rise. *Geochemitry, Geophysics, Geosystems*. **16**, 2726-2774. Feely, R.A., Lewison, M., Massoth, G.J., RObert-Baldo, G., Lavelle, W., Byrne, R.H., Von Damm, K.L., and Curl, C. Jr. (1987) Composition and Dissolution of Black Smoker Particulates From Active Vents on the Juan de Fuca Ridge. *Journal of Geophysical Research*. **92**, 347-363.

Field, M.P. and Sherrel, R.M. (2000) Dissolved and particulate Fe in a hydrothermal plume at 945'N, East Pacific Rise: slow Fe(II) oxidation kinetics in Pacific plumes, Geochim. Cosmochim. Atca, 64, 619-628.

Findlay A. J., Gartman A., MacDonald D. J., Hanson T. E., Shaw T. J. and Luther G. W. (2014) Distribution and size fractionation of elemental sulfur in aqueous environments: The Chesapeake Bay and Mid-Atlantic Ridge. *Geochim. Cosmochim. Acta* **142**, 334–348.

Fitzsimmons, J.N., Boyle, E.A., Jenkins, W.J. (2014) Distal transport of dissolved hydrothermal iron in the deep South Pacific Ocean. Proc. Natl. Acad. Sci. U.S.A. 111 (47)

Garcia, Jr, A.A. and G.K. Druschel (2014) Elemental sulfur coarsening kinetics.**15** (1):11.

Gartman, A., Findlay, A.J., Luther, G.W. (2014) Nanoparticulate pyrite and other nanoparticles are a widespread component of hydrotheraml vent black smoker emissions, Chemical Geology, 366, 32-41.

German, C.R., Fleer, A.P., Bacon, M.P., and Edmond, J.M. (1991) Hydrothermal scavenging at the Mid-Atlantic Ridge: Radionuclide distribution. Earth and Planetary Science Letters, 105, 170-181.

German C. R., Legendre L. L., Sander S. G., Niquil N., Luther G. W., Bharati L., Han X. and Le Bris N. (2015) Hydrothermal Fe cycling and deep ocean organic carbon scavenging: Model-based evidence for significant POC supply to seafloor sediments. *Earth Planet. Sci. Lett.* **419**, 143–153.

German C. R., Bowen a, Coleman M. L., Honig D. L., Huber J. a, Jakuba M. V, Kinsey J. C., Kurz M. D., Leroy S., McDermott J. M., de Lépinay B. M., Nakamura K.,

Seewald J. S., Smith J. L., Sylva S. P., Van Dover C. L., Whitcomb L. L. and Yoerger D. R. (2010) Diverse styles of submarine venting on the ultraslow spreading Mid-Cayman Rise. *Proc. Natl. Acad. Sci. U. S. A.* **107**, 14020–5.

German C. R. and Seyfried W. E. (2014) *Hydrothermal Processes*. 2nd ed., Elsevier Ltd.

German C. R., Bowen a, Coleman M. L., Honig D. L., Huber J. a, Jakuba M. V, Kinsey J. C., Kurz M. D., Leroy S., McDermott J. M., de Lépinay B. M., Nakamura K., Seewald J. S., Smith J. L., Sylva S. P., Van Dover C. L., Whitcomb L. L. and Yoerger D. R. (2010) Diverse styles of submarine venting on the ultraslow spreading Mid-Cayman Rise. *Proc. Natl. Acad. Sci. U. S. A.* **107**, 14020–5.

Goh, S.W., Buckly, A.N., Lamb, R.N. Rosenbergy, R.A., Moran, D. (2006) The oxidation states of copper and iron in mineral sulfides, and the oxides formed on initial exposure of chalcopyrite and bornite to air. *Geochimica et Cosmochimica Acta*. 70, 2210-2228.

Gordon, R.M., Martin, J.H., and Knauer, G.A. (1982) Iron in north-east Pacific waters, Nature, **299**, 611-612.

Hitchcock, A. P. (2009) aXis2000 Is an IDL-Based Analytical Package

Haase K. M., Petersen S., Koschinsky A., Seifert R., Devey C. W., Keir R., Lackschewitz K. S., Melchert B., Perner M., Schmale O., Süling J., Dubilier N., Zielinski F., Fretzdorff S., Garbe-Schönberg D., Westernströer U., German C. R., Shank T. M., Yoerger D., Giere O., Kuever J., Marbler H., Mawick J., Mertens C., Stöber U., Walter M., Paulick H., Peters M., Strauss H., Sander S., Stecher J., Warmuth M., Weber S. and Ostertag-Henning C. (2007) Young volcanism and related hydrothermal activity at 5°S on the slow-spreading southern Mid-Atlantic Ridge. *Geochemistry, Geophys. Geosystems* **8**, 1–17.

Hayman N. W., Grindlay N. R., Perfit M. R., Mann P., Leroy S. and De Lépinay B. M. (2011) Oceanic core complex development at the ultraslow spreading Mid-Cayman Spreading Center. *Geochemistry, Geophys. Geosystems* **12**, Q0AG02, doi:10.1029/2010GC003240.

Holland, H.D. (1984) *The Chemical Evolution of the Atmosphere and Oceans*: Princeton University Press Princeton, NJ, 582.

Ice G. E. and Pang J. W. L. (2009) Tutorial on x-ray microLaue diffraction. *Mater. Charact.* **60**, 1191–1201.

Kadko D. (1993) An assessment of the effect of chemical scavenging within submarine hydrothermal plumes upon ocean geochemistry. Earth and Planetary Science Letters, **120**, 361–374.

Kadko, D., Michael, B.P., and Hudson, A. (1986/1987) Enhanced scavenging of ^{210}Pb and ^{210}Po by processes associated with the East Pacific Rise near 8^{o}45'N Earth and Planetary Science Letters, 81, 349-357.

Kadko, D., Feely, R., and Massoth, G. (1991) Scavenging of ^{234}Th and phosphate removal from the hydrothermal effluent plume over north cleft segment of Juan de Fuca Ridge. J. Geophys. Res. 99, 5017-5024.

Kilcoyne A. L. D., Tyliszczak T., Steele W. F., Fakra S., Hitchcock P., Franck K., Anderson E., Harteneck B., Rightor E. G., Mitchell G. E., Hitchcock A. P., Yang L., Warwick T. and Ade H. (2003) Interferometer-controlled scanning transmission X-

ray microscopes at the Advanced Light Source. *J. Synchrotron Radiat.* **10**, 125–136.
Kinsey J. C. and German C. R. (2013) Sustained volcanically-hosted venting at ultraslow ridges: Piccard Hydrothermal Field, Mid-Cayman Rise. *Earth Planet. Sci. Lett.* **380**, 162–168. Available at: http://dx.doi.org/10.1016/j.epsl.2013.08.001.
Koschinsky A., Garbe-Schönberg D., Sander S., Schmidt K., Gennerich H. H. and Strauss H. (2008) Hydrothermal venting at pressure-temperature conditions above the critical point of seawater, 5??S on the Mid-Atlantic Ridge. *Geology* **36**, 615–618.
Kunzl, V. (1932) Linear dependence of energy levels on the valency of elements. Collect. Czech. Commun. **4**, 213-224.
Lam, P.J., Bishop, J.K.B., Henning, C.C., Marcus, M.A., Waychunas, G.A., and Fung, I.Y. (2006) Wintertime phytoplankton bloom in the subarctic Pacific supported by continental margin iron. **20**.
Li, M., Toner, B.M., Baker, B.J., Breier, J.A., Sheik, C.S., Dick, G.J. (2014) Microbial uptake as a mechanism for dispersing iron from deep-sea hydrothermal vents. *Nature Communications.* **5**.
Li, M., Baker, B.J., Anantharaman, K., Jain, S., Breier, J.A., Dick, G.J. (2015) Genomic and transcriptomic evidence for scavenging of diverse organic compounds by widespread deep-sea archaea. *Nature Communications.* **5**.
Luther G.W. III (1990) Frontier molecular orbital approach in geochemical process. In: Stumm W (ed.) Aquatic Chemical Kinetics. Berlin: Springer, 1990, 173-98.
Luther G.W. III (1991) Pyrite synthesis via polysulfide compounds. Geochimica Cosmochimica Acta. 55, 2839-49.
Luther G.W. III, Church, T.M., Scudlark. J.R., Cosman, M. (1986) Inorganic and organic sulfur cycling in salt-marsh porewaters. Science. 232, 479-9.
Luther, G.W. III, Glazer, B.T., Hohmann, L., Popp, J.I., Taillefert, M., Rozan, T.F., Brendel, P.J., Theberge, S.M., Nuzzio, B.D. (2001) Sulfur speciation monitored in situ with solid state gold amalgam voltammetric electrodes: polysulfides as a special case in sediments, microbial mats and hydrothermal waters. J Environ Monitor, 3, 31-6.
MacDowell A. A., Celestre R. S., Tamura N., Spolenak R., Valek B., Brown W. L., Bravman J. C., Padmore H. A., Batterman B. W. and Patel J. R. (2001) Submicron X-ray diffraction. *Nucl. Instruments Methods Phys. Res. Sect. A Accel. Spectrometers, Detect. Assoc. Equip.* **467**–**468**, 936–943.
Manceau, A., Marcus, M.A., Tamura, N. (2000) Quantitative Speciation of Heavy Metals in Soils an Sediments by Synchrotron X-ray Techniques in Reviews in Mineralogy and Geochemistry, 49 (1) 341-428.
Manceau A. and Nagy K. L. (2012) Quantitative analysis of sulfur functional groups in natural organic matter by XANES spectroscopy. *Geochim. Cosmochim. Acta* **99**, 206–223..
Mande, C. and Sapre, V.B. (1982) Chemical shifts in X-ray absorption spectra. in Advances in X-ray spectroscopy - contributions in honour of Professor Y. Cauchois. (ed. C. Bonnelle and C. Mande) Chap. 17, pp. 287-301. Pergamon Press.

Marcus, M.A., Manceau, A., and Kersten, M. (2004a) Mn, Fe, Zn and As speciation in a fast-growing ferromanganese marine nodule. *Geochem.Cosmochim. Acta*, **68**, 3125-3136.

Marcus, M.A., MacDowel, A., Celestre, R., Manceau, A., Miller, T., Padmore., H.A., Sublett, R.E. (2004b) Beamline 10.3.2 at ALS: a hard X-ray microprobe for environmental and material sciences. J. Synchrotron Rad. 11, 239-247.

Marcus, M.A., Westphal, A.J., and Fakra, S.C. (2008) Classificationo f Fe-bearing species from K-edge XANES data using two-parameter correlation plots. *Journal of Synchrotron Radiation.* **15**, 463-468.

McDermott J. M. (2014) Geochemistry of deep-sea hydrothermal vent fluids from the Mid-Cayman Rise , Caribbean Sea. PhD thesis. Chemical Oceanography, MIT/WHOI Joint Program in Oceanography, Woods Hole, MA, USA.

McDermott J. M., Ono S., Tivey M. K., Seewald J. S., Iii C. S. and Solow A. R. (2015a) Identification of sulfur sources and isotopic equilibria in submarine hot-springs using multiple sulfur isotopes. *Geochim. Cosmochim. Acta*.

McDermott J.M., Seewald, J.S., German, C.R., and Sylva, S.P. (2015b) Pathways for abiotic organic synthesis at submarine hydrothermal fields. *PNAS.* 112, 7668-7672.

McNulty, I., Frigo, S.P., Retsch, C.C., Wang, R.Y., Feng, Y.P., Qian, Y., Trakhtenberg, E., Tieman, B., Cha, B.C., Goetze, K., Mooney, T. (1998) Design and performance of the 2-ID-B scanning X-ray microscope. SPIE Proc. 3449: 67.

Millero, F.J. (2001) Physical Chemistry of Natural Waters. Wiley Interscience. Wiley & Sons, New York, pp 323 – 347.

Mottl, M.J. (1983) Metabasalts, axial hot springs and the structure of hydrothermal systems at Mid-Ocean Ridges. Geology Society of America Bulletin 94, 161-180.

Mottl, M.J. and McConachy, T.F. (1990) Chemical processes in buoyant hydrothermal plumes on the East Pacific Rise near 21^{o}N. Geochim. Cosmochim. Acta. 54 (7), 1911-1927.

Myneni, S.C. (2000) X-Ray and vibrational spectroscopy of sulfate in earth minerals.Reveiws in Mineralogy and Geochemistry. **40** (1)

Neder R. B., Burghammer M., Grasl T. H., Schulz H., Bram A. and Fiedler S. (1999) Refinement of the kaolinite structure from single-crystal synchrotron data. *Clays Clay Miner*. **47**, 487–494.

Newville, M., Sutton, S., Rivers, M., Eng, P. (1999) Micro-beam X-ray absorption and fluorescence spectroscopies at GSECARS: APS beamline 131D. Journal of Synchrotron Radiation, **6**, 353-355.

Nye V., Copley J. and Plouviez S. (2012) A new species of Rimicaris (Crustacea: Decapoda: Caridea: Alvinocarididae) from hydrothermal vent fields on the Mid-Cayman Spreading Centre, Caribbean. *J. Mar. Biol. Assoc. United Kingdom* **92**, 1057–1072.

Ono S., Shanks W. C., Rouxel O. J. and Rumble D. (2007) S-33 constraints on the seawater sulfate contribution in modern seafloor hydrothermal vent sulfides. *Geochim. Cosmochim. Acta* **71**, 1170–1182.

Oosting, S.E. and Von Damm, K.L. (1996) Bromide/chloride fractionation in seaflor

hydrothermal fluids from 9-10°N East Pacific Rise. *Earth Planet. Sci. Lett.* **144**, 133-145.

Pasteris, J.D., Freeman, J.J., Goffredi, S.K., and Buck, K.R. (2001) Raman spectroscopic and laser scanning confocal microscopic analysis of S in living S-precipitating marine bacteria. Chemical Geology **180**, 3-18

Pester N. J., Rough M., Ding K. and Seyfried W. E. (2011) A new Fe/Mn geothermometer for hydrothermal systems: Implications for high-salinity fluids at 13??N on the East Pacific Rise. *Geochim. Cosmochim. Acta* **75**, 7881–7892. Available at: http://dx.doi.org/10.1016/j.gca.2011.08.043.

Plouviez S., Jacobson A., Wu M. and Van Dover C. L. (2015) Characterization of vent fauna at the Mid-Cayman Spreading Center. *Deep Sea Res. Part I Oceanogr. Res. Pap.* **97**, 124–133.

Prietzel J., Thieme J., Neuhaeusler U., Susini J. and Koegel-Knabner I. (2003) Speciation of sulfur in soils and soil particles by X-ray spectromicroscopy. *Eur. J. Soil Sci.* **54**, 423–433.

Proskurowski G., Lilley M. D., Seewald J. S., Früh-Green G. L., Olson E. J., Lupton J. E., Sylva S. P. and Kelley D. S. (2008) Abiogenic hydrocarbon production at lost city hydrothermal field. *Science* **319**, 604–7. Available at: http://www.ncbi.nlm.nih.gov/pubmed/18239121.

Pyzik A. J. and Sommer S. E. (1981) Sedimentary iron monosulfides: Kinetics and mechanism of formation. *Geochim. Cosmochim. Acta* **45**, 687–698.

Ravel and Newville (2005) ATHENA, ARTEMIS, HEPHAESTUS: data analysis of X-ray absorption spectroscopy using IFEFIT. Journal of Synchrotron Radiation. **12**, 537-541.

Reveillaud J., Reddington E., McDermott J., Algar C., Meyer J. L., Sylva S., Seewald J., German C. R. and Huber J. A. (2016) Subseafloor microbial communities in hydrogen-rich vent fluids from hydrothermal systems along the Mid-Cayman Rise. *Environ. Microbiol.* **18**, 1970–1987.

Reed, D.C., Breier, J.A., Jiang, H., Anantharaman, K., Klausmeier, C.A., Toner, B.M., Hancock, C., Speer, K., Thurnherr, A.M., and Dick, G.J. (2015) Predicting the response of the deep-ocean microbiome to geochemical perturbations by hydrothermal vents. *The ISME Journal*. **9**, 1857-1869.

Rickard D. and Luther G. W. (1997) Kinetics of pyrite formation by the H2S oxidation of iron (II) monosulfide in aqueous solutions between 25 and 125°C: The mechanism. *Geochim. Cosmochim. Acta* **61**, 135–147.

Rickard D. and Luther G. W. (2007) *Chemistry of iron sulfides*.Chem.Rev, 107, 514-562.

Rosencrantz E. and Mann P. (1991) Sea MARC II mapping of transform faults in the Cayman Trough, Caribbean Sea. *Geology* **19**, 690–693.

Rouxel, O. Shanks, III, W.C., Bach, W., Edwards, K.J. (2008) Integrated Fe- and S-isotope study of seafloor hydrothermal vents at East Pacific Rise 9-10°C N. Chem. Geol. 252, 214-227.

Rouxel, O., Toner, B.M., Manganini, S.J., German, C.R. (2016) Geochemistry and iron isotope systematics of hydrothermal plume fall- out at East Pacific Rise 9°50'N, Chemical Geology, 441, 212-234.

Saito, M.A., Noble, A.E., Tagliabue, A., Goepfert, T.J., Lamborge, C.H., Jenkins, W.J. (2013) Slow-spreading submarine ridges in the South Atlantic as a significant oceanic iron source. Nature Geoscience, 6 (9), 775-779.

Shanks III, W.C. (2001) Stable isotopes in seafloor hydrothermal systems: vent fluids, hydrothermal deposits, hydrothermal alteration, and microbial process. Reviews in Mineralogy and Geochemisry **43**, 468-525.

Sheik C.S., Anantharaman, K., Breier, J.A., Sylvan, J.B., Edwards, K.J., and Dick, G.J. (2014) Spatially resolved sampling reveals dynamic microbial communities in rising hydrothermal plumes across a back-arc basin. The ISME Journal, 1-12.

Shock E. L. (1990) Geochemical constraints on the origin of organic compounds in hydrothermal systems. *Orig. Life Evol. Biosph.* **20**, 331–367.

Shock E. L. and Schulte M. D. (1998) Organic synthesis during fluid mixing in hydrothermal systems. *J. Geophys. Res. Planets* **103**, 28513–28527. Available at: http://doi.wiley.com/10.1029/98JE02142.

Solomon, D., Lehmann, J., Kinyangi, J., Liang, B., Heymann, K., Dathe, L., Hanely, K. (2009) Carbon 1s NEXAFS spectroscopy of biogeochemically relevant referenc organic compounds. *Soil, Sci. Soc. Am. J.* **73**, 1817-1830.

Steudel, R. (2003) Aqueous Sulfur Sols. in Elemental Sulfur and Sulfur-Rich Compounds I. 230, 153-166.

Syverson D. D., Borrok D. M. and Seyfried W. E. (2013) Experimental determination of equilibrium Fe isotopic fractionation between pyrite and dissolved Fe under hydrothermal conditions. *Geochim. Cosmochim. Acta* **122**, 170–183.

Takai, K., Nakamura, K., Toki, T., Tsunogai, U., Miyazaki, M., Miyazaki, J., Hirayma, H., Nakagawa, S., Nunoura, T., Horikoshi, K., (2008) Cell proliferation at 122^{o}C and isotopically heavey CH_4 production by a hyperthermophilic methanogen under high-pressure cultivation. Proceedings of the National Academy of Sciences of the United States of American **105**, 10919-10954.

Tamura N., Celestre R. S., MacDowell A. A., Padmore H. A., Spolenak R., Valek B. C., Meier Chang N., Manceau A. and Patel J. R. (2002) Submicron x-ray diffraction and its applications to problems in materials and environmental science. *Rev. Sci. Instrum.* **73**, 1369.

Teo B. K. (1986) *EXAFS: Basic Principles and Data Analysis,* in Inorganic Chemistry Concepts, 9.

Tivey, M.K. (2007) Generation of seafloor hydrothermal vent fluids and associated mineral deposits, Oceanography, 20 (1), 50-65.

Toner B. M., Fakra S. C., Manganini S. J., Santelli C. M., Marcus M. a., Moffett J. W., Rouxel O., German C. R. and Edwards K. J. (2009) Preservation of iron(II) by carbon-rich matrices in a hydrothermal plume. *Nat. Geosci.* **2**, 197–201.

Toner B., Marcus M., Edwards K., Rouxel O. and German C. (2012) Measuring the Form of Iron in Hydrothermal Plume Particles. *Oceanography* **25**, 209–212.

Toner B. M., Nicholas, S.L., and Coleman Wick, J. (2014) Scaling up : fulfilling the promise of X-ray microprobe for biogeochemical research. , 4–9.

Toner, B. M., German, C. R., Dick, G. J., and Breier, J. A. (2016). Deciphering the Complex Chemistry of Deep-Ocean Particles Using Complementary Synchrotron X - ray Microscope and Microprobe Instruments.*Accounts of Chemical Research* **49**, 128-137.

Vairavamurthy, A. (1998) Using X-ray absorption to probe sulfur oxidation states in complex molecules. *Spectrochim. Acta Part A Mol. Biomol. Spectrosc.* **54**, 2009–2017.

Vairavamurthy, M.A., Maletic, D., Wang, S., Manowitz, B., Eglinton, T., and Lyons, T. (1997) Characterization of sulfur-containing functional groups in sedimentary humic substances by X-ray absorption absorption near-edge structure spectroscopy. *Energy fuels*, **11**, 546-553.

Vairavamurthy, A., Manowitz, B., Luther III, G.W., Yeon, Y. (1993) "Oxidation state of sulfur in thiosulfate and implications for anaerobic energy metabolism." Geochimica et Comochimica Acta. *Geochim. Cosmochim. Acta* **57**, 3199.

Vairavamurthy, M.A., Orr, W.L., and Manowitz, B. (1995) Geochemical Transformations of Sedimentary Sulfur: An Introduction. in American Chemical Society. pp, 1-14.

Walker, S.L. and Baker, E.T. (1988)Particle-size distribution within hydrothermal plumes over the Juan De Fuca Ridge. *Marine Geology*. **78**, 217-226.

Warwick T., Ade H., Kilcoyne D., Kritscher M., Tylisczcak T., Fakra S., Hitchcock A., Hitchcock P. and Padmore H. (2002) A new bend-magnet beamline for scanning transmission X-ray microscopy at the Advanced Light Source. *J. Synchrotron Rad.* **9**, 254–257.

Werne, J.P. (2004) Organic sulfur biogeochemsitry: Recent advances and future research directions. Geological Society of America Special Paper 379.

Yücel M., Gartman A., Chan C. S. and Iii G. W. L. (2011) Hydrothermal vents as a kinetically stable source of iron-sulphide-bearing nanoparticles to the ocean. *Nat. Geosci.* **4**, 367–371.

Yücel M., Konovalov S. K., Moore T. S., Janzen C. P. and Luther G. W. (2010) Sulfur speciation in the upper Black Sea sediments. *Chem. Geol.* **269**, 364–375.

Zeng T., Arnold W. A. and Toner B. M. (2013) Microscal Characterization of Sulfur Speciation in Lake Sediments. **47**, 1287-1296.

Zopfi, J., Ferdelman, T.G., Fossing, H. (2004) Distribution and fate of sulfur intermediates-sulfite, tetrathionate, thiosulfate, and elemental sulfur- in marine sediments. Geological Society of America Special Paper 379, 97-116.

APPENDIX

1. BACKGROUND FOR μXRD METHODS

X-Ray Diffraction (XRD) has been used for about a century for elucidating the structure of materials on the macroscopic scale (0.1-10mm) and has become the foundation of soil science research in determining the structure of soil inorganic constituents (Brindley and Brown 1980; MacDowell et al., 2001). MicroLaue diffraction combines the oldest x-ray diffraction method, Laue diffraction, with the most modern x-ray sources, optics and detectors. The technique combines an intense source, nondispersive monochromator that can be inserted into or out of the polychromatic x-ray beam to pass either a polychromatic or a tunable monochromatic beam onto the sample, a nondispersive focusing system (typically a Kirkpatrick-Baez Mirrors) that focuses either monochromatic or polychromatic beams to the same spot, a precision 3D stage to position the sample, and an x-ray sensitive area detector (Figure 1; Ice and Pang, 2009).

Ultra-brilliant X-ray synchrotron sources provide a nondestructive way to characterize the local crystal structure with submicron spatial resolution. X-rays produced by synchrotron radiation are several orders of magnitude brighter than those produced from X-ray tubes and rotating anodes in laboratory equipment. The high collimation and brightness of synchrotron radiation fostered the development of X-ray micro focusing optics, yielding the structure of micrometer sized crystals (Neder et al., 1999). Laue diffraction allows us to make direct comparisons with and provide guidance for emerging theoretical models for grain growth, in homogenoous deformation, and fracture (Ice and Pang, 2009).

For analysis, a long-distance microscope is used to position a sample on a stage so its surface intersects the beam near the focus of the nondispersive focusing optics. A polychromatic Laue pattern is collected with x-ray sensitive area detector. Fast and high resolution CCD (charge coupled device) detectors (Figure 2). Then, the pattern is indexed

with an automated indexing program using the known unit cell para meters of the undeformed material, usually silicon (Ice and Pang, 2009).

X-ray microdiffraction beamline end-station 12.3.2 at the ALS has optics designed to meet the requirement of a stable beam position and size on the sample while changing the radiation wavelength (Tamura et al., 2002). In 12.3.2 arrangement, the sample remains fixed except for translation motion in the plane of the sample. The detector can be rotated into an appropriate position around the sample. The sample is illuminated with focused white radiation and diffracted X-rays are recorded on a CCD detector as a Laue diffraction pattern. The pattern is indexed from a known structure to give crystal orientation. The combination of white and monochromatic beam measurements allows for the determination of the total strain/stress tensor (6 components) inside each sub-micron-sized illuminated volume of the sample. Then by scanning the photon energy and knowing the direction of the Laue beams and crystal orientation, d-spacing measurements can be made.

The relation between the CCD camera and the Bragg angle is calibrated by moving the CCD camera radially from the sample and recording the silicon Laue patterns at various distances from the sample. Lines drawn through the succession of the same Laue spots intersect at the sample point and this defines the sample position relative to the CCD X-ray detection surface. Using the silicon Laue pattern as a reference allows for detailed calibration of the roll, tilt, and yaw of the CCD X-ray detection surface (Figure 2).

Routine microbeam monochromatic powder diffraction will be used for samples with sufficient nanoparticulate phases. A large portion of the sample will be inaccessible to powder diffraction with a ~1 μm diameter microbeam. For these particles, Laue micro-diffraction will be used. Custom codes using an algorithms can automatically index the Laue patterns using the CCD/sample geometry and the known crystal structure of the sample, by fitting it to a range of crystalline sulfides known to be in the sample (Chung

and Ice, 1999). Sulfides will be chosen for our database based upon Fe and S 1s XANES results (see results in CHAPTERS 3 and 4).

2. METHODS

Micro-Laue X-ray diffraction data was collected at the Advanced Light Source in Berkeley, CA, instrument 12.3.2. Samples include SUPR22-0.5m, SUPR24-5m, SUPR26-15m, SUPR28-30m, and SUPR30-50m. These measurements generated ~400 diffraction data files each. These data will be curated using a custom software program developed by the Advanced Light Source to collect and analyze X-ray microdiffraction data, called X-ray Microdiffraction Analysis Software (XMAS). The data output from XMAS will include crystallographic patterns for the vent particles. To identify the mineral form, these patterns will be fit against a database of sulfides using a supercomputer.

Microbeam monochromatic powder diffraction was also conducted at 12.3.2. Samples include SUPR22-0.5m, SUPR24-5m, SUPR26-15m, SUPR28-30m, and SUPR30-50m. These measurements generated ~10 diffraction data files each (Figure 3a,b). From the monochromatic XRD patterns we can integrate along 2theta and obtain a 1D pattern using XMAS (Figure 3c). Then, the 1D pattern will be analyzed using a custom software program called JADE (Materials Data Inc.).

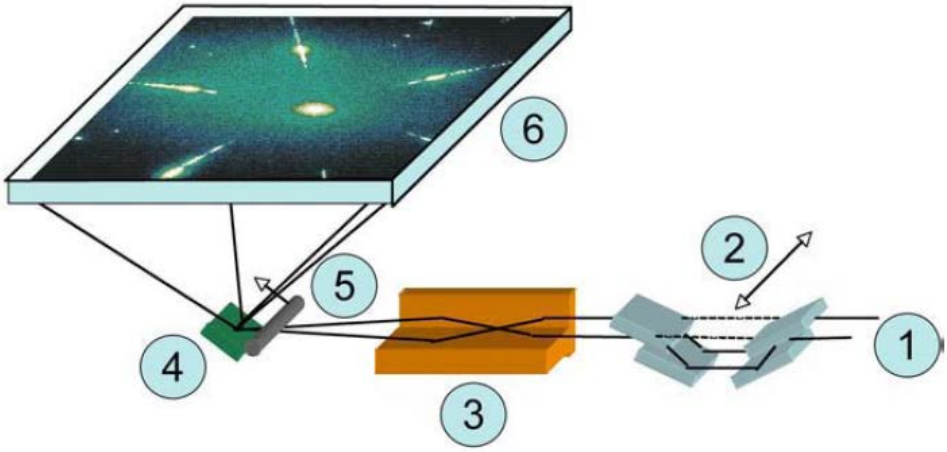

Figure 1: Schematic for sample orientation relative to detector and incident X-rays at 12.3.2. This shows a generic polychromatic microdiffraction system with six key elements: (1) an x-ray source; (2) nondispersive monochromator that can be moved into or out of the beam; (3) achromatic focusing optics; (4) a precision sample stage; (5) an x-ray absorbing wire (not in the current setup); and, (6) an x-ray sensitive area detector. (figure from Ice et al., 2009)

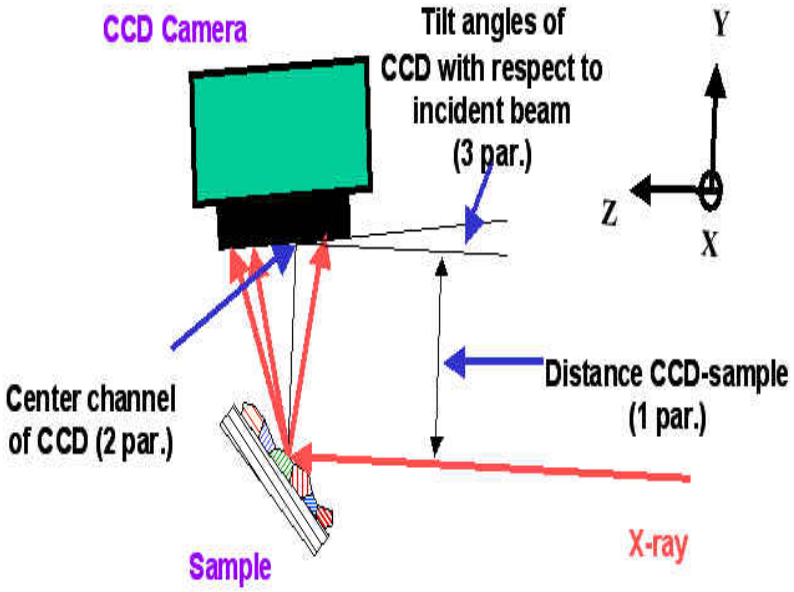

Figure 2: Schematic of tilt angles of CCD camera with relation to X-ray source and sample orientation.

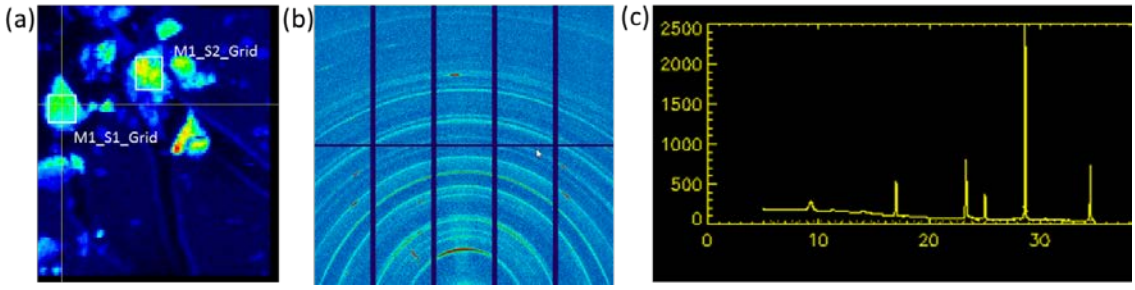

Figure 3: Workflow for microbeam monochromatic powder diffraction data analysis. (a) XRF data was collected at 12.3.2; (b) monochromatic powder diffraction was collected at discrete locations; (c) the data was converted to 1D pattern that will be assessed in JADE.